Infrared-Induced Quasiparticles in Superconducting Qubits

Zur Erlangung des akademischen Grades eines

Doktors der Naturwissenschaften (Dr. rer. nat.)

von der KIT-Fakultät für Physik des
Karlsruher Instituts für Technologie (KIT)

genehmigte
Dissertation

von
M.Sc. Markus Griedel
aus Konstanz

Tag der mündlichen Prüfung: 24. April 2026
1. Referent: Prof. Dr. Alexey V. Ustinov
2. Referent: Prof. Dr. Matthieu Le Tacon

Abstract

Quasiparticle (QP) poisoning limits the coherence of superconducting qubits, yet the microscopic mechanisms that create nonequilibrium QPs and practical strategies to suppress them remain active research topics. This thesis presents the results of experiments conducted to quantitatively investigate the impact of pair-breaking radiation on superconducting transmon qubits within the frequency spectrum typically emitted by the warmer stages of a low-temperature cryostat. It also introduces an efficient cryogenic filter aimed at suppressing this source of decoherence.

A calibrated blackbody radiator illuminates a transmon qubit chip via a controllable radiation path within the 0.1 THz to 1 THz (0.5 K to 10 K) range, while monitoring the qubit properties at millikelvin temperatures. The induced QPs possess energies close to the superconducting gap, placing them in the sparsely explored low-energy QP regime. The experimental findings are compared with analytical and numerical models, allowing the photon-to-QP conversion time to be determined. Analysis of different qubit architectures indicates that this conversion time increases with the qubit's offset-charge sensitivity.

To mitigate QP poisoning, a novel low-pass filter material based on a sapphire-powder composite is developed. Mie scattering calculations predict a tunable transition between the pass band and the stop band, which is confirmed by infrared spectroscopy measurements. Cryogenic characterization demonstrates the desirable low loss in the microwave pass band. Incorporating such filters into the radiation path of a blackbody setup efficiently suppresses the production of excess QPs by infrared photons and can be adapted to specific requirements by adjusting the geometry and the filter material composition.

Zusammenfassung

Quasiteilchen begrenzen die Kohärenz supraleitender Qubits, doch die mikroskopischen Mechanismen, die Quasiteilchen außerhalb des Tieftemperaturgleichgewichts erzeugen, sowie praktische Strategien zu ihrer Unterdrückung sind weiterhin Gegenstand aktueller Forschung. Diese Arbeit präsentiert die Ergebnisse von Experimenten, die den Einfluss paarbrechender Strahlung auf supraleitende Transmon-Qubits quantitativ untersuchen. Der untersuchte Frequenzbereich ist vergleichbar mit den Photonen, die typischerweise von den wärmeren Stufen eines Kryostaten emittiert werden. Außerdem wird das Konzept eines neuen effizienter kryogener Filters vorgestellt, der auf die Unterdrückung dieser Quasiteilchen abzielt.

Ein kalibrierter Schwarzkörperstrahler bescheint einen Transmon-Qubit-Chip über einen kontrollierbaren Strahlungspfad im Bereich von 0,1 THz bis 1 THz (0,5 K bis 10 K), während die Qubiteigenschaften bei Millikelvin-Temperaturen überwacht werden. Die induzierten Quasiteilchen besitzen Energien nahe der supraleitenden Lücke und befinden sich damit in dem bislang nur wenig untersuchten niederenergetischen Quasiteilchen-Regime. Die experimentellen Ergebnisse werden mit analytischen und numerischen Modellen verglichen, was die Bestimmung der Photon-zu-Quasiteilchen-Umwandlungszeit ermöglicht. Die Analyse verschiedener Qubit-Architekturen weist darauf hin, dass diese Umwandlungszeit mit der Offset-Ladungsempfindlichkeit des Qubits zunimmt.

Zur Minderung der Quasiteilchen wird ein neuartiges Tiefpass-Filtermaterial auf Basis eines Saphir-Pulver-Verbundstoffs entwickelt. Mie-Streuungsrechnungen sagen einen einstellbaren Übergang zwischen Durchlassband und Sperrband voraus, was durch infrarotspektroskopische Messungen bestätigt wird. Kryogene Charakterisierung demonstriert die gewünschten geringen Verluste im Mikrowellen-Durchlassband. Die Integration solcher Filter in den Strahlungspfad des Schwarzkörpersystems unterdrückt effizient die Erzeugung überschüssiger Quasiteilchen durch Infrarotphotonen. Ein solcher Filter kann durch Anpassung der Geometrie und der Filtermaterial-Zusammensetzung an spezifische Anforderungen angepasst werden.

Contents

1. Introduction

Superconducting circuits constitute one of today's most promising candidate platforms for scalable quantum computing [1, 2]. Recent processors have already demonstrated quantum advantage for specific tasks [3, 4]. The fundamental building block of a quantum computer is the qubit, the quantum analog of the classical bit. These qubits use a Josephson junction as a nonlinear inductor shunted with a capacitor, forming an anharmonic quantum oscillator with the two lowest levels used for operation [5–7]. State-of-the-art qubits, with transition frequencies in the microwave regime, reach coherence times on the order of $\sim 100\,\mu s$ [8–11]; typical times per elementary quantum operation (gate) are on the order of $\sim 10\,ns$ to $100\,ns$ [2, 12]. With this, roughly 10^3 operations per coherence time are possible. Using such qubits, larger circuits have been built with on the order of a few dozen to one thousand qubits [13–16]. However, for a large-scale, fault-tolerant quantum computer, hundreds to thousands of physical qubits are necessary to encode a single logical qubit, since quantum states cannot be cloned, so redundancy must be achieved by spreading the quantum information across multiple entangled physical qubits. In this way, errors in single qubits can be detected and corrected without disturbing the logical state [11, 17–25]. Qubits can lose their information, since they are highly susceptible to noise, decoherence, and gate imperfections [8].

Coherence in single qubits is limited by two major effects: first, coupling to two-level systems (TLS), which are defects in amorphous structures on the sample, for example in the Josephson tunnel barrier [26–36]; second, quasiparticles (QPs), which are excitations above the superconducting ground state and can be thought of as broken Cooper pairs [37–43]. These QPs can be produced by incoming photons that have enough energy to break a Cooper pair. For the typically used superconductor, aluminum, this required energy is $> 87\,h\,GHz$, corresponding to twice the superconducting gap 2Δ. Therefore, photons from the very far infrared and sub-terahertz regime all the way to the optical regime and above have enough energy to induce QPs.

To mitigate the effects of QPs, substantial research effort has been devoted in recent years. The first breakthrough was the development of more charge-insensitive qubits, the transmon [7], which is nowadays used in all large-scale quantum processors [13, 14, 44] and is the superconducting qubit type achieving the highest energy relaxation times [8, 9]. Further improvements were achieved by the use of other superconducting materials with a higher superconducting gap in the capacitor pads of the qubits, minimizing the density and production of QPs in these structures. But even with these more charge-insensitive qubits, coherence is sensitive to QP tunneling events, as expected theoretically [45–48] and also measured in numerous studies [38, 49–51], including this work. In recent years major progress has been made towards mitigation of QP tunneling events through gap engineering [11, 49, 52–55]. However, this does not reduce the number of QPs but only suppresses their tunneling rate. A more fundamental approach is to limit the production of QPs by infrared light through shielding in a light-tight enclosure [56, 57]. This is implemented in all superconducting qubit measurements nowadays in one form or another. However, the coaxial readout lines used for microwave qubit readout must enter this sample enclosure, and the typical dielectric, Teflon (polytetrafluoroethylene, PTFE), is transparent over large ranges of the infrared frequency spectrum, as shown in this work. Therefore, a low-pass

filter with a sharp cutoff frequency is needed. Typical approaches [58–60] often include variants of Eccosorb [61], a commercial material with large infrared absorption but substantial loss in the microwave regime [62]. Therefore, these filters can significantly reduce infrared photon flux, but they often introduce substantial microwave loss and have no tunability of the cutoff frequency. Especially for qubit applications targeting higher frequencies in the 20 GHz regime or even the 100 GHz range, which is part of ongoing research [63, 64], this becomes an increasingly serious problem.

Therefore, it is of research interest to investigate QPs in superconducting qubits [38, 50, 51, 56, 65–74] and find better ways to mitigate them [11, 49, 53–55, 75–78]. Two closely related questions arise: How do infrared photons induce QPs in superconducting qubits, and how does this depend on qubit design? How can infrared radiation be filtered efficiently along the microwave lines to suppress QP generation without degrading microwave performance?

This thesis aims to contribute to this effort by measuring the effect of infrared-induced QPs on transmon qubits and comparing the results to theory [45, 46, 79–81] to gain insight into the infrared-photon to QP conversion properties. A controlled irradiation scheme allows quantitative comparison between measured QP-induced decoherence and theoretical models of infrared absorption and QP dynamics, extending previous studies [50, 51, 56, 82]. Furthermore, different qubit architectures with different offset-charge sensitivity are compared with respect to their response to infrared photons. This thesis presents a cryogenic measurement setup using a blackbody radiator whose temperature, and therefore photon and power emittance, can be controlled with a resistive heater and a thermometer. Through a controlled path, this radiation is injected directly into the sample box of the qubit without causing thermal heating of the sample or other parts of the cryostat. The photons lead to QP production in the superconducting leads, which tunnel through the junction and cause decoherence and other effects in the qubit.

Furthermore, a novel infrared filter material is demonstrated, exploiting that the electromagnetic interaction is strongest when the wavelength and the diameter of a particle are comparable, while it decreases rapidly for larger wavelength. Mixing different-size particles can therefore be used to build a broadband extinction filter, where the cutoff frequency is tunable by adjusting the mixture. A compound of sapphire spheres with different diameters is used. Its filtering properties are modeled using analytical scattering theory and measured in an infrared spectrometer, from which a promising low-pass performance is foreseen with large attenuation in the stop band and close to zero attenuation over the full pass band. From the material, a prototype coaxial filter is built, which is characterized at millikelvin temperatures. The filter concept explored in this thesis aims to overcome limitations of existing approaches.

This thesis is outlined as follows: Ch. 2 provides the theoretical background on superconducting theory including Josephson junctions and the microscopic description of the superconductor in the framework of BCS theory, which introduces QPs. Furthermore, different generation mechanisms of QPs are introduced as well as impacts of QPs on superconducting properties. In Ch. 3 the basic concepts of qubits are explained, including their decoherence and the Hamiltonian description of the different charge-sensitivity regimes. The impact of QPs on the qubit is also investigated theoretically. Ch. 4 summarizes the experimental methodology, describing the readout chain, the cryogenic measurement setup, and the design of the different samples. Furthermore, characterization measurements of the samples are presented. Chapter 5 presents measurements with a cryogenic blackbody source that delivers controlled infrared photon flux to the qubits. Observed changes in frequency, relaxation, and dephasing times reveal how IR-generated QPs evolve and degrade coherence, and address the first central question on QP dynamics in superconducting qubits. In Ch. 6 the novel sapphire-powder-based infrared filter

material is discussed. The idea of this filter material is presented, supported by scattering-theory-based calculations and measurements with an infrared spectrometer to characterize the stop band and compare it to other materials that are measured as well. Furthermore, measurements of a prototype filter in the microwave pass band regime are presented and cryogenic stop band measurements in the blackbody radiation setup used in Ch. 5. This chapter addresses the second central question of how to efficiently suppress infrared radiation along the microwave lines without compromising microwave performance. Finally, Ch. 7 concludes and discusses all the findings from a broader perspective and gives an outlook on potential follow-up research directions.

2. Quasiparticles in superconductors

In this chapter, the theoretical background on superconductors (Sec. 2.1) and the Josephson junction (Sec. 2.2), a key nonlinear element of superconducting qubits, is presented. Furthermore, quasiparticles (QPs) as a consequence of the microscopic description of superconductivity are introduced (Sec. 2.3), as well as their dynamics (Sec. 2.4), sources (Sec. 2.5) and effects (Sec. 2.6). Much of this chapter follows the textbook by Tinkham [83] and the thesis by Serniak [84], which are recommended for a more in-depth view.

2.1. Superconductivity

The discovery and theoretical understanding of superconductivity constitute pivotal milestones in condensed matter physics. The phenomenon was first observed in 1911 by Heike Kamerlingh Onnes, who measured the sudden disappearance of electrical resistance in mercury below 4.2 K [85]. Subsequent experiments revealed similar superconducting transitions in various metals and alloys, though the underlying mechanism remained elusive for decades. In 1933, the Meissner–Ochsenfeld experiment demonstrated that superconductors expel magnetic fields and thus are not merely perfect conductors; they are also ideal diamagnets [86]. The microscopic explanation for this was developed in 1957, nearly 50 years later, with the *Bardeen–Cooper–Schrieffer (BCS)* theory [87]. The theory shows that a weak attractive interaction between electrons, mediated by lattice vibrations (phonons), can overcome Coulomb repulsion and cause an instability of the Fermi-sea ground state. As a result, electrons with opposite momenta and spins form bound pairs, known as *Cooper pairs*. These pairs behave as bosons and condense into a macroscopic quantum state described by a single wavefunction, leading to the emergence of superconductivity. This theory and the excitations above this ground state, *quasiparticle excitations*, are discussed in more detail in Sec. 2.3. A superconductor has a characteristic energy gap 2Δ, corresponding to the energy required to break Cooper pairs.[1] At absolute zero, the gap is given by $\Delta(T=0) = 1.764\, k_B T_C$, where T_C denotes the critical temperature.[2] As the temperature approaches T_C from below, thermal excitations populate states above the gap and the gap gradually closes at T_C; the system returns to the normal-conducting state. The concept of a macroscopic quantum state described by a single wavefunction was first introduced phenomenologically by the Ginzburg–Landau theory in 1950 [88]. Although the Ginzburg–Landau theory successfully captures many macroscopic properties of superconductors, it does not describe the microscopic mechanism of electron pairing mediated by lattice vibrations. However, the theory was later shown to be derivable from the microscopic BCS theory [89]. Within this framework, the wavefunction is expressed as

$$\Psi(\mathbf{r}) = \sqrt{n(\mathbf{r})}\, e^{i\phi(\mathbf{r})}, \tag{2.1}$$

[1] This gap was experimentally observed but was not explained by the phenomenological Ginzburg–Landau theory used in this chapter but follows from BCS theory (Sec. 2.3).

[2] The factor 1.764 arises from BCS theory and is equivalent to π/e^{γ}, where γ is the Euler–Mascheroni constant.

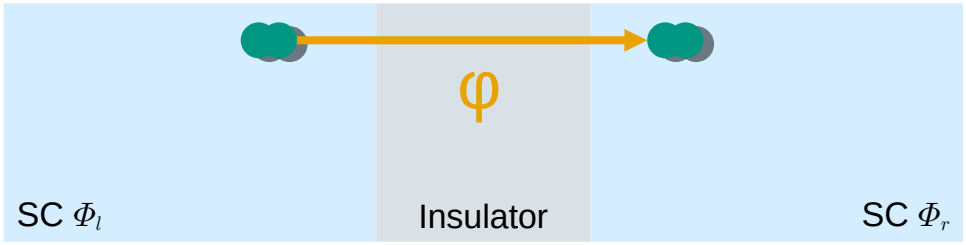

Figure 2.1.: Schematic drawing of a Josephson junction. The two superconductors are shown in light blue with the phase ϕ_l on the left side and ϕ_r on the right side of an insulating or normal-conducting barrier (gray). Cooper pairs can tunnel through this barrier due to an overlap of the superconducting wavefunction. The phase difference between the two sides is φ, the Josephson phase.

where $n(\mathbf{r})$ denotes the local density of Cooper pairs and $\phi(\mathbf{r})$ denotes their phase. From this wavefunction, a coherence length ξ can be defined. It describes the spatial scale over which $\Psi(\mathbf{r})$ varies significantly. The coherence length also characterizes the penetration of superconducting correlations (proximity effect) into adjacent nonsuperconducting materials, which is relevant in the following.

2.2. Josephson junctions

Based on this phenomenological understanding, Josephson predicted in 1962 [90] that a supercurrent can flow through a weak link (e.g., a thin normal-conducting or insulating barrier) between two superconductors, known as a *Josephson junction* (short just *junction*, or JJ), as depicted in Fig. 2.1.

A Josephson junction can be characterized by a phase drop, $\varphi = \phi_r - \phi_l$, occurring between the two sides (l and r), the *leads*, of the junction; ϕ_l and ϕ_r denote the macroscopic superconducting phases of the left and right electrodes, respectively. This quantity is referred to as the *Josephson phase*. Josephson formulated two fundamental *Josephson equations*. The first Josephson equation predicts a supercurrent I_S flowing across the junction at zero voltage as a function of the critical current, denoted I_c, and the Josephson phase, φ:

$$I_S = I_c \sin\varphi. \tag{2.2}$$

The second Josephson equation describes the dynamics of the phase drop φ when a dc voltage V is applied across the junction:

$$\dot{\varphi} = \frac{2e}{\hbar} V, \tag{2.3}$$

where e is the elementary charge and $\hbar$ is the reduced Planck constant. Combining the two Josephson equations gives the Josephson potential

$$U(\varphi) = \int IV \,\mathrm{d}t = -\frac{\Phi_0 I_c}{2\pi} \cos\varphi = -E_J \cos\varphi, \tag{2.4}$$

where $\Phi_0 = \frac{h}{2e}$ is the flux quantum, and with $E_J = \frac{\Phi_0 I_c}{2\pi}$, the *Josephson energy* is introduced.

A significant relation exists between the superconducting energy gap Δ, the normal-state resistance R_n, and the critical current I_c, as captured by the Ambegaokar–Baratoff relation [91]:

$$I_c = \frac{\pi\,\Delta}{2eR_n}, \tag{2.5}$$

valid for identical superconducting leads in the tunneling (weak-coupling) limit at zero temperature. This can also be expressed in the form of the Josephson energy:

$$E_J = \frac{\pi\hbar\,\Delta}{4e^2 R_\mathrm{n}}, \tag{2.6}$$

where R_n is the normal-state resistance of the junction. This relation links Cooper-pair tunneling and single-electron transport and will be relevant when discussing QP tunneling in Sec. 2.6.2.

Josephson junctions are now recognized as essential components in superconducting circuits. They provide the nonlinearity through the $\cos\varphi$–potential (Eq. 2.4) crucial for superconducting qubits, as discussed in Sec. 3.2.

2.3. BCS theory and quasiparticles

Having introduced the phenomenological description in the previous chapter, the discussion now turns to the microscopic framework that explains why superconductivity occurs. Named after its inventors Bardeen, Cooper, and Schrieffer, the BCS theory expands the electron model of metals with an attractive interaction between electrons. This principle is encapsulated in the BCS Hamiltonian:

$$\hat{H} = \sum_{ks} \xi_k\, \hat{c}^\dagger_{ks}\hat{c}_{ks} + \frac{1}{N}\sum_{kk'} V_{kk'}\hat{c}^\dagger_{k\uparrow}\hat{c}^\dagger_{-k\downarrow}\hat{c}_{-k'\downarrow}\hat{c}_{k'\uparrow}, \tag{2.7}$$

The first term describes the kinetic energy of electrons in a normal metal. Here $\hat{c}^\dagger_{ks}$ and $\hat{c}_{ks}$ are creation and annihilation operators for electrons with momentum k and spin s. The quantity $\xi_k = \hbar^2k^2/(2m_e) - \epsilon_F$ is the single-electron kinetic energy measured relative to the Fermi energy ϵ_F. The second term is the *BCS-pairing Hamiltonian*, where N is the number of available momentum states (or lattice sites), introduced to normalize the interaction term. The phonon-mediated potential $V_{kk'}$ provides an attractive interaction that pairs electrons with opposite momenta into Cooper pairs; consequently $V_{kk'}$ must be negative.

The *condensation energy* (also called the BCS pair potential) quantifies the energy saved when an electron joins a Cooper pair. It is defined as

$$\Delta_k = -\sum_{k'} V_{kk'}\,\langle\hat{c}_{-k'\downarrow}\hat{c}_{k'\uparrow}\rangle. \tag{2.8}$$

In general Δ_k is complex; its phase is the macroscopic superconducting phase.

The four-operator term in Eq. 2.7 can be replaced by its mean-field approximation. Substituting the definition of the condensation energy (Eq. 2.8) into Eq. 2.7 and discarding second-order fluctuation terms yields the mean-field BCS Hamiltonian:

$$\hat{H}^\mathrm{MF}_\mathrm{BCS} = \sum_{ks} \xi_k\,\hat{c}^\dagger_{ks}\hat{c}_{ks} - \sum_k \Big(\Delta^*_k\,\hat{c}_{-k\downarrow}\hat{c}_{k\uparrow} + \Delta_k\,\hat{c}^\dagger_{k\uparrow}\hat{c}^\dagger_{-k\downarrow} + \mathrm{const}\Big). \tag{2.9}$$

For the derivation see Ref. [83]. The first term reproduces the kinetic part, while the second term contains the pairing contributions that survive the mean-field truncation. The result shows the Cooper pair structure through bilinear operators. The Cooper pair contribution carries the opposite sign to the normal-metal term, therefore forming a Cooper pair lowers the total energy.

In this mean-field form, the Hamiltonian can be diagonalized by a linear transformation that defines new fermionic operators $\hat{\gamma}_k$. Originally shown by Bogoliubov [92] and Valatin [93], this transformation is called the Bogoliubov transformation and is given by

$$\begin{aligned} \hat{c}^\dagger_{k\uparrow} &= u_k^* \, \hat{\gamma}_{k\uparrow} + v_k \, \hat{\gamma}^\dagger_{-k\downarrow}, \\ \hat{c}^\dagger_{-k\downarrow} &= -v_k^* \, \hat{\gamma}_{k\uparrow} + u_k \, \hat{\gamma}^\dagger_{-k\downarrow}, \end{aligned} \tag{2.10}$$

where the coefficients satisfy $|u_k|^2 + |v_k|^2 = 1$. The operators $\hat{\gamma}^\dagger_k$ ($\hat{\gamma}_k$) create (annihilate) the so-called Bogoliubov quasiparticle excitations (QPs). These QPs are fermions that obey the usual anticommutation relation $\{\hat{\gamma}^\dagger_k, \hat{\gamma}_{k'}\} = \delta_{kk'}$ and are quantum superpositions of electron creation ($\hat{c}^\dagger$) and hole creation ($\hat{c}$) operators. Replacing the electron and hole operators in Eq. 2.9 by the Bogoliubov operators diagonalizes the Hamiltonian when the coefficients u_k and v_k are chosen as

$$|v_k|^2 = 1 - |u_k|^2 = \frac{1}{2}\Big(1 - \frac{\xi_k}{\sqrt{\xi_k^2 + \Delta_k^2}}\Big) = \frac{1}{2}\Big(1 - \frac{\xi_k}{\varepsilon_k}\Big). \tag{2.11}$$

Here the QP energy $\varepsilon_k \equiv \sqrt{\xi_k^2 + |\Delta_k|^2}$ is introduced. All u_k are taken to be real, so the phase of v_k follows the phase of Δ_k. The Hamiltonian becomes diagonal and reads

$$\hat{H}^{\text{eff}}_{\text{BCS}} = E_{\text{GS}} + \sum_k \varepsilon_k \big(\hat{\gamma}^\dagger_{k\downarrow}\hat{\gamma}_{k\downarrow} + \hat{\gamma}^\dagger_{k\uparrow}\hat{\gamma}_{k\uparrow}\big), \tag{2.12}$$

where the superconducting ground-state energy is

$$E_{\text{GS}} = \sum_k \Big(\xi_k - \varepsilon_k + \Delta_k \, \langle \hat{c}^\dagger_{k\uparrow}\hat{c}^\dagger_{-k\downarrow}\rangle\Big). \tag{2.13}$$

The summation term yields the energy of the QP excitations for both spin polarizations above this ground state. For further simplification a momentum-independent interaction $V_{kk'} = V$ is assumed below the Debye frequency ($|\xi_k|, |\xi_{k'}| < \hbar\omega_D$), known as the *BCS approximation*. Consequently, the pairing energy $\Delta_k = \Delta$ becomes momentum independent. The QP excitation energy is exactly the above-defined $\varepsilon = \sqrt{\xi^2 + \Delta^2}$. The minimum of this dispersion is Δ (at $\xi_k = 0$), so Δ is identified as the superconducting energy gap, in agreement with the phenomenological gap introduced in the previous section.

The structure closely mirrors the normal-metal Hamiltonian (first term in Eq. 2.7), where the operators c_{ks} are replaced by γ_{ks}. Creating a QP removes a particle from the condensate and costs the energy ε_k. Because each QP is a superposition of electrons and holes, its charge depends on the excitation energy. The charge expectation value reads

$$\langle \hat{Q} \rangle = e\big(|u_k|^2 - |v_k|^2\big). \tag{2.14}$$

Consequently, QPs near the gap behave like neutral excitations, while high-energy QPs carry the full electron charge.

The BCS ground state

The BCS ground state $|\Psi_{\text{BCS}}\rangle$ must satisfy

$$\hat{\gamma}_{k\uparrow}\,|\Psi_{\text{BCS}}\rangle = \hat{\gamma}_{k\downarrow}\,|\Psi_{\text{BCS}}\rangle = 0. \tag{2.15}$$

These relations state that the BCS ground state is annihilated by all Bogoliubov annihilation operators; it is therefore the vacuum of QPs. By *guessing* this lowest-energy eigenstate (the ground state)[3], one obtains

$$|\Psi_{\mathrm{BCS}}\rangle = \prod_k \left(u_k + v_k\, e^{i\phi}\, \hat{c}^\dagger_{k\uparrow}\hat{c}^\dagger_{-k\downarrow}\right)|0\rangle. \tag{2.16}$$

The coefficients u_k and v_k are taken to be real; the macroscopic phase coherence appears explicitly as the factor $e^{i\phi}$. This phase coherence is the characteristic phase of a superconductor. Physically, $|u_k|^2$ and $|v_k|^2$ are the probabilities that a Cooper pair with momentum k is empty or occupied, respectively. The state $|0\rangle$ is the *true vacuum*[4] of the normal metal (empty of electrons). The BCS ground state carries zero total spin and zero total momentum. Only the v_k term contains creation operators, so the ground state mixes each pair state with the corresponding empty-pair state. The mixing amplitudes u_k and v_k depend on the single-particle energy ξ_k through the coherence factors (see Eq. 2.11). Acting with a Bogoliubov creation operator on this ground state yields an excited state:

$$\hat{\gamma}^\dagger_{k\uparrow}|\Psi_{\mathrm{BCS}}\rangle = \hat{c}^\dagger_{k\uparrow}\prod_{k'\neq k}\left(u_{k'} + v_{k'}\, e^{i\phi}\, \hat{c}^\dagger_{k'\uparrow}\hat{c}^\dagger_{-k'\downarrow}\right)|0\rangle. \tag{2.17}$$

This operation breaks a Cooper pair in the ground state, leaving an unpaired electron-hole excitation. The resulting state is an eigenstate with energy $\varepsilon_k = \sqrt{\xi_k^2 + \Delta^2}$ above the ground state energy (Eq. 2.13).

Excitation picture and density of states

Two complementary descriptions of Bogoliubov QPs exist: the *single-particle picture* and the *excitation picture*. The difference stems from the choice of vacuum state. The vacuum is defined by $\hat{\gamma}_{ks}|\mathrm{vac}\rangle = 0$. In the excitation picture the BCS ground state is taken as the vacuum; in the single-particle picture the filled Fermi sea of electrons is referred to as the vacuum.

In this work the excitation picture is chosen by the chosen Bogoliubov transformation (Eq. 2.10). In the excitation picture introduced above, all equilibrium QPs are already incorporated in the BCS ground state, which therefore serves as the vacuum. By analogy with a normal metal, the superconducting density of states (DOS) ρ_s follows from

$$\rho_s(\varepsilon)\,\mathrm{d}\varepsilon = \rho_n(\xi)\,\mathrm{d}\xi. \tag{2.18}$$

In the weak-coupling BCS regime $\Delta \ll \varepsilon_F$ the normal-state DOS $\rho_n(\xi) = \rho_0$ may be approximated as a constant with its value at the Fermi surface.[5] This yields the BCS DOS

$$\rho_s(\varepsilon) = \begin{cases} \rho_0 \dfrac{\varepsilon}{\sqrt{\varepsilon^2 - \Delta^2}}, & \varepsilon > \Delta, \\ 0, & \varepsilon < \Delta. \end{cases} \tag{2.19}$$

Fig. 2.2 (left) displays this result. The expression exhibits the known energy gap of width 2Δ for a pair of QP excitations at zero temperature.

[3] This state is the lowest-energy eigenstate only when the system contains an even number of electrons.
[4] The choice of vacuum is a convention that will become clear in the next section. By *true* vacuum state, the normal-metal vacuum state is meant, which is empty of electrons.
[5] The energies ξ differ from ε_F by only a few meV.

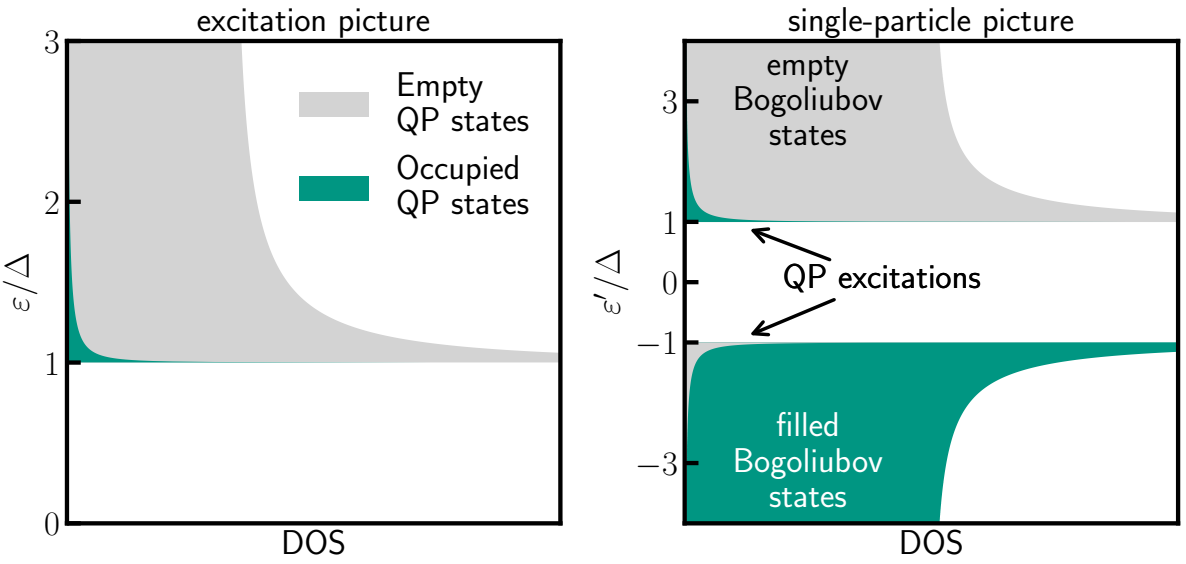

Figure 2.2.: Density of states (DOS) on the horizontal axis, as a function of energy ε' on the vertical axis. Left: Density of states in the excitation picture. When translating from the single-particle picture, negative-energy states (holes) become positive-energy QP excitations (QPs). Right: The single-particle picture; here the QPs correspond to unfilled states below the Fermi surface and filled states above it. In the excitation picture, the energy windows therefore have twice the degeneracy compared to those in the single-particle picture. The negative-energy states (only filled states) are treated as the vacuum by renormalization.

In the excitation picture, QPs that are true excitations out of the ground state are distinguished from those that are part of the condensate, and the hole-like states below the Fermi surface are reinterpreted as particle-like excitations.[6] Fig. 2.2 (right) shows the DOS in the single-particle picture. In this description QPs are understood both as excitations above the ground state and as constituents of the Cooper pair condensate; the difference originates from a different Bogoliubov transformation. From now on the work proceeds exclusively in the excitation picture and refers to excitations out of the condensate simply as QPs.

2.4. Quasiparticle generation, trapping and recombination

In the last sections QPs were introduced as excitations above the condensate arising from the BCS theory. It is more convenient to work with the QP number density n_{qp} normalized to the Cooper pair density n_{CP} rather than with the total QP number N_{qp}:

$$x_{\mathrm{qp}} = \frac{n_{\mathrm{qp}}}{n_{\mathrm{CP}}} = \frac{N_{\mathrm{qp}}}{N_{\mathrm{CP}}}. \tag{2.20}$$

Factoring out the Cooper pair density makes the quantity material independent. Consequently, results from different superconductors can be compared directly. For aluminum the Cooper pair density is of order $1 \times 10^{22}\,\mathrm{cm}^{-3}$ at $T = 0$,[7] This normalized QP density x_{qp} is the central

[6] Particle–hole symmetry is assumed, i.e., no charge imbalance between removing an up-spin electron and adding a down-spin hole.

[7] The estimate follows from the atomic density of aluminum $6 \times 10^{22}\,\mathrm{cm}^{-3}$ [94] and the fact that aluminum contributes three valence electrons, all of which participate in the condensate at zero temperature.

parameter used later to describe QP-induced qubit decay and dephasing (Sec. 3.3, Ch. 5). The normalized QP density x_{qp} follows from integrating the occupied QP states in the excitation picture:

$$x_{\mathrm{qp}} \;=\; \frac{1}{\rho_0 \Delta} \int_0^\infty f(\varepsilon)\, \rho_s(\varepsilon)\, \mathrm{d}\varepsilon. \tag{2.21}$$

Here $f(\varepsilon)$ is the QP distribution function and $\rho_s(\varepsilon)$ the superconducting density of states. The integration extends to zero energy so that subgap states—arising from deviations of the real DOS from the ideal BCS form—are also taken into account.

In general, the time evolution of the distribution function is

$$\frac{\mathrm{d}f(\varepsilon)}{\mathrm{d}t} = g(\varepsilon) + I^s_{\text{e-ph}} + I^p_{\text{e-e}} + I_{\text{e-e}}. \tag{2.22}$$

The first term, $g(\varepsilon)$, is the QP generation rate, the second and third terms represent QP–phonon scattering and the pair-recombination rate, while the last term accounts for QP–QP scattering. These terms are referred to as collision integrals.

By integrating Eq. 2.22 over energy and using the definition (2.21), one obtains an approximate rate equation for the normalized density itself [50, 95]:

$$\frac{\mathrm{d}x_{\mathrm{qp}}}{\mathrm{d}t} = -\, r\, x_{\mathrm{qp}}^2 \;-\; s_0\, x_{\mathrm{qp}} \;+\; g. \tag{2.23}$$

The coefficient r is a combination of the pair-recombination and pair-breaking rate (QP–QP scattering), s_0 is the trapping rate that describes QP loss to homogeneously distributed residuals (e.g., normal-metal islands or defects), and g is the generation rate. The electron–phonon term in Eq. 2.22 introduced above preserves QP number and therefore does not contribute here.

2.5. Sources of quasiparticle excitations

In this section temperature and photons as sources of QPs and the resulting QP distribution functions, introduced in the previous section, are discussed.

2.5.1. Thermal quasiparticles

At finite temperatures $T > 0$, QPs can be thermally excited above the superconducting gap. Only temperatures below the critical temperature $T_{\mathrm{C}} = \Delta/(1.764 k_B)$ are relevant. Thermal QP excitations in equilibrium follow a Fermi–Dirac energy distribution, analogous to electronic excitations in a normal metal above the Fermi surface [83],

$$f(\varepsilon) = f_{\mathrm{FD}}(\varepsilon) = \frac{1}{e^{\varepsilon/k_B T} + 1}. \tag{2.24}$$

The QP density is assumed to remain small so that QPs are localized close to the gap edge. Under these conditions, the thermal QP density is given by [46]

$$x_{\mathrm{qp}}^{\mathrm{th}} \approx \sqrt{\frac{2\pi k_B T}{\Delta}}\, e^{-\Delta/k_B T}, \tag{2.25}$$

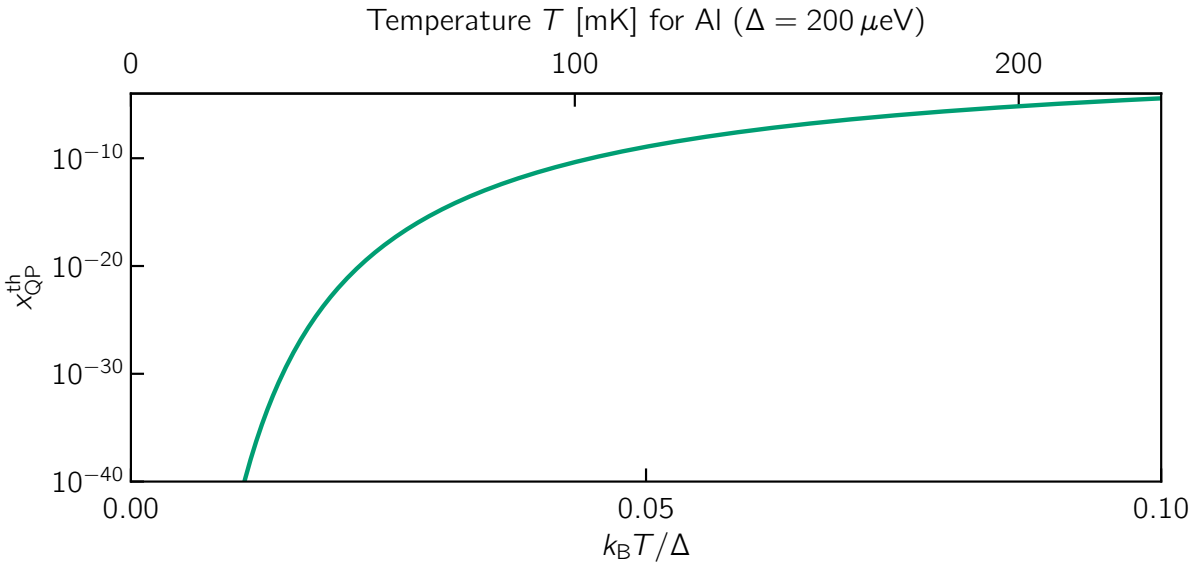

Figure 2.3.: Thermally generated QP density $x_{\mathrm{qp}}^{\mathrm{th}}$ as a function of normalized temperature T/Δ, following the approximation in Eq. 2.25. Additionally, on the top axis the corresponding temperature of aluminum with a gap of $\Delta \approx 200\,\mu$eV is given.

valid for finite temperatures below T_{C}. This relation between QP density and temperature is shown in Fig. 2.3. Due to the exponential suppression with decreasing temperature, experiments are performed at temperatures far below the transition temperature of the superconductor to minimize thermal QPs. From Fig. 2.3, the equilibrium QP density expected for aluminum devices at millikelvin temperatures is $\sim 10^{-50}$ (theoretical value at $T/\Delta \sim 0.015$). Experimentally, however, values in the range 1×10^{-9} to 1×10^{-5} are observed in qubit devices — 10^3–10^6 times higher [38, 50, 56, 66–71][8], indicating that additional QP generation mechanisms play an important role, or that the devices are not fully thermalized to the bath.

This thermal Fermi–Dirac distribution predicts, at millikelvin temperatures, a thermal QP population just above the gap edge, $\varepsilon \gtrsim \Delta$, which exponentially decreases towards higher energies. This behavior is shown for an example effective QP temperature of $T_{\mathrm{eff}} = 170\,\mathrm{mK}$ and aluminum in Fig. 2.4 (dashed line). Such a distribution with QPs close to the gap edge is therefore referred to as "cold" QPs and distinguished from "hot" QPs with energies significantly above the gap ($\varepsilon > 3\Delta$) [38, 96]. These "hot" QPs can cascade, through phonon scattering or breaking of other Cooper pairs, into "cold" QPs [38, 96, 97].

Thermalization is particularly difficult at very low temperatures because Cooper pairs, being a bosonic condensate, do not participate in the thermalization process. In addition, the thermal coupling between the phonons and the electrons or QPs is heavily suppressed. The power transfer between electrons and phonons drops with T^5 [98]:

$$P_{e\text{-}ph} \propto \left(T_e^5 - T_{ph}^5\right). \tag{2.26}$$

Therefore, the effective temperature, and thus the energy, of the QPs can differ from the temperature of the phonon bath at cryogenic temperatures.

[8] and many more

2.5.2. Photon-induced quasiparticles

One additional QP production process is through pair-breaking photons. The following discussion is restricted to QPs with kinetic energies below 3Δ ("cold" QPs). QPs with $\varepsilon > 3\Delta$ can break a Cooper pair in a multiplication process (original QP $\rightarrow$ original QP + 2 new gap-edge QPs), which cascades further. Due to the large density of states near the gap, this process is comparable in strength to phonon scattering. Thus, the number of QPs is assumed to be small compared to the number of Cooper pairs.

For photon-induced QPs, the simple Fermi–Dirac assumption used for thermal QPs is no longer valid. The general kinetic equation for the distribution function, Eq. 2.22, must therefore be solved. Since the number of QPs is small compared to the number of Cooper pairs, the last term—which is quadratic in the QP number—can be neglected. The QP generation rate (the first term in Eq. 2.22) depends on the details of the photon-induced pair-breaking process, but in the most general form it can be written as

$$g(\varepsilon) = \eta(\varepsilon)\, N_{\mathrm{ph}}(\varepsilon)\, \rho_s(\varepsilon), \tag{2.27}$$

where $\rho_s(\varepsilon)$ is the superconducting DOS, $N_{\mathrm{ph}}(\varepsilon)$ is the photon number spectral density of the QP-generating radiation, and $\eta(\varepsilon)$ describes the conversion between photons and QPs. As an approximation, $\eta(\varepsilon) = \eta$ is taken to be constant; it will be seen in Ch. 5 that this fits well to experimental results. All pair-breaking photons thus have the same probability to generate QPs. The QP generation rate can then be related to the number of photons radiated by a blackbody at fixed temperature,

$$N_{\mathrm{ph}}(\varepsilon) \propto \frac{\varepsilon^3}{e^{\varepsilon/k_B T_{\mathrm{BB}}} - 1}. \tag{2.28}$$

The photon flux n_{ph} of such a radiator is obtained by integrating the intensity spectrum over frequency and effective emission cone. This gives the first term in the distribution function, the generation process.

To understand the other terms in Eq. 2.22, a look at the phonons is necessary. Phonons are assumed to be well thermalized to the base temperature of the cryogenic experiment, $T_{\mathrm{ph}} \sim 20\,\mathrm{mK}$. The phonon occupation is then given by

$$N(\varepsilon) = \frac{1}{e^{\varepsilon/k_B T_{\mathrm{ph}}} - 1}. \tag{2.29}$$

At $T_{\mathrm{ph}} = 20\,\mathrm{mK}$, $N(\varepsilon) \ll 1$ for $\varepsilon \sim \Delta$ ($1.76 k_B T_{\mathrm{ph}} \sim 3\,\mu\mathrm{eV}$), strongly suppressing phonon-mediated generation versus relaxation.

Electron–phonon scattering will, on average, relax QPs towards the gap (cooling them) from energy ε to ε_1. Taking into account scattering in both directions (towards and away from the gap), the single-particle electron–phonon collision integral [79, 84, 99] is obtained as

$$\begin{aligned} I^s_{e\text{-}ph} =& \frac{1}{\tau_0 \Delta \rho_0} \int_\Delta^\varepsilon \mathrm{d}\varepsilon_1 \left(\frac{\varepsilon - \varepsilon_1}{\Delta}\right)^2 \left(1 - \frac{\Delta^2}{\varepsilon\varepsilon_1}\right) \rho_s(\varepsilon_1) \\ &\times \Big\{ [1 - f(\varepsilon)] f(\varepsilon_1) N(\varepsilon - \varepsilon_1) \\ &\quad - f(\varepsilon)[1 - f(\varepsilon_1)][N(\varepsilon - \varepsilon_1) + 1] \Big\} \\ &+ \frac{1}{\tau_0 \Delta \rho_0} \int_\varepsilon^\infty \mathrm{d}\varepsilon_1 \left(\frac{\varepsilon_1 - \varepsilon}{\Delta}\right)^2 \left(1 - \frac{\Delta^2}{\varepsilon\varepsilon_1}\right) \rho_s(\varepsilon_1) \\ &\times \Big\{ [1 - f(\varepsilon)] f(\varepsilon_1) [N(\varepsilon_1 - \varepsilon) + 1] \\ &\quad - f(\varepsilon)[1 - f(\varepsilon_1)] N(\varepsilon_1 - \varepsilon) \Big\}, \end{aligned} \tag{2.30}$$

and, in analogy, a pair-scattering collision integral that describes recombination and pair-breaking processes:

$$\begin{aligned} I^p_{e\text{-}ph} =& \frac{1}{\tau_0 \Delta \rho_0} \int_\Delta^\infty \mathrm{d}\varepsilon_1 \left(\frac{\varepsilon + \varepsilon_1}{\Delta}\right)^2 \left(1 + \frac{\Delta^2}{\varepsilon\varepsilon_1}\right) \rho_s(\varepsilon_1) \\ &\times \Big\{ [1 - f(\varepsilon)][1 - f(\varepsilon_1)] N(\varepsilon + \varepsilon_1) \\ &\quad - f(\varepsilon) f(\varepsilon_1) [N(\varepsilon + \varepsilon_1) + 1] \Big\}. \end{aligned} \tag{2.31}$$

The parameter τ_0 is the characteristic electron–phonon scattering time. In aluminum it is $\tau_0 = 438\,\mathrm{ns}$ [100].

Numerical solution of the steady–state kinetic equation (Eq. 2.22, $\partial f/\partial t = 0$) with these collision integrals yields the nonequilibrium $f(\varepsilon)$ as shown in Fig. 2.4 for exemplary blackbody temperatures. The linear conversion in the generation term is chosen such that it roughly matches the order of magnitude of the QP density x_qp of a thermal distribution at an effective QP temperature of $T_\mathrm{eff} = 170\,\mathrm{mK}$. For the temperature range shown here, the QPs lie even closer to the gap than for the thermal distribution.

To obtain the QP density x_qp for a blackbody generation term, the steady-state case of the rate equation (Eq. 2.23) must be solved. The generation g is obtained by integrating Eq. 2.27, the recombination r by integrating the pair-scattering collision integral in Eq. 2.31; this is done numerically for the same parameters as above. The ratio η/s_0 is chosen arbitrarily to match the experimentally observed QP density of $x_\mathrm{qp} \sim 10^{-5}$. Figure 2.5 shows the approximately linear scaling of x_qp with the photon flux from the blackbody radiator. This is due to the dominance of scattering and generation over the recombination term, since the QP density is low and the recombination rate scales quadratically with x_qp.

This motivates parametrizing the conversion from the photon number flux n_ph to the normalized QP density x_qp as linear:

$$x_\mathrm{qp} = \alpha\, n_\mathrm{ph}, \tag{2.32}$$

where α is a linear photon–QP conversion coefficient. With n_ph expressed in s^{-1} and x_qp dimensionless, α has units of seconds. Physically, α quantifies how efficiently incoming photons generate QPs at the junction: smaller α corresponds to a higher conversion efficiency (more QPs generated per photon flux and Cooper pair), while larger α indicates less efficient conversion.

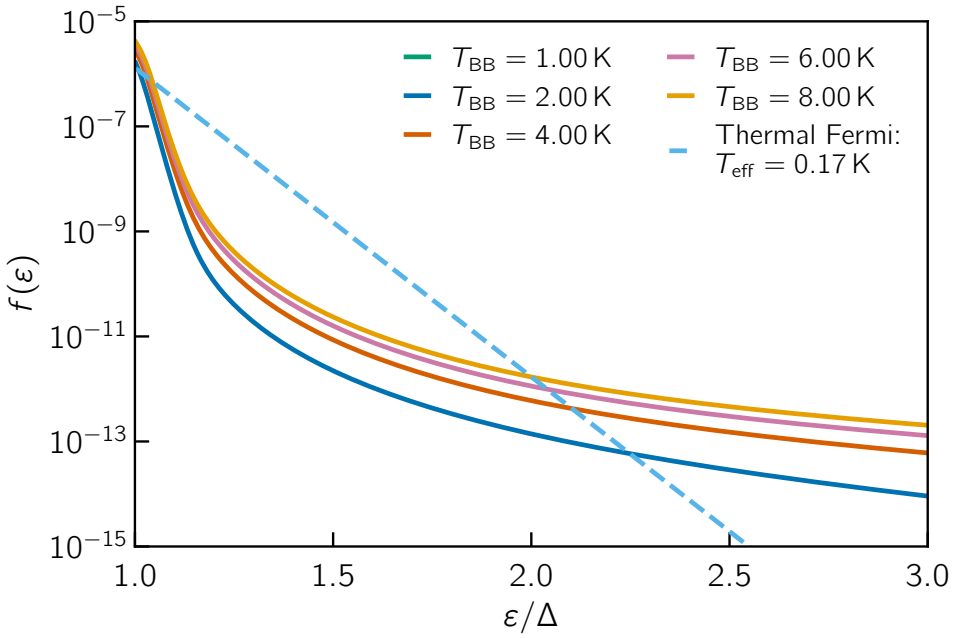

Figure 2.4.: The QP distribution function $f(\varepsilon)$ for different blackbody temperatures T_{BB} as a function of the QP energy with respect to the gap ε obtained from numerical steady-state solution of Eq. 2.22. For details on the scaling see main text. Additionally, the thermal distribution at an effective QP temperature of $T_{eff} = 170\,mK$ is shown for comparison.

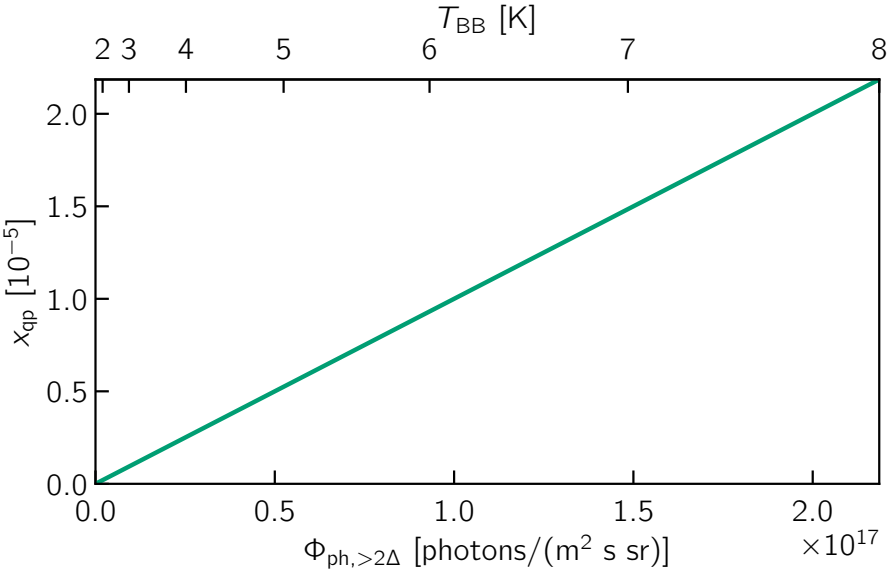

Figure 2.5.: The QP density x_{qp} as a function of the blackbody temperature (top axis), which can be converted into a normalized photon flux ϕ (bottom axis). This is the steady-state result of the rate equation (Eq. 2.23); for the parameterization, see main text.

This is only a motivated assumption with a large free parameter space and no full theoretical model. It will, however, describe the measured data well (Ch. 5).

Above, photons with a blackbody frequency distribution and energies below 3Δ were discussed, but high-energy photons, such as cosmic rays, can also produce QP bursts in the superconductor, as can other high-energy particles, e.g., muons. These processes have been investigated in

numerous experiments [72, 101–103]. Strong microwave drive can also lead to multiphoton absorption, producing pair-breaking phonons that diffuse into the superconductor [97]. Such pair-breaking phonons can also be caused by other effects, such as mechanical stress relaxation [104]. These effects would produce primarily "hot" QPs, but are not relevant in the experiments conducted in this thesis.

2.6. Quasiparticle effects in superconductors

QPs represent the fundamental excitations of a superconductor and are produced through different processes, as discussed in the previous sections. This section examines how QPs modify the properties of superconductors and Josephson junctions.

2.6.1. Gap modulation

The influence of QPs on the superconducting energy gap is considered first. Eq. 2.8 shows that the gap depends on the QPs. Using the Fermi–Dirac distribution $f(\varepsilon_{k'})$ (Eq. 2.24) for thermal QPs leads to the self-consistency condition for the energy gap

$$\Delta_k = -V \sum_{k'} \frac{\Delta_{k'}}{2\varepsilon_{k'}} \tanh\left(\frac{\varepsilon_{k'}}{2k_B T}\right). \tag{2.33}$$

This equation is solved for $\Delta(T) \to 0$ to determine the critical temperature T_C where the superconductor becomes normal conducting, which is equivalent to $\varepsilon_k \to \xi_k$. Converting the sum to an integral and using Fermi-surface symmetry yields [83]

$$k_B T_c = 1.13\, \hbar\omega_D e^{-1/\rho_0 V}. \tag{2.34}$$

Measurements of T_C in BCS superconductors thus allow an estimate of the pairing potential V. The temperature dependence of the gap due to thermal QPs is given by the approximation [83]

$$\frac{\Delta(T)}{\Delta(0)} = \tanh\Big[1.74\sqrt{\frac{T_\mathrm{c}}{T} - 1}\Big]. \tag{2.35}$$

This is also shown in Fig. 2.6. The gap is closed by QP population until it vanishes at $T = T_\mathrm{c}$. For aluminum with $T_\mathrm{c} = 1.2\,\mathrm{K}$ and temperatures below 100 mK the gap is approximately constant at its zero temperature value of $\Delta_0/h = 43.5\,\mathrm{GHz}$.

More generally, any QP distribution modifies the superconducting gap [47]:

$$\Delta_\mathrm{qp} = \Delta\big(1 - x_\mathrm{qp}\big). \tag{2.36}$$

The measurements will reveal a QP density $x_\mathrm{qp} \sim 1 \times 10^{-5}$ in the experiments in Ch. 5, therefore the gap modification can be neglected in this study.

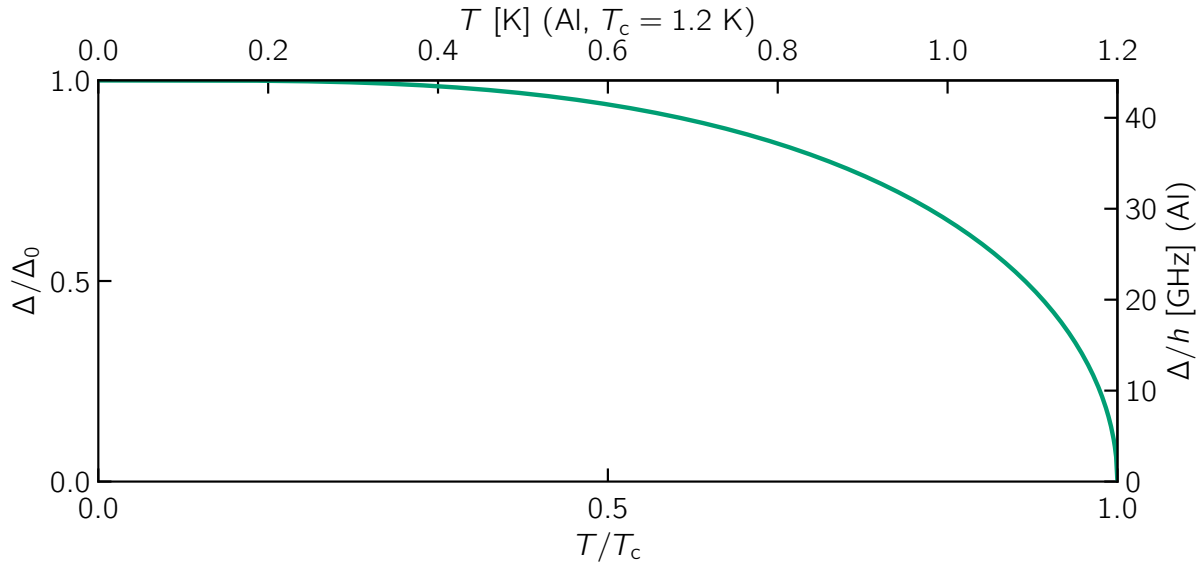

Figure 2.6.: Normalized BCS gap $\Delta(T)/\Delta(0)$ as a function of reduced temperature T/T_c. The right and top axis show the values for aluminum, with $T_C = 1.2\,\mathrm{K}$ and $\Delta_0 = 43.5\,\mathrm{GHz}$.

2.6.2. Quasiparticle tunneling through a Josephson junction

Tunneling contacts between superconductors were introduced phenomenologically in Sec. 2.2. In addition to Cooper pair tunneling, QPs can also tunnel through Josephson junctions.

The analysis follows Catelani et al. [46]. Consider a Josephson junction (Fig. 2.1) with leads (l, r) made from identical superconductors, $\Delta^l = \Delta^r = \Delta$. The total Hamiltonian of such a system reads

$$\hat{H} = \hat{H}_\varphi + \hat{H}_{\mathrm{QP}} + \hat{H}_{\mathrm{QP},\varphi}, \tag{2.37}$$

where $\hat{H}_\varphi$ describes the Josephson phase degree of freedom, which is independent of QPs and describes the junction or later the qubit (Sec. 3.3). $\hat{H}_{\mathrm{QP}}$ is the BCS Hamiltonian in both leads:

$$\hat{H}_{\mathrm{QP}} = \sum_{l,s} \varepsilon_l\, \hat{\gamma}^\dagger_{ls} \hat{\gamma}_{ls} + \sum_{r,s} \varepsilon_r\, \hat{\gamma}^\dagger_{rs} \hat{\gamma}_{rs}, \tag{2.38}$$

and $\hat{H}_{\mathrm{QP},\varphi}$ describes QP tunneling:

$$\hat{H}_{\mathrm{QP},\hat{\varphi}} = t \sum_{l,r,s} e^{i\hat{\varphi}/2} \hat{c}^\dagger_{rs} \hat{c}_{ls} + \mathrm{H.c.}. \tag{2.39}$$

Here, $\hat{c}^\dagger_{r/l,s}$, $\hat{c}_{r/l,s}$ are electron operators (superpositions of Bogoliubov operators via Eq. 2.10), and t is the electron-tunneling amplitude. This Hamiltonian couples the electrons to the phase degree of freedom.

Expressing the electron operators in terms of Bogoliubov operators (Appendix A.1, [46, 84]) yields

$$\begin{aligned} \hat{H}_{\mathrm{QP},\hat{\varphi}} = t \sum_{l,r,s} \Bigg\{ & \left[(u_r u_l - v_r v_l) \cos\frac{\hat{\varphi}}{2} + i(u_r u_l + v_r v_l) \sin\frac{\hat{\varphi}}{2} \right] \hat{\gamma}^\dagger_{rs} \hat{\gamma}_{ls} \\ & + \left[(u_r v_l + v_r u_l) \cos\frac{\hat{\varphi}}{2} + i(u_r v_l - v_r u_l) \sin\frac{\hat{\varphi}}{2} \right] \hat{\gamma}^\dagger_{rs} \hat{\gamma}^\dagger_{l\bar{s}} \Bigg\} + \mathrm{H.c.}. \end{aligned} \tag{2.40}$$

Here u_k and v_k are taken real and the phase parameter between them is expressed explicitly by φ; $\bar{s}$ is the spin opposite to s. Thus, not only the electrons but also the QPs are coupled to the Josephson phase. The first term corresponds to QP tunneling between leads (QP-number-preserving terms), while the second term creates pairs of QPs with opposite spin (QP-pair-creation terms). Without external energy input—drive or infrared photons—only QP-number-conserving terms contribute, involving nonequilibrium QPs already present in the leads. With additional radiation ($\gtrapprox 2\Delta$), the pair-creation terms become active, leading to photon-assisted QP generation and tunneling [38, 81], discussed in Sec. 3.3.3.

In the low-energy limit ($\varepsilon \ll \Delta$), $u_k \approx v_k \approx \sqrt{1/2}$ (Eq. 2.11) and the pair-creation term is neglected. With identical spin direction in the leads ($v_l = v_r$), the Hamiltonian simplifies to

$$\hat{H}_{\mathrm{QP},\hat{\varphi}} = t \sum_{r,l,s} i \, \sin \frac{\hat{\varphi}}{2} \, \hat{\gamma}_{rs}^{L\dagger} \hat{\gamma}_{ls}^{R} + \mathrm{H.c.}. \tag{2.41}$$

Using Fermi's golden rule, the QP-induced transition rate between the eigenstates $|i\rangle$ and $|j\rangle$ takes the form [46, 84]:

$$\Gamma_{ij}^{\mathrm{QP}} = \frac{1}{\hbar} \sum_{l,r,s} \left| \left\langle j, r \middle| \hat{H}_{\mathrm{QP},\hat{\varphi}} \middle| i, l \right\rangle \right|^2 \delta_{\epsilon_i - \epsilon_j + \epsilon_l - \epsilon_r}, \tag{2.42}$$

with states $|i, l\rangle$ combining Josephson and QP states. The summation is over all QP states and the Kronecker delta enforces energy conservation. The average is taken over all possible initial QP states.is understood over all possible QP initial states. This transition rate factorizes into Josephson phase and QP parts [46]:

$$\Gamma_{ij}^{\mathrm{QP}} = \left| \left\langle j \middle| \sin \frac{\hat{\varphi}}{2} \middle| i \right\rangle \right|^2 \tilde{S}_{\mathrm{QP}}[\omega_{ij}], \tag{2.43}$$

where $\omega_{ij} = (\epsilon_i - \epsilon_j)/\hbar$ is the transition frequency between states $|i\rangle$ and $|j\rangle$. The QP spectral function is

$$\tilde{S}_{\mathrm{QP}}[\omega_{ij}] = \frac{8t^2}{\hbar} \int_0^\infty \mathrm{d}\varepsilon_l \int_0^\infty \mathrm{d}\varepsilon_r \, f(\varepsilon_l) \left[1 - f(\varepsilon_r)\right] \rho_s(\varepsilon_l) \rho_s(\varepsilon_r) \delta(\varepsilon_i - \varepsilon_j + \varepsilon_l - \varepsilon_r), \tag{2.44}$$

with the QP energy distribution $f(\varepsilon)$ (Eq. 2.24) and the DOS $\rho_s(\varepsilon)$ (Eq. 2.19), accounting for the degeneracy of the left (initial) and right (final) states. This QP spectral function includes the coherence effects from the QP tunneling process. The tunnel conductance is $g_T = 4\pi e^2 \rho_0^2 t^2$. The Ambegaokar–Baratoff relation (Eq. 2.6) gives $E_J = g_T \Delta/(4e^2)$, so $t^2 = E_J/(\pi \Delta \rho_0^2)$ and

$$\Gamma_{\mathrm{QP}} \equiv \frac{16 E_J}{\pi \hbar}, \tag{2.45}$$

yielding

$$\tilde{S}_{\mathrm{QP}}[\omega_{ij}] = \Gamma_{\mathrm{QP}} \, S_{\mathrm{QP}}[\omega_{ij}]. \tag{2.46}$$

Comparing the definition of $\tilde{S}_{\mathrm{QP}}$ (Eq. 2.44 and Eq. 2.46) with the definition of the quasiparticle density x_{qp} (Eq. 2.21), one finds [46]

$$S_{\mathrm{QP}}[\omega_{ij}] = x_{\mathrm{qp}} \sqrt{\frac{2\Delta}{\hbar \omega_{ij}}}. \tag{2.47}$$

The QP-induced transition rate is thus determined by the spectral function, i.e., the spectral density of QP-induced noise at the transition frequency $S_{\mathrm{QP}}(\omega_{ij})$, a prefactor Γ_{QP} characterizing the junction (given in Eq. 2.45), and the system-specific matrix element of $\sin(\hat{\varphi}/2)$, making a calculation of the transition rate possible.

The implications for superconducting qubits are discussed in detail in Sec. 3.3.

3. Charge qubits in different regimes

In this chapter, a brief overview of quantum information processing (Sec. 3.1) with superconducting qubits is presented and an overview of the qubit parameter regime is given (Sec. 3.2). Furthermore, the influence of QPs on qubits is discussed (Sec. 3.3). For a more comprehensive treatment, see standard textbooks such as Nielsen and Chuang [105] and Benenti et al. [106] for general aspects of quantum computation and information theory; as well as the lecture notes by Martinis and Osborn [107], the *Quantum Engineer's Guide to Superconducting Qubits* by Krantz et al. [1], and the article by Koch et al. [7] for detailed discussions on superconducting implementations. For the QP-qubit interaction the thesis by Serniak [84] and various publications by Catelani et al. [45, 46, 79] are recommended.

3.1. Qubits — a generic view

In 1982, Richard Feynman proposed using one quantum system to simulate another [108], a quantum computer. In classical computation, the fundamental building block is the transistor, which acts as a binary logic element storing a single *bit* of information. Logical operations (also referred to as *gates*) act deterministically on these states, such as e.g. the NOT gate ($0 \to 1$, $1 \to 0$). In the field of quantum computing, the classical bit is replaced by a controllable, coherent quantum two-level system: the *qubit*. A qubit can occupy not only the energy eigenstates

$$|0\rangle = \begin{pmatrix} 1 \\ 0 \end{pmatrix}, \quad |1\rangle = \begin{pmatrix} 0 \\ 1 \end{pmatrix}, \tag{3.1}$$

but also any coherent superposition of them:

$$|\Psi\rangle = \alpha|0\rangle + \beta|1\rangle = \cos\frac{\theta}{2}|0\rangle + e^{i\phi}\sin\frac{\theta}{2}|1\rangle. \tag{3.2}$$

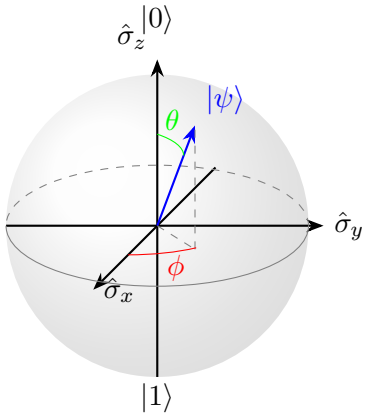

Figure 3.1.: Single-qubit state $|\Psi\rangle = \cos\frac{\theta}{2}|0\rangle + e^{i\phi}\sin\frac{\theta}{2}|1\rangle$ represented on the Bloch sphere. The eigenstates $|0\rangle$ and $|1\rangle$ are located at the north and south poles, respectively.

This parametrization naturally maps to the surface of the Bloch sphere (see Fig. 3.1). The coefficients preceding the eigenstates are the probability amplitudes. Therefore, the state can alternatively be expressed in the form of the Bloch vector

$$\vec{r} = \big(\sin\theta\cos\phi,\ \sin\theta\sin\phi,\ \cos\theta\big). \tag{3.3}$$

In typical experiments, resonant and near-resonant drive pulses implement controlled rotations about the Pauli axes $\sigma_{x,y,z}$, thereby realizing universal single-qubit gates (X,Y,Z). A measurement in the computational basis corresponds to the measurement of the observable $\hat{\sigma}_z$ and projects the qubit onto either the state $|0\rangle$ or $|1\rangle$. Hence, any projective measurement yields only a single classical outcome and recovering the full state reconstruction requires averaging measurement outcomes over many identically preparations. *Mixed states* correspond to statistical ensembles of pure states that occupy points inside the sphere and are conveniently written as a density matrix [1]:

$$\hat{\rho} = \frac{1}{2}\left(I + \vec{r}\,\vec{\sigma}\right) = \begin{pmatrix} |\alpha|^2 & \alpha\beta^* \\ \alpha^*\beta & |\beta|^2 \end{pmatrix}, \tag{3.4}$$

where I is the 2×2 identity matrix. The time evolution of the density matrix is governed by the *von Neumann equation*:

$$i\hbar\frac{d\hat{\rho}}{dt} = [\hat{H}, \hat{\rho}], \qquad \hat{H} = \frac{\hbar\omega_q}{2}\hat{\sigma}_z, \tag{3.5}$$

where $\hat{H}$ is the system Hamiltonian, with the energy splitting $\hbar\omega_q$ between the two eigenstates.

While multi-qubit entanglement is the basis of quantum processor operation, understanding these single-qubit concepts suffices for the subsequent chapters.

Decoherence of qubits

Real qubits interact with their environment; this converts pure states into mixed states — *decoherence*. Within the standard Bloch–Redfield framework [1] two rates quantify the process:

1. Longitudinal (energy) relaxation $\Gamma_1 = 1/T_1$ (along the Bloch sphere's z axis)
2. Transverse relaxation (decoherence) $\Gamma_2 = 1/T_2 = \Gamma_1/2 + \Gamma_\phi$ (loss of phase coherence in the xy plane), where Γ_ϕ is the pure dephasing

For an initial state as described by Eq. 3.2 driven with detuning $\delta\omega = \omega_q - \omega_d$, the time evolution of the density matrix is given by

$$\rho_{\mathrm{BR}}(t) = \begin{pmatrix} 1 + \big(|\alpha|^2 - 1\big)e^{-\Gamma_1 t} & \alpha\beta^* e^{i\delta\omega t}e^{-\Gamma_2 t} \\ \alpha^*\beta e^{-i\delta\omega t}e^{-\Gamma_2 t} & |\beta|^2 e^{-\Gamma_1 t} \end{pmatrix}, \tag{3.6}$$

In the long-time limit $t \gg (T_1, T_2)$ the system relaxes into the ground state. Understanding coherence limitation is therefore a central goal for the development of a large-scale quantum processor.

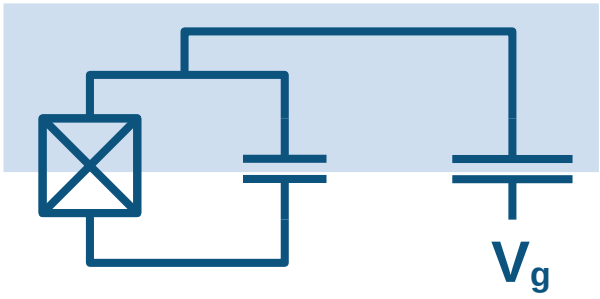

Figure 3.2.: Circuit diagram of a simple superconducting qubit: a Josephson junction shunted by a capacitance, together with a voltage gate. The blue shaded area marks the qubit island.

3.2. Superconducting qubit realizations

Macroscopic quantum devices based on Josephson junction (Sec. 2.1) have emerged as a leading realization of qubits, since they offer advantages such as frequency tunability, compatibility with large-scale fabrication, and less complex readout schemes [109]. The existence of such macroscopic quantum tunneling was demonstrated in the 1980s by John Clarke, Michel H. Devoret, and John M. Martinis in such superconducting circuits [110–113]. This work was later recognized with the Nobel Prize in 2025 [114]. Nakamura realized the first superconducting circuit implementation of a qubit in 1999 [5].

A superconducting qubit can be realized by engineering an anharmonic oscillator from a capacitor and a nonlinear inductor (the Josephson junction).[1] This multi-level system can effectively be rendered as a qubit by restricting the accessible energy levels. Figure 3.2 shows a circuit diagram of a superconducting qubit: a *qubit island* is separated by the Josephson junction and the capacitor, the Hamiltonian of this system reads

$$\hat{H} = 4E_C(\hat{n} - n_g)^2 - E_J \cos(\hat{\varphi}), \tag{3.7}$$

where $\hat{n}$ is the Cooper pair number operator, $n_g = C_g V_g / 2e$ is the offset charge, and $\hat{\varphi}$ is the Josephson phase. The Hamiltonian is fully characterized by two free parameters: the Josephson energy E_J and the charging energy E_C. The Josephson energy is given by $E_J = \frac{\Phi_0 I_0}{2\pi}$ (Eq. 2.4), and governs the tunneling of Cooper pairs across the junction. The charging energy is expressed as $E_C = \frac{(2e)^2}{2C}$, where C is the total capacitance, including the shunting capacitance and the capacitance of the Josephson junction. Replacing the single junction by a *DC-SQUID*[2] renders E_J tunable via magnetic flux, enabling qubit frequency tunability.

Qubit regimes are described by the variable in which the quantum information is mainly encoded. Throughout this thesis fixed-frequency transmon-type devices ($E_J/E_C = 25$ to 200) are employed, where the information is partly encoded in the charge n and partly in the phase φ. Other archetypes (not treated here) include charge qubits (information primarily in n, $E_J/E_C \sim 1$) — the *Cooper pair box*, phase qubits (information in φ realised with large L_J) [113,

[1] Other options, such as geometric constrictions or kinetic inductances, lack sufficient anharmonicity or have high dissipation.

[2] Superconducting quantum interference device (SQUID). Such a device formed by two parallel junctions can be used, for example, to measure the magnetic flux very precisely. For more details, see Ref. [115].

116, 117], and flux qubits (information in the magnetic flux through a superconducting loop) [6, 67, 118, 119]. For a comparison of different superconducting qubit archetypes, see Chapter 17 of the book *Fundamentals and Frontiers of the Josephson Effect* [120].

3.2.1. Hamiltonian in the phase basis

The Hamiltonian can also be expressed in the phase basis. The number operator is then defined as $\hat{n} = |\varphi\rangle(-i\partial_\varphi)\langle\varphi|$, with $|\varphi\rangle = |\varphi + 2\pi\rangle$,[3] leading to the following phase basis Hamiltonian:

$$H = 4E_C \left(-i\partial_{\hat{\varphi}} - n_g\right)^2 - E_J \cos\hat{\varphi}. \tag{3.8}$$

In this form, the time-independent Schrödinger equation of the qubit can be solved analytically using the Mathieu approach and choosing a suitable parameterization (e.g. [7, 121]). This yields the eigenenergies

$$\varepsilon_i(n_g) = E_C \, a_{2[n_g + k(i,n_g)]}\left(-\frac{E_J}{2E_C}\right), \tag{3.9}$$

where $a_\nu(q)$ denotes *Mathieu's characteristic value*[4] and $k(i, n_g)$ is an integer-valued sorting function of the eigenvalues [7]. The index i labels the plasmon mode number of the qubit. From the eigenenergies, the qubit transition frequencies ω_{ij} are defined by

$$\hbar\omega_{ij} = \varepsilon_i - \varepsilon_j. \tag{3.10}$$

For typical superconducting qubits, these energy transitions lie in the µeV to few-meV range and can therefore be probed by microwave photons. This phase basis Hamiltonian (Eq. 3.8) also proves convenient when looking at the transmon qubit regime (Sec. 3.2.3).

3.2.2. Hamiltonian in the charge basis

Expressing the Josephson term in the Hamiltonian (Eq. 3.11) in the charge basis with charge eigenstates yields a Hamiltonian with one degree of freedom:

$$\hat{H} = \sum_n \left(4E_C \left(n - n_g\right)^2 |n\rangle\langle n| - \frac{E_J}{2}\left(|n\rangle\langle n+1| + |n+1\rangle\langle n|\right)\right), \tag{3.11}$$

where the identity $e^{i\varphi} = |n\rangle\langle n+1|$ is used to express the $\cos\varphi = \frac{1}{2}\left(e^{-i\varphi} + e^{i\varphi}\right)$ term. In this Hamiltonian, the Josephson term couples nearest-neighbor charge states, corresponding to the transfer of Cooper pairs across the junction. This charge basis is favored in simulations, since it is straightforward to diagonalize numerically. Such simulations of the spectrum up to a maximum index $i_{\max}$ are accurate if the charge basis is truncated at a state i with

$$i \gg \sqrt{i_{\max}} \left(\frac{E_J}{32E_C}\right)^{1/8}, \tag{3.12}$$

as discussed in Ref. [122]. This form will be used later when calculating transition matrix elements numerically in Sec. 3.2.3 and also to explain dispersive readout in Sec. 3.2.4.

[3] Since the number operator has integer eigenvalues, the conjugate variable φ is compact.
[4] See, for example, Ref. [7] for definitions and properties.

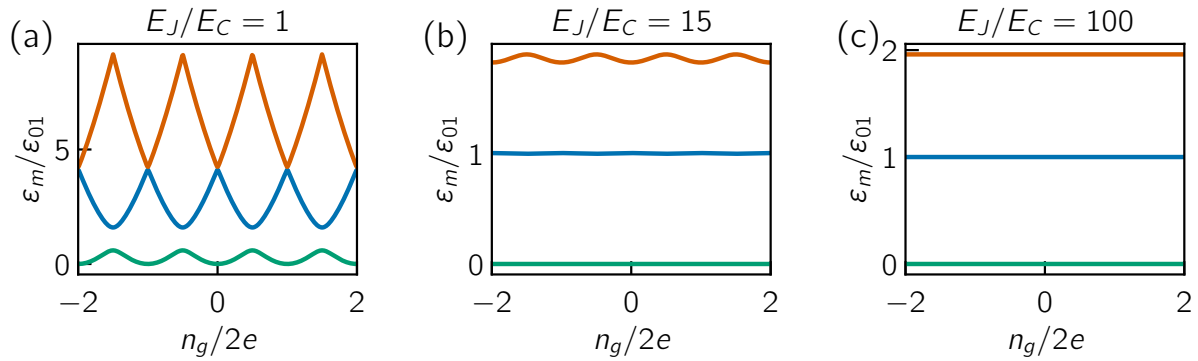

Figure 3.3.: Lowest three energy levels E_m in units of $E_{01}(n_g = 1/2)$ of the charge qubit as a function of applied offset charge n_g for the regimes: (a) $E_J/E_C = 1$, (b) $E_J/E_C = 15$, and (c) $E_J/E_C = 100$.

3.2.3. Qubit regimes

Figure 3.3 shows the lowest three eigenenergies as a function of the offset charge n_g for different E_J/E_C ratios. The eigenenergies exhibit an integer Cooper pair ($n_g = n \pm 1$) periodicity. Specifically, the so-called *deep transmon* regime with $E_J/E_C = 100$ [Fig. 3.3 panel (c)] is compared to the charge-sensitive Cooper pair box regime with $E_J/E_C = 1$ [Fig. 3.3 panel (a)] and an intermediate transmon regime with $E_J/E_C = 15$ [Fig. 3.3 panel (b)]. The regime choice represents a trade-off between the *charge dispersion* and the *anharmonicity* of the qubit. The following subsections introduce these two quantities and then discuss the transmon regime in which the qubits in this thesis are operated.

Charge dispersion

The *charge dispersion* of the eigenenergy ε_i is defined as

$$\Delta_{\varepsilon_i} = |\varepsilon_i(0) - \varepsilon_i(1/2)|. \tag{3.13}$$

It is the amplitude of the energy-level variation with offset charge and therefore also the sensitivity of the qubit frequency to QPs. In Fig. 3.4(a), the charge dispersion of the different energy levels is shown as a function of E_J/E_C. The charge dispersion decreases approximately exponentially with $\sqrt{E_J/E_C}$ for $E_J \gg E_C$ [7]. It leads to pure dephasing via small fluctuations in the offset charge (Sec. 3.2.5). Other sources of dephasing are typically in the ∼10 kHz range and therefore dominate the charge dispersion in the transmon regime [123–125].

Anharmonicity

As explained above, these qubits are not single two-level systems but rather multilevel, nonlinear oscillators. The separation of the computational subspace from the higher energy levels is expressed by the *anharmonicity* $\alpha = \omega_{12} - \omega_{01}$. In Fig. 3.4, the normalized anharmonicity is plotted as a function of E_J/E_C for three different charge states: $n_g = 0$, where ω_{01} is maximal; $n_g = 1/2$, where ω_{01} is minimal; and $n_g = 1/4$, the single-charge degeneracy point. For small E_J/E_C ratios, the anharmonicity is positive for $n_g = 1/2$ and $n_g = 1/4$ and negative for $n_g = 0$. For large ratios of E_J/E_C, it converges to $-E_C$ for all n_g, crossing the point of zero anharmonicity. To operate this multilevel, nonlinear system as a qubit, the anharmonicity needs

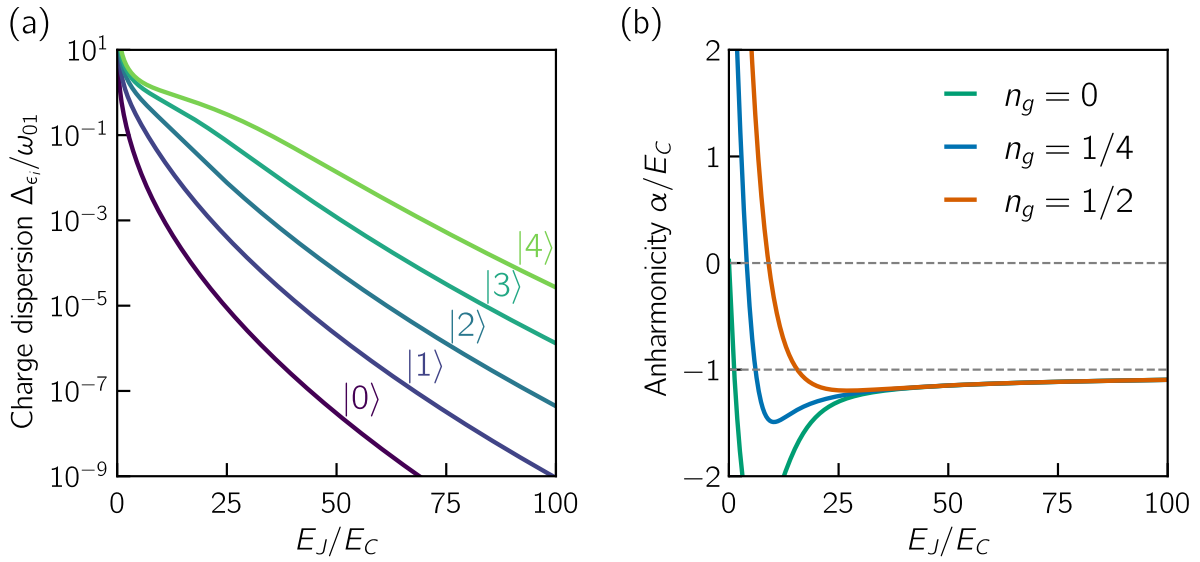

Figure 3.4.: Left: Charge dispersion Δ_{ε_i} normalized by the qubit transmition energy $\hbar\omega_{01}$ as a function of E_J/E_C for the lowest five energy levels. Right: Anharmonicity α as a function of E_J/E_C at the offset-charge points $n_g = 0$, $n_g = 1/4$, and $n_g = 1/2$. Adapted from [84].

to be large enough to prevent leakage into higher energy states. Since multiple operations need to be performed on a qubit within its coherence time for quantum computation to work, fast pulsed gates with a carrier frequency of ω_{01} are required (see Sec. 4.3). These short pulses have a broad spectral width.[5] Therefore, the anharmonicity limits gate times, which needs to be considered in time-resolved measurements as performed in Ch. 5. Leakage minimization by pulse-envelope optimization is a considerable research interest [126–129].

Transmon regime

Taking into account the discussion of the last two paragraphs, a natural choice for the E_J/E_C ratio of the qubit is the so-called *transmon* regime with $E_J/E_C \gg 1$.[6] It provides a good trade-off between sufficient anharmonicity and suppressed sensitivity to charge noise. First proposed by Koch et al. [7], it is one of the most widely used qubit designs in state-of-the-art research. Since the charge dispersion decreases exponentially with E_J/E_C, it is negligible in the regime with $E_J/E_C \gg 1$ (Fig. 3.4) [7]. Other sources of dephasing easily dominate over the charge dispersion. As shown in Fig. 3.4 (right), the anharmonicity converges to $\alpha = E_C$. The insensitivity to charge noise scales exponentially while the anharmonicity scales linearly to first order with E_J/E_C; this balance enables fast gates and prolonged coherence times.

[5] For a Gaussian envelope, the pulse length must be $\gtrsim 3/\alpha$ to avoid excess leakage into higher levels, and for a rectangular pulse even $\gtrsim 5/\alpha$.

[6] This is nowadays a common working definition. One sometimes also finds other limits, for example $E_J/E_C > 50$. Koch et al. [7] used the definition $E_J/E_C > 20$. Another transmon definition, maybe responsible for the name, is the point of zero anharmonicity crossing (*trans*), visible in Fig. 3.4 (right panel). This limit is much lower and typically not used, since the charge dispersion in this region is still in the 10 kHz to 1 MHz range for typical qubit capacitances. In this thesis the qubits are between $E_J/E_C = 25$ and 200, and are all refered to as transmons.

In the transmon regime, the eigenenergies can be obtained by expanding the $\cos(\hat{\varphi})$ term in the Hamiltonian (Eq. 3.8) around $\varphi = 0$ [7], keeping only terms up to fourth order in φ. The dependence on n_g is negligible and therefore dropped. The Hamiltonian becomes that of a harmonic oscillator with a quartic perturbation:

$$\hat{H} \approx \sqrt{8E_J E_C}\left(\hat{a}^\dagger \hat{a} + \frac{1}{2}\right) - \frac{E_C}{12}\left(\hat{a} + \hat{a}^\dagger\right)^4, \tag{3.14}$$

where $\hat{a}$ and $\hat{a}^\dagger$ are the annihilation and creation operators. From this approximate Hamiltonian, the eigenenergies follow as

$$\varepsilon_j \approx -E_J + \sqrt{8E_J E_C}\left(j + \frac{1}{2}\right) - \frac{E_C}{12}\left(6j^2 + 6j + 3\right). \tag{3.15}$$

The fundamental transition energy is

$$\varepsilon_{01} = \hbar\omega_{01} = \sqrt{8E_J E_C} - E_C. \tag{3.16}$$

From this expression, the anharmonicity can also be calculated, yielding $\alpha \approx E_C$. This illustrates potential limitations of this approximation, since the deviation from the exact anharmonicity is of the order of 10 % at a ratio $E_J/E_C = 100$.

OCS transmon

In this thesis, not only transmons in the deep transmon regime are investigated, but also transmon qubits in a more charge-sensitive regime. Following the nomenclature of Serniak et al., this regime is called the *offset-charge-sensitive* (OCS) regime and the qubits are referred to as *OCS transmons*. This term denotes an intermediate qubit regime that is charge sensitive but not overly so, such that it still retains good coherence. The E_J/E_C ratio lies between approximately 12 and 50. In this regime, many of the transmon approximations remain good estimates, as will be seen throughout this thesis.

3.2.4. Dispersive readout

Dispersive readout is a fundamental technique used in this thesis to measure the quantum state of a superconducting qubit indirectly by coupling it off-resonantly to a microwave resonator, as illustrated in Fig. 3.5. This enables minimally destructive qubit-state measurement, since no direct energy transfer occurs.[7] The resonator can be implemented as a 3D cavity or on chip, as in this work. The resonator frequency shifts are used to measure the qubit state and are denoted by χ_g and χ_e for the qubit in the ground or excited state, respectively. The coupled system can be described by a modified Jaynes–Cumming Hamiltonian [7, 131, 132]:

$$\begin{aligned}\hat{H}_{\mathrm{JC}} &= \hat{H}_q + \hat{H}_r + \hat{H}_g \\ &= \sqrt{8E_J E_C}\hat{a}^\dagger\hat{a} - \frac{E_C}{2}\hat{a}^\dagger\hat{a}\hat{a}\hat{a}^\dagger + \hbar\omega_r\left(\hat{b}^\dagger\hat{b} + \frac{1}{2}\right) + \hbar g\left(\hat{b}^\dagger\hat{a} + \hat{b}\hat{a}^\dagger\right),\end{aligned} \tag{3.17}$$

[7] It is only nearly quantum-non-demolishing, since high photon numbers cause measurement-induced state transitions [130].

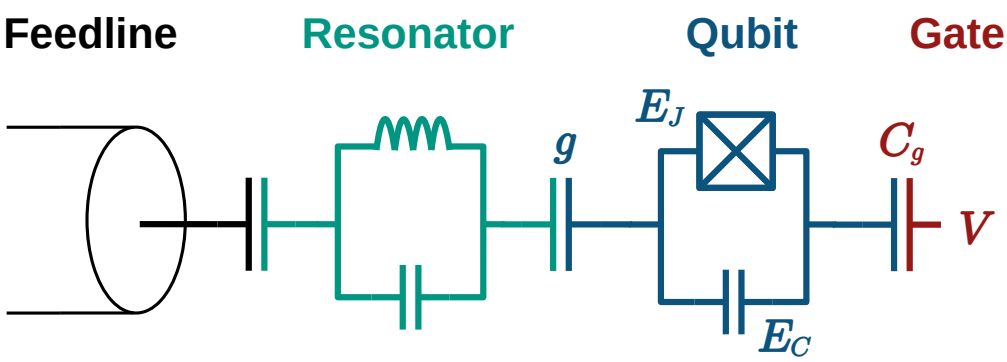

Figure 3.5.: Schematic of the readout chain of the qubit. The qubit (blue) is capacitively coupled on one side to a readout resonator (green), which is in turn coupled to the feedline (black). The coupling strength between the resonator and the qubit is g. For one sample also a voltage gate (red) is used to control the offset charge, see Sec. 4.2.3.

where the first term describes the qubit (reduced from Eq. 3.14), the second the resonator mode with energy $\hbar\omega_r$, and the third term represents the capacitive coupling.[8] The strength of the capacitive coupling can be approximated [132] as

$$g \approx \frac{C_g}{\sqrt{C_r C_{\text{tot}}}}\sqrt{\omega_r \omega_{01}}, \tag{3.18}$$

where C_g is the coupling capacitance.

Of primary interest is the relative dispersive shift between ground and excited state for a transmon; for the derivation see Sec. A.2 in the Appendix:

$$\chi_{eg} = -4g_{eg}^2 \frac{\alpha}{\omega_{01}^2 - \omega_r^2} \approx \frac{2g_{eg}^2\alpha}{\delta(\delta - \alpha)}, \tag{3.19}$$

where $g_{eg} = g|n_{eg}|$ and $\delta = \omega_{01} - \omega_r$ is the detuning, assumed large compared to g_{eg} and α. Another important dispersive shift is the resonator shift from the few-photon regime to the many-photon bright state:

$$\chi_g = \chi_0 \approx \frac{g_{eg}^2}{\omega_{01} - \omega_r}. \tag{3.20}$$

In the bright state, the resonator effectively decouples from the qubit. This shift is useful for determining the coupling strength in frequency-domain measurements of the resonator alone.

3.2.5. Decoherence of superconducting qubits

The concept of coherence was introduced in a general manner in Sec. 3.1. In the superconducting qubit community the decoherence is typically expressed as decoherence times, defined as the inverse of the decoherence rates:

$$T_1 := \frac{1}{\Gamma_1} = \sum_i \frac{1}{\Gamma_1^{(i)}}, \qquad T_\phi := \frac{1}{\Gamma_\phi}. \tag{3.21}$$

[8] For the qubit Hamiltonian the total capacitance changes and becomes $C_{\text{tot}} = C_\text{B} + C_\text{J} + C_\text{g}$.

In general, the decoherence (and dephasing) over multiple different loss channels $\Gamma_1^{(i)}$. Median transmon energy-relaxation time has substantially increased in the last few decades from median relaxation times of nanoseconds [5, 133] to 0.425 ms to 1.68 ms for fixed-frequency transmon qubits [8, 9] and 68 µs to 288 µs in large-scale processors [10, 11].[9] However, several environment-specific channels still limit performance, and the most dominant decay channels are summarized below.

Purcell effect

A qubit detuned by $\Delta = \omega_{01} - \omega_r$ from its readout resonator can relax by emitting a photon that leaks from the resonator at rate κ [134]:

$$\Gamma_{1,\text{Purcell}} = 2g^2 \frac{\kappa/2}{(\kappa/2)^2 + \Delta^2}. \tag{3.22}$$

A similar mechanism applies to other (weakly) coupled systems, such as other on-chip resonant modes or modes in the sample box. The Purcell limit can already be estimated at the design stage by simulating the resonances on the chip and in the sample enclosure. The Purcell effect is well understood [7, 135] and can be mitigated by careful chip design and Purcell filters in the readout lines [136–138], which are inline broadband resonators operating as bandpass filters and are also used in the samples in this thesis (Sec. 4.4.2). Therefore, it is in most cases not the dominant loss channel.

Two-level systems

Electric fields in the tunnel barrier, surface oxides, and other amorphous dielectrics can couple the qubit to defects in these materials. At millikelvin temperatures, within the standard tunneling model [139, 140], these defects can be modeled as two-level systems (TLS). If the tunneling object carries an electric charge, it possesses an electric dipole moment with which it can couple to the electric fields of the qubit. For TLS transition frequencies close to the qubit frequency, the TLS can thus absorb qubit excitations and quickly dissipate them into the phonon bath, effectively limiting the coherence time of the qubit [26, 141]. A detailed study of an all-aluminum transmon has shown that even with the small amount of field energy in the oxide in modern planar transmon circuits, the loss from surface TLS is of the same order as the measured T_1 values [134]. Consequently, many current publications identify TLS as their main source of decoherence [11, 142]. This is the reason why there is increasing use of different superconductors for qubit electrodes [9, 143–145],[10] interest in localizing TLS [30, 146], and fabrication methods and designs trying to limit TLS densities [147–149].

Charge noise

As discussed in the previous section, the qubit frequency depends on the offset charge; this dependence is strongly suppressed for qubits in the transmon regime, but a residual dependence

[9] Strictly speaking, the coherence depends on the qubit frequency; the frequency-independent quality factor $Q_q = \omega_{01} T_1$ would therefore be a better measure. However, this thesis sticks to coherence times, since they are more familiar in the field, and coherence times are only compared for qubits in a similar frequency range.

[10] The other reason is the higher gap of other superconductors, reducing QP-induced decoherence.

is still present. Environmental fluctuations in the offset charge can couple to the qubit, resulting in pure dephasing. Charge noise is often described as a combination of $1/f$ noise and Nyquist noise [1]. As discussed above, quasiparticle tunneling also leads to fluctuations of the offset charge and therefore causes decoherence. Since this mechanism is central to the topic of this thesis, the following section (Sec. 3.3) is devoted entirely to quasiparticle–qubit interactions.

Other noise sources

Shot noise shifts the qubit frequency via a fluctuating photon population in modes to which the qubit is coupled, such as the readout resonator [123–125, 150]. These photon-number fluctuations can be caused by thermal or quantum fluctuations and lead to dephasing of the qubit. This effect can be reduced by careful filtering, attenuation, and thermalization of the input and output lines. Many current publications report that their dephasing time is limited by shot noise [125, 150]. In flux-tunable qubits, flux noise can be limiting when the qubit is not operated at the *sweat spot* [7, 119].

Turning decoherence into a feature

While mitigating loss is crucial for quantum computing, the extreme sensitivity of superconducting qubits to their surroundings also makes them powerful *quantum sensors*. By altering the environment of the qubit in a controlled way and monitoring the qubit coherence, frequency, or other observables, one can gain detailed insight into the underlying physics of the system. This strategy has been used, for example, to map individual TLS via stain or electric-field tuning [30, 146, 151]. In this work a similar idea is applied. By altering the QP concentration with infrared radiation and monitoring the resulting changes in qubit coherence and frequency, information about the QP dynamics can be obtained (see Ch. 5).

3.3. Quasiparticle effects on qubits

This section incorporates QPs into the description of the qubit Hamiltonian. When a QP tunnels across the junction, a charge of $\pm e$ is transported. This process is equivalent to changing the offset charge n_g by $\pm 1/2$. To describe this effect, a *charge parity* P is introduced, defined as the parity of the total number of electrons on the island (not Cooper pairs). The parity switches between $P = \pm 1$, such that effectively n_g is shifted by $\pm 1/2$ when the parity flips. The ground state, as the lowest-energy state, is an even state. An even parity ($P = 1$) corresponds to an even number of QP tunneling events across the junction, while an odd parity ($P = -1$) corresponds to an odd number. This definition is natural because the Hamiltonian (Eq. 3.7) is symmetric under integer Cooper pair changes ($n_g \to n_g \pm 1$), i.e., changes by $2e$. It is therefore convenient to express the offset charge as

$$n_g \to n_g + \frac{P-1}{4}, \tag{3.23}$$

which separates QP-tunneling effects (through P) from $2e$ offset-charge variations. From an experimental point of view, this separation is well motivated, since charge-parity switches occur on millisecond timescales, whereas slow drifts in n_g occur on timescales of minutes [38, 73, 82,

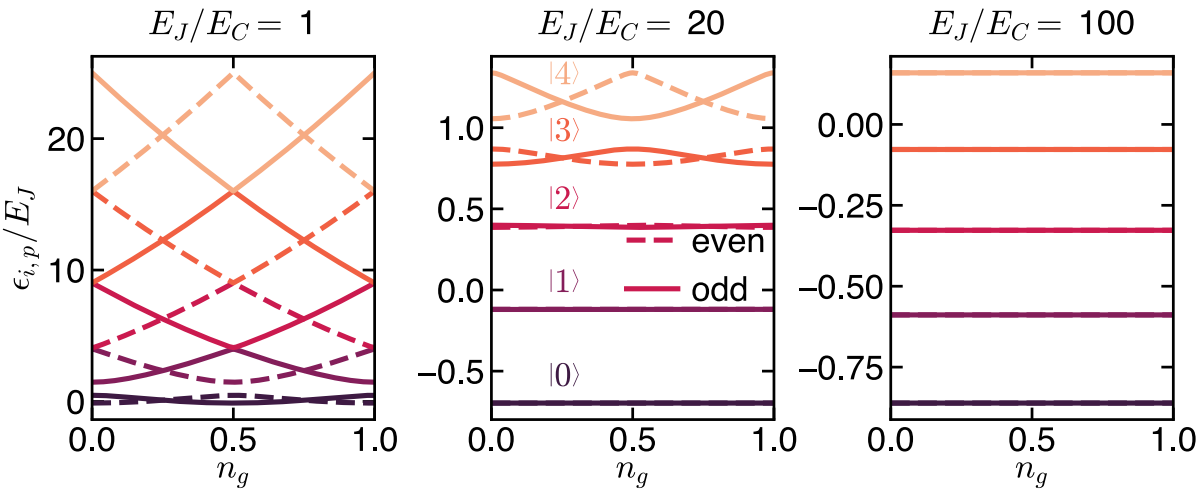

Figure 3.6.: Eigenenergies normalized by E_J as a function of offset charge n_g for three different charge-sensitivity regimes: left: $E_J/E_C = 1$, middle: $E_J/E_C = 20$, and right: $E_J/E_C = 100$. For the first five eigenenergies the odd (solid lines) and even (dashed lines) parity branches are shown. Adapted from Ref. [84].

152–154]. The convention is chosen such that the charge parity does not contribute for even parity. The qubit Hamiltonian then becomes

$$\hat{H} = 4E_C \left(\hat{n} - n_g + \frac{P-1}{4}\right)^2 - E_J \cos(\hat{\varphi}). \tag{3.24}$$

In this picture, the energy spectrum of the qubit can be resolved into even- and odd-parity branches, provided the qubit is operated in a charge-sensitive regime (Fig. 3.6). The eigenenergies ε_i split into two parity manifolds, $\varepsilon_{i,o}$ (odd, solid lines) and $\varepsilon_{i,e}$ (even, dashed lines). In this representation, the charge dispersion can also be defined as the difference between the two parity branches:

$$\Delta_{\varepsilon_i} = |\varepsilon_{i,e}(0) - \varepsilon_{i,o}(0)|. \tag{3.25}$$

QPs affect various qubit properties, including the decay and dephasing rates as well as the qubit frequency.

Quasiparticle-induced energy relaxation

Section 2.6.2 introduced the tunneling process of QPs through a Josephson junction. When a QP tunnels through the junction in a qubit, the transition rate between two qubit states is modified. The total system Hamiltonian is given by Eq. 2.37 where H_φ becomes the isolated qubit Hamiltonian in the phase basis, as given in Eq. 3.8. The decay rate (Eq. 2.43) is separated into the noise spectral density, which is set by the QP density (Eq. 2.47) and the matrix element $\langle \sin(\hat{\varphi}/2) \rangle_{01}$ set by the qubit Hamiltonian. The matrix element will be evaluated for different parameter regimes in Sec. 3.3.1 and Sec. 3.3.2.

Quasiparticle-induced frequency shifts

Quasiparticles not only induce transitions between qubit states but also modify the energies of the levels. Two main effects contribute to these energy shifts. First, the Josephson energy is renormalized, leading to a correction [46]

$$\delta E_{i,E_J} = E_J \left(x_{\mathrm{qp}} + 2x_{\mathrm{qp}}^A\right) \langle i| \cos\hat{\varphi} |i\rangle, \tag{3.26}$$

where x_{qp}^A can be interpreted as the effective density of occupied Andreev bound states [46, 83].[11]

The second modification arises from QP tunneling [46]:

$$\delta E_{i,\mathrm{qp}} = \sum_{k\neq i} \left| \left\langle k \left| \sin\frac{\hat{\varphi}}{2} \right| i \right\rangle \right|^2 F_{\mathrm{qp}}(\omega_{ik}), \tag{3.27}$$

where $F_{\mathrm{qp}}(\omega_{ik})$ is a function of the QP distribution given explicitly in Ref. [46]. Only the combination entering in the high-frequency limit, relevant for transition frequencies, will be used (see Sec. II and Appendix A of Ref. [46]):

$$F_{\mathrm{qp}}(\omega) + F_{\mathrm{qp}}(-\omega) = -\frac{1}{\pi\hbar} E_J \left[x_{\mathrm{qp}} \sqrt{\frac{2\Delta}{\hbar|\omega|}} - 2\pi x_{\mathrm{qp}}^A \right]. \tag{3.28}$$

As can be seen, the calculation of the energy shifts reduces to the calculation of matrix elements of the phase operators: the matrix element of $\langle \sin(\hat{\varphi}/2)\rangle_{ij}$ has already appeared above, and here matrix elements of $\langle \cos(\hat{\varphi})\rangle_{ii}$ are additionally involved. The modified energy levels of the qubit imply modified transition frequencies between neighboring levels. Analogously to the energy shifts, the change in the transition frequency between levels i and $i+1$ can be decomposed into two parts:

$$\delta\omega_i := \delta\omega_{i,i+1} = \delta\omega_{i,E_J} + \delta\omega_{i,\mathrm{qp}}. \tag{3.29}$$

This will be used in Sec. 3.3.1 to calculate the frequency shift in the transmon regime.

Quasiparticle-induced dephasing

While the energy-relaxation rate is proportional to the spectral noise density at the transition frequency ($\propto S(\omega)$), the pure dephasing rate is proportional to the spectral noise at zero frequency ($\propto S(0)$) [156]. However, the definition of S (Eq. 2.44) exhibits a divergence at zero frequency. It has been shown that a finite dephasing rate can nevertheless arise in the case of QP noise, since a finite dephasing time (or equivalently a finite energy-relaxation time) broadens this divergence [45]. Sec. A.3 in the Appendix presents the main derivation steps. The pure dephasing rate is given by the sum of two contributions:

$$\Gamma_\phi = \Gamma_\phi^c + \Gamma_\phi^s. \tag{3.30}$$

[11] Andreev bound states are not discussed in detail, since their dependence cancels out, as shown below. For details on Andreev reflection see Ref. [155].

The QP distribution is modeled in quasi-equilibrium (compare Sec. 2.5.2) as $f(\varepsilon) = e^{-\varepsilon/T_{\text{eff}}}$, with T_{eff} the effective quasi-equilibrium QP temperature. The occupation probability for a QP at energy $\delta E = k_B T_{\text{eff}}$ then becomes $f_0 = e^{-\Delta/T_{\text{eff}}} \ll 1$, yielding

$$\Gamma_\phi^s \approx \frac{32 E_J}{\pi\hbar} |A_s|^2 e^{-\Delta/k_B T_{\text{eff}}} \left(\frac{\Delta}{k_B T_{\text{eff}}} + \ln \frac{\pi k_B T_{\text{eff}}}{8 E_J |A_s|^2} \right), \tag{3.31}$$

and similarly

$$\Gamma_\phi^c \approx \frac{32 E_J}{\pi\hbar} |A_c|^2 e^{-\Delta/k_B T_{\text{eff}}} \frac{k_B T_{\text{eff}}}{\Delta}, \tag{3.32}$$

where the dominance of one term over the other primarily depends on the matrix elements $|A_s|^2$ and $|A_c|^2$, which are given by

$$A_s = \frac{1}{2} \left(\langle 1| \sin\frac{\hat{\varphi}}{2} |1\rangle - \langle 0| \sin\frac{\hat{\varphi}}{2} |0\rangle \right), \tag{3.33}$$

$$A_c = \frac{1}{2} \left(\langle 1| \cos\frac{\hat{\varphi}}{2} |1\rangle - \langle 0| \cos\frac{\hat{\varphi}}{2} |0\rangle \right). \tag{3.34}$$

These expressions reduce the QP-induced dephasing to an effective QP temperature T_{eff} and matrix-elements. The matrix elements depend on the exact qubit parameters and can in principle vary significantly, making one or the other contribution dominant. In contrast to the QP-induced relaxation rate and qubit frequency shifts, the QP-induced dephasing is not determined solely by the quasiparticle density, but rather by the effective QP temperature T_{eff}. The previous sections have shown that the influence of quasiparticles on different qubit properties can be expressed in terms of a spectral density function and a matrix element.

3.3.1. Transmon approximations

This subsection considers an analytic approximation of the matrix elements for the transmon regime, obtained by performing a harmonic approximation. Ref. [46] showed that corrections to this approximation are only of order $e^{-\omega_{01}/E_C}$, since in the transmon the anharmonicity is weak, of order $\sim E_C$, and $E_C \ll \omega_{01}$ (Sec. 3.2.3). The harmonic Hamiltonian is given by

$$\hat{H}_\varphi = 4 E_C \hat{n}^2 + \frac{(\hbar\omega_{01})^2}{8 E_C} \hat{\varphi}^2. \tag{3.35}$$

Let n and m denote two states of this harmonic oscillator. The matrix element $\left\langle \sin(\hat{\varphi}/2) \right\rangle$ is then given by

$$\left\langle m \left| \sin\frac{\hat{\varphi}}{2} \right| n \right\rangle = e^{-\ell^2/16} \sqrt{\frac{m!}{n!}} \left(\frac{\ell}{2\sqrt{2}} \right)^{n-m} L_m^{(n-m)} \left(\ell^2/8 \right) \sin\left(\frac{\pi(n-m)}{2} \right), \tag{3.36}$$

where $\ell = 2\sqrt{\frac{2E_C}{\hbar\omega_{01}}}$ and $L_m^{(\alpha)}(x)$ are the Laguerre polynomials [46]. Since $E_C \ll \hbar\omega_{01}$, the expression for the matrix element is expanded up to second order in ℓ, which for the ground and first excited state yields[12]

$$\left| \left\langle 0 \left| \sin\frac{\hat{\varphi}}{2} \right| 1 \right\rangle \right|^2 \simeq \frac{E_C}{\hbar\omega_{01}}. \tag{3.37}$$

[12] The same result is obtained if a less crude approximation is used and correction terms in the Hamiltonian up to cubic order in $E_C/\hbar\omega_{01}$ are included [46, 80].

By a similar, but more careful analysis, one can obtain the parity-switching matrix elements within a single level [46] to first order in E_C/ω_{01}:

$$\langle i|\cos\hat{\varphi}|i\rangle \simeq 1 - \frac{E_C}{4\hbar\omega_{01}}\left(i+\frac{1}{2}\right), \tag{3.38}$$

$$\langle i|\sin\hat{\varphi}|i\rangle \propto e^{-\hbar\omega_{01}/E_C}. \tag{3.39}$$

Relaxation rate

With these approximations, the QP-induced transition rate in a transmon can be calculated from qubit properties and the QP density. Inserting Eq. 3.37 and Eq. 2.47 into Eq. 2.42 gives

$$\Gamma_{01}^{\mathrm{QP}} \approx \sqrt{\frac{2\omega_{01}\Delta}{\pi^2\hbar}}\, x_{\mathrm{qp}}, \tag{3.40}$$

an approximate expression for the QP-induced decay rate.

Frequency shift

For the calculation of the frequency shift, Eq. 3.38 is inserted into Eq. 3.26 and Eq. 3.37 into Eq. 3.27. Combined with Eq. 3.29, one obtains

$$\delta\omega_{i,E_J} = -\frac{1}{2}\,\omega_{01}\left(x_{\mathrm{qp}} + 2x_{\mathrm{qp}}^{A}\right), \tag{3.41}$$

$$\delta\omega_{i,\mathrm{qp}} = \frac{E_C}{\hbar\omega_{01}}\left(F_{\mathrm{qp}}(\omega_{01}) + F_{\mathrm{qp}}(-\omega_{01})\right). \tag{3.42}$$

If these are combined and Eq. 3.28 is substituted, one finds for the shift of the transition frequency in the transmon limit

$$\delta\omega_{01} = -\frac{1}{2}\,\omega_{01}x_{\mathrm{qp}}\left[\frac{1}{\pi}\sqrt{\frac{2\Delta}{\hbar\omega_{01}}}+1\right]. \tag{3.43}$$

Note that the part proportional to the Andreev-state population x_{qp}^{A} cancels out.

Pure dephasing time

Since the matrix element $\langle\sin(\hat{\varphi}/2)\rangle_{ii}$ is exponentially suppressed, Γ_ϕ^s (Eq. A.13) vanishes in the transmon limit and the pure dephasing rate (Eq. A.12) reduces to

$$\Gamma_\phi = \Gamma_\phi^c = \frac{1}{\pi\hbar}E_C\, e^{-\Delta/k_BT_{\mathrm{eff}}}\frac{k_BT_{\mathrm{eff}}}{\Delta}. \tag{3.44}$$

Using the same quasi-equilibrium approximation of the distribution function $\left(f(\varepsilon) = e^{-\varepsilon/k_BT_{\mathrm{eff}}}\right)$, the energy relaxation Γ_{01} becomes [46]

$$\Gamma_{01} \approx \frac{2}{\pi}\,\omega_{01}e^{-\Delta/k_BT_{\mathrm{eff}}}\sqrt{\frac{\pi k_BT_{\mathrm{eff}}}{\hbar\omega_{01}}}. \tag{3.45}$$

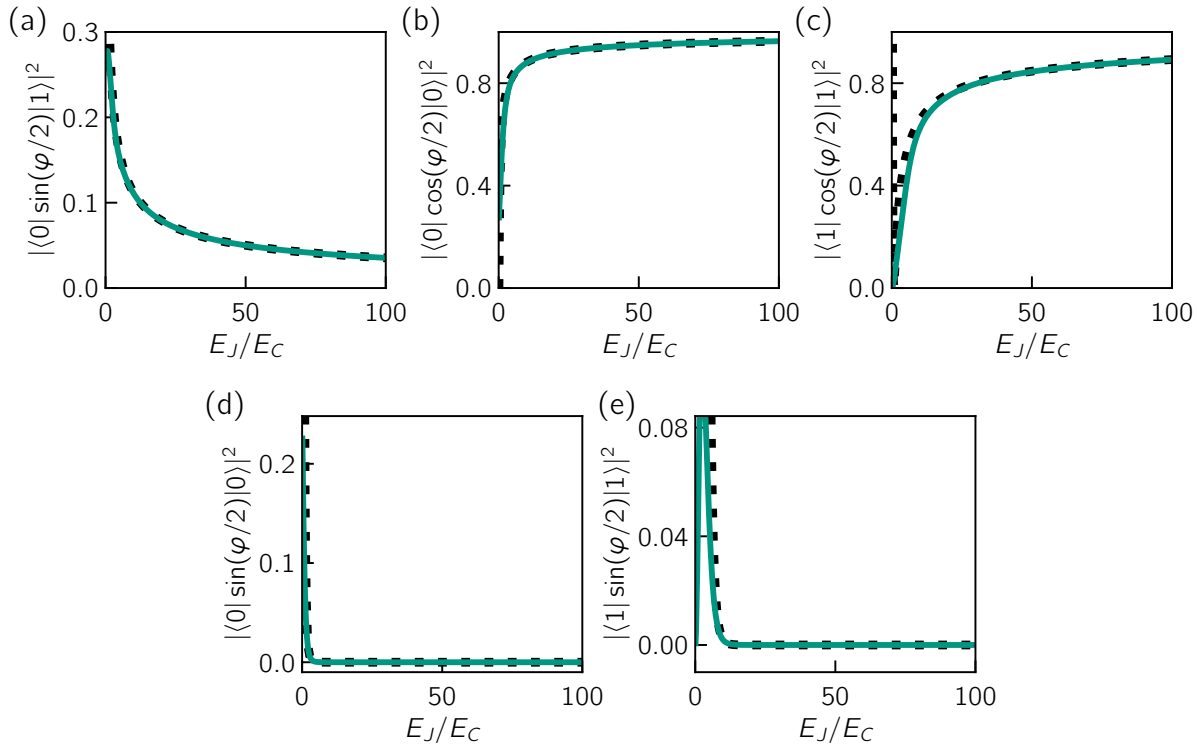

Figure 3.7.: Comparison between numerical calculation (green solid line) and transmon approximation (black dashed line). The matrix elements are plotted against E_J/E_C: (a) $\langle 0\,|\sin\frac{\hat{\varphi}}{2}|\,1\rangle$, (b) $\langle 0\,|\cos\frac{\hat{\varphi}}{2}|\,0\rangle$, (c) $\langle 1\,|\cos\frac{\hat{\varphi}}{2}|\,1\rangle$, (d) $\langle 0\,|\sin\frac{\hat{\varphi}}{2}|\,1\rangle$, (e) $\langle 1\,|\sin\frac{\hat{\varphi}}{2}|\,1\rangle$.

Comparing Eq. 3.45 and Eq. 3.44 yields

$$\frac{2\Gamma_\phi}{\Gamma_{01}} = \frac{E_C}{2\hbar\omega_{01}}\frac{k_B T_{\text{eff}}}{\Delta}\sqrt{\frac{\pi k_B T_{\text{eff}}}{\hbar\omega_{01}}} \ll 1. \tag{3.46}$$

Therefore, in a transmon qubit the energy-relaxation contribution to the dephasing time T_2 is dominant.

3.3.2. Matrix elements: numerical calculation

The above approximations assume low anharmonicity and small E_C/ω_{01}, to test the range of E_J/E_C in which this approximation is valid, a numerical calculation of the matrix elements is necessary. For this, the qubit Hamiltonian is written in the charge basis Eq. 3.11 and the identity $e^{i\varphi} = |n\rangle\langle n+1|$ is used to express the sine and cosine terms.

In the transmon approximation, parity states were not resolved, since they are not distinguishable in that regime. In the present charge basis, however, it is clear that a QP tunneling through the junction always changes the parity of the qubit. Thus, same-parity transition matrix elements vanish, i.e., transitions occur only between states with even and odd parity, but not within the even or within the odd subsector.

Fig. 3.7 shows the numerically calculated matrix elements relevant for the decay rate and the frequency shifts (green), together with the transmon approximations (black dashed lines) given by Eq. 3.37 and Eq. 3.38. The numerical calculation is performed including the first 100 charge

states, which is sufficient for the parameter space considered here [122], and at an offset charge of $n_g \approx 0.25$. One finds that the transmon approximation agrees very well with the numerical result also for parameter regimes with $10 \lesssim E_J/E_C \lesssim 100$, i.e., throughout the OCS regime. Therefore, the analytic transmon approximations can be used for the investigated samples with $E_J/E_C > 25$ in Ch. 5.

3.3.3. Photon-assisted tunneling

If there is additional energy input from the environment into the system in the form of radiation with energy $\hbar\omega_{\mathrm{BB}} > 2\Delta$, additional QPs can be generated. This not only increases the QP density x_{qp} (Sec. 2.5.2) but can also lead to an additional tunneling process through the Josephson junction, where a Cooper pair is broken and one of the QPs acquires sufficient energy to tunnel through the junction. This process is called *photon-assisted tunneling* (PAT). The origin of this second process lies in the second term in Eq. 2.40, which was neglected previously. With the additional energy input, energy conservation for the second term, which creates additional QPs, can be fulfilled and it is no longer forbidden by energy conservation. A detailed derivation of this process for a single mode ω_{BB} can be found in Refs. [81, 84]. The following provides a brief overview and an extension to broadband blackbody radiation.

The additional photon-assisted term in Eq. 2.40 yields the photon-assisted relaxation rate

$$\Gamma_{ij}^{\mathrm{PAT}} = \Gamma_{\mathrm{PAT}} \left(\left| \left\langle j \left| \cos\frac{\hat{\varphi}}{2} \right| i \right\rangle \right|^2 S_{\mathrm{P}}^{-}[\omega_{ij}] + \left| \left\langle j \left| \sin\frac{\hat{\varphi}}{2} \right| i \right\rangle \right|^2 S_{\mathrm{P}}^{+}[\omega_{ij}] \right). \tag{3.47}$$

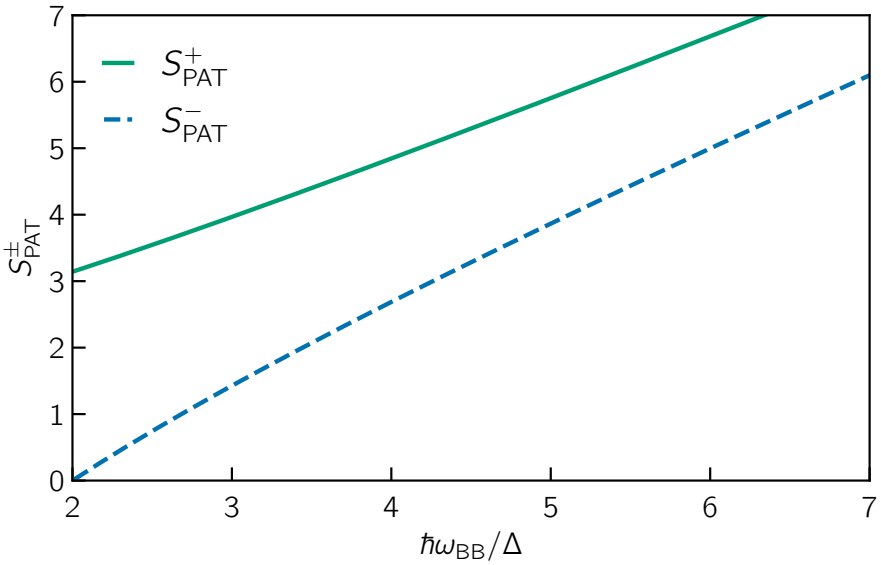

Figure 3.8.: Spectral functions $S_{\mathrm{PAT}}^{\pm}$ as a function of the pair-breaking photon frequency.

Analogous to Eq. 2.44 and Eq. 2.46, one obtains

$$\begin{aligned}\tilde{S}_{\mathrm{P}}^{\pm}[\omega_{ij}] &= \Gamma_{\mathrm{PAT}}\, S_{\mathrm{P}}^{\pm}[\omega_{ij}] \\ &= \frac{2E_J}{\pi\hbar}\int_{2\Delta/\hbar}^{\infty} \mathrm{d}\omega_{\mathrm{BB}}\, E(\omega_{\mathrm{BB}}, T_{\mathrm{BB}}) \left(\frac{1}{\hbar\omega_{\mathrm{BB}}}\right)^2 \\ &\qquad \int_0^{\infty}\mathrm{d}\epsilon_l \int_0^{\infty}\mathrm{d}\epsilon_r\, \rho_s(\epsilon_l)\rho_s(\epsilon_r)\left(u_r v_l \pm v_r u_l\right)^2 \\ &\qquad\qquad \times \delta\left(\hbar\omega_{\mathrm{BB}} - \epsilon_l - \epsilon_r + \epsilon_i - \epsilon_j\right),\end{aligned} \tag{3.48}$$

where $E(\omega_{\mathrm{BB}}, T_{\mathrm{BB}})$ is the electric-field energy distribution at the junction for the blackbody of temperature T_{BB}. The first line integrates over all available photon states contributing to the PAT, the second line integrates over the available energy states on both sides of the junction, and the third line ensures energy conservation. Note the difference in the energy-conservation term compared to the case without photons: energies up to $\hbar\omega_{\mathrm{BB}}$ above the qubit energy difference $\hbar\omega_{ij}$ are now available. The total energy available to produce QPs in this process can be expressed as $z = (\hbar\omega_{ij} + \hbar\omega_{\mathrm{BB}})/\Delta$. In the derivation of Eq. 3.48, the approximation for the available final states $1 - f(\varepsilon_l) \approx 1$ is used, since only very few QPs are initially present.

$S_{\mathrm{PAT}}^{\pm}[\omega_{ij}]$ encodes the spectral properties of the photon-assisted process [81] and can be obtained by numerical integration, as shown in Fig. 3.8.

4. Experimental methodology

In this chapter, an overview of the experimental methods and measurement techniques is presented. First, an overview of the microwave readout in a reflection measurement is given (Sec. 4.1). Next, the cryogenic measurement setup and the microwave readout scheme are described (Sec. 4.2). Subsequently, various measurement methodologies in the frequency domain are demonstrated, along with pulsed measurement techniques (Sec. 4.3). Finally, the on-chip experimental setup for the qubit devices is explained, including the characterization of the devices studied (Sec. 4.4).

4.1. Microwave reflectometry

As discussed in Sec. 3.2.4, in the dispersive regime the measurement of the qubit state reduces to a precise measurement of the coupled resonator frequency. As shown in Fig. 3.5, the qubit–resonator system is capacitively coupled to the end of a $50\,\Omega$ reflection line.[1]

4.1.1. Scattering parameters

In the context of microwave networks, scattering parameters characterize how electromagnetic waves interact with a network element. For a single port coupled to a transmission line, the relevant scattering matrix element is the complex reflection coefficient $S_{11} = V_1^{\text{out}}/V_1^{\text{in}}$, where V_i^{in} and V_i^{out} denote the complex voltage amplitudes of the incident and reflected signals, respectively [157]. In the setup used here, a two-port configuration is employed: one active port carries the probe signal to the sample inside a cryostat, and one receiving port extracts the reflected signal from the cryostat. Sec. 4.2 explains how a circulator is used to separate the incoming from the outgoing signal in the reflection line of the sample in this case.

The amplitude of S_{11} is measured in decibels (dB), defined as one tenth of a bel, where a single bel represents a power ratio [157]:

$$L_P = 10 \log_{10} \frac{P}{P_{\text{ref}}}. \tag{4.1}$$

The reference power is $P_{\text{ref}} = 1\,\text{mW}$, yielding the unit decibel-milliwatt (dBm). Since scattering parameters formally represent ratios of voltages, the voltage ratio must be converted to a power

[1] The term *reflection line* emphasizes that the reflected rather than the transmitted signal is measured. In standard microwave terminology, this is simply a transmission line terminated at one end. In many designs, a nonterminated *transmission line* is used instead, and the term *transmission line* is therefore used as a general term in the next sections.

ratio using the characteristic impedance $Z_0 = 50\,\Omega$ of the transmission line. Using $P = V^2/Z_0$, the power ratio becomes

$$L_P = 10\log_{10}\frac{P}{P_{\text{ref}}} = 10\log_{10}\frac{V^2}{V_{\text{ref}}^2} = 20\log_{10}\frac{V}{V_{\text{ref}}}. \tag{4.2}$$

In the same way, amplification and attenuation of microwave components in the network are also expressed in decibels (dB).

4.1.2. Reflection readout of resonators

In the experiments of this thesis, a $\lambda/4$ coplanar waveguide (CPW) or stripline resonator is used. It is characterized by its resonance-frequency modes $\omega_n = n\omega_r$, with $\omega_r = 1/\sqrt{LC}$ for the fundamental mode, and the quality factor

$$\frac{1}{Q_L} = \frac{1}{Q_i} + \frac{1}{Q_c}, \qquad Q_L = \frac{\omega_r}{\kappa} \tag{4.3}$$

where Q_L is the loaded quality factor, accounting for both internal (Q_i) and coupling (Q_c) losses, and κ is the full width at half maximum (FWHM). For the readout resonator in the strong-coupling regime (compare Sec. 3.2.4), the coupling quality factor Q_c is designed to dominate the loaded quality factor ($Q_L \approx Q_c$). The coupling quality factor is determined primarily by geometric design parameters, while the internal quality factor Q_i provides insight into material quality, fabrication processes, interface cleanliness, and other loss mechanisms.

All networks in this thesis are matched to an impedance of $Z_0 = 50\,\Omega$. One can conceptually think of a resonator as an impedance discontinuity—a section of the transmission line of length l in which the impedance changes from the characteristic value Z_0 to a frequency-dependent value $Z_1(\omega)$. The frequency-dependent input impedance of the resonator can be approximated as [157]

$$Z_1(\omega) = Z_0\left(\frac{Q_c}{Q_i} + 2\mathrm{i}Q_c\frac{\omega-\omega_0}{\omega_0}\right). \tag{4.4}$$

The corresponding reflection coefficient of such a resonator becomes

$$S_{11}(\omega) = 1 - \frac{2Q_L/Q_c}{1 + 2\mathrm{i}Q_L(\omega-\omega_0)/\omega_0}. \tag{4.5}$$

One can readily verify that the on-resonance scattering parameter ($\omega = \omega_0$) is $S_{11}^{\text{R}} = 1 - 2Q_L/Q_c$, while far off resonance ($|\omega - \omega_0| \gg \omega_0/Q_L$), $S_{11}^{\text{OR}} \to 1$, indicating total reflection with no coupling into the resonator. Normalizing the scattering parameter to center the resonance in the complex plane[2]

$$\left|\tilde{S}_{11}\right| = \frac{Q_L/Q_c}{\sqrt{1 + 4Q_L^2(\omega-\omega_0)^2/\omega_0^2}}, \quad \arg(\tilde{S}_{11}) = \arctan\left(\frac{2Q_L(\omega-\omega_0)}{\omega_0}\right). \tag{4.6}$$

The signal traces a circle in the complex plane, as shown in Fig. 4.1(a). The center of this circle is located at $1 - Q_L/Q_c$ on the real axis. The amplitude response is a Lorentzian dip that vanishes in the overcoupled regime (Fig. 4.1(b)) and the phase varies by more than π in the overcoupled regime (approaching 2π for strong overcoupling), see Fig. 4.1(c).

[2] $\tilde{S}_{11} = (S_{11}^{\text{R}} + S_{11}^{\text{OR}})/2 - S_{11}$

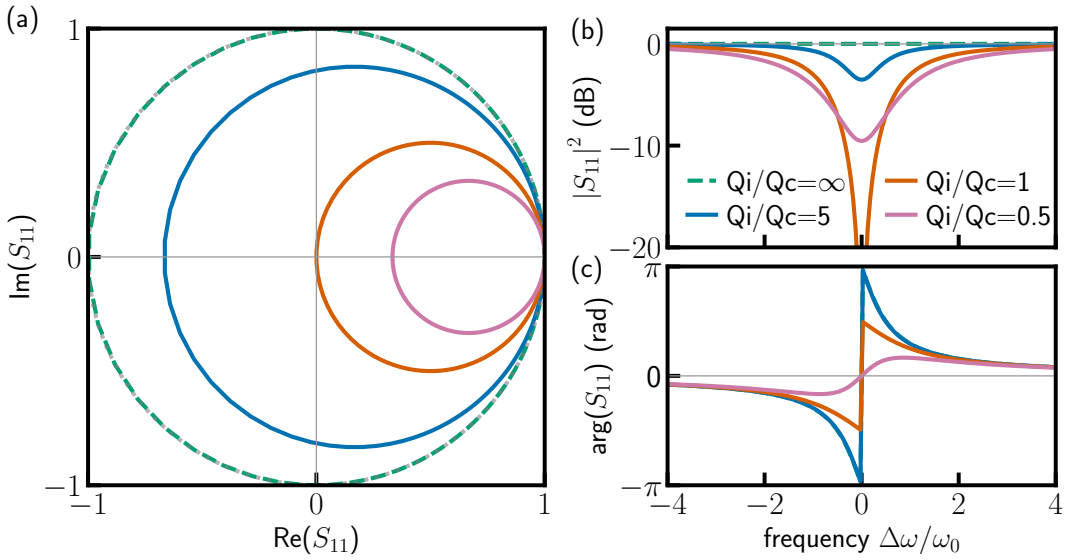

Figure 4.1.: Complex-plane representation of the reflection coefficient S_{11} for a capacitively coupled resonator. (a) Normalized S_{11} data trace a circle in the complex plane; the radius and position of the circle encode the quality factors Q_L and Q_c. (b) Amplitude as a function of frequency for different coupling regimes. (c) Phase evolution for overcoupled, critically coupled, and undercoupled resonators, illustrating the different total phase excursions.

The values of Q_L and Q_c (and thereby Q_i) can be directly extracted from a circle fit.This approach is used to characterize the readout resonators coupled to the qubits . The fitting algorithm employed in Sec. 4.4 also includes additional parameters to correct for impedance mismatches, cable delays, and other experimental imperfections in the measurement setup [158].

4.2. Cryogenic measurement setup

Experiments on superconducting qubits must be conducted at millikelvin temperatures to achieve low thermal QP populations (see Sec. 3.3) and minimal thermal excitation of qubit states for the aluminum junctions in the experiments of this thesis. In addition to these low cryogenic temperatures, precise control and state preparation of the qubits are required. Additionally, for the goals of this research, QPs must be injected into the device via infrared photon absorption without significantly heating the qubit substrate, requiring a special setup in the cryostat, explained in Sec. 5.1.

4.2.1. Dilution refrigerator

Fig. 4.2(b) sketches the cryostat (Bluefors LD250). Two pulse-tube stages precool the system to 45 K and 3 K with minimal vibration. These precooling stages cool a mixture of helium-3 (He-3) and helium-4 (He-4), which undergoes further cooling via expansion through a Joule–Thomson valve [159, 160]. A continuous ^{3}He/^{4}He dilution unit provides the final stage of cooling. Below 870 mK, the mixture separates into a ^{3}He-rich normal phase atop a dilute superfluid phase, as illustrated in Fig. 4.2(a). When ^{3}He atoms cross the phase boundary, they absorb latent heat. Those that evaporate into the still are pumped away, precooled in the heat exchangers, and recirculated, maintaining temperatures as low as $\sim$ 10 mK [161]. Practical limits arise

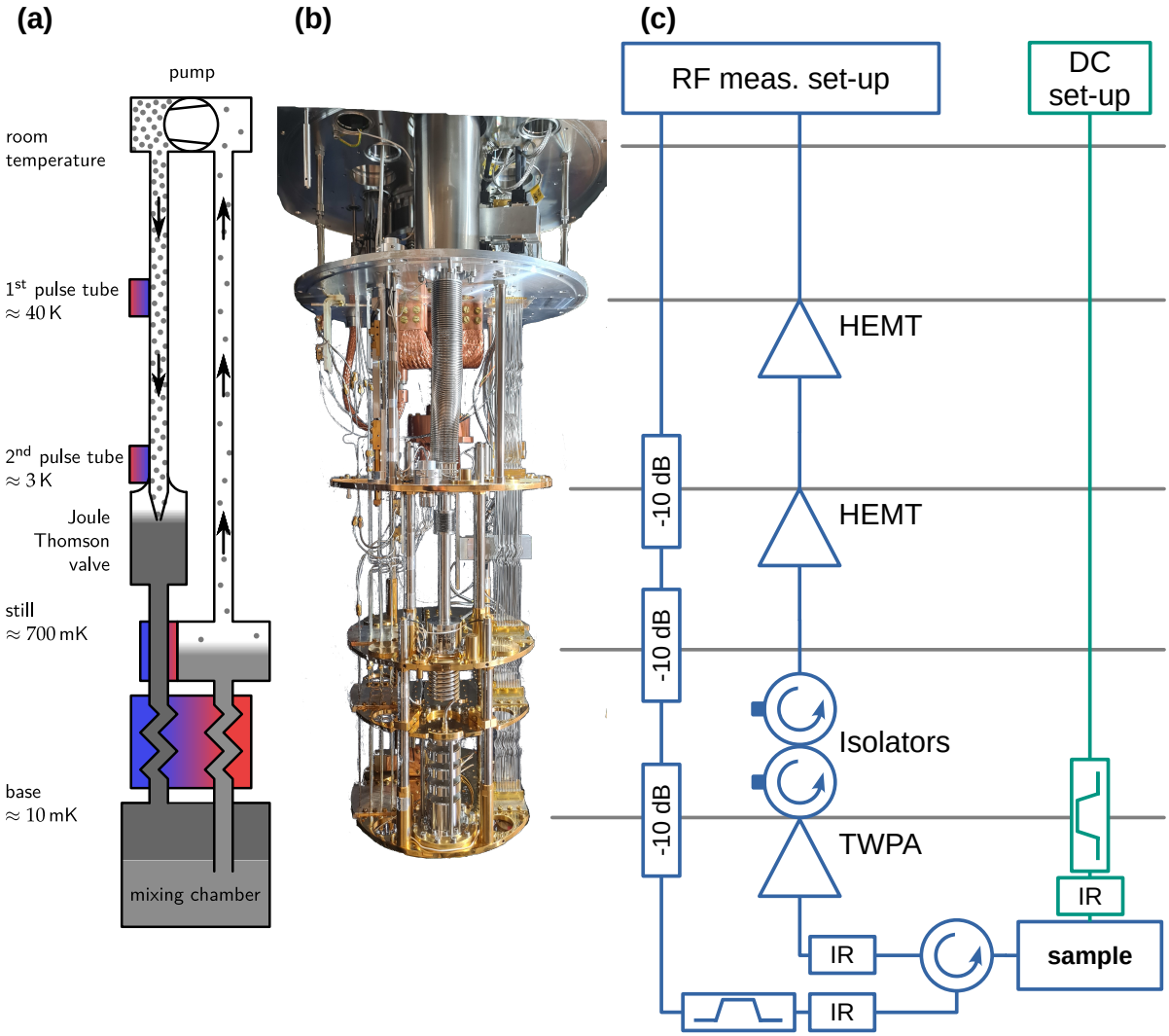

Figure 4.2.: Schematic overview of the dilution refrigerator and measurement setup. (a) Simplified diagram of the He-3/He-4 circulation cycle within the dilution refrigerator, showing the pulse-tube precooling stages (40 K and 3 K), the Joule–Thomson expansion valve, the mixing chamber where phase separation and evaporative cooling occur, and the still chamber where He-3 is recirculated. Stage temperatures are labeled. Adapted from Ref. [162]. (b) Photograph of the Bluefors cryostat interior. (c) Cabling diagram showing the signal paths from room temperature through the various temperature stages down to the mixing chamber, for the microwave (RF) part in blue and for the DC part in green, which is only used for the offset-charge-sensitive sample (see Sec. 4.4.2). The microwave part includes the attenuation stages, amplifiers, and filtering elements described in Sec. 4.2.2 (infrared filters are not shown explicitly). The DC part includes the filter stages described in Sec. 4.2.3.

from the finite cooling power ($\sim 10\,\mu W$ at base) and parasitic heat loads through supports and wiring; these are mitigated with low-thermal-conductivity materials (stainless steel, PTFE, superconducting leads) and evacuated, gold-plated radiation shields. An additional $\sim 150\,mK$ intermediate stage between the still and mixing chamber is available as well. The samples are mounted on the mixing-chamber plate. The mixing-chamber plate is sometimes also referred to as *cold plate*, *cold stage*, *mxc stage*, or *base*.

4.2.2. Microwave signal paths

As discussed in the section on dispersive readout (Sec. 3.2.4), qubit state measurement is performed via resonators operating in the microwave frequency range. This subsection describes the complete signal path from room-temperature electronics to the qubit chip at base temperature, addressing both thermal and signal-integrity considerations. The fundamental challenge is twofold: (1) the thermal noise in the microwave signal from room temperature (corresponding to an effective temperature of $\approx 300\,\mathrm{K}$) is far above the energy scales of the qubit, and (2) careful thermal management is required to prevent excessive heating of the mixing-chamber stage. These challenges are addressed through strategic attenuation, filtering, and careful choice of materials for the coaxial readout lines. The measurement lines are shown schematically in Fig. 4.2(c).

Input signal path and attenuation

The microwave signal generated at room temperature is accompanied by significant thermal noise. To minimize the thermal load and excess noise photons reaching the qubit, approximately 60 dB of attenuation is applied, distributed across several cryostat stages. While attenuators reduce the overall signal and noise power, they introduce Johnson–Nyquist noise proportional to their temperature. The noise temperature at the qubit for a multi-stage attenuation system is given by [157][3]

$$T_n = T_1 + \sum_{i=1}^{N} \frac{T_{i+1}}{\prod_{j=1}^{i} a_j}, \tag{4.7}$$

where T_i is the physical temperature of stage i, $a_i > 1$ is the power attenuation factor of stage i, and T_1 is the base temperature at the sample. This formula shows that noise from warmer stages is reduced by the cumulative attenuation factor $\prod_{j=1}^{i} a_j$ of all preceding stages. Ideally, all attenuation would be placed at the coldest stage to minimize cumulative noise; however, practical cooling-power limitations prohibit this. In this setup, a distributed attenuation strategy is employed: approximately 10 dB at the 3 K stage, 10 dB at the still stage, 20 dB at the mixing-chamber stage, and approximately 20 dB integrated into the cabling itself (via high-loss stainless-steel cables).

Output signal path and amplification

The reflected microwave signal returning from the qubit cavity (typically containing only a few photons) must be amplified by approximately the same factor as the input attenuation ($\sim 60\,\mathrm{dB}$ total). The input-referred noise of the amplification chain must be as low as possible to preserve the quantum information in the few-photon signal. Therefore, amplifiers are placed inside the cryostat at the coldest accessible temperature where cooling power permits. The readout chain employs three amplification stages:

- *Traveling-wave parametric amplifier (TWPA) at the mixing chamber:* The TWPA is a near-quantum-limited amplifier providing approximately 15 dB–20 dB of power gain, with gain variability due to frequency and pump-tone optimization. The TWPA operates by modulating the inductance (nonlinearity) of a long Josephson-junction chain via an applied

[3] Assumed here is a large attenuation, such that $a_{j-1} \approx a_j$.

microwave pump tone, thereby amplifying the signal through parametric upconversion (see Ref. [163] for details).

- *High-electron-mobility transistor (HEMT) at the* 3 K *stage:* HEMTs are field-effect transistors constructed from semiconductor heterostructures and can operate at cryogenic temperatures due to their high electron mobility in the two-dimensional electron gas at low temperatures. This device provides approximately 40 dB power gain. In this setup, an LNF-LNC4_8C from Low Noise Factory™ was used.
- *HEMT at the* 45 K *stage:* A second HEMT at the 45 K precooling stage provides an additional ≈ 35 dB of gain. In this setup, an LNF-LNR1_15A from Low Noise Factory™ was used.

The wiring between the stages is realized with coaxial cables matched to an impedance of 50 Ω. In the output path, from the mixing chamber to the 3 K stage, superconducting niobium cables are used, which offer minimal signal loss while simultaneously providing essentially no thermal conductance between stages. After the first HEMT amplification at 3 K, silver-plated stainless-steel cables are used. These cables provide acceptable thermal isolation (through the stainless-steel substrate) while maintaining adequate microwave transmission (via the silver surface coating), exploiting the skin effect whereby microwave signals at gigahertz frequencies propagate primarily on the conductor surface.

Filtering

Low-pass filtering is applied at the mixing-chamber stage to both input and output signal lines, with a cutoff frequency of approximately 18 GHz on the input and on the output. For final experiments with the Q27 sample (see Sec. 4.4.2), narrower bandpass filters are used: 3.6 GHz–8.4 GHz on the input and 6.5 GHz–9 GHz on the output, tuned to match the specific qubit and resonator frequencies. These filters prevent out-of-band noise, pump tones from the TWPA, and other spurious signals from reaching the sample. Additionally, infrared-blocking filters, fabricated from sapphire-powder–epoxy composites, are incorporated into both the input and output lines to suppress thermal radiation from warmer stages of the cryostat. These filters are discussed in detail in Ch. 6. The qubit sample is further protected using isolators and circulators to prevent unwanted reflections and coupling of the TWPA pump tone into the measurement path. Specifically, two ferrimagnetic isolators and two 4-port circulators provide directional control, and an additional circulator is placed directly at the sample to ensure that only reflected signals from the resonator reach the readout chain.

4.2.3. DC supply path

For one sample (Q27, see Sec. 4.4) an additional voltage gate is used. For this, a variable DC current in the range between −25 mA and 25 mA needs to be applied. The DC bias is applied through coaxial lines that are similar to the return lines for the microwave signal: silver-plated stainless steel from room temperature to 3 K and niobium–titanium from 3 K to the mixing-chamber stage. The lines are low-pass filtered at base temperature with a cutoff frequency of 150 Hz, and a copper-powder-based infrared filter is installed [164].

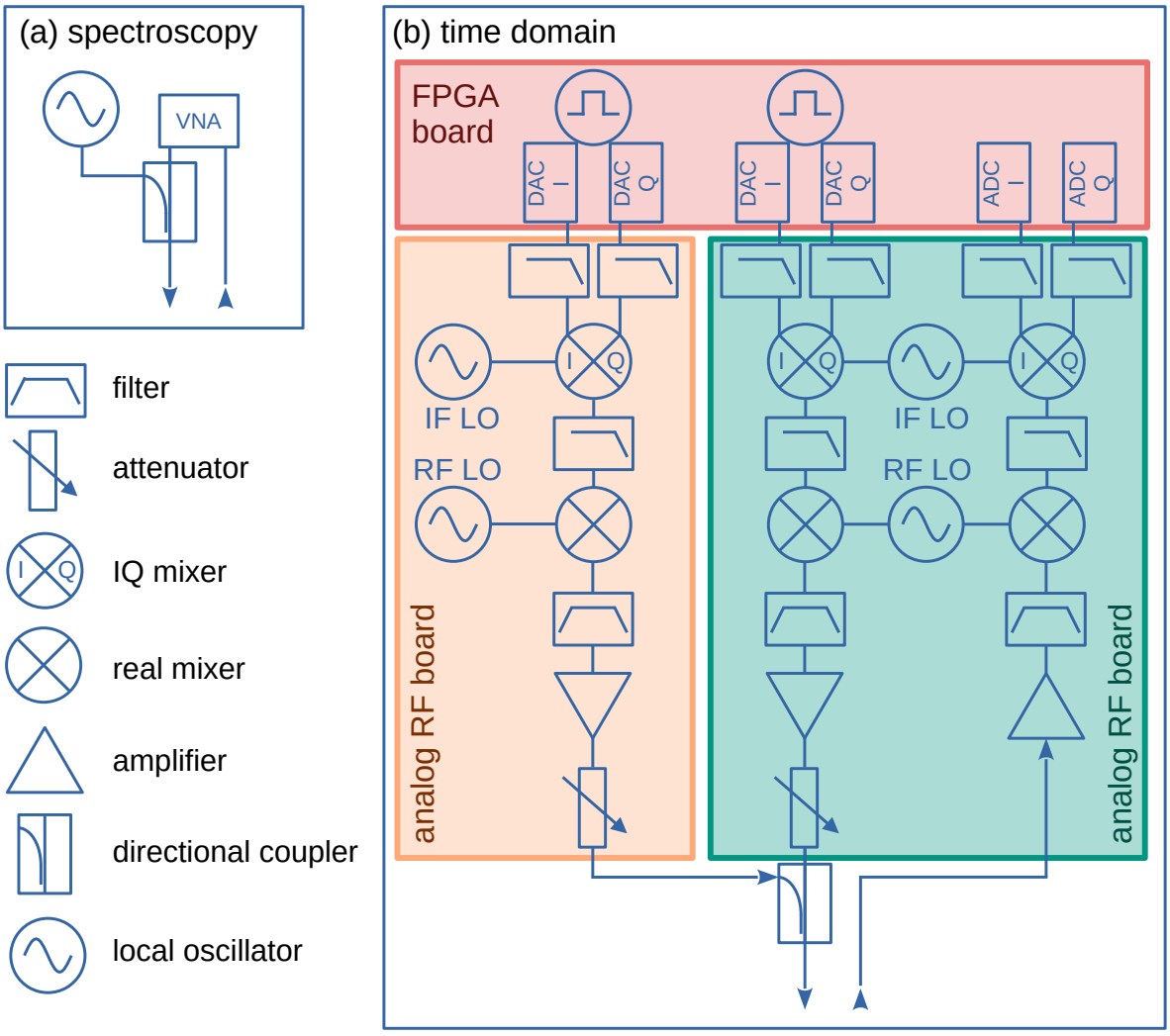

Figure 4.3.: Room-temperature measurement setups. (a) Spectroscopy setup with a VNA and microwave source for two-tone measurements. (b) Time-domain setup, containing three boards: one hosting the FPGA electronics and digital-to-analog converters (DAC) (red), and two separate analog frontend boards for qubit manipulation (orange) and readout (green) pulses, respectively. On these boards, the signal from the DACs in the MHz range is upconverted to the GHz band—or back downconverted.

4.3. Microwave measurement techniques

4.3.1. Frequency-domain spectroscopy

For routine characterization of resonators and qubits, steady-state (continuous-wave) spectroscopy measurements are used. The experimental setup for such measurements is depicted in Fig. 4.3(a), employing a vector network analyzer (VNA)[4] and an auxiliary microwave source for two-tone experiments.[5] The VNA generates a sinusoidal signal at port 1 and measures the complex reflection or transmission at port 2 by phase-coherent mixing, with the swept spectral data

[4] Specifically, a Keysight E5080B.
[5] The secondary microwave source used was either a Keysight N5173B signal generator or an equivalent device.

containing contributions from the complete measurement chain (cryogenic and room-temperature electronics) as well as the resonator response on the samples.

For characterization of the dispersive readout of qubits coupled to resonators (as detailed in Sec. 3.2.4), two distinct microwave tones are required: one at the resonator frequency ω_r and another at the qubit frequency ω_q. In these experiments, the secondary tone is coupled to the VNA drive path via a power divider or directional coupler, taking the same input-attenuation and filtering path into the cryostat and coupled through the resonator into the qubit. The VNA simultaneously monitors the resonator signal while the secondary source probes the qubit transition, enabling correlation between the two.

A particularly useful measurement routine is the *two-tone power scan*: the VNA is parked at a fixed frequency point on the transmission dip caused by the resonator (either the center for maximum phase response or the flank for maximum amplitude response, depending on the goal). The secondary microwave source frequency and power are swept, while continuously measuring the VNA reflection signal. When the secondary tone matches a qubit transition frequency, it excites the qubit, thereby shifting the resonator frequency (due to the qubit–resonator coupling). This shift appears as a dip or peak in the measured reflectance, providing high-contrast signatures of qubit transitions. At high drive powers, multiple transition lines (corresponding to higher-order transitions) may be resolved; at lower powers, the signal is dominated by the $|0\rangle \leftrightarrow |1\rangle$ transition.

4.3.2. Time-domain measurements

For detailed characterization of qubit dynamics beyond steady-state measurements—including coherence times, energy relaxation, and transient responses—time-resolved (time-domain) measurements must be employed. In these experiments, the qubit is manipulated and measured using carefully timed microwave pulses, enabling direct observation of phenomena such as Rabi oscillations, energy relaxation times (T_1), and coherence decay times (T_2), which are important characteristics introduced in Sec. 3.1.

To manipulate and measure the qubit in the time domain, a microwave pulse is constructed as the product of two components: a time-dependent envelope that controls the instantaneous amplitude (see Sec. 3.2.3 for a discussion of different envelopes) and a high-frequency carrier wave at the qubit or resonator transition frequency. In these experiments, rectangular pulses are used for most measurements due to their simplicity and adequate fidelity at moderate drive strengths. For very short pulse durations, below 50 ns (required at high drive powers), Gaussian pulses are employed. A particularly important pulse is the π-pulse, which has precisely the correct amplitude and duration to coherently transfer the qubit population from the ground state $|0\rangle$ to the excited state $|1\rangle$ via a full π rotation on the Bloch sphere.

Comprehensive qubit characterization relies on several fundamental pulse sequences, three of which are essential for understanding qubit properties. Fig. 4.4 illustrates the measurement protocols on the Bloch sphere.

- *Rabi oscillations* (Fig. 4.4(a)): To demonstrate coherent quantum control of the qubit, observing Rabi oscillations is essential. A single manipulation pulse is applied to the qubit, followed immediately by a readout pulse. The key experimental parameter—either the pulse duration τ (at fixed amplitude) or the drive power (at fixed duration, termed *power*

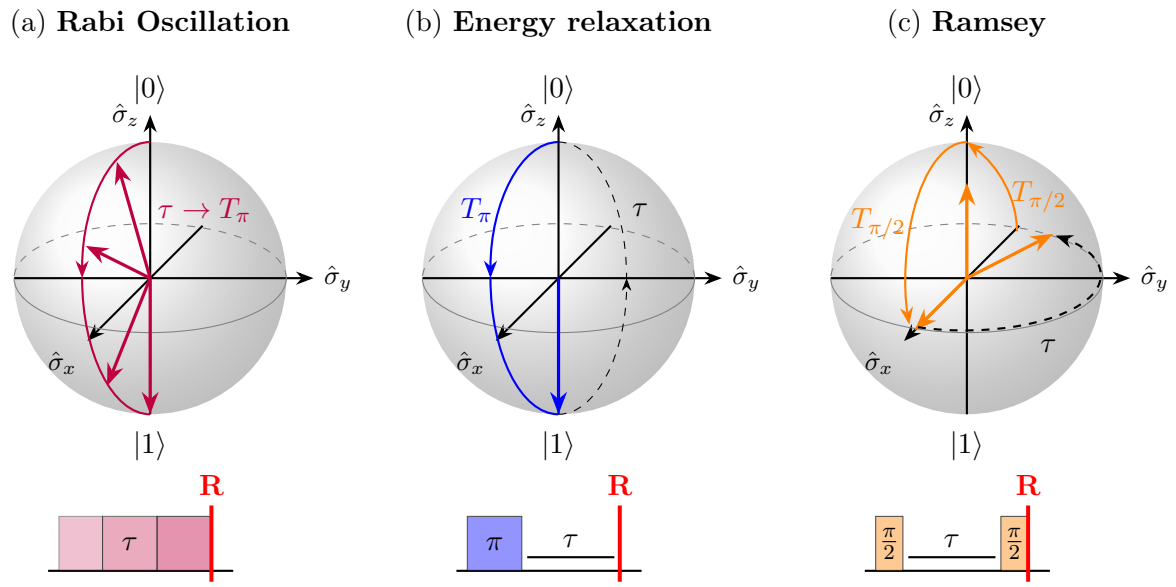

Figure 4.4.: Time-domain qubit measurement sequences. *Top row:* Trajectories on the Bloch sphere showing the qubit evolution for each sequence. *Bottom row:* Pulse timing diagrams (not to scale). (a) *Rabi oscillations:* A variable-duration manipulation pulse followed by a fixed readout pulse. (b) T_1 *measurement:* A π-pulse prepares the excited state, followed by a variable-delay waiting period, then readout. (c) *Ramsey interferometry:* Two sequential $\pi/2$-pulses with a variable-delay free evolution period between them, then readout.

Rabi)—is varied systematically. The measured expectation value of the Pauli σ_z operator exhibits coherent oscillations:

$$\langle \sigma_z \rangle(\tau) = e^{-\tau/T_R} \cos\left(\frac{\pi\tau}{T_\pi}\right), \tag{4.8}$$

where T_π is the duration of a π-pulse at the given amplitude, and T_R is the Rabi damping time, reflecting the exponential decay of oscillation contrast due to decoherence and dephasing during the pulse. Half the oscillation period directly yields T_π. This measurement serves a dual purpose: it provides direct evidence of coherent quantum control and simultaneously calibrates the drive pulse amplitude and length.

- *Energy relaxation time (T_1)* (Fig. 4.4(b)): After the qubit is prepared in the excited state by applying a π-pulse, it spontaneously decays back to the ground state, known as the energy-relaxation process introduced in Sec. 3.1. By measuring the excited-state population as a function of wait time τ after the π-pulse, the energy relaxation time T_1 is extracted:

$$\langle \sigma_z \rangle(\tau) = 1 - 2e^{-\tau/T_1}. \tag{4.9}$$

- *Ramsey interferometry (decoherence time T_2)* (Fig. 4.4(c)): The Ramsey pulse sequence probes dephasing and frequency resolution. A $\pi/2$-pulse (half the duration of a π-pulse) creates an equal superposition of ground and excited states, placing the qubit on the equator of the Bloch sphere. During a subsequent free-evolution period of duration τ, the qubit precesses in this superposition state. A second $\pi/2$-pulse then projects this accumulated phase back onto the measurement axis. The resulting measured signal is

$$\langle \sigma_z \rangle(\tau) = -e^{-\tau/T_2^{\mathrm{R}}} \cos(\Delta\omega \cdot \tau), \tag{4.10}$$

where T_2^{R} is the Ramsey dephasing time, and $\Delta\omega = \omega_{01} - \omega_{\mathrm{d}}$ is the frequency detuning between the applied drive frequency ω_{d} and the true qubit transition frequency ω_{01}. The oscillating cosine term arises from precession of the qubit state during free evolution. The oscillation frequency directly yields the qubit transition frequency with high precision,[6] and the exponential envelope quantifies dephasing.

Time-domain setup

For the experiments in this work, a flexible time-domain measurement platform developed and constructed by the Institut für Prozessdatenverarbeitung und Elektronik (IPE) at KIT [165–168] was employed. This platform is built around reconfigurable field-programmable gate array (FPGA) hardware operating at tens of gigasamples per second, enabling arbitrary pulse generation and real-time signal processing. Microwave pulses are synthesized as follows: the pulse envelope (amplitude and phase modulation) is generated at an intermediate carrier frequency ($\approx 100\,\mathrm{MHz}$) by the digital-to-analog converters (DACs) on the FPGA board, then mixed with a local oscillator (LO) signal at the target microwave frequency using an IQ mixer. After interacting with the sample, the reflected signal is downconverted using the same LO signal through an identical IQ mixer configuration, recovering the I and Q quadratures at intermediate frequency. Analog-to-digital converters then digitize these quadratures for further analysis (Fig. 4.3).

Two similar analog frontend modules—one for drive signal generation and one for readout signal acquisition, each with independent LOs and IQ mixers—allow simultaneous and fully independent qubit manipulation and measurement, enabling complex pulse sequences. The full system is illustrated schematically in Fig. 4.3. For some measurements, a *direct RF board* was also used. By using ultrafast analog-to-digital converters, direct generation of microwave-frequency ($\sim 10\,\mathrm{GHz}$) pulses is possible, such that no LO and mixer setup (analog frontend board) is needed [169].

4.3.3. Data acquisition and processing

For all measurements presented in this thesis, data acquisition and preliminary analysis were performed using *QKIT* [170], a Python-based software package originally developed within the research group at KIT. QKIT provides a unified interface for communicating with and coordinating multiple measurement instruments (VNA, signal generators, time-domain setup) and cryogenic equipment (temperature control). It supports rapid, multidimensional parameter sweeps in which multiple independent variables are systematically varied, with measurements taken at each point in the parameter space.

Acquired data, along with comprehensive metadata describing the experimental conditions (instrument settings, temperature, etc.), are automatically stored in hierarchical data format (HDF5) [171] with a universally unique identifier (UUID) assigned to each experimental run.[7] This structured format facilitates later data retrieval, statistical analysis, and correlation across multiple experiments. QKIT also includes a real-time data viewer enabling live plotting of acquired spectra and parameters during measurement, providing immediate feedback for parameter optimization and quality assessment.

[6] Much better than steady-state spectroscopy, since the frequency resolution is inversely proportional to the maximum evolution time $\tau_{\max}$.

[7] The UUID is a 6-digit string encoding of the integer-cast Unix timestamp.

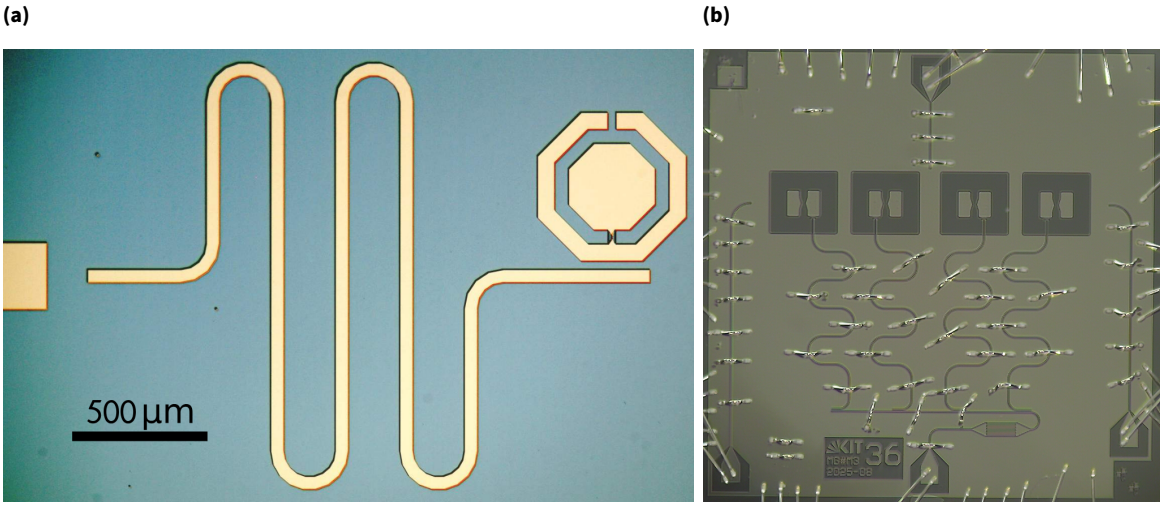

Figure 4.5.: Microscope images of (a) the concentric transmon sample Q200 fabricated at NIST (picture from Ref. [172]) and (b) the Q27 four-qubit chip fabricated in-house, with a reflection line, a Purcell filter, and four resonators with one qubit each. The center two qubits share a voltage gate; the leftmost and rightmost qubits have individual voltage gates. The Q60 four-qubit chip has a similar layout, without the voltage gates.

4.4. Qubit samples

As shown in the preceding chapter, the sensitivity to QPs depends on the offset-charge sensitivity of the qubit. Therefore, three different samples with different offset-charge sensitivities are used in this work: one deep in the transmon regime with $E_J/E_C \approx 200$, the *deep transmon Q200*; one in the offset-charge-sensitive (OCS) regime with $E_J/E_C \approx 27$, the *OCS transmon Q27*; and one in the intermediate transmon regime with $E_J/E_C \approx 60$, the *intermediate transmon Q60*. The three samples are implemented in different geometries and fabrication methods. The first is a single concentric transmon qubit coupled to a microstrip resonator, shown in Fig. 4.5(a). This chip was fabricated at NIST[8] by Martin Sandberg and David Pappas and was graciously provided to the group. The other two are four-qubit samples with coplanar-waveguide (CPW) resonators fabricated in-house in the cleanroom facility, one shown exemplarily in Fig. 4.5(b).

4.4.1. Deep transmon sample Q200

The optical structures (resonator and capacitive pads) are fabricated from titanium nitride (TiN), while the Josephson junction is an $\mathrm{Al/Al_{O_x}/Al}$ stack. TiN was chosen over aluminum for its higher critical temperature $T_c = 3.4\,\mathrm{K}$ and resulting larger superconducting gap $2\Delta = 160\,\mathrm{GHz}$, yielding low microwave loss [173, 174]. Additionally, TiN does not form lossy surface oxides [145, 175, 176]. This sample is well characterized and has been used in prior experiments [177, 178].

4.4.2. OCS transmon sample Q27

The in-house samples are fabricated using a Josephson-junction-first (JJF) approach, where junctions are defined by electron-beam lithography prior to deposition of the resonator, capac-

[8] National Institute of Standards and Technology in Boulder, Colorado.

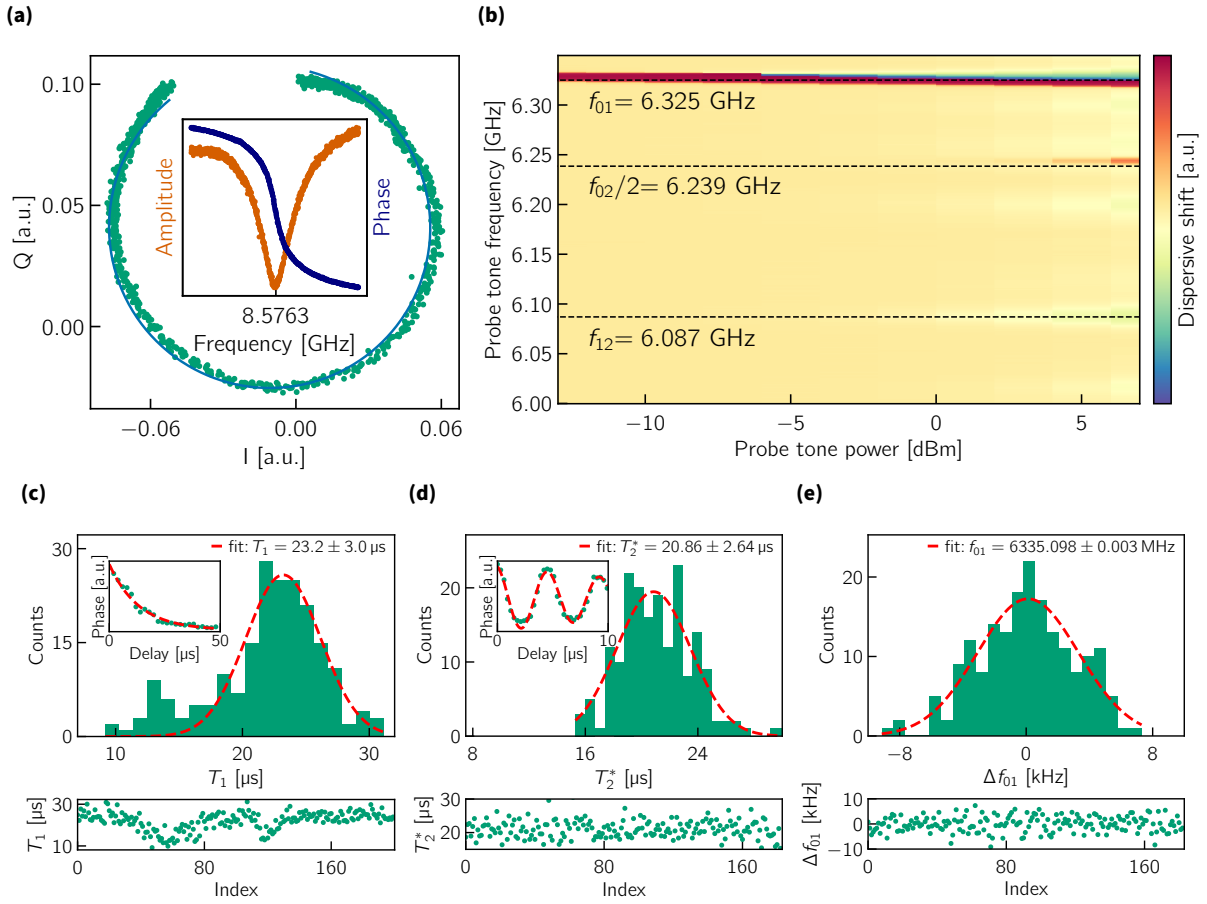

Figure 4.6.: Characterization of the Q200 sample. (a) Resonator circle fit; inset shows fitted amplitude and phase response. (b) Two-tone spectroscopy as a function of drive frequency and power, showing the first three qubit transitions. (c) Qubit relaxation time T_1: histogram of individual fit results (top), time trace over measurement index (bottom), and a representative decay fit (inset). (d) Ramsey dephasing time T_2: histogram and time trace of fitted values, with a representative Ramsey decay fit (inset). (e) Histogram and time evolution of the extracted qubit frequency from the Ramsey fits.

itance, and readout-line structures. This minimizes contamination and interface defects that could degrade performance. The optical structures are fabricated from niobium with critical temperature $T_c = 9.2\,\mathrm{K}$ and superconducting gap $2\Delta/h \approx 700\,\mathrm{GHz}$, chosen for its large energy gap. To prevent oxidation of niobium, the layer is capped with thin aluminum that is subsequently oxidized in a controlled manner. Aluminum oxide has a substantially lower loss tangent than niobium oxides [148]. The fabrication is described in Sec. A.5 in the Appendix. Each four-qubit chip contains floating-transmon qubits with two capacitor pads and a single Josephson junction between them. Each qubit is coupled to an individual CPW $\lambda/4$ readout resonator, such that the next-order resonance is at $3\omega_r$ and lies outside the measurement band. All four resonators are capacitively coupled to a common reflection line interrupted by a broadband Purcell filter (approximately 7.5 GHz, bandwidth $\approx 1\,\mathrm{GHz}$ FWHM) to suppress Purcell losses. The four resonators are designed to lie between 7 GHz and 7.5 GHz with a spacing of 100 MHz. The design is shown in Fig. 4.5(b).

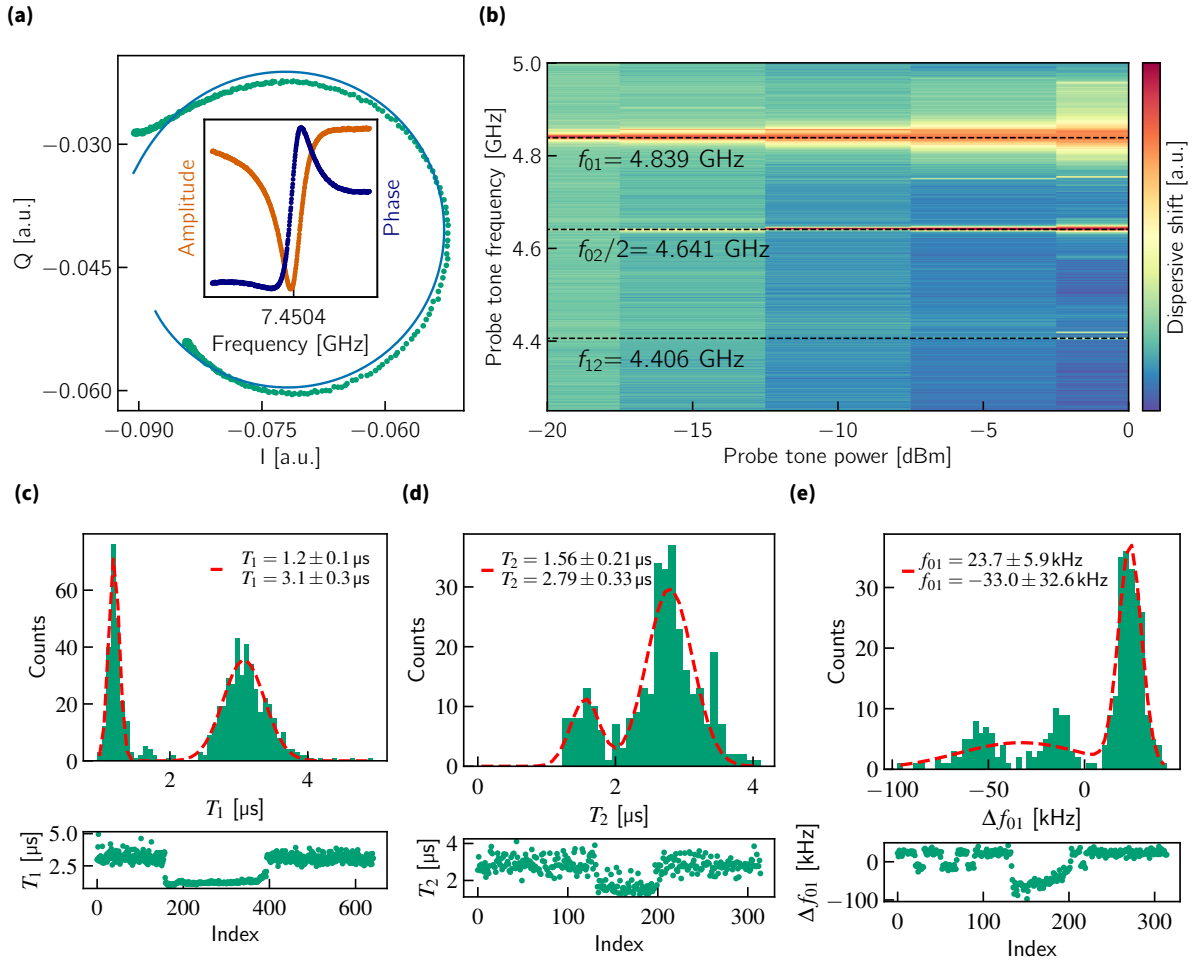

Figure 4.7.: Characterization of Q27. (a) Resonator circle fit in the complex plane; inset shows fitted amplitude and phase response. (b) Two-tone spectroscopy as a function of drive frequency and power, showing the first three qubit transitions. (c) Qubit relaxation time T_1: histogram of individual fit results (top), time trace over measurement index (bottom). (d) Ramsey dephasing time T_2: histogram and time trace of fitted values. (e) Histogram and time evolution of the extracted qubit frequency from the Ramsey fits.

For the measurements presented in this thesis, the leftmost qubit on the chip is used. The design capacitance of the transmons on this chip is 44 fF.[9] The sample is additionally equipped with a charge gate to tune the offset charge n_g on the qubit island, which is coupled with a coupling capacitance of $C_{\text{gate}} = 14.4\,\text{aF}$, obtained from the periodicity of the charge dependence.

For the coherence-time measurements in Fig. 4.7 and Table 4.1, 650 measurements are conducted in sequence. Each measurement consists of a T_1 and a Ramsey measurement. The offset charge is varied at each measurement in a loop by applying a voltage to the charge gate between 0 mV and 25 mV in steps of 1 mV. This results in a measurement cycle of 26 measurements for a full charge-gate sweep. The T_1, T_2^*, and qubit frequency averaged over the two charge states, $\bar{f}_{01}$, do not vary with offset charge. Therefore, the data are averaged over all offset-charge states. Two

[9] The capacitance is simulated in Sonnet [179]. The junction is replaced with a linear inductance and the resonance frequency is simulated for different inductance values. From a fit of the resonance frequencies versus the inductance, the design capacitance is extracted.

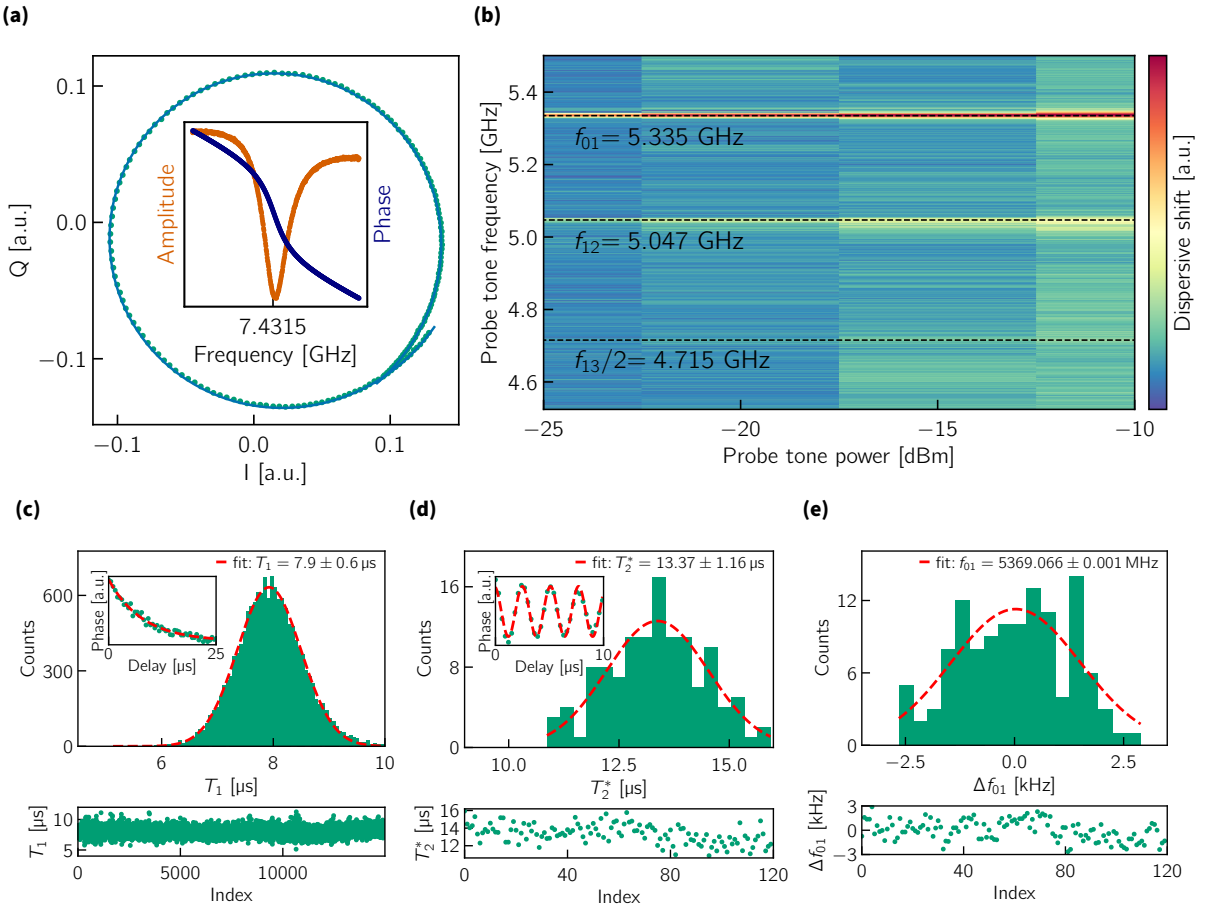

Figure 4.8.: Characterization of Q60. (a) Resonator circle fit; inset shows fitted amplitude and phase response. (b) Two-tone spectroscopy as a function of drive frequency and power, showing the first three qubit transitions. (c) Qubit relaxation time T_1: histogram of individual fit results (top), time trace over measurement index (bottom), and a representative decay fit (inset). (d) Ramsey dephasing time T_2: histogram and time trace of fitted values, with a representative Ramsey decay fit (inset). (e) Histogram and time evolution of the extracted qubit frequency from the Ramsey fits.

stable regimes are visible; see the bottom panels of Fig. 4.7(c,d). This is again attributed to coupled TLSs, as observed in the concentric transmon qubit and explained in Refs. [36, 180].

4.4.3. Intermediate transmon sample Q60

The same chip and resonator design and a similar fabrication method as for the OCS transmon are used; the small differences are explained in Sec. A.5 in the Appendix. The design capacitance is $C = 71\,\mathrm{fF}$. For the measurements in this thesis, the rightmost sample on the chip is used (compare Fig. 4.5(b)). Further consistency measurements of the qubit, second from the right (Q60q2), can be found in Sec. A.7.3 in the Appendix.

4.4.4. Sample characterization

The three samples are all characterized using the same measurement protocols, which were described in Sec. 4.3 (resonator circle fit, two-tone spectroscopy, time-domain T_1 and Ramsey

Table 4.1.: Key characterisation parameters of the three transmons used in this work. All quoted uncertainties are one standard deviation. The qubit labels refer to their extracted E_J/E_C ratios.

	Q200	Q27	Q60
f_r / GHz	8.5763	7.4504	7.4315
Q_i ($\times 10^3$)	15.9	4.8	20.2
Q_c ($\times 10^3$)	10.3	22.0	4.6
f_{01} / GHz	6.335	4.839	5.369
E_J/h / GHz	32.4	9.7	15.4
E_C/h / MHz	162.6	353.0	254.7
C / fF	119.1	54.9	76.0
E_J/E_C	199.2	27.4	60.6
δf_{01} / MHz	$<10^{-4}$	0.56	0.001
$g/2\pi$ / MHz	71.5	89	75
$\langle T_1 \rangle$ / µs	23.2(30)	1.2(1) / 3.1(3)*	7.9(6)
$\langle T_2^* \rangle$ / µs	20.9(26)	1.56(21) / 2.79(33)*	13.4(12)

*Two meta–stable regimes attributed to TLS switching (see text).

experiments). Fig. 4.6 shows the characterization measurements for the concentric transmon (Q200); Fig. 4.7 and Fig. 4.8 present the corresponding measurements for the OCS (Q27) and intermediate (Q60) devices. The results are listed in Table 4.1. Panel (a) displays the signal from the readout resonator coupled to the qubit in the complex plane; the inset shows the amplitude and phase data as a function of frequency. From the circle fit to the data, the resonator frequency f_r, and the internal and coupling quality factors Q_i and Q_c are obtained. From two-tone spectroscopy, the principal qubit transition f_{01} is found; panel (b) shows this transition along with higher-order transitions. From these, the energy levels are calculated and compared to numerical diagonalizations of the Hamiltonian[10] to obtain the charging energy E_C and Josephson energy E_J. By comparing resonator frequencies in the low-power regime (coupled to the qubit) and the high-power regime (effectively decoupled), as described in Sec. 3.2.4, the qubit–resonator coupling constant g is obtained.

To obtain qubit coherence and dephasing times, time-resolved measurements are performed. Panel (c) shows the histogram distribution of multiple measurements with a Gaussian fit, from which the mean T_1 value and its standard deviation are obtained. The inset displays a representative single measurement trace and fit; below the histogram, the time trace of the individual measurements is shown. From Ramsey measurements, a mean T_2^* time and a precise qubit frequency f_{01} can be obtained. Panel (d) shows the Ramsey decoherence time T_2^* and panel (e) the extracted qubit-frequency deviation Δf_{01} as a histogram over multiple measurements with a Gaussian fit, along with the time trace below.

For the Q200 and Q27 sample, the T_1 time exhibits jumps between two different stable regimes. This behavior resembles that reported by Schlör et al. [36]. In the interacting-defect model [180], such behavior can arise from a fluctuator close to a thermal level that switches thermally between states. This fluctuator can then change the frequency of a coupled ensemble of TLSs close in frequency, turning the coupling on and off and thereby producing the observed jumps in qubit coherence time. A characteristic signature of such behavior is a simultaneous jump in

[10] The Hamiltonian in the charge basis (Eq. 3.11) is diagonalized numerically for different sets of E_J and E_C until the closest possible match of the simulated and measured transition frequencies is found.

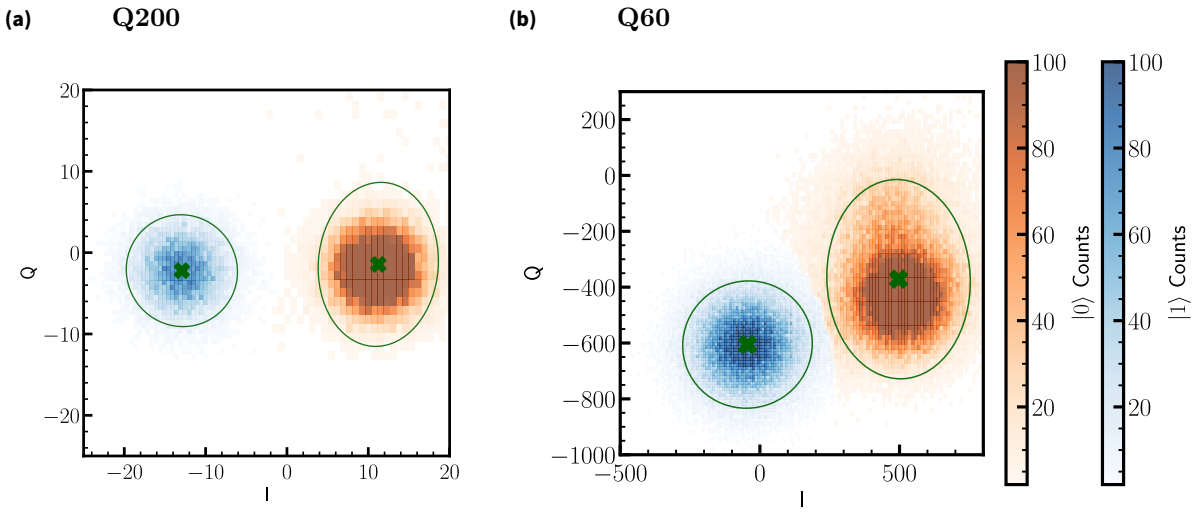

Figure 4.9.: Single-shot measurements of qubits prepared in the ground state (blue) and excited state (orange) shown in the I–Q plane for (a) the Q200 sample and (b) the Q60 sample. The two distinct clouds correspond to the two qubit states. By applying a Gaussian mixture model to the data, a likelihood-based state assignment is performed. The means of the states and the 2σ confidence ellipses are shown in dark green.

multiple qubit parameters, such as T_1, T_2, and qubit frequency, which was also observed. The T_2^* data show no temporal dependence; they were measured separately. The inset displays an exemplary measurement with a damped-sine fit. Again, no dependence on the measurement time is observed.

For the Q27 sample a double-Gaussian fit is used to obtain the coherence times of the two stable regimes, given in Table 4.1. For Q200 only the dominant regime is fitted (Fig. 4.6). Similarly, the Ramsey dephasing times and frequencies are obtained. The primary transition frequencies of the two regimes have a difference of $f_{01,>} - f_{01,<} = (50 \pm 10)\,\mathrm{kHz}$, which is an order of magnitude smaller than the offset-charge detuning of $\delta f_{01} \approx 560\,\mathrm{kHz}$. The frequency trace suggests possibly three stable regimes, but only two — consistent with the T_1 and T_2^* measurement traces — are analyzed here.

4.5. Single-shot measurements

In a single-shot measurement, the state of a qubit is determined from a single instance of the measurement process, rather than from averaging over many repeated measurements. This capability is crucial for quantum computing applications, where the ability to quickly and accurately read out the state of individual qubits multiple times before the qubits decay is essential. For single-shot measurements to work effectively, the amplification of the readout signal must provide a high signal-to-noise ratio to distinguish the qubit states in a single measurement with only a few readout photons. Additionally, the coupling between the qubit and the readout resonator must be optimized to ensure that the qubit states can be determined from the resonator response without excessive backaction that disturbs the qubit state. With such single-shot measurements, it is possible to measure the state population of a qubit directly after preparation in a given state. Fig. 4.9 shows an example of 1000 single-shot measurements of a qubit prepared in the ground state (blue) and excited state (orange) as a 2D histogram. This is shown for the deep transmon sample (a) and the intermediate transmon sample (b); for

the OCS transmon, no single-shot readout was possible, probably due to too weak coupling between the qubit and resonator. The two distinct clouds in the I–Q plane correspond to the two qubit states. By applying a Gaussian mixture model to the data, a likelihood-based state assignment is performed for each measurement, allowing determination of the state population of the qubit.[11] The precision with which the qubit state can be determined is quantified by the qubit *assignment fidelity*:

$$F_{\text{assign}} = \frac{P(0 \mid 0) + P(1 \mid 1)}{2}, \tag{4.11}$$

where

$$\begin{aligned} P(0 \mid 0) &\approx \frac{N_{0|0}}{N_{0|0} + N_{1|0}}, \\ P(1 \mid 1) &\approx \frac{N_{1|1}}{N_{1|1} + N_{0|1}}, \end{aligned} \tag{4.12}$$

is the probability to measure $|0\rangle$ ($|1\rangle$) when $|0\rangle$ ($|1\rangle$) is prepared. A value of 1 indicates perfect state assignment, while a value of 0.5 means no information about the qubit state is gained. For state-of-the-art qubits and readout systems, an assignment fidelity of over 99.9 % is possible [181–183]. For the qubits studied here, an assignment fidelity of approximately 97.6 % is achieved for the deep transmon sample and 94.0 % for the four-qubit Manhattan sample.

Qubit temperature

The excited-state population can also be interpreted as an effective qubit temperature. For a qubit nominally prepared in the ground state, it is assumed that the measured excited-state population is dominated by thermal excitations. For this analysis, the qubit space in the I–Q plane is first characterized by a measurement of equally prepared ground and excited states (Fig. 4.9) to determine the positions of $|0\rangle$ and $|1\rangle$. The qubit is then prepared in the ground state for 2000 measurements and the qubit state is extracted for each measurement. Due to thermal excitations, the qubit can be found with a finite probability in the excited state. This probability is given by

$$P_{|1\rangle} = \frac{1}{1 + \exp\left(\frac{\hbar\omega_{01}}{k_B T_{\text{eff}}}\right)}, \tag{4.13}$$

where ω_{01} is the qubit transition frequency, k_B is the Boltzmann constant, and T_{eff} is the effective qubit temperature. In this model, the qubit is assumed to be a two-level system, which is valid for low temperatures compared to the qubit transition frequency ($\hbar\omega_{01} \gg k_B T_{\text{eff}}$). By inverting Eq. 4.13, the effective qubit temperature is extracted. In the measurement, the mixing-chamber temperature is varied from 10 mK to 240 mK and the state of the qubit, prepared in the ground state, is measured (Fig. 4.10). With increasing mixing-chamber temperature, the excited-state population increases, and population of even higher excited states becomes visible. From these data, the effective qubit temperature is extracted at every mixing-chamber temperature (Fig. 4.11). As expected, the effective qubit temperature increases with increasing mixing-chamber temperature. A base effective qubit temperature of approximately 50 mK to 80 mK is found.

[11] In such measurements, it is not possible to distinguish the source of an incorrect state assignment. It could be a readout error, a qubit relaxation event (for excited-state preparation), or thermal excitation.

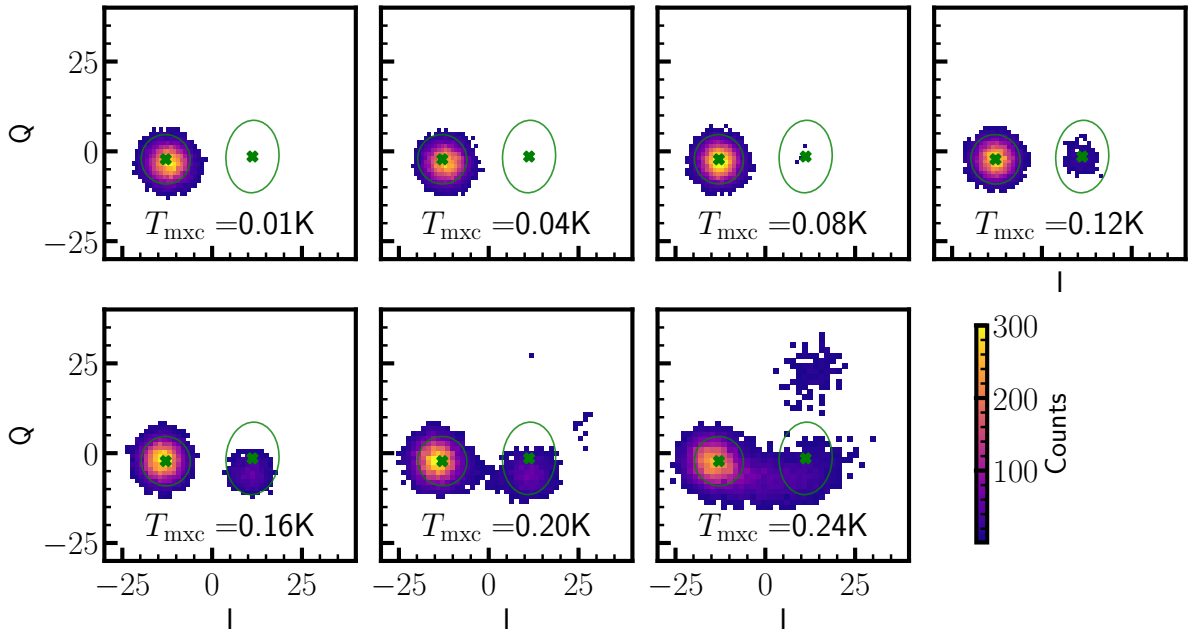

Figure 4.10.: Readout result of Q200 prepared in the ground state in the I–Q plane, as a 2D histogram with the corresponding colorbar (brighter means more measurement counts in the corresponding pixel). The individual panels correspond to different mixing-chamber temperatures. In each panel, the expected (from calibration measurements) mean position for the first two qubit states together with the σ confidence ellipses marked in green. The excited-state population (second cloud) increases with increasing mixing-chamber temperature. At higher temperatures, population of even higher excited states is visible.

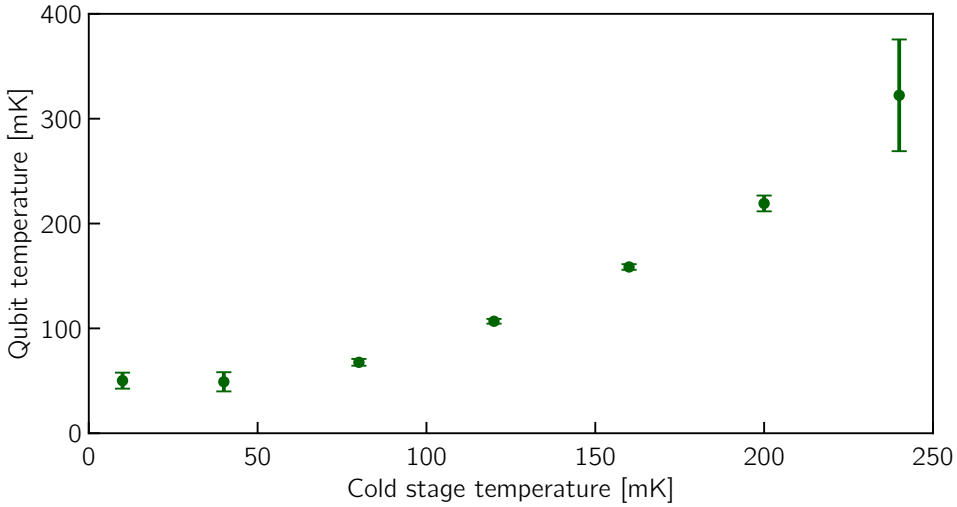

Figure 4.11.: Increasing effective qubit temperature with increasing mixing-chamber temperature, extracted from the histogram data in Fig. 4.10.

5. Qubits irradiated by Infrared photons

This chapter discusses experiments in which three qubits in different charge-sensitivity ranges are deliberately exposed to broadband infrared radiation from a blackbody source to investigate QP effects. The three devices studied in this chapter are introduced and characterised in Sec. 4.4.

In this chapter, the cryogenic setup to illuminate the qubit with infrared radiation is explained (Sec. 5.1) and characterized (Sec. 5.2). Subsequently, it is investigated whether the qubit can be excited by infrared radiation (Sec. 5.3), and the qubit properties are studied under infrared radiation (Sec. 5.4) to gain insight into the infrared-induced QPs.

5.1. Infrared measurement setup

A central aspect of this research involves controlled irradiation of superconducting qubits with infrared (IR) radiation to study QPs and their effects on qubit properties. This section describes the complete infrared photon injection system, which must simultaneously generate a tunable photon flux, transmit these photons to the qubit at the cold stage without heating the cryogenic stages, and shield the qubit from stray electromagnetic fields and thermal background radiation. The system consists of four independent photon-transport lines, a multiport splitter, and a multilayer light-tight sample enclosure providing both optical isolation and magnetic shielding. The transmission lines for the infrared photons include dedicated sections in which different materials can be inserted to test their infrared transmission; this is used in Sec. 6.9. The four lines enable direct comparison of these materials within a single cooldown. A schematic and a photograph of the setup are shown in Fig. 5.1. The individual components are shown in Fig. 5.2 and are discussed in the following.

Light-tight sample enclosure

The light-tight box (Fig. 5.2(a)) consists of three concentric layers, each with a distinct function. The innermost layer is made of copper and coated with a copper-powder–epoxy mixture. This coating creates a rough, absorptive surface that suppresses reflections of stray photons inside the enclosure and absorbs them. Inside the copper shell (Fig. 5.2(b)), a mounting plate is screwed directly to the cold stage, ensuring good thermal contact between the mounted samples and the cold stage. Surrounding the copper shell is a superconducting aluminum layer that helps to shield the qubit from high-frequency electromagnetic noise. The outermost layer consists of mu-metal, which provides magnetic shielding from external fields. Effective shielding is essential for the operation of superconducting qubits [57, 184], especially in the experiments in this thesis that are designed to measure infrared radiation impacts and therefore require a low background of stray photons and magnetic fields.

The light-tightness of the completed enclosure was verified indirectly by testing its watertightness. After successful testing, a small pumping channel with multiple bends was incorporated to allow

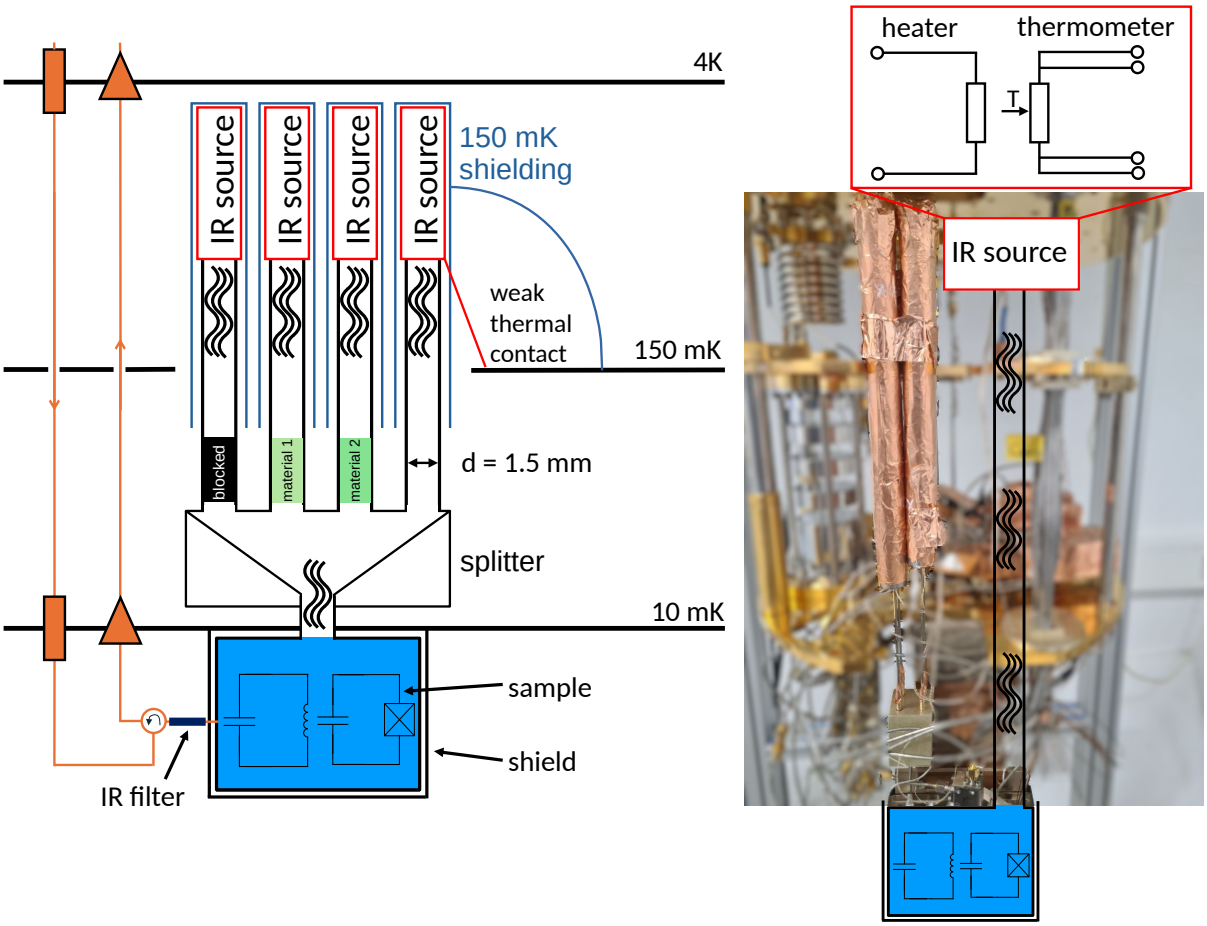

Figure 5.1.: Schematic and photograph of the infrared measurement setup. *Left:* Cross-sectional schematic showing the blackbody radiator mounted above the intermediate plate of the dilution refrigerator at approximately 150 mK, the circular hollow stainless-steel waveguide (inner diameter 1.5 mm), the multiport splitter at the mixing-chamber stage, and the final superconducting aluminum waveguide segment leading into the light-tight sample enclosure. One of the waveguide lines is left open and one is completely blocked for reference measurements. In the other two, different materials can be inserted to investigate their transmission. Thermal shielding and mechanical anchoring to the intermediate plate are indicated. *Right:* Photograph of the assembled waveguide and enclosure showing the actual implementation. The light-tight sample enclosure (with its three-layer structure, not visible) houses the qubit chip mounted on a thermally anchored copper plate. All electrical and microwave connections pass through coaxial SMA feedthroughs with integrated infrared filters.

evacuation of the interior volume while maintaining optical isolation. The sample enclosure has several coaxial microwave feedthroughs with SMA connectors, each incorporating an additional infrared filter.[1] From there, the microwave readout lines are connected as described in Sec. 4.3. Inside the enclosure, a separate, inner sample box is installed and connected to the feedthroughs with copper coaxial cables. The chips are glued into the sample box with silver conductive paste and wirebonded with aluminum wires from the bonding pads to the connectors. The ground plane is bonded with multiple bonds around the sample to the sample box to ensure good grounding. Additional bonds are placed across the microwave reflection line and resonators to connect the ground planes, prevent the formation of parasitic slotline modes, and enhance the quality of the resonators [135, 185].

[1] Sapphire powder filters (fabricated in house) are used, described in detail in Ch. 6.

Infrared radiation path to the sample

Infrared photons are generated by a blackbody radiator above the intermediate plate of the cryostat and guided through a circular waveguide with an inner diameter of 1.5 mm directly toward the cold stage. The waveguide ensures optical transmission while effectively limiting thermal conduction from the hot source to the cold qubit environment. The main part of the waveguide is fabricated from stainless steel to reduce heat transport between the radiator and the cold stage. At the cold stage, a splitter is installed to enable the use of multiple lines in the same cooldown and thus to test different materials for their infrared transmission at millikelvin temperatures (see also measurements in Sec. 6.9). Four blackbody radiators are installed in the cryostat, each with a separate line to the splitter. Typically, one line is left open, one is completely blocked, and two can be filled with various materials, as shown in Fig. 5.1. The materials are inserted into a dedicated section of the tube directly above the splitter and are thermalized to the cold stage. The splitter is made from silver-plated copper and thermalized to the mixing-chamber plate outside the light-tight box. The silver coating inside improves reflectivity and ensures that any absorbed heat is transferred efficiently to the mixing-chamber plate. In this way, comparison measurements can be performed in a single cooldown through the same line entering the sample enclosure. This connection from the splitter through the shielding is implemented with an additional stainless-steel waveguide (see Fig. 5.2(b)). The final 2 cm of the waveguide inside the light-tight box, just before entering the sample box, are made from superconducting aluminum, further minimizing residual heat conduction. The waveguide terminates in the lid of the sample box, directly above the chip.

Blackbody radiator and shielding

The blackbody radiator (Fig. 5.2(c)) is machined from copper and houses a 50 Ω resistor that serves as the heater element. In addition, a temperature-sensitive resistor is mounted for temperature monitoring and feedback control. The resistors are glued to the copper body using silver epoxy, ensuring good heat transfer between the heater, thermometer, and copper radiator. The blackbody heaters are labeled *X01–X04* in this characterization section. The radiator is weakly thermalized to the intermediate plate of the dilution refrigerator (approximately 150 mK) through a thin copper wire. This weak coupling allows the radiator to cool down again after controlled heating while preventing excessive power dissipation into the intermediate stage. To reduce parasitic heat exchange, the radiator and the first 15 cm of the waveguide are surrounded by 10–20 layers of *Superisolierung*[2]. The entire assembly is further enclosed in a stainless-steel tube that is mechanically anchored and thermalized to the same intermediate plate. This provides shielding of the individual heaters and minimizes radiative heating of the cryostat stages and of the other radiators. These elements are visible in Fig. 5.2(c–g).

Temperature control and operation

The blackbody radiator temperature is stabilized by a proportional–integral–derivative (PID) control loop using the internal heater and thermometer. The loop adjusts the heater power in response to the thermometer feedback. With this control, a temperature stability better than

[2] *Superisolierung* consists of multiple layers of thin (∼ 6–12 µm) metallized Mylar foil, typically used in dewars for liquid cryogenics.

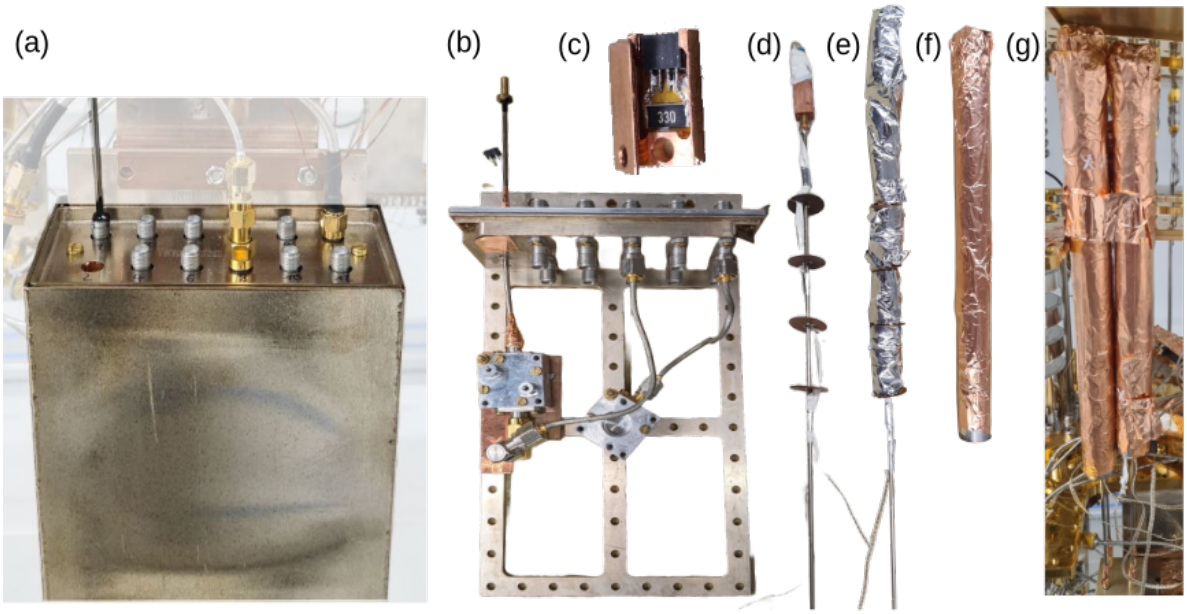

Figure 5.2.: Photographs of the various components of the infrared probing setup. (a) Outside of the layered shielding compartment. (b) Inside the multilayer shielding, the sample is mounted in a sample box (left). The infrared flux tube enters the shielding and the sample box from the top. (c) Copper infrared radiator with internal resistor and thermometer, connected to six pins on the top. (d) Radiator screwed directly onto a 2 mm diameter (1.5 mm inner diameter) stainless-steel tube. The wires are fed to the bottom of the tube, and four copper radiation shields are placed on the tube to protect the experiments below. (e) Radiator and tube covered in 10–20 layers of *Superisolierung*. (f) Stainless-steel shield placed over each radiator and tube. The radiation shield is wrapped in copper foil from the outside to thermalize it to the intermediate plate at ~ 150 mK. (g) Mounted radiators and tubes in the cryostat. Four radiators, each with its own tube, are installed above the mixing-chamber stage. At the mixing-chamber stage, the tubes join in a splitter (see also Fig. 5.1).

10 mK over long measurement times is achieved, ensuring a stable and reproducible incident photon flux on the qubit. Typical PID parameters are tuned for optimal response without oscillation. The control and monitoring are performed using an *SRS™ SIM931* resistance bridge for the thermometer measurement and a *ControlByWeb™* 5-port voltage source for the heater voltage. The PID control is implemented with the in-house developed TIP software package [186].

5.2. Infrared setup characterization

This section presents the characterization of the measurement setup. The setup must generate a sufficient number of photons and guide them efficiently to the qubit chip, while avoiding heating of the mixing chamber or the qubit through radiation or dissipative heat transport. It must not interfere with other experiments in the cryostat, and the different heaters must operate independently with minimal crosstalk. The thermal link to the intermediate plate is tailored for operational heat pulses and cooldown times on the order of minutes.

The following subsections discuss the properties of the final setup and demonstrate suppression of crosstalk between the radiators due to stray radiation to on average 3 %, as well as the absence of significant sample heating up to a blackbody temperature of over 20 K.

5.2.1. Radiated photon number and power

The copper radiator is modeled as a black body with spectral radiance

$$I(f;T) = \frac{2\pi h f^3}{c^2\left(e^{\frac{hf}{k_B T}} - 1\right)}\,\xi_{\text{geo}}, \tag{5.1}$$

where h denotes Planck's constant, c the speed of light, k_B the Boltzmann constant, and T the radiator temperature. The geometrical factor $\xi_{\text{geo}} = \varepsilon A$ accounts for the effective emission area $A = \pi(0.75\,\text{mm})^2$ and the estimated radiation emissivity $\varepsilon \approx 0.7 \pm 0.3$ of the copper surface [187, 188]. The photon flux at frequency f follows by dividing by the photon energy hf:

$$N(f;T) = \frac{I(f;T)}{hf}. \tag{5.2}$$

The waveguide transmits only frequencies above its cutoff $f_c = \frac{1.841c}{\pi d}$ [157, p. 124], where d is the inner diameter. For $d = 1.5\,\text{mm}$, this yields $f_c \approx 117\,\text{GHz}$. All photons above this cutoff therefore have enough energy to break a Cooper pair in aluminum (with $\Delta/\hbar \approx 87\,\text{GHz}$), making this a suitable design choice. Integration of Eq. 5.1 over frequency above f_c gives the total radiated power as a function of blackbody temperature (right axis of Fig. 5.3). Integration of Eq. 5.2 yields the total photon rate as a function of blackbody temperature (left axis).

In this approximation only forward propagation is included, assuming that any emission at larger angles from the radiator is absorbed and thermalized at the wall of the cold stainless-steel tube and does not propagate all the way to the sample. This approximation is not exact and represents one source of systematic uncertainty. The largest source of uncertainty is the approximation of the radiation emissivity. For oxidized copper at high temperatures, an emissivity ε in the range 0.35–0.985 has been reported, depending on surface roughness, cleanliness, and the oxidation process [187–190], with no significant temperature dependence expected.[3] This range of ε is used to estimate the error, together with an estimated 20 % uncertainty of the total emission due to angled emission. This uncertainty range is indicated by the shaded area in Fig. 5.3.

The radiation of the black body is always referred to as *infrared* radiation; however, the infrared frequency range is normally defined between the end of the microwave regime at $\sim 300\,\text{GHz}$ (1 mm) and the beginning of the optical regime at $\sim 430\,\text{THz}$ (0.7 µm). Here the terminology is stretched and covers everything that is radiated by the black body and could break Cooper pairs in the aluminum ($\gtrsim 87\,\text{GHz}$).

The conversion presented in Fig. 5.3 provides an estimate to convert the blackbody temperature to photon flux or radiated power. However, care is required since this estimate has a large error dominated by the unknown internal reflection of the tube and the emissivity of the radiator. Furthermore, it only provides an estimate of photons reaching the sample box, but not of photons that actually get absorbed in a superconducting circuit in the sample box. Therefore, it has to be understood as an order-of-magnitude estimate.

[3] This follows from a temperature-stable phonon absorption via the Berreman effect [189].

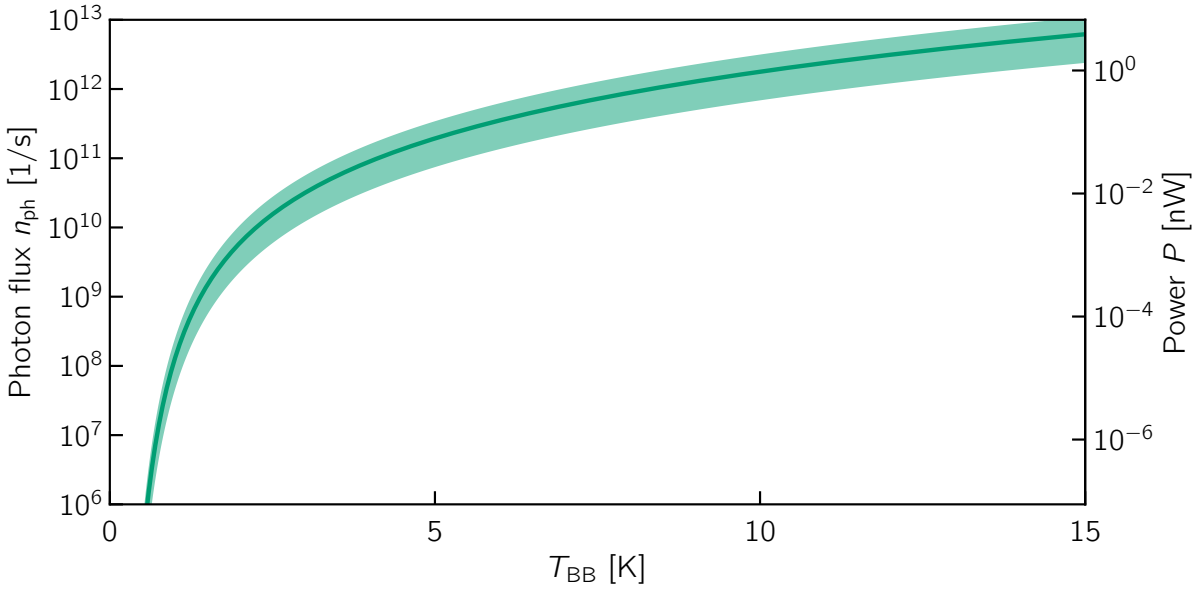

Figure 5.3.: Infrared photon flux (left axis) and power (right axis) reaching the qubit sample versus radiator temperature. The waveguide cutoff is included in the calculation. The shaded area indicates the error interval dominated by the uncertainty in the geometrical factor.

5.2.2. Mixing-chamber heating

The infrared radiators emit radiation in all directions. The shielding described above is installed to suppress radiation in all directions except into the waveguide to the sample, thereby preventing heating of adjacent radiators and surrounding components. Multilayer superinsulation wraps the heaters and the stainless-steel tubes, which are enclosed by a stainless-steel outer housing thermalized to the intermediate cryostat stage (Fig. 5.2(g)). The shielding also suppresses dissipative heat transport mechanisms due to the multiple layers in series. The mixing-chamber temperature remains below 50 mK during radiation experiments. This performance is achieved for radiator temperatures up to 25 K, as determined from measurements of the mixing-chamber temperature while heating one radiator, shown in Fig. 5.4(a).

5.2.3. Thermal coupling to intermediate plate

The heaters couple weakly to the intermediate plate at approximately 150 mK to ensure cooldown after each measurement. The thermal coupling strength G_{bath} balances cooldown time, minimum achievable temperature, and heat load on the intermediate plate and thus on other heaters thermalized to it. Excessive heating of the intermediate plate must be avoided to prevent significant self-radiation and indirect coupling between individual heaters. The thermal coupling G_{bath} and heat capacity C of individual heaters can be determined from the response to a defined voltage pulse of $V = 0.1\,\mathrm{V}$ applied for 60 s across the heater with a resistance of $R = 50\,\Omega$ [191, 192]. During the pulse, the temperature rises according to

$$T(t) = T_{\mathrm{bath}} + A\left(1 - e^{-t/\tau_{\mathrm{rise}}}\right), \tag{5.3}$$

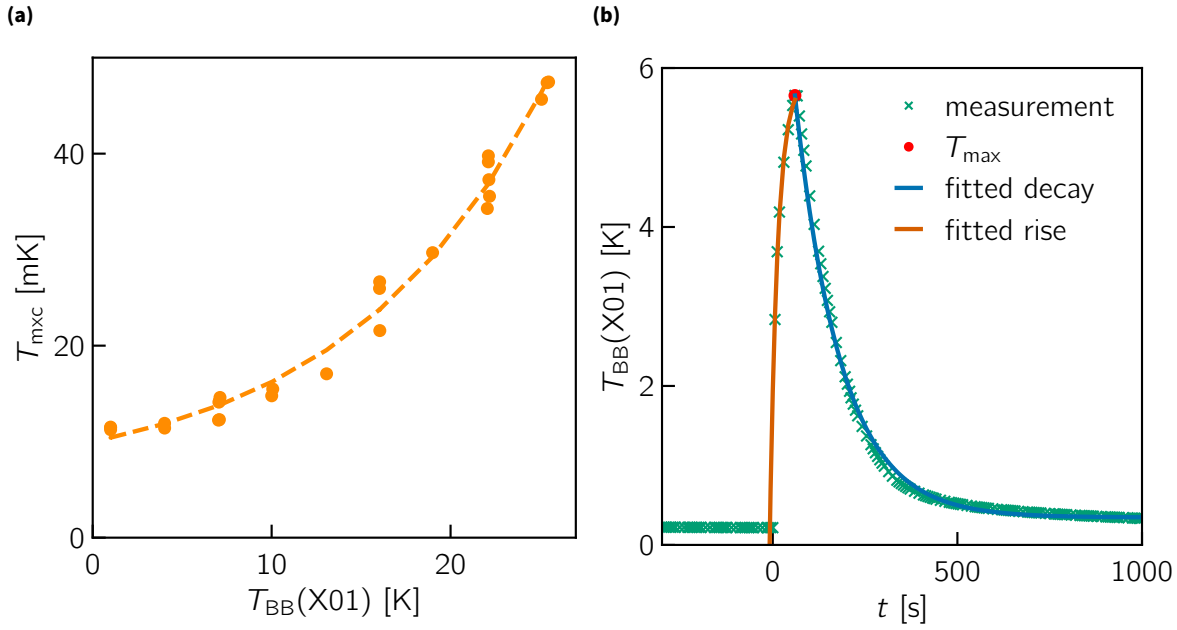

Figure 5.4.: (a) Mixing-chamber temperature measurement when sweeping the blackbody heater temperature of heater X01 (orange points), demonstrating operation at high radiation levels without significant mixing-chamber heating. The dashed line is a guide to the eye. (b) Application of a heating pulse of $V = 0.1\,\mathrm{V}$ for a time of 60 s to the blackbody heater X01 and measurement of its temperature as a function of time (green points). Fitted rise (orange) and decay (blue) curves follow the procedure explained in the text to determine the heat capacity and thermal coupling to the bath. The peak temperature is marked in red.

where $T_{\mathrm{bath}} \approx 150\,\mathrm{mK}$ denotes the bath temperature, τ_{rise} the rise time constant, and A a fit parameter. After the pulse ends, the temperature decays as

$$T(t) = T_{\mathrm{max}} + Be^{-(t-t_{\mathrm{pulse}})/\tau_{\mathrm{decay}}}, \tag{5.4}$$

where T_{max} is the peak temperature at t_{pulse}, τ_{decay} the decay time constant, and B a fit parameter.[4]

This fit can be applied to the measured response shown in Fig. 5.4(b), since it only shows a single exponential. The time constants relate to the heat capacity C and the thermal coupling strength to the bath G_{bath} via [191]

$$\tau_{\mathrm{decay}} = \frac{C}{G_{\mathrm{bath}}}, \quad \tau_{\mathrm{rise}} = \frac{C}{T_{\infty}P}, \tag{5.5}$$

with applied power $P = V^2/R$ and steady-state temperature T_{∞} from the rise fit. This assumes coupling to a single thermal bath via one effective channel. Fitting yields $G_{\mathrm{bath}} \approx 2.5\,\mu\mathrm{W\,K^{-1}}$, which is reasonable for the 20 µm-thick copper wire used for the thermal link. The fit gives further $C \approx 307\,\mu\mathrm{J\,K^{-1}}$, which corresponds to a copper mass of $\sim 4\,\mathrm{g}$ at 1 K and is in good agreement with the actual mass of the radiator; however, the specific heat of copper is strongly temperature dependent in this range [193]. The corresponding thermal time constant is on the order of minutes, consistent with the targeted cooldown time between measurement pulses. Observations of the intermediate-stage temperature confirm that the heat load on the intermediate plate remains small compared to its cooling power.

[4] A and B correspond to the steady-state temperature increase for an infinitely long pulse.

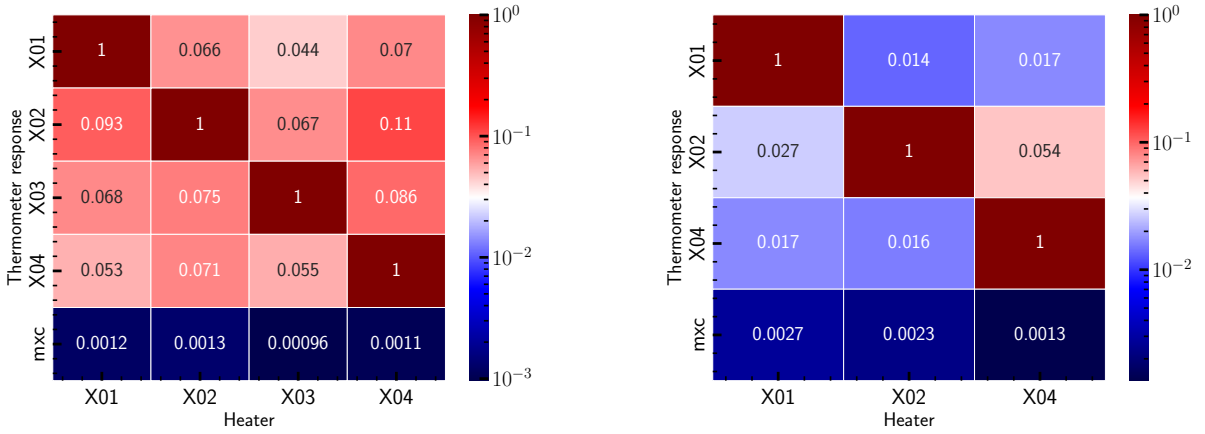

Figure 5.5.: Temperature-correlation heatmaps between heaters and between heaters and mixing chamber. The four blackbody heaters are labeled X01–X04. Left: Without additional shielding, correlations to neighboring heaters reach up to 11 %. Right: With improved shielding, correlations are suppressed to 1.5 %–5.4 % (X03 was not connected in this cooldown).

5.2.4. Crosstalk between heaters and the mixing chamber

The primary leakage path for infrared photons to the qubit consists of parallel routes from other heaters, which experience heating through radiative crosstalk from neighboring units. Experiments performed without shielding of the radiators show substantial crosstalk between the heaters. As a measure of the crosstalk, the temperature correlation is used. This correlation is approximately linear (see Fig. A.3 and Fig. A.4 in the Appendix); therefore, it can be reduced to a single number (the linear slope), given in Fig. 5.5 (left panel) for all radiator combinations (radiators labeled X01–X04) as a heatmap. The temperature correlations between heaters reach up to 11 % for neighboring units. The temperature correlation between all radiators and the cold stage (labeled "mxc") is below 1 %. Installation of heat shields suppresses inter-heater correlations to 1.5 %–5.4 %, as shown in a similar measurement presented in Fig. 5.5 (right panel).

5.3. Effective qubit temperature under radiation

To demonstrate that the shielding of the individual radiators is sufficient to protect the qubit, the effective qubit temperature is measured using the methods introduced in Sec. 4.4, where qubit state populations map to an effective qubit temperature. For this measurement, the qubit is prepared in the ground state, and the state populations are measured versus radiator temperature, both without (Fig. 5.6) and with shielding (Fig. 5.7). Without shielding, the excited state population increases with radiator temperature. With shielding, the excited-state population remains essentially unchanged. Effective qubit temperatures, calculated from state distributions following the procedure in Sec. 4.4, are shown in Fig. 5.8. Without shielding, the qubit temperature rises with radiator temperature. With shielding, it remains stable at approximately 95 mK. Two different qubits were used: the deep transmon (Q200) for measurements without shielding and the intermediate transmon (Q60) for measurements with shielding. State separation is less distinct for Q60, though state assignment remains possible (see Sec. 4.4). Larger errors with shielding stem from this imperfect state separation. The large errors without shielding at high radiator temperatures arise from population of higher qubit states beyond the two-level approximation (visible in Fig. 5.6).

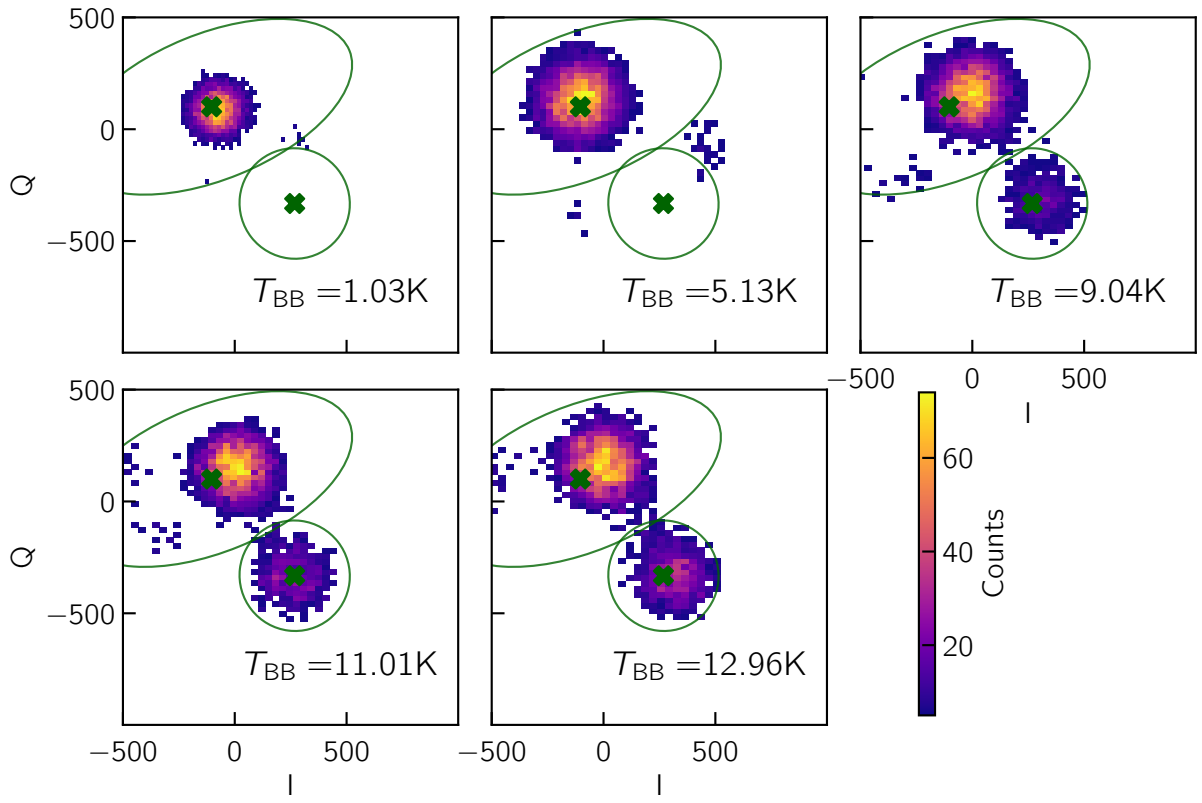

Figure 5.6.: IQ cloud representation of the qubit ground state of Q200 (Sec. 4.4) at varying blackbody temperatures (different panels) without additional shielding.

This also demonstrates that infrared photons, and therefore the generated QPs, do not excite the qubit from the ground state into higher excited states. Therefore, the infrared-induced QPs are effectively "cold" QPs close to the gap edge (see Sec. 2.5.1). This is the first important result of this thesis.

5.4. Qubit property measurements under infrared radiation

In the following experiments, the radiator temperature is varied across a few kelvin, tuning the pair-breaking photon flux incident on the chip over four orders of magnitude. For this, the open radiation path is used (see Fig. 5.1 and description in Sec. 5.1). For comparison, the measurements are also performed with a closed radiation path to distinguish effects that are not caused by direct photon hits on the chip but by background effects such as heating or photon flux in neighboring waveguides due to crosstalk. The three samples Q200, Q60, and Q27, introduced and characterized in Sec. 4.4, are used for the experiments. For the Q27 sample, an average is taken over all offset charge states by sweeping a gate voltage at every blackbody radiation point to avoid charge effects. For all photon-flux values, T_1 and Ramsey experiments are performed following the protocols introduced in Sec. 4.3, analogous to the characterization measurements at base temperature explained in Sec. 4.4. The temperature of the radiator is converted to the corresponding number of pair-breaking photons arriving at the qubit, using the conversion approximation discussed in Sec. 5.2.

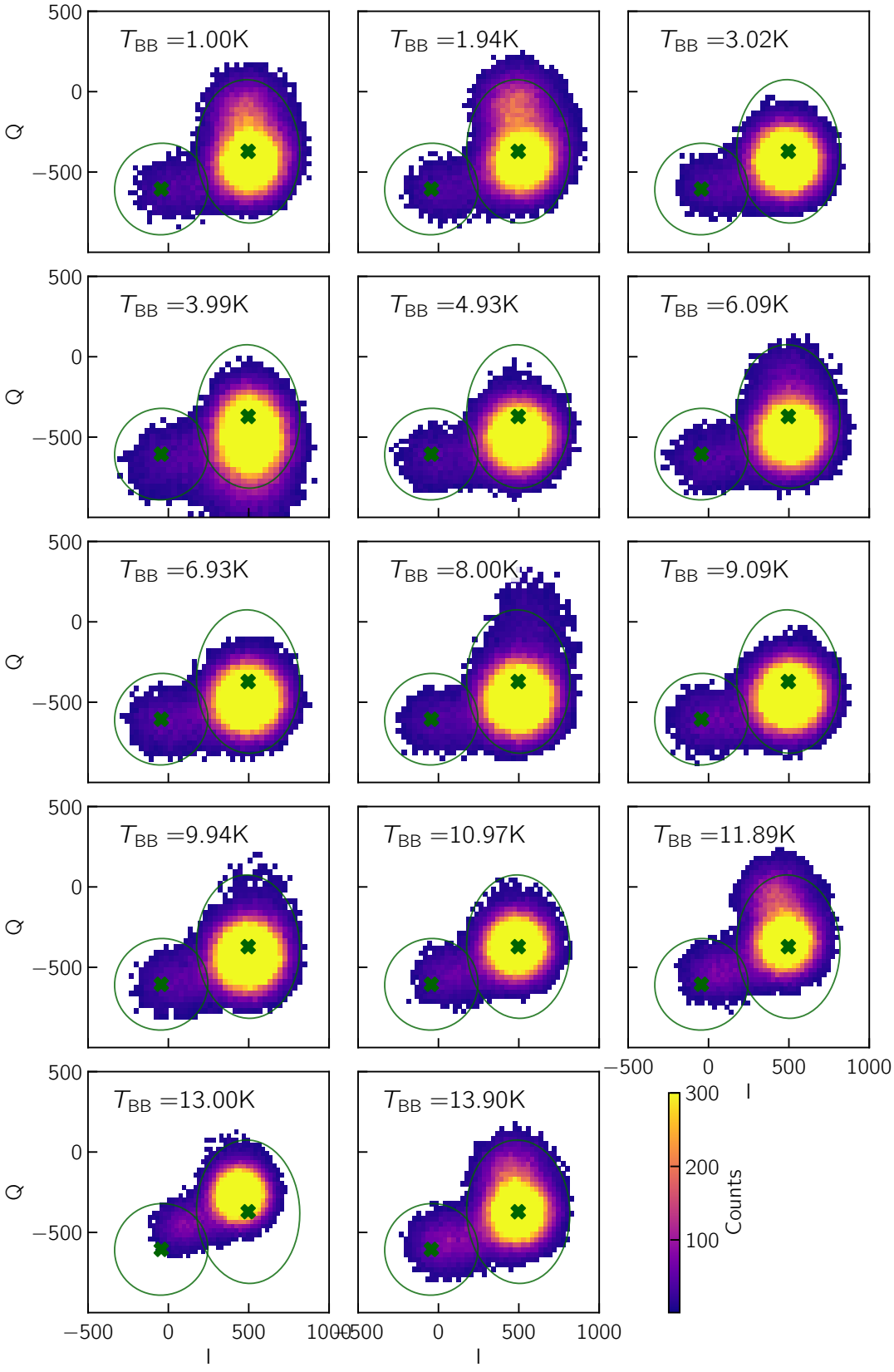

Figure 5.7.: IQ cloud representation of the qubit ground state of Q60 (Sec. 4.4) at varying blackbody temperatures (different panels) with shielding.

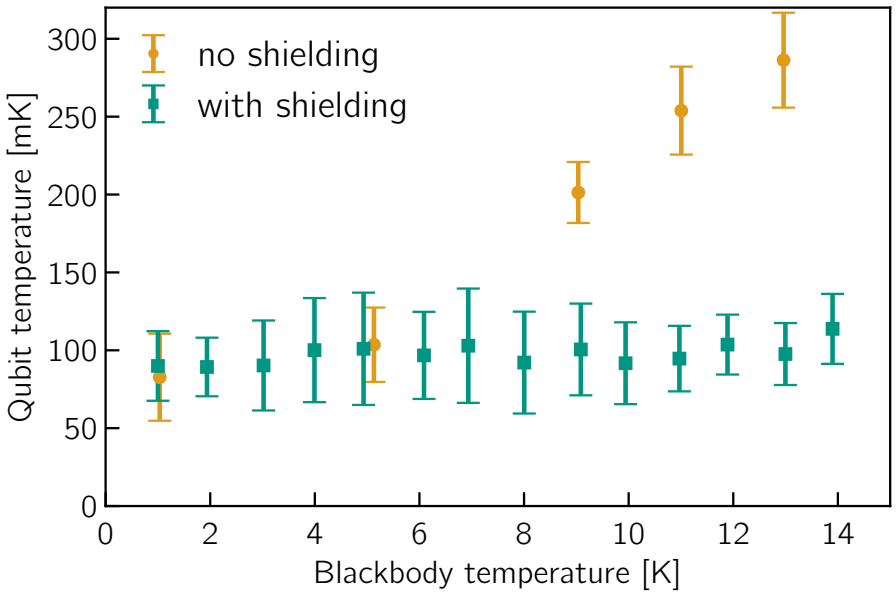

Figure 5.8.: Effective qubit temperature versus radiator temperature. Without shielding (orange): strong increase due additional heating channels. With shielding (green): stable at $\approx 95\,\mathrm{mK}$. No qubit excitation by infrared photons is visible.

5.4.1. T_1 measurements

The dependence of the qubit relaxation time on the number of photons from the blackbody radiator is analyzed. In Sec. 3.3 a linear dependence between the QP density and the decay rate was derived, with the proportionality constant depending on the qubit system. Therefore, an indirect probe of the QP density is possible. In Sec. 2.5.2 it was discussed that it is reasonable to assume a linear relation between the number flux of pair-breaking photons and the QP density (Eq. 2.32); the proportionality factor is the conversion time constant α. This conversion time can be understood as the average time needed at a constant photon flux to break a Cooper pair and generate a QP. From the investigation of different qubit samples (Q200, Q60, and Q27) with different architectures, materials, and charge sensitivity, the impact of the design on the conversion rate, which is a measure of the sensitivity to pair-breaking photons, can additionally be compared.

In Fig. 5.9 and Fig. 5.10 the measurement results are shown. The three subfigures (a–c) correspond to the three different investigated qubits: Q200, Q60, and Q27, which are described together with their properties in detail in Sec. 4.4. In Fig. 5.9 the top panels show the measured decrease of the T_1 time with increasing photon number (orange). The top axis shows the temperature of the blackbody radiator and the bottom axis the logarithmic photon number flux n_{ph} estimated using the conversion from blackbody temperature to photon number flux explained in Sec. 5.2.1. Each measurement point represents the average of multiple T_1 measurements (similar to the methodology explained in the characterization of the sample in Sec. 4.4.4) at the corresponding blackbody temperature. The error arises from the statistical distribution and propagated fitting uncertainties. In the main panel of the plot, the inverse, the decay rate Γ_1, is plotted, showing a linear increase with the photon arrival rate at the qubit, as confirmed by a linear fit (note the logarithmic horizontal axis). For clarification of the linearity, the same data are plotted on a linear photon number flux axis in the right panel of each plot.

(a) Deep transmon sample Q200

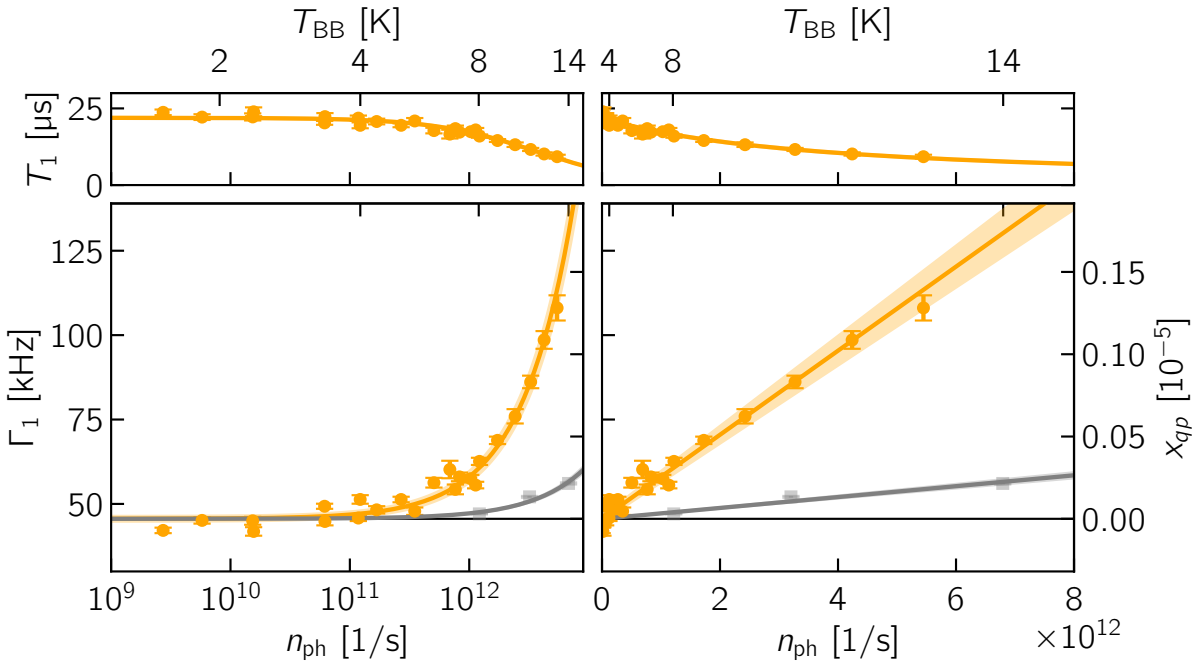

(b) Intermediate transmon sample Q60

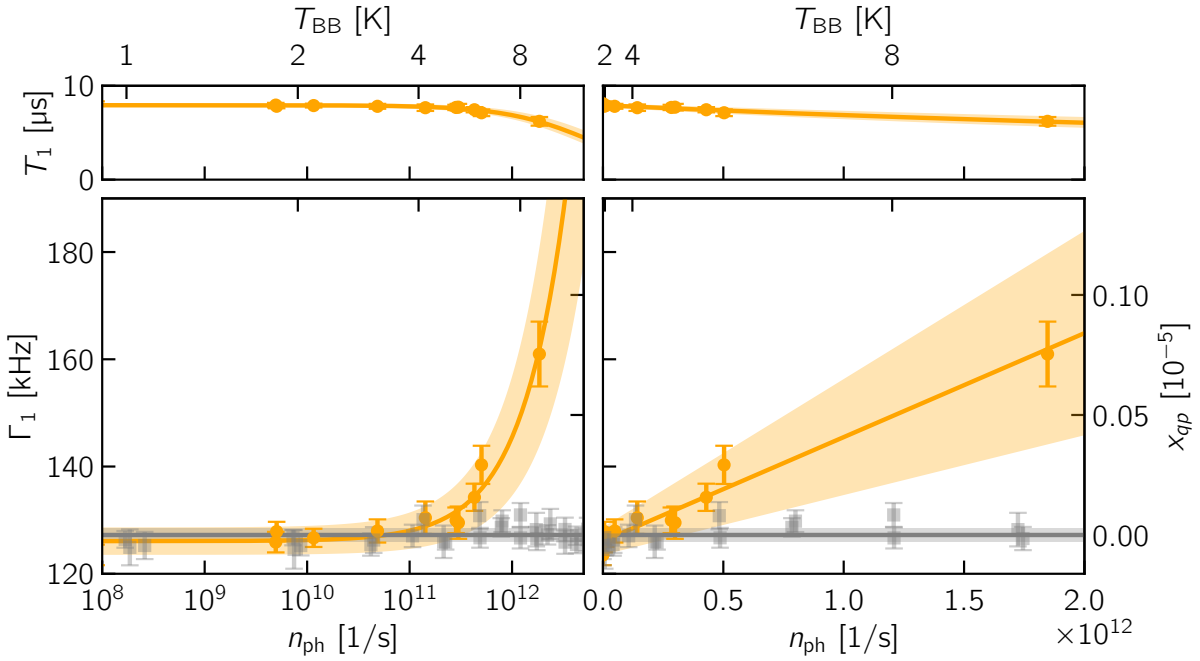

Figure 5.9.: Energy-relaxation measurements with infrared radiation from a blackbody radiator for the three investigated samples. The left and right panels show the same data on a logarithmic horizontal photon-flux axis on the left and a linear horizontal axis on the right. The top axis shows the blackbody temperature. Top panels: T_1 decreases with increasing number of photons (orange). Main panels: The measured decay rate as a function of photon rate (orange). Solid lines show a linear fit to the data with error (shaded area). In gray the background measurement is shown, with a linear fit. Corresponding induced QP density x_{qp} on the right axis. (a) Deep transmon sample Q200. (b) Intermediate transmon sample Q60.

(c) OCS transmon sample Q27

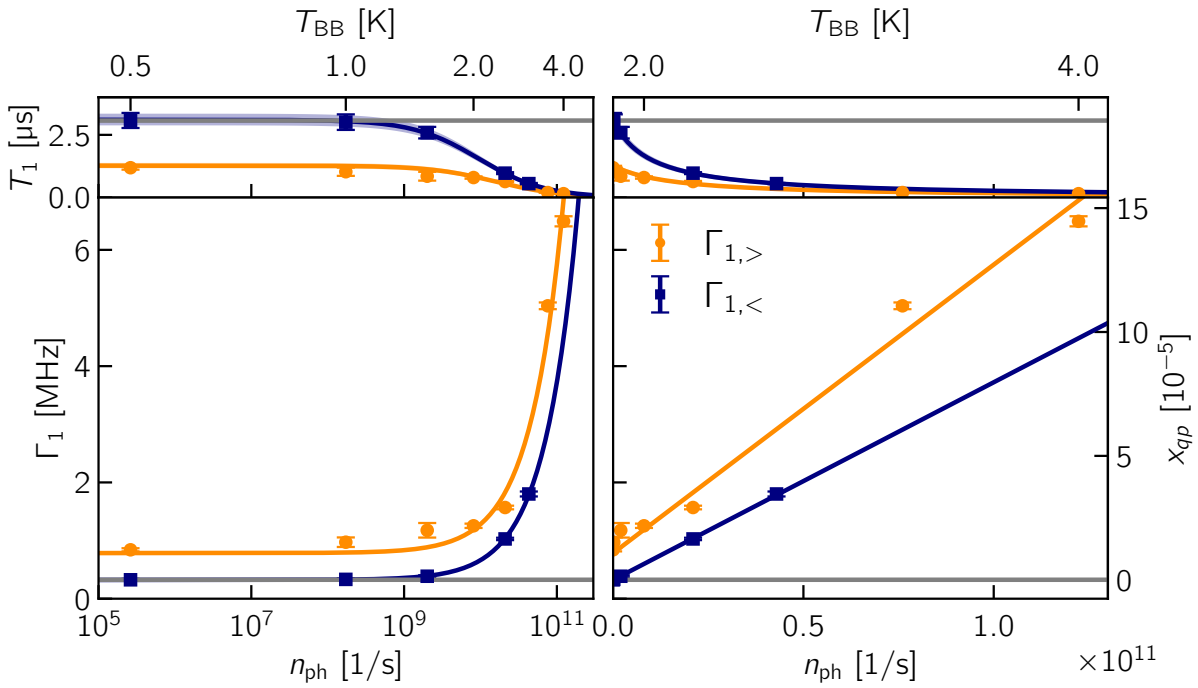

Figure 5.10.: Continued from Fig. 5.9. (c) OCS transmon sample Q27; the two curves correspond to the two stable regimes, high frequency (orange) and low frequency (blue), described in Sec. 4.4.

Table 5.1.: Summary of photon-to-QP conversion coefficients α extracted from T_1 measurements for the different samples. Here E_J/E_C characterizes the charge sensitivity.

sample	E_J/E_C	α (s)
Q200	199	$(1.12 \pm 0.11) \times 10^{-18}$
Q60	61	$(4.3 \pm 0.6) \times 10^{-19}$
Q27, high-f_{01} regime	27	$(1.17 \pm 0.03) \times 10^{-16}$
Q27, low-f_{01} regime	27	$(8.0 \pm 0.4) \times 10^{-17}$

The photons break Cooper pairs and introduce QPs in the system, which lead to the additional decay. In Sec. 3.3 it has been shown that for the investigated transmons the decay rate is proportional to the QP density, see Eq. 3.40. With this knowledge, the measured decay rate is converted into a measure of QP density, which is shown on the right axis of the main plots in Fig. 5.9. The linear dependence on the incident photon number demonstrates that the QP density depends linearly on the photon flux over several orders of magnitude. The Q27 sample in Fig. 5.9(c) shows jumps between two stable regimes on the timescale of hours (as discussed in the characterization in Sec. 4.4), attributed to TLS coupling. The decay rate Γ_1, and therefore the QP density, of these two stable regimes is shown as a function of incoming photon flux in Fig. 5.10(c) in blue and orange, respectively. In the Appendix (Sec. A.7) the histograms and timetraces for every blackbody temperature are shown from which the two states are extracted.

The resulting conversion coefficients α from the fit are summarized in Table 5.1 for all qubits and span almost four orders of magnitude, from $\sim 1 \times 10^{-19}$ s for Q200 up to $\sim 1 \times 10^{-16}$ s

Table 5.2.: Summary of photon-to-QP conversion coefficients α' extracted from f_{01} measurements for the different samples. Here E_J/E_C characterizes the charge sensitivity.

sample	E_J/E_C	α' (s)
Q200	199	$(1.12 \pm 0.11) \times 10^{-18}$
Q60	61	$(1.28 \pm 0.08) \times 10^{-17}$
Q27, high-f_{01} regime	27	$(7.2 \pm 0.4) \times 10^{-16}$
Q27, low-f_{01} regime	27	$(6.5 \pm 0.6) \times 10^{-16}$

for Q27. For the Q60 sample additional measurements on another qubit on the same chip are performed, resulting in comparable values, details in Sec. A.7.3 in the Appendix.

For the Q200 sample, the background measurement with the blocked radiation path in Fig. 5.9(a) reveals substantial crosstalk between the different radiators at high temperature, resulting in a higher error on the data points taken at higher radiation photon flux. This is due to the nonoptimal shielding in this experiment, as discussed in Sec. 5.1. For the Q60 sample, the background measurement (gray) in Fig. 5.9(b) is flat and does not show any crosstalk or heating effects. This reflects improved shielding, as detailed in the characterization of the setup shielding in Sec. 5.1. For the Q27 sample, no background measurement was performed, since only one radiator was installed in the cooldown. A comparison of the two different background measurements is shown in Sec. A.7.1 in the Appendix.

5.4.2. Ramsey measurements of transition frequency f_{01}

In addition to the qubit energy-relaxation experiments, Ramsey experiments are also performed under infrared radiation. These experiments give insight into the precise qubit frequency and the dephasing rate of the qubit. These experiments are performed following the measurement protocols introduced in Sec. 4.3, analogous to the characterization measurements described in Sec. 4.4.

First, the change in the qubit frequency is investigated. In Sec. 3.3 it was explained that with increasing QP density the qubit energy levels also change and therefore the qubit transition frequency is expected to decrease. The qubit frequency shift is linear with the QP density to first order (Eq. 3.43), and thus provides an independent way to extract the QP density.

Figure 5.11 and 5.12 show the change of the qubit primary transition frequency δf_{01} as a function of the infrared photon flux for the three investigated samples: Q200 (Fig. 5.11(a)), Q60 (Fig. 5.11(b)), and Q27 (Fig. 5.12(c)). The blackbody temperature (top axis) is converted to a photon number flux (bottom axis) similarly to the T_1 measurements above. The frequency change is negative, as expected from the QP theory (Sec. 3.3.1). The frequency shift is attributed fully to a QP effect produced by the infrared radiation; therefore, the nonequilibrium QP density due to the infrared radiation can be calculated from the frequency shift for each infrared photon flux point using Eq. 3.43, which is depicted on the right axis of the plots. The QP density shows a linear dependence on the photon flux similar to the T_1 measurements above, best visible in the right panel with the linear horizontal axis. Also from the transition-frequency measurement the photon-flux-to-QP conversion coefficient can be extracted from the linear fit, illustrated in Fig. 5.11, giving the α' values in Table 5.2. The prime denotes the distinction from α extracted from the T_1 measurement, which can differ due to model uncertainties and because T_1 and f_{01} may have different sensitivities to the detailed QP energy distribution.

(a) Deep transmon sample Q200

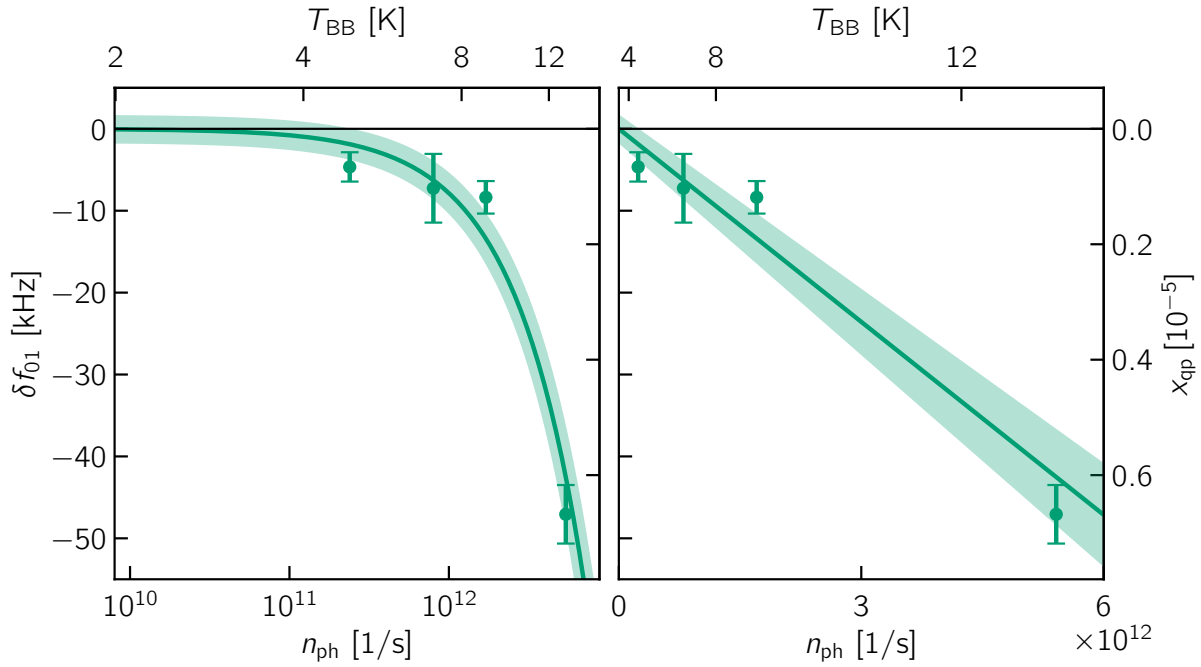

(b) Intermediate transmon sample Q60

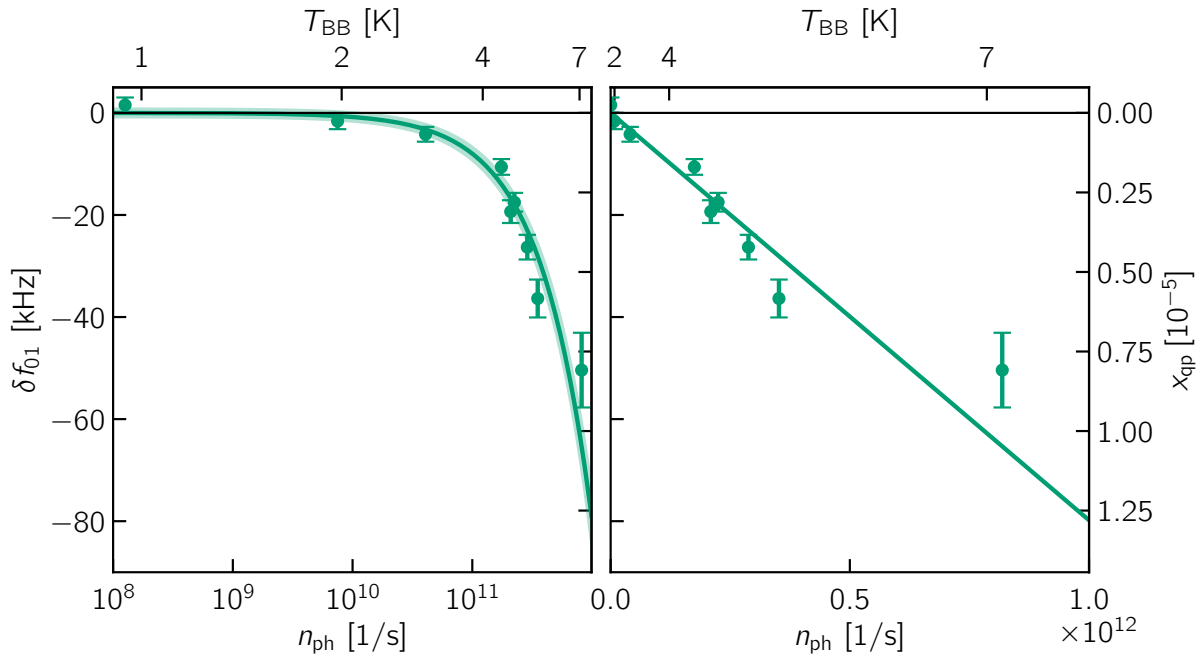

Figure 5.11.: Change in transition frequency from Ramsey measurements. Left panels: transition frequency change δf_{01} (green points) with the incident photon flux and the linear theory fit (solid line). The shaded area shows the fit error. The top axis shows the temperature of the blackbody radiator, the bottom axis the corresponding photon number rate n_{ph} on a logarithmic horizontal axis. The right axis shows the QP density x_{qp} responsible for the frequency shift, using Eq. 3.43. Right panels: same data on a linear photon number rate n_{ph} axis. (a) deep transmon sample Q200, (b) intermediate transmon sample Q60.

(c) OCS transmon Q27

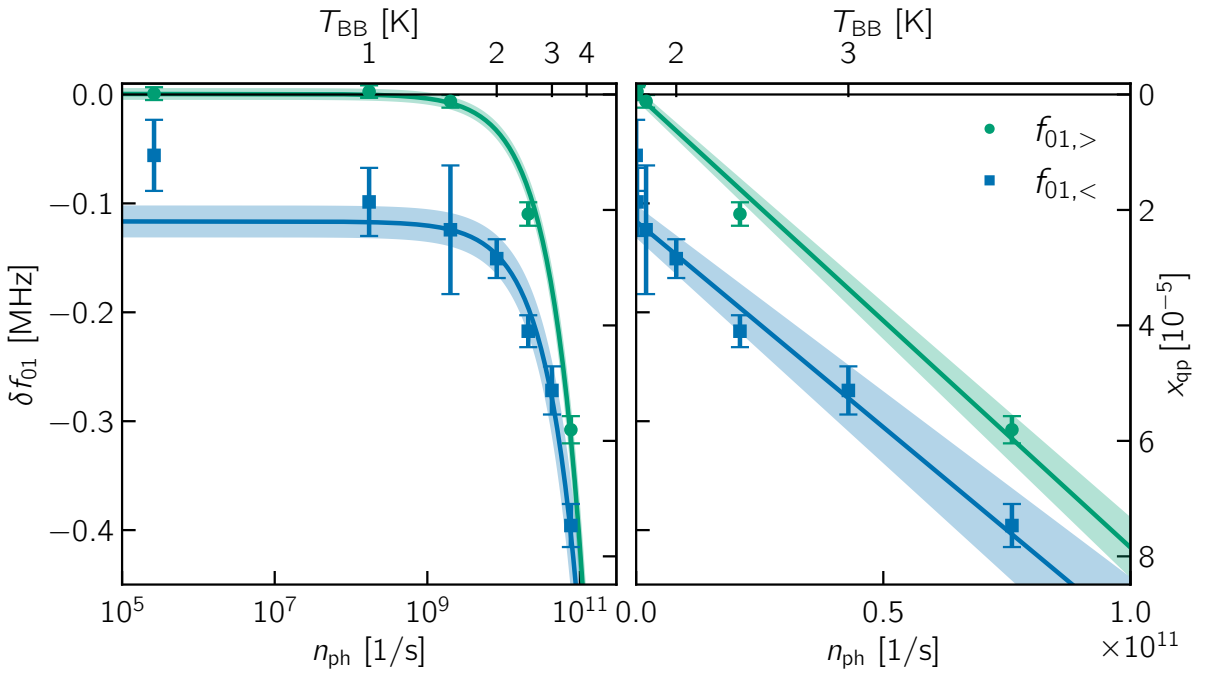

Figure 5.12.: Continued from Fig. 5.11. (c) OCS transmon sample Q27; green and blue are the two stable regimes between which the qubit shifts during the measurements (more details in the main text).

Table 5.3.: Slopes obtained from fits to the energy–relaxation ($\Gamma_1/2$) and pure–dephasing (Γ_ϕ) rates.

sample	slope $\Gamma_1/2$ fit	slope Γ_ϕ fit
Q200	$(6 \pm 0.3) \times 10^{-9}$	$(2.14 \pm 0.22) \times 10^{-8}$
Q60	$(9.5 \pm 0.25) \times 10^{-9}$	$(2.49 \pm 0.46) \times 10^{-7}$
Q27, high-f_{01} regime	$(2.48 \pm 0.06) \times 10^{-5}$	$(-4.4 \pm 1.4) \times 10^{-6}$
Q27, low-f_{01} regime	$(1.70 \pm 0.08) \times 10^{-5}$	$(1.13 \pm 0.33) \times 10^{-5}$

5.4.3. Ramsey decoherence time T_2

The Ramsey (dephasing) and energy–relaxation measurements are combined to determine the pure dephasing rate Γ_ϕ under infrared irradiation. For every photon-flux value, the dephasing rate Γ_2 is taken from the Ramsey sequence, while the corresponding relaxation rate Γ_1 is calculated from the fit in Sec. 5.4.1. Subtracting both quantities (see Sec. 3.1) yields Γ_ϕ.

Figure 5.13 displays Γ_2, the fitted Γ_1 curve, and the extracted Γ_ϕ for the three samples: Q200 (panel a) and Q60 (panel b). A pronounced, approximately linear rise not only of Γ_2 but also of Γ_ϕ with photon flux is observed. The solid lines show the linear fit to the data points; the slopes of these fits are summarized in Table 5.3. The magnitude of the slope of Γ_ϕ remains comparable and even dominant to the slope of $\Gamma_1/2$, in disagreement with the large suppression (Eq. 3.46) predicted by the theoretical model in Sec. 3.3.1.

With the same procedure, measurements of the OCS transmon sample are performed and plotted in Fig. 5.14. Similar to the above measurements, the two regimes are visible in the dephasing-rate measurement as well. In contrast to the other two samples, these measurements show no clear

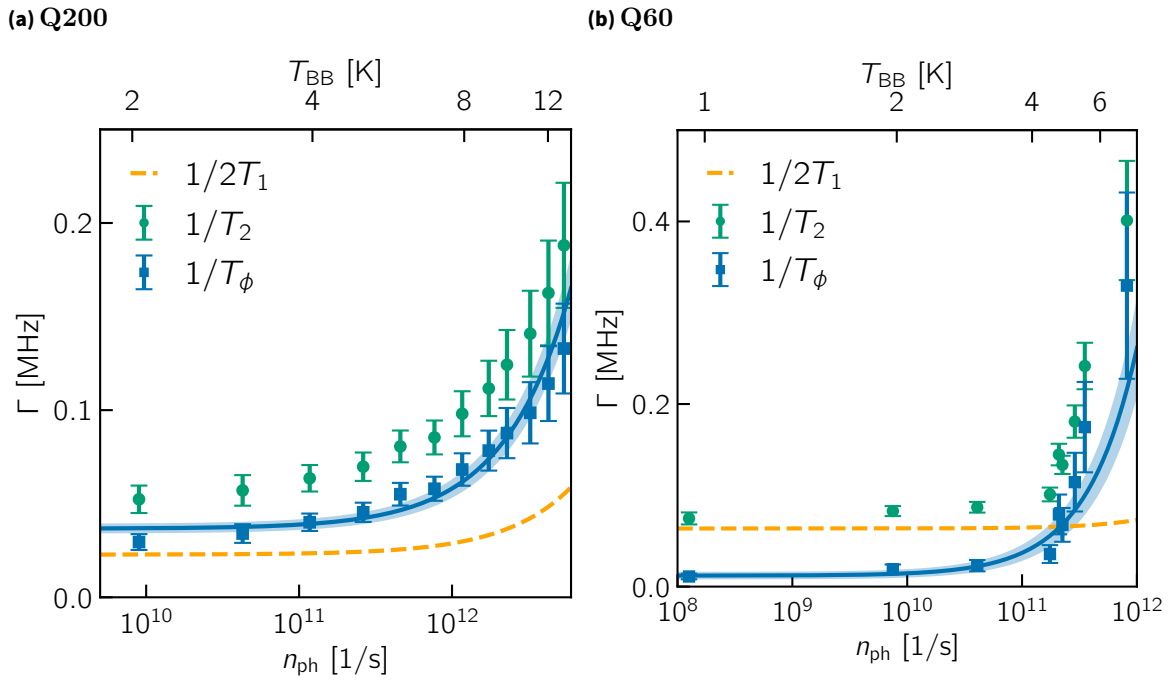

Figure 5.13.: Qubit Ramsey dephasing rate $1/T_2$ and extracted pure dephasing rate $1/T_\phi$ as a function of the pair-breaking photon rate reaching the qubit. Ramsey decoherence measurements (green bars), $\frac{1}{2}\Gamma_1$ from the fit in Fig. 5.9 (orange line), and calculated pure dephasing time (blue bars) with linear fit (blue line) and fit error (blue shaded area) as a function of the incoming photon number rate n_{ph} on a logarithmic horizontal axis. (a) Q200. (b) Q60.

increase in pure dephasing rate with the infrared photon flux (compare values in Table 5.3). The linear fit of the low-frequency regime yields a nonsignificant slope, and the slope of the linear fit of the high-frequency regime is dominated by the single data point at $n_{ph} \approx 2 \times 10^{10}\,s^{-1}$; the other data points can be described by a constant fit within the uncertainties. The last measurement point at a photon flux of $n_{ph} \approx 8 \times 10^{10}\,s^{-1}$ could be thought of as wrongly associated with the high-frequency regime; however, comparing the values of the extracted frequencies in Sec. 5.4.2 makes this unlikely.

5.4.4. Comparison and discussion

The extracted conversion coefficients from infrared photon flux to QP density α span almost four orders of magnitude, from $\sim 1\times10^{-19}$ s (Q60 and Q200) up to $\sim 1\times10^{-16}$ s (Q27). The conversion coefficients are extracted from two different measurements, the relaxation time measurement (Table 5.1) and the Ramsey measurement of the qubit transition frequency (Table 5.2). In Fig. 5.15 these conversion coefficients are compared for the three investigated samples. Green (blue) points correspond to α (α') extracted from T_1 (f_{01}) measurements. The samples are characterized by their E_J/E_C value as a measure of their charge sensitivity, where larger E_J/E_C corresponds to lower charge sensitivity. A trend emerges for the conversion coefficient: it decreases from the OCS regime at $E_J/E_C \approx 27$ by two orders of magnitude in the deep transmon regime at $E_J/E_C \approx 200$. However, care is required in this comparison, since all samples are fabricated differently, are positioned differently on the chip, and are measured in different cooldowns. The Q200 sample even has a different material for the capacitor pads. This interpretation therefore

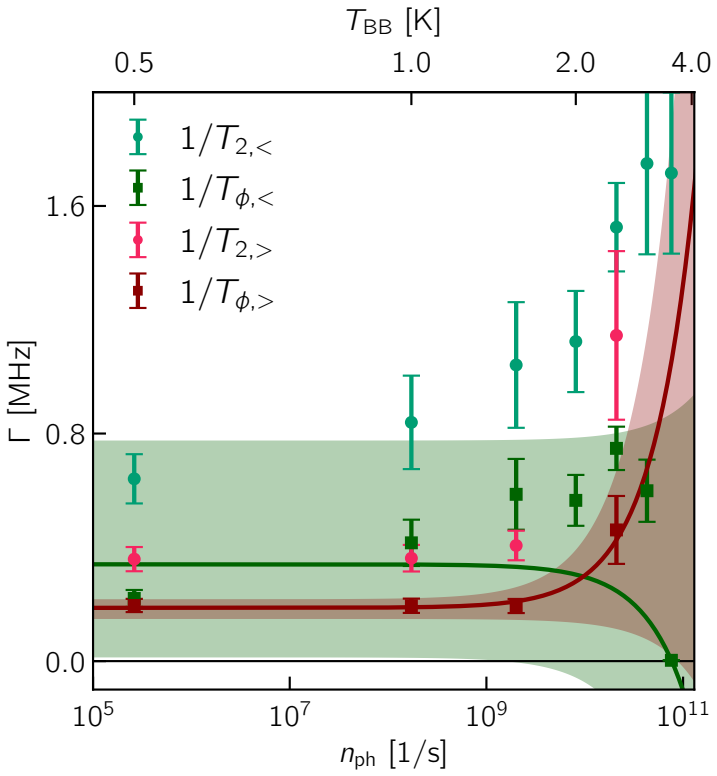

Figure 5.14.: Measured Ramsey dephasing rates Γ_2 of the OCS transmon sample Q27, separated into the two different stable regimes (light green and red points) (see main text for details). Together with the measurement results from Sec. 5.4.1 the pure dephasing rate Γ_ϕ is extracted, fitted with a linear fit, and plotted in darker green and red for the two TLS regimes. The error is shown by the shaded area. The data are plotted against the incoming photon number rate on the logarithmic horizontal axis, extracted from the blackbody temperature, shown on the top axis.

requires caution regarding the apparent tendency toward a higher conversion coefficient at higher charge sensitivity and requires further measurements for verification.

This behavior is not expected from the simplified theory introduced in this thesis. However, it might be explained by photon-assisted tunneling (PAT, Sec. 3.3.3) events that are not included in the fitted theory but have been shown theoretically and experimentally to depend on the Josephson energy [81, 82]. A quantitative treatment of PAT theory in this context is beyond the scope of this thesis but could be addressed in future work.

The conversion coefficient α is expected to depend on the material, the specific geometry of the junction and qubit, and the position of the junction in relation to the infrared waveguide. Thus, the variation of the conversion rates by orders of magnitude between 1×10^{-19} s and 1×10^{-15} s is reasonable. This agrees with previous measurements using infrared or terahertz radiation and with theoretical expectations ([46, 51, 82] and Sec. 3.3). The recent experiments by Benevides et al. [51] report a photon-to-QP conversion for terahertz photons from a laser at a single frequency between 1×10^{-15} s and 1×10^{-18} s, depending on the laser position on the qubit chip for a qubit in the transmon regime. This is in the same order of magnitude as the measured values presented here for the broad blackbody frequency spectrum. Unlike the focused terahertz laser, these experiments radiate photons into the sample box and therefore onto a broad area on the chip. In Sec. 5.2.1 it was discussed that the conversion from blackbody temperature to photon number flux is only an order-of-magnitude estimate, due to large uncertainties in the emissivity

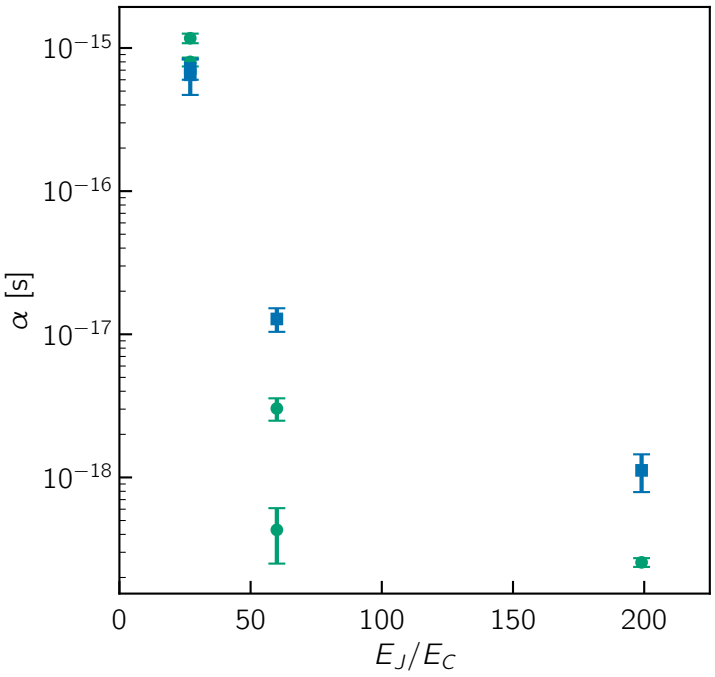

Figure 5.15.: Photon-to-QP conversion coefficient for all samples, characterized by their E_J/E_C value. Green (blue) points correspond to the fit values from the T_1 (f_{01}) measurements in Fig. 5.9 (Fig. 5.11).

ε. The conversion coefficient α is directly proportional to the emissivity ε; therefore, it should also be understood only as an order-of-magnitude estimate.

The conversion coefficients extracted from the energy relaxation rates α are systematically lower than those extracted from the transition-frequency measurements α'. However, by construction both α and α' parametrize the same photon-flux-to-QP conversion process. The systematic offset between them therefore likely reflects model assumptions, rather than a fundamental physical difference between the two extraction methods. In the theoretical model introduced in Sec. 3.3.1, the frequency change is caused by two effects, the change of the Josephson energy and QP-mediated transitions, resulting in cancellation of terms and potentially leaving more room for errors, which may result in an overestimation of the QP density inferred from the frequency shift.

From the linearity of the conversion one can conclude that the produced QPs are all close to the gap. This agrees with the state population measurement results in Sec. 5.3. QPs with higher energy would produce phonon bursts, generating additional QPs; these effects are observable in high-energy particle and photon impact experiments [53]. This is plausible, since the peak energies of the photons produced by the blackbody radiator at the maximal temperature of 15 K are at ~ 500 GHz and therefore of the order of only five times the gap energy of aluminum ($2\Delta \approx 100$ GHz) and thus much lower than high-energy particle events. Therefore, the QPs condense quickly to the gap energy.

QPs are assumed to be created in the aluminum; however, there are also higher-gap materials for the capacitor pads on the chip, niobium for the intermediate and OCS qubits and titanium nitride for the transmon sample. However, the QPs need to tunnel through the junction to be detectable by the measurements, and the mean free path of QPs in superconducting aluminum is on the scale of a few nanometers [194]. Thus, QPs from the capacitor pads dissipate, are

trapped, or recombine before they can reach the junction barrier. However, Benevides et al. [51] showed that it makes a difference for the photon-to-QP conversion rate if they shine their laser through the capacitor pad or only through the substrate. Therefore, the absorption probability of the capacitor pads is probably also relevant. The superconducting energy gaps of the different materials (aluminum, niobium, and titanium nitride) differ only by a factor of roughly three, so this alone cannot fully explain the difference in the measured conversion coefficient between the samples, since the energy gap enters only as a square root in the relations for the frequency shifts and decay rates (Eq. 3.43 and Eq. 3.40). The qubits Q60 and Q27 are made from the same materials but show more than an order-of-magnitude difference in the conversion coefficient. The chip architecture is expected to play a role, since parasitic resonances in the infrared frequency range could cause higher absorption, or more superconducting material could cause more absorption.

In other publications [51, 82] the power of the incoming radiation is used as a measure instead of the photon number flux. However, in these publications only single frequencies are investigated, either by a single-frequency source or by investigation of single absorption (antenna) modes of the qubit. At single frequencies the power and the photon number flux differ only by the Planck constant h, so it makes no difference whether the power or the photon number flux is used. The pair-breaking probability should not depend on the energy (frequency) of the photon, since the energy of the QP produced by tunneling is not relevant for it to cause decoherence. A model with a linear conversion from photon number to QP density fits the data better than a model with a linear conversion from radiated power to QP density (see plot in Sec. A.7.4 in the Appendix).

In Eq. 3.2.5 TLS are introduced as a main loss mechanism in superconducting qubits, and measurements hint that TLS are present in the qubits and cause decoherence (Sec. 4.4.2). Direct TLS excitation by infrared radiation is unlikely because TLS have discrete frequencies that need to be close to the qubit frequency to couple to the qubit. The frequency of the infrared radiation is likely too low to produce additional defects in the system but too high to influence defects close to the qubit frequency. However, Thorbeck et al. observed frequency jumps of TLS with high-energy radiation on a qubit chip [195]. A definitive exclusion of TLS-related effects would require dedicated spectroscopy, similar to that performed by the group of J. Lisenfeld [151] under infrared radiation at different temperatures.

In previous studies, absorption in specific antenna modes was observed [65, 82, 184, 196]. In the measurements presented here no frequency-dependent absorption of infrared radiation is observed.

The measurements of the energy relaxation and the transition frequency align well with the theoretical expectations from the models for the QP influences on the superconducting qubit and the conversion from flux of pair-breaking photons to QPs. For the measurements of the pure dephasing rate, the theoretical expectation of no dependence on QP density is not observed for all qubits; only the charge-sensitive qubit shows no clear increase of dephasing rate with increasing QP density. Other measurements in the transmon regime have shown agreement with the theoretical model [51]. This could arise from thermal effects due to parasitic heating, which was largest for the measurement of the concentric transmon sample (compare background data with the blocked infrared waveguide in Sec. 5.4.1) and smallest for the charge-sensitive qubit, where only one radiation line was installed (compare Sec. 5.1). Such heating can introduce additional noise channels and residual qubit excitations that increase dephasing independently of the QP population. This is, however, a speculative explanation from an experimental point of view.

Overall, the experiments demonstrate a quantitatively consistent and approximately linear conversion of incident pair-breaking photons into QPs across three qubit regimes.

In the context of the presented results, it would be interesting to investigate in more detail how the infrared photon-to-QP conversion scales with the offset-charge sensitivity of the qubit. For this purpose, a sample with qubits of different charge sensitivity on the same chip would be particularly useful. Ideally, these qubits would be positioned symmetrically around the center of the chip, directly under the opening where the infrared radiation enters the sample box. Furthermore, other qubit architectures, designs, and fabrication methods are also promising to explore, in order to determine whether one of these factors minimizes the absorption of infrared radiation and therefore the QP density. For example, an investigation of the effect of gap engineering [184] would be possible.[5] This would also test other studies that suggest resonant absorption of radiation due to antenna modes [65, 82, 184, 196]. In the present measurements, no signs of resonant absorption, and thus no clear frequency-dependent absorption signature, were observed in the accessible range between approximately 100 GHz and 1 THz. To test QP dynamics further, improved single-shot readout of the qubit chip would be necessary, because this would allow parity measurements and thus a direct time-resolved probe of QP tunneling events across the junction. A tunable sample would also provide additional insight, for example by enabling TLS spectroscopy [151] under infrared radiation, which would help to disentangle QP-induced from TLS-related decoherence or probe the effect of QPs on TLS.

[5] A short explanation of gap engineering can be found in Sec. A.4 in the Appendix.

6. Quasiparticle mitigation through infrared filtering

In the previous chapters, QPs have been shown to cause decoherence in superconducting qubits and to be efficiently generated by infrared photons. This chapter investigates how to mitigate these QPs by implementing suitable infrared filters. Other strategies of mitigation including gap engineering and QP traps (explained briefly in Sec. A.4 in the Appendix) are often only mitigating the effects but not the production itself. This approach aims for a direct mitigation of the pair-breaking photons.

Standard coaxial cables used for qubit readout are transparent to infrared radiation and thus provide a path for photons into the qubit sample box, even if the qubit is otherwise well shielded in a light-tight enclosure. As a result, coaxial signal lines often constitute the dominant pathway for pair-breaking photons into otherwise well-shielded sample enclosures [56, 82]. The goal is an infrared filter that blocks pair-breaking photons while preserving excellent microwave transmission, i.e., to realize low-pass filters with a sharp cutoff and minimal insertion loss in the passband, and a wide stopband from the centimeter-regime up to the optical regime. The term *infrared filters* is therefore used here in a broad sense.

In this chapter, compound filter options suitable for coaxial readout lines are studied in detail, including analytic calculations using scattering theory, infrared and microwave absorption measurements, and millikelvin qubit measurements. A majority of the findings of this chapter are also summarized in Ref. [197]. This chapter is organized as follows. Sec. 6.1 describes the relevant frequency ranges, associated challenges, and existing infrared filter solutions. Sec. 6.2 introduces a new sapphire-powder-based filter concept, Sec. 6.3 explains the theory of scattering in compound materials, and in Sec. 6.4 the theoretical model is applied to simulate the filter material. Sec. 6.5 and Sec. 6.6 present infrared spectroscopy of candidate materials. Sec. 6.7 covers the microwave characterization of first prototype filters. Sec. 6.8 discusses the broadband performance, and Sec. 6.9 reports millikelvin infrared measurements using qubits as detectors. Together, these results establish characterized design principles for novel infrared filters.

6.1. Infrared filtering — a challenging task

A low-noise environment at ultralow temperatures in the millikelvin range is a key requirement for many quantum applications, such as superconducting qubits. The frequency landscape of photons to which a cryogenic setup is exposed can be separated into a measurement region (passband) in the microwave regime and a noise region at higher frequencies. The frequency landscape is illustrated in Fig. 6.1.

Exposure to photons with energies above the superconducting gap generates QPs by breaking Cooper pairs (see Sec. 2.3). This process leads to decoherence and reduced fidelity in quantum operations, as discussed in detail in Ch. 5. Shielding superconducting devices from infrared

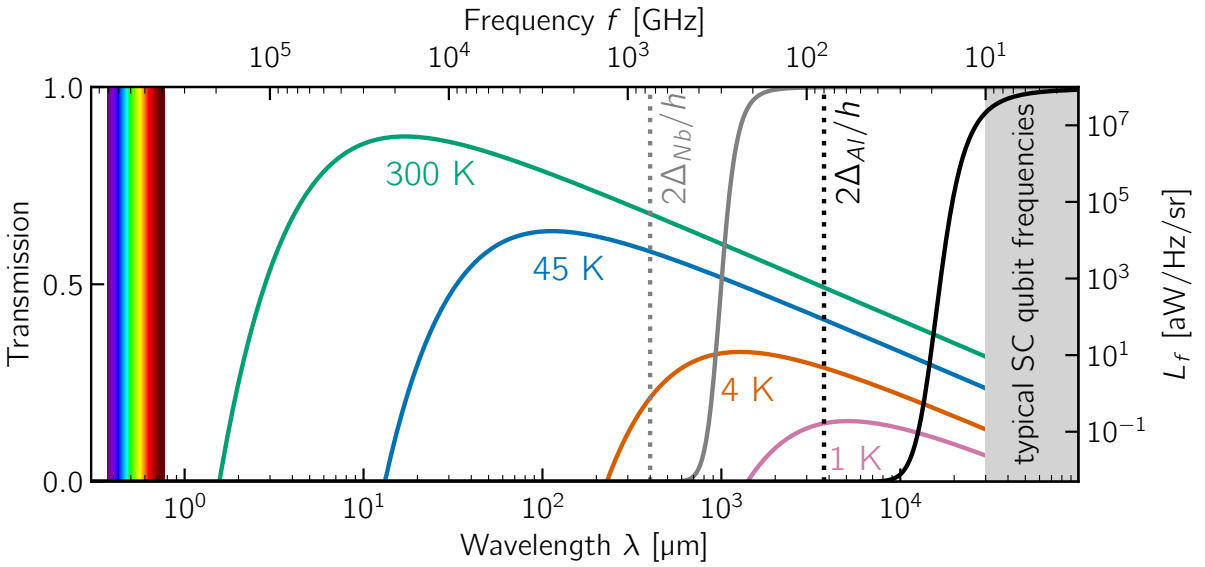

Figure 6.1.: Frequency spectrum. Solid colored lines represent Planck radiation spectra at different temperatures. Dotted black (gray) lines indicate the superconducting gap energies 2Δ for aluminum (niobium) and the solid lines the corresponding optimal cutoff. The visible light spectrum is shown on the far left. The typical superconducting qubit frequencies are indicated on the right.

radiation at frequencies above the superconducting gap is therefore essential for maintaining their performance [56, 72, 198]. Despite extensive shielding, a significant vulnerability remains: Teflon (polytetrafluoroethylene, PTFE), which is widely used as a dielectric in coaxial cables for qubit readout, is largely transparent to infrared radiation [59]. This transparency allows unwanted infrared photons to propagate along the signal lines, bypassing conventional electromagnetic shielding.

To address this, measurement setups require low-pass filters with sharp cutoffs positioned below the superconducting gap energy of the relevant superconductor; for example, for aluminum below 40 GHz (light gray line in Fig. 6.1) or for niobium below 250 GHz (black line in Fig. 6.1). The ideal filter exhibits negligible insertion loss within the passband and strong attenuation in the stopband at all frequencies above the cutoff (often spanning several orders of magnitude in frequency). This performance ensures high-fidelity transmission of qubit readout signals while effectively suppressing higher-frequency infrared noise.

In the centimeter-wave regime (20 GHz–300 GHz), traditional electrical filters such as RC and LC circuits can be combined with geometric filters [199, 200] to provide substantial attenuation. Even at these lower frequencies, blackbody radiation from warmer cryogenic stages can be problematic. For instance, the 1 K stage of a dilution refrigerator emits blackbody radiation that peaks around tens of GHz, resulting in a substantial photon flux above the pair-breaking energy (2Δ) of aluminum (see Fig. 6.1).

At far-infrared (FIR) frequencies (300 GHz to 20 THz; 1 mm to 15 µm), the performance of electrical filters degrades, and their transmission becomes non-negligible. In this regime, blackbody radiation from higher-temperature stages becomes the dominant source of noise. As the frequency increases into the mid-infrared (MIR, 20 THz–200 THz; 15 µm to 1.5 µm), room-temperature blackbody radiation becomes the primary concern. In the near-infrared (NIR, 200 THz–400 THz; 1.5 µm to 750 nm), additional noise arises from telecommunication signals. Since pair-breaking photon energies for superconductors extend across these infrared regions and even into the visible

spectrum, a practical filter chain must provide broadband attenuation spanning five orders of magnitude in frequency to ensure comprehensive protection.

Infrared-blocking filters are indispensable in the field of superconducting qubits [59, 164, 201–205]. The most widely used infrared filters in low-temperature microwave experiments are compound filters [58, 205] based on Eccosorb CR110 or CR124 [61], a commercial, magnetically loaded epoxy compound. Eccosorb is valued for its high absorption of infrared and microwave frequencies. However, its absorption band reaches into the desired microwave passband for qubit operation. In addition, its magnetic content can interfere with experiments that are sensitive to external magnetic fields [57]. The strong microwave attenuation is most likely caused by metallic fillers used to enhance absorption.

Consequently, Eccosorb-based filters realize excellent infrared attenuation but at the cost of increased microwave loss and potential magnetic contamination, which conflicts with the requirements of sensitive superconducting qubit measurements. At present, however, Eccosorb remains the best available option.

6.2. Novel filter idea: sapphire powder mixtures

The goal of this work is to realize a composite material that combines strong infrared extinction with negligible microwave loss and no metallic or magnetic components. The proposed approach uses a composite material containing dielectric sapphire grains of various sizes, chosen to correspond to specific wavelength ranges that need to be filtered.

Incident radiation interacts strongly when the wavelength approaches the sphere diameter. This behavior is described by Mie scattering [206], which treats how spherical particles scatter electromagnetic waves when the wavelength is comparable to their size.[1] A key feature of this mechanism is the resonant enhancement of scattering efficiency at particular wavelengths. In the optical limit at low wavelengths, where the particle size is much smaller than the wavelength, the extinction efficiency is constant. When the particle size approaches the incident wavelength, strong interference effects can increase the scattering efficiency by up to a factor of five. By blending a range of particle sizes, the filter achieves broadband attenuation and effectively covers frequencies from the sub-terahertz up to the optical domain.

For wavelengths larger than the sphere diameter, the scattering efficiency decreases rapidly. The sharp transition between high transmission and strong attenuation in this crossover regime allows for a sharp low-frequency cutoff, set by the largest particle size in the mixture. In the optical limit at low wavelengths, the extinction efficiency becomes constant, allowing for significant extinction even for wavelengths smaller than the smallest sphere in the blend.

Sapphire (aluminum oxide, Al_2O_3) is selected as the grain material since it is a non-metallic and non-magnetic dielectric and is known for its low microwave loss [207, 208]. This choice avoids magnetically induced decoherence and is compatible with low-loss microwave operation.

[1] The theoretical background is explained in detail in Sec. 6.3.

6.3. Scattering theory in compound materials

For a homogeneous medium of length ℓ the extinction coefficient μ, which determines the attenuation of light, is given by the Beer–Lambert law [209]

$$T = \frac{I}{I_0} = \exp(-\mu\ell), \tag{6.1}$$

where T denotes the transmission, and I_0 and I denote the incident and transmitted intensity, respectively. This law describes the extinction of radiation in media where the interaction is relatively weak and the wavelength of the radiation differs significantly from the internal structure. The extinction coefficient is related to the imaginary part κ of the complex refractive index $m = n - i\kappa$ by

$$\mu = \frac{4\pi\kappa}{\lambda_0}, \tag{6.2}$$

where λ_0 is the wavelength in vacuum. Since the refractive index of a material remains approximately constant over wide frequency ranges—punctuated only by narrow absorption bands associated with vibrational, rotational, or electronic resonances—it is not possible to identify a single material that simultaneously exhibits low absorption in the microwave regime and strong absorption at infrared frequencies. For this reason, composite absorbers are required, combining materials with minimal microwave loss with strong extinction at shorter wavelengths.

In describing the efficiency of such absorbers, it is important not only to consider direct absorption but rather the total extinction, accounting for all light removed from the forward direction, whether by absorption or scattering. When discussing extinction, it is common to refer to the *extinction cross section* σ_{ext}, which represents the effective area by which a particle removes energy from the incident beam. It is defined as the sum of absorption and scattering contributions,

$$\sigma_{\text{ext}} = \sigma_{\text{abs}} + \sigma_{\text{scat}}. \tag{6.3}$$

This can also be described by the area-independent extinction (or scattering, absorption) efficiency,

$$Q_{\text{ext}} = \frac{\sigma_{\text{ext}}}{\pi r^2}, \tag{6.4}$$

which normalizes the extinction cross section to the geometric cross-sectional area of the particle.

Moreover, small particles can exhibit a pronounced wavelength dependence of the extinction cross section even when the bulk refractive index is constant. To illustrate this principle, consider a single spherical particle of radius r and refractive index m. Its scattering and absorption cross sections at any wavelength can be rigorously calculated within the framework of *Mie theory*[2]. Figure 6.3(a) illustrates such a scattering event for an incoming photon from the left. The scatterer is a sapphire sphere with $n = 3.69$ and $2r = 50\,\mu\text{m}$, embedded in a dielectric matrix (epoxy [211], $n \approx 1.5$), which reacts to incident radiation at $\lambda = 100\,\mu\text{m}$ by scattering photons almost isotropically.

[2] The theory is named after Gustav Mie, who, in 1908, developed it to explain the characteristic absorption and scattering of light by small gold particles suspended in water [206]. Mie was not necessarily the first to investigate this problem. Earlier work by Peter Debye on radiation pressure in space also contributed to its development [210, pp. 54–59].

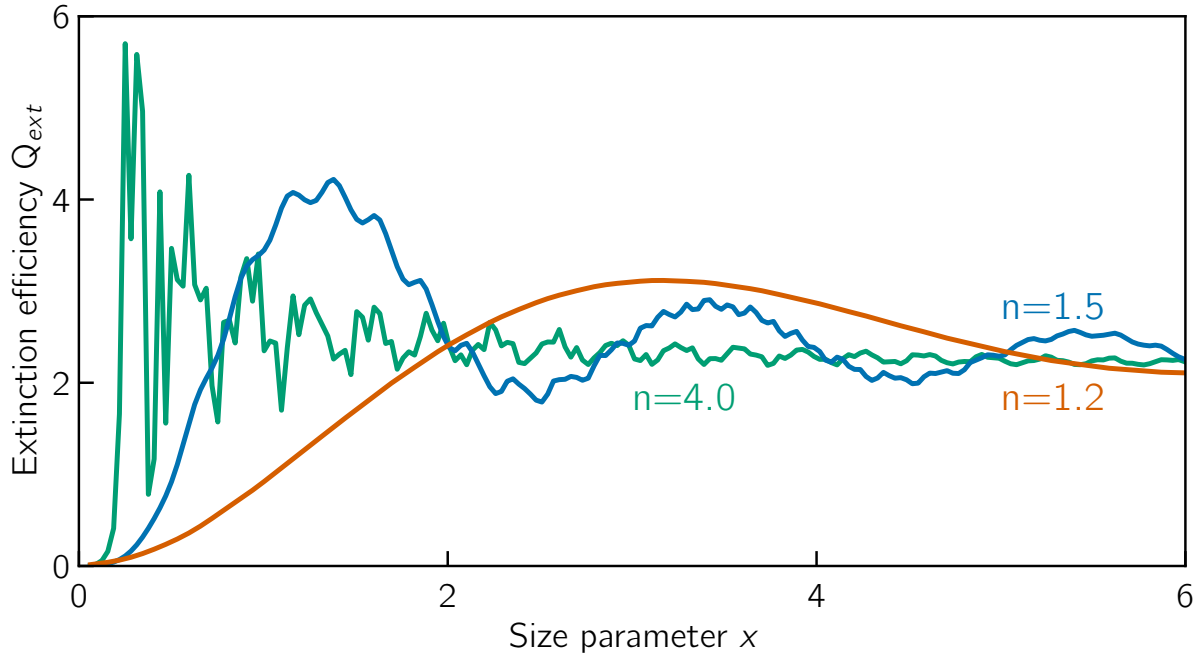

Figure 6.2.: Extinction efficiency of spheres with different refractive index n (complex part $\kappa = 0.01$) as a function of the size parameter x in vacuum, illustrating a resonant extinction efficiency Q_{ext} if the size parameter is of order unity.

Since the relevant parameter is the ratio between particle size and wavelength, the *size parameter* is defined as

$$x = \frac{2\pi r}{\lambda}, \tag{6.5}$$

where λ denotes the wavelength of the incident light. Mie theory constitutes an exact solution of Maxwell's equations, retaining the full angular and wavelength dependence of the scattered field. The only required input parameters are the size parameter x and the particle's relative refractive index m. According to Ref. [212], the extinction efficiency is given by

$$Q_{\text{ext}} = \frac{2}{x^2} \sum_{j=1}^{\infty} (2j+1)\, \Re\left(a_j + b_j\right), \tag{6.6}$$

where a_j and b_j are the *Mie coefficients*. These coefficients are defined as

$$a_j = \frac{m\psi_j(mx)\psi_j'(x) - \psi_j(x)\psi_j'(mx)}{m\psi_j(mx)\xi_j'(x) - \xi_j(x)\psi_j'(mx)}, \tag{6.7}$$

$$b_j = \frac{\psi_j(mx)\psi_j'(x) - m\psi_j(x)\psi_j'(mx)}{\psi_j(mx)\xi_j'(x) - m\xi_j(x)\psi_j'(mx)}, \tag{6.8}$$

where ψ_j and ξ_j are the Riccati–Bessel functions that encode the wavelength dependence. For a sphere of fixed radius, the size parameter $x = \frac{2\pi r}{\lambda}$ provides a measure directly related to frequency. The different scattering regimes, also illustrated in Fig. 6.2, can be summarized as follows.

In the limit of small x, corresponding to long wavelengths or low frequencies, the scattering efficiency follows the Rayleigh approximation, scaling as $Q_{\text{scat}} \propto x^4 \propto \lambda^{-4}$. The scattering is

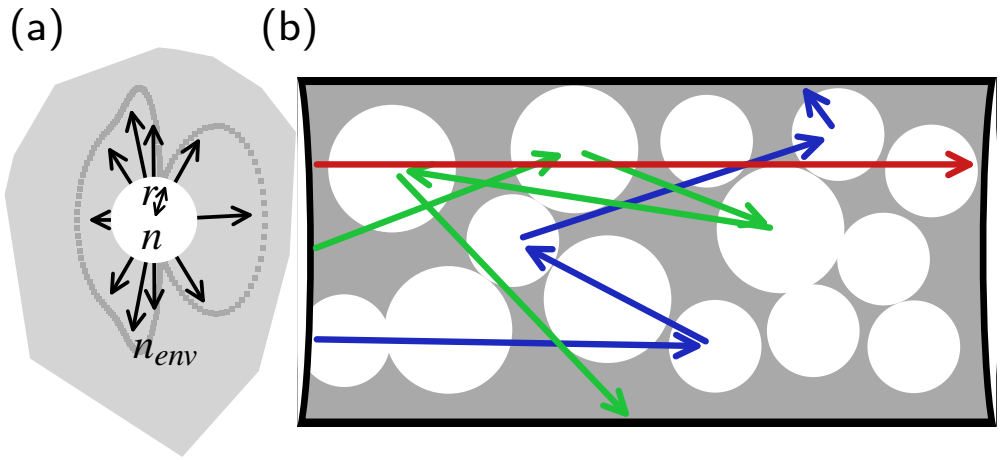

Figure 6.3.: (a) Scattering of a photon coming in from the left with wavelength $\lambda = 100\,\mu\text{m}$ on a sapphire sphere (white) of diameter $2r = 50\,\mu\text{m}$ and refractive index $n = 3.69$ in an epoxy matrix with $n_{\text{env}} = 1.5$ (gray). The arrows and the gray dashed line depict the distribution of the scattering probability. (b) Schematic drawing of the filter concept. Sapphire spheres (white) of different sizes in an epoxy matrix (gray) are filled into a tube (black border). The arrows illustrate incoming radiation from the left.

isotropic and results from the induced dipole moment in the small particle. For larger values of x, where $mx \gg j^2$, the first terms in the Mie series can be approximated by $\psi_j \sim \sin(mx - j\pi/2)$. This approximation shows the oscillatory behavior of the scattering with respect to wavelength (Fig. 6.2). One notable feature of Mie scattering is a maximum at x of order unity, where the extinction cross section exceeds the asymptotic upper (optical) limit of $Q_{\text{scat}} = 2$ reached at $x \to \infty$. In summary, spherical particles exhibit low scattering (and thus low extinction) in the low-frequency range, followed by pronounced scattering at higher frequencies, which persists toward arbitrarily large frequencies.

If the sphere is embedded in a non-absorbing environment with real refractive index n_{env}, Mie theory can still be applied by redefining the refractive index and size parameter as

$$m = \frac{n - i\kappa}{n_{\text{env}}}, \qquad x = \frac{2\pi r}{\lambda/n_{\text{env}}}. \tag{6.9}$$

The strong scattering contribution effectively increases the optical path length of light within the material, thereby enhancing the probability of absorption. According to Mie theory, this frequency dependence holds similarly for multiple individual spheres. As a result, in composite media (as shown in Fig. 6.3(b)) it is reasonable to assume that a significant fraction of the scattered light eventually becomes absorbed either within the medium itself or at its boundaries.

For an initial, simplified model, several assumptions are adopted: the particles are considered non-interacting, no electromagnetic coupling or multiple scattering is taken into account, the volume fraction of particles is kept low, and the distribution within the host medium is assumed homogeneous. Under these conditions, the total extinction cross section can be expressed as a sum of the contributions from each particle species [212],

$$\sigma_{\text{ext,total}} = \sum_i \sigma_{\text{ext},i}. \tag{6.10}$$

The extinction coefficient for a blend of different scatterers is given by

$$\mu_{\text{ext,tot}} = N_{\text{tot}} \sigma_{\text{ext,tot}}, \tag{6.11}$$

where N_{tot} is the total number density per volume,

$$N_{\text{tot}} = \sum_i \frac{1/V_i}{\xi \left(1 + \rho_{\text{sapphire}}/\rho_{\text{epoxy}}\right)}, \tag{6.12}$$

and the total extinction cross section

$$\sigma_{\text{ext,tot}} = \sum_i \gamma_i Q_{\text{ext},i} \pi r_i^2. \tag{6.13}$$

Here, r_i is the radius of spheres of species i, ξ is the number of different spheres in the mixture, and the density ratio is given as $\rho_{\text{sapphire}}/\rho_{\text{epoxy}} \approx 3.6$. The calculation of $\sigma_{\text{ext,tot}}$ also includes a weighting factor $\gamma_i = V_i / \sum_j V_j$, which takes into account the relative number of individual spheres per volume, where V_i is the volume of a sphere of species i.

6.4. Calculations of expected scattering behavior

Fig. 6.4 shows the calculated extinction efficiency Q_{ext} for sapphire spheres with diameters between 0.45 µm and 700 µm (individual colors) up to a wavelength of 100 mm. The extinction efficiency is obtained using the *MiePython* software package [213], which implements Mie solutions of Maxwell's equations in a Python library. For the calculations, the complex refractive index measured by Querry et al. [214] for wavelengths up to 60 µm is used; these data are shown in Fig. A.12 in the Appendix. At approximately 20 µm, a resonance due to vibrational modes becomes visible. Beyond this wavelength, the refractive index is assumed constant, as no additional vibrational modes are expected in this spectral region. The surrounding epoxy matrix is included as the embedding dielectric medium, which changes the effective refractive index and thus the effective wavelength in the medium. The extinction efficiency shows the same behavior for all sphere diameters: it is constant in the low-wavelength regime, the optical scattering regime; it shows a peak and a periodic pattern in the mid-wavelength regime around the diameter of the sphere, the Mie scattering regime; and it decays rapidly toward longer wavelengths, the Rayleigh regime. The common resonance mode at a wavelength of approximately 20 µm originates from the resonance in the refractive index caused by a vibrational mode in the sapphire [214].

The extinction coefficient of a mixture of different spheres can be calculated from these extinction efficiencies using Eq. 6.11 and the relative fractions γ_i. By this mixing, the scattering efficiency can remain above the geometric-optics limit over a wide frequency range. The steep Rayleigh roll-off of the largest sphere then provides a well-defined cutoff toward longer wavelengths.

The primary mixtures investigated in this work are the sapphire powder (SP) mixtures *SP0.45-80* and *SP0.45-700*. The mixture SP0.45-80 consists of five different sphere sizes from 0.45 µm to 80 µm ($\xi = 5$), whereas SP0.45-700 contains eight different sizes from 0.45 µm to 700 µm ($\xi = 8$). The corresponding mixing fractions and refractive indices are given in Table 6.1, together with the wavelength $\lambda_{x'}$ for which the size parameter x is equal to one. This wavelength provides a measure of the maximal extinction of the corresponding sphere. In Fig. 6.4, the black dashed and solid lines show the extinction coefficient of these two mixtures on a logarithmic scale. The

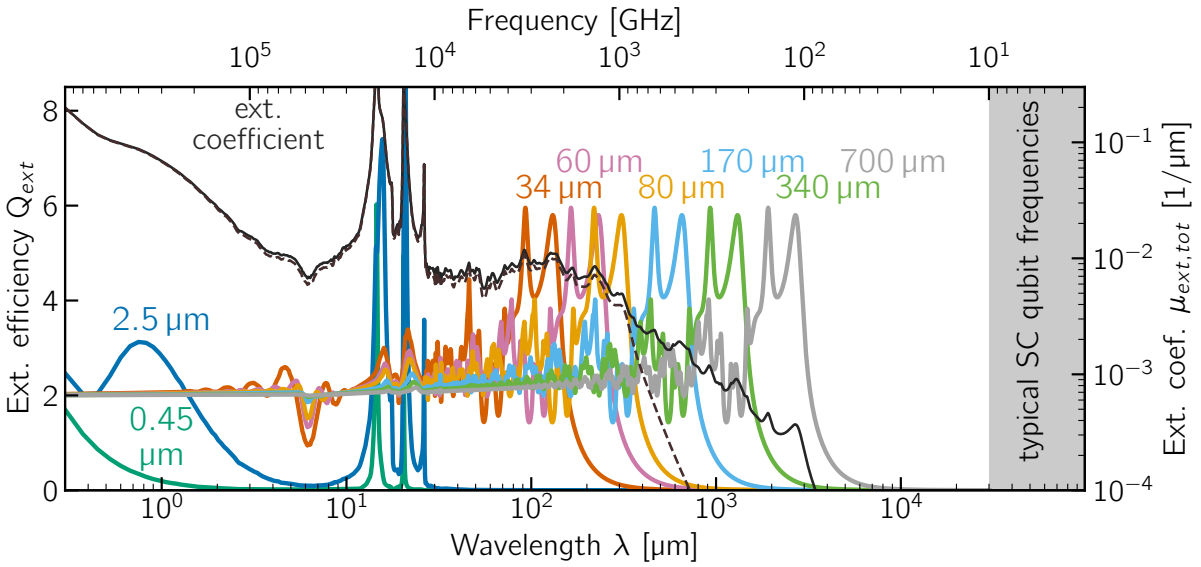

Figure 6.4.: Calculated Mie scattering for sapphire spheres of varying sizes in an epoxy resin matrix as a function of wavelength (colored lines, left axis). The black solid (dashed) line shows the total extinction efficiency of the composition SP0.45-700 (SP0.45-80) containing different sphere sizes (right axis).

Table 6.1.: Parameters for the investigated sapphire spheres. The wavelength $\lambda_{x'}$, refractive index [214] components $n(\lambda_{x'})$ and $\kappa(\lambda_{x'})$ are given for $x = 1$. The mixing fraction γ is specific for the SP0.45-700 (SP0.45-80) mixture.

a [μm]	$\lambda_{x'}$ [μm]	$n(\lambda_{x'})$	$\kappa(\lambda_{x'})$	γ(SP0.45-700)	γ(SP0.45-80)
0.45	1.41	1.73	1.80×10^{-2}	9.9×10^{-1}	9.9×10^{-1}
2.5	7.85	1.36	3.43×10^{-2}	5.8×10^{-3}	5.8×10^{-3}
34	106.8	3.69	3.00×10^{-2}	2.3×10^{-6}	2.3×10^{-6}
60	188.5	3.69	3.00×10^{-2}	4.2×10^{-7}	4.2×10^{-7}
80	251.3	3.69	3.00×10^{-2}	1.8×10^{-7}	1.8×10^{-7}
170	534.1	3.69	3.00×10^{-2}	1.8×10^{-8}	0
340	1068	3.69	3.00×10^{-2}	2.3×10^{-9}	0
700	2199	3.69	3.00×10^{-2}	2.6×10^{-10}	0

extinction is high over a broad wavelength range spanning multiple orders of magnitude. The mixtures reproduce features of the individual spheres, such as the resonant extinction due to the vibrational mode. At wavelengths on the order of $\lambda_{x'}$ of the largest sphere in the mixture, a sharp decrease in extinction appears. This behavior defines a sharp cutoff for a potential infrared filter at higher frequencies, set by the size of the largest grains in the mixture, while maintaining significant scattering efficiency for wavelengths smaller than those corresponding to the smallest grains.

6.5. Investigated material samples

For this work, samples of the two SP mixtures as well as samples of single-diameter sapphire spheres are prepared. These are compared to various other material samples. As sapphire spheres, commercially available sapphire powders [215] are used. All powders are listed in Table 6.1 with their median particle diameters, assuming a spherical shape. The primary mixtures are the

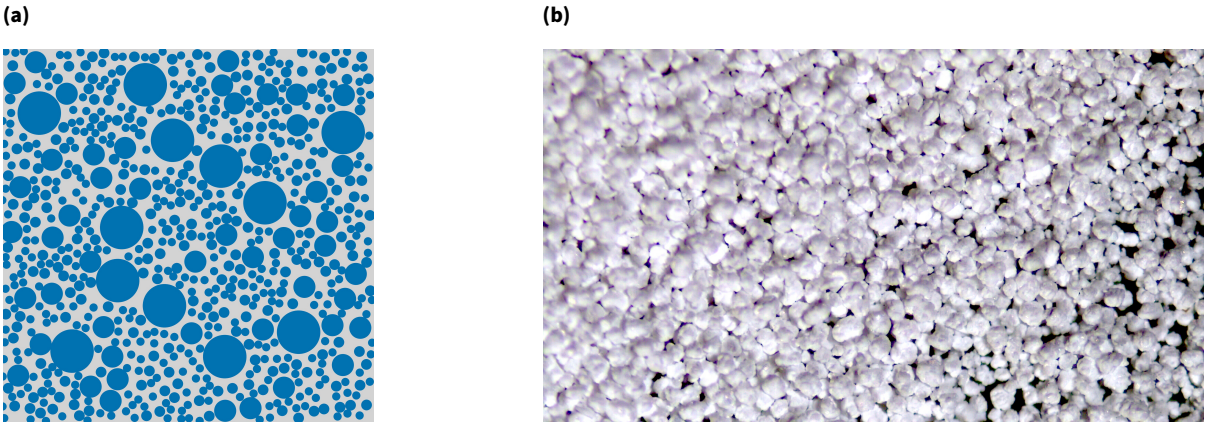

Figure 6.5.: (a) Schematic drawing of the distribution of differently sized sapphire spheres (blue) in the SP0.45-80 mixture embedded in an epoxy matrix (gray). (b) Optical microscope image of the SP0.45-80 material mixture.

mixtures *SP0.45-80* and *SP0.45-700*. The mixture SP0.45-80 consists of five different sphere sizes ($\xi = 5$) from 0.45 µm to 80 µm; SP0.45-700 contains eight different sphere sizes ($\xi = 8$) from 0.45 µm to 700 µm. The weighting factors γ_i of the different diameters describe the number ratio in the two mixtures. The given numbers for γ_i in Table 6.1 correspond to mixing by equal masses of the different-diameter spheres. Fig. 6.5(a) shows a schematic drawing of the distribution of different grain diameters in the SP0.45-80 mixture. Fig. 6.5(b) shows an optical microscope image of the same mixture. These particle distributions are chosen because they increase the particle number with decreasing diameter and thereby counter the scaling of the scattering cross section with particle size, thus approximating a smooth extinction over the targeted stopband from a few 100 GHz up to 200 THz.

Additionally, mixtures of single-diameter spheres are investigated. The powder mixtures are combined with UHU+ Endfest 300 [211] (epoxy) in a 1:1 weight ratio. The epoxy binds the particles together, providing mechanical stability and a uniform distribution. It also acts as a dielectric medium with a moderate refractive index ($n \approx 1.5$ [211]), which helps to minimize microwave losses and reduces reflections at grain boundaries. This preserves signal integrity within the operational frequency band. Each batch of sapphire grains contains a manufacturer-selected distribution of sizes; the given median is used in the Mie calculation. The broader distribution of grain sizes is not detrimental but rather beneficial, as it smooths the extinction efficiency spectrum shown in Fig. 6.4.

The samples are prepared by mixing the two components of the epoxy resin in equal volume fractions and then stirring in separately prepared powder mixtures. This mixture is vacuum-degassed for five minutes to eliminate entrapped air. Afterwards, the samples are cured at ambient conditions for 18 h to 24 h or heated to 50 °C for shorter curing times. These samples are compared to various other materials: mixtures of stainless steel and copper (grain size below 45 µm) powder prepared in an epoxy matrix with a 1:2 powder-to-epoxy weight ratio; polytetrafluoroethylene (PTFE, Teflon); transparent and black high-density polyethylene (HDPE); and the commercial infrared-absorbing epoxies Stycast 2850FT and Eccosorb CR124 [61]. For infrared spectrometer measurements, round disks with a diameter of 13 mm and thicknesses of 1 mm, 1.5 mm, 2 mm, and 2.5 mm are prepared. The metal-based mixtures, as well as the Stycast 2850FT and Eccosorb CR124 samples, are prepared in a similar manner. The HDPE and PTFE samples are cut from larger sheets.

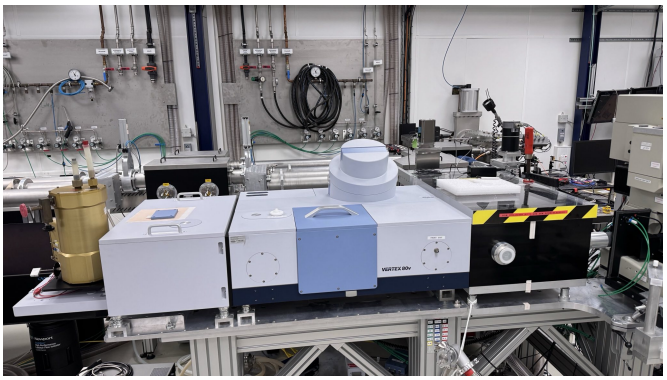


Figure 6.6.: Left: Picture of the *Bruker VERTEX 80v* spectrometer. Right: Sample wheel in the vacuum chamber of the spectrometer.

6.6. Room-temperature infrared spectrometer measurements

The primary objective of this study is to evaluate the effectiveness of various materials in suppressing the transmission of infrared light. Therefore, a spectrometer is used to measure infrared transmission within the wavelength range 2 µm to 900 µm at room temperature.

6.6.1. Experimental setup

The measurements are conducted with a *Bruker VERTEX 80v* (Fig. 6.6) using a silicon carbide Globar source. The *Bruker VERTEX 80v* is a Fourier-transform spectrometer in which broadband infrared radiation from the Globar source is sent into a Michelson interferometer, where a beamsplitter divides the beam into two paths. One path reflects from a fixed mirror, the other from a moving mirror. After recombination, the varying path length in one arm due to the moving mirror produces constructive and destructive interference, resulting in a time-dependent intensity signal at the detector (the interferogram). Before the beam reaches the detector, it passes through the sample under investigation. The sample is mounted in a vacuum chamber between the interferometer and the detector. A rotating wheel (Fig. 6.6) allows switching between up to twelve samples and an empty position used as a bright reference (100 %) measurement. The interferogram for each sample is converted into a transmission spectrum by comparison to the bright reference and a Fourier transformation. The spectrometer permits switching between detectors and beamsplitters without manual intervention. For the wavelength ranges 1 µm to 19.4 µm and 19.4 µm to 84.7 µm, DLaTGS and DTGS-FIR detectors, respectively, are employed; both are deuterated triglycine sulfate detectors. For wavelengths above 84.7 µm, a silicon bolometer cooled to 1.6 K is used together with two filters: one with a lower cutoff at 100 µm (100 cm^{-1}) and another at 285.7 µm (35 cm^{-1}). The beamsplitter is changed for each wavelength range: potassium bromide (KBr) for 1 µm to 84.7 µm, a multilayer Mylar beamsplitter for 84.7 µm to 238.1 µm, and a 150 µm Mylar beamsplitter for longer wavelengths. Some long-wavelength measurements use a 125 µm Mylar beamsplitter.[3] Measurements are taken with a spectral resolution between 1 cm^{-1} and 4 cm^{-1}. Depending on the expected intensity, an

[3] The 125 µm Mylar beamsplitter provides a higher sensitivity at wavelengths approaching 1 mm but has a dip in sensitivity at approximately 425 µm; compare Fig. 6.7.

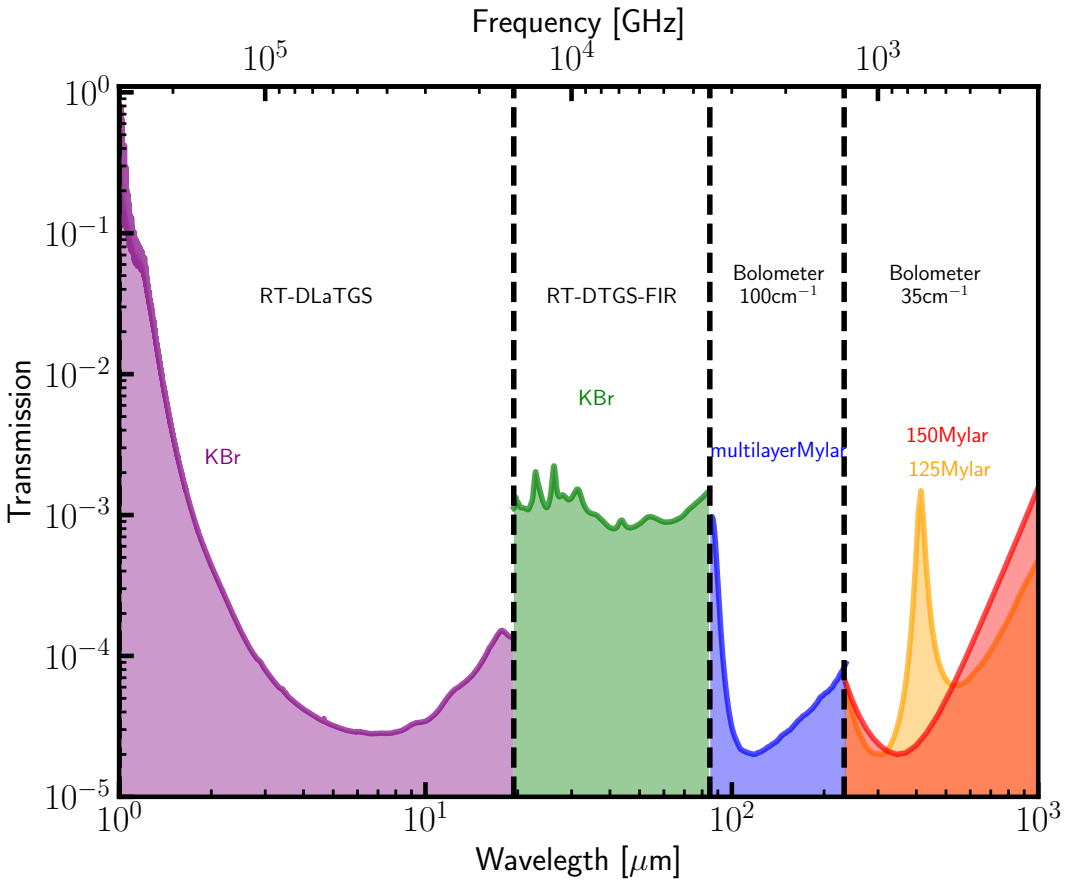

Figure 6.7.: Background measurements providing the sensitivities of the different detector–beamsplitter combinations (filled colored areas). The set wavelength limits of the detectors are indicated by vertical dashed lines.

aperture of either 4 mm or 10 mm is used. All measurement settings are summarized in Table A.3 in the Appendix.

6.6.2. Data processing

The choice of detector and beamsplitter defines the wavelength-dependent experimental sensitivity. Calibration involves measuring transmission through vacuum for all detectors to establish a 100 % reference line. Transmission values are defined relative to this reference. Fig. 6.7 shows the detector sensitivity limits derived from the 100 % reference.

The detector–beamsplitter combinations exhibit frequency-dependent sensitivities. The deuterated triglycine sulfate detectors show approximately parabolic sensitivity curves, with minimum detectable transmissions of 3×10^{-5} at 6 µm and 1×10^{-3} at 40 µm. The bolometer minimum detectable transmission is 2×10^{-5} at 350 µm. This wavelength-dependent sensitivity defines the lower bound for measurable transmission through the samples. The bolometer, combined with the 35 cm^{-1} filter and the 100 µm Mylar beamsplitter, displays peak sensitivity around 400 µm and increased sensitivity again toward the long-wavelength end near 1000 µm, which is reflected in the measured data.

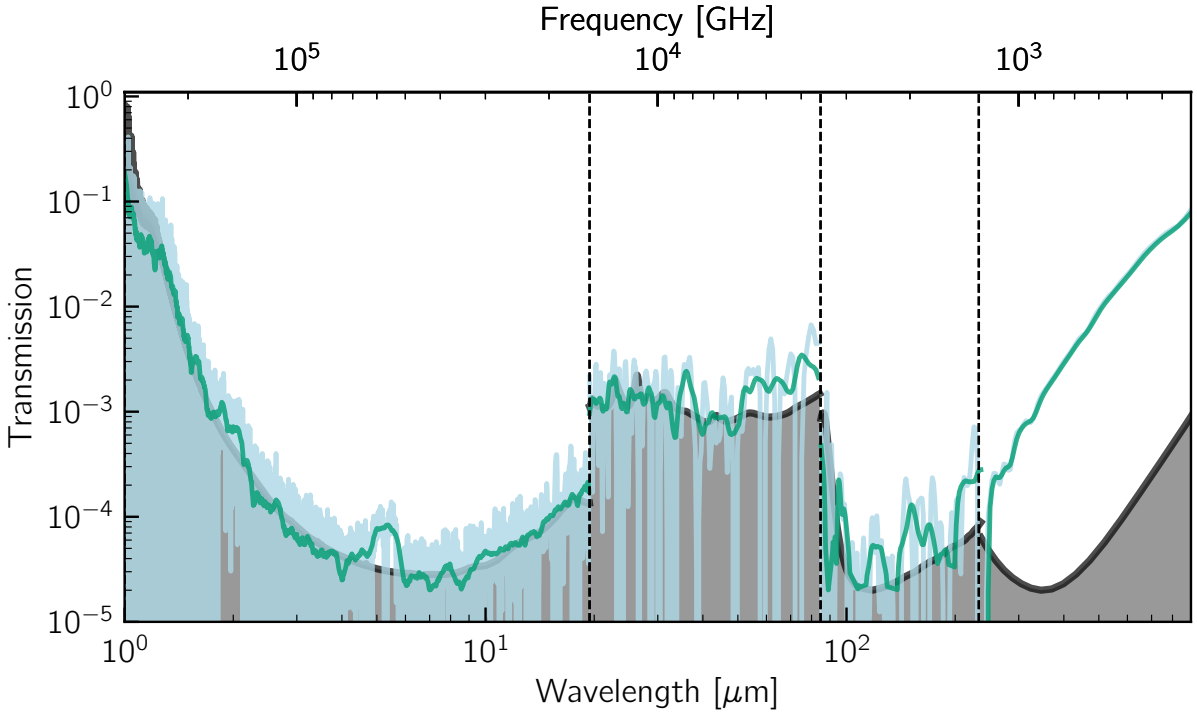

Figure 6.8.: Transmission fraction through a highly absorbing material measured using a Bruker IFS 66v/S spectrometer. The light blue line is the raw measurement trace, the green line represents the smoothed data using a Savitzky–Golay filter. The gray area indicates the wavelength-dependent sensitivity limit.

Fig. 6.8 illustrates the raw and smoothed transmission for a highly absorbing sample, with detector limits marked in black. The measurement lies at or close to the sensitivity limit. The traces also show substantial noise. To make the data more comparable and to extract information about the materials, the transmission T is converted into absorption A:

$$\frac{I}{I_0} = T = 1 - A. \tag{6.14}$$

The absorption spectra are then smoothed using a third-order Savitzky–Golay filter[4] [216], with a window length of 150 points for the DLaTGS detector and 30 points for both the DTGS-FIR detector and the 1.6 K bolometer. The reported measurement error arises mainly from the variance within the smoothing window and from calibration variations (most notably in the bright measurements). The different wavelength ranges measured with different detectors and filters are then combined into the absorption spectra presented in the following sections. All transmission measurements (with Savitzky–Golay filtering applied) are provided in Sec. A.7 in the Appendix.

6.6.3. Infrared absorption measurements of different materials

The infrared absorption of the materials introduced above is measured for samples with a thickness of 1.5 mm. These absorption spectra are compared in Fig. 6.9; note the different scales

[4] A Savitzky–Golay filter is similar to a running average, but instead of performing an average (a fit of a constant) a polynomial of order n is fitted to the window segment.

of the individual subplots. The transmission values at selected wavelengths are listed in Table A.2 in the Appendix.

At wavelengths below 200 µm, the SP0.45-80 and SP0.45-700 mixtures (Fig. 6.9(a)) are nearly fully absorbing, dominated by spheres in the range from 0.45 µm to 80 µm. In the range between 20 µm and 100 µm, all samples show higher average absorption together with larger uncertainties. This behavior reflects the use of a different detector in this spectral region that has lower sensitivity. The measured transmission is at or below the detector limit of about 1×10^{-4} on average (compare Sec. A.8.2). A potentially lower absorption of the sapphire powder compounds in this region, possibly caused by missing spheres with diameters between 2.5 µm and 34 µm, cannot be resolved. Within the experimental sensitivity, the sapphire-sphere mixtures therefore exhibit nearly perfect absorption in the MIR range. In the FIR range (200 µm to 1000 µm), the absorption decreases, consistent with the Rayleigh scattering limit for wavelengths larger than the largest grain size in the mixtures. The higher absorption of SP0.45-80 compared to SP0.45-700 is discussed below.

Sample compounds consisting of single-diameter spheres (Fig. 6.9(b)) also show high absorption. The 170 µm sample approaches the Rayleigh scattering limit around 500 µm, resulting in reduced absorption. A similar decline is expected for spheres with diameters of 340 µm and 700 µm at wavelengths of approximately 1070 µm and 2200 µm, respectively (see Fig. 6.4), which lie outside the measurement window. In the MIR range, these sapphire samples exhibit a double peak near 2 µm, which coincides with the peak observed for the epoxy resin (Fig. 6.9(c)). This is expected, because there are no sufficiently small particles present to produce significant extinction in this spectral range. The large spheres leave considerable space between them through which short wavelengths can propagate, since there are fewer particles in a given volume. As Eq. 6.11 shows, the extinction coefficient depends on the total number density. For the 700 µm spheres, a smaller peak near 4 µm appears. Its origin is unclear. A possible explanation is that it arises from optical paths located entirely within sapphire, because the epoxy sample shows no passband at these wavelengths. Such a path becomes more probable for larger spheres, where only a few spheres in direct contact are needed. Given a sample thickness of (1.5 ± 0.2) mm and a sphere size of (0.7 ± 0.2) mm, two to three spheres in direct contact are sufficient. This hypothesis is supported by thickness-dependent measurements (Sec. 6.6.4): for thicker samples (2 mm and 2.5 mm), the peak disappears, while for thinner samples (1 mm) it also appears for smaller spheres (see Fig. A.13).

The absorption of PTFE, HDPE, Stycast 2850FT, Eccosorb CR124, and UHU plus Endfest 300 samples mixed with copper or stainless steel powders is shown in Fig. 6.9(c,d). Transparent HDPE and PTFE show very low absorption, predominantly in the FIR region, demonstrating that they are largely transparent to thermal infrared radiation. For the transparent samples, especially PTFE, oscillations are observed in the FIR region due to Fabry–Perot resonances; these are discussed in Sec. A.8.3 in the appendix. Black HDPE (likely containing a carbon filler) blocks radiation almost completely in the lower MIR range (1 µm to 200 µm) and becomes more transparent toward the FIR. Stycast 2850FT and epoxy resin show strong MIR absorption, with increasing transmission at longer wavelengths. The metal powder samples and Eccosorb CR124 exhibit the highest absorption across the full infrared range and continue to absorb strongly even into the microwave regime (see Sec. 6.8). They do not reach a typical asymptotic Rayleigh limit.

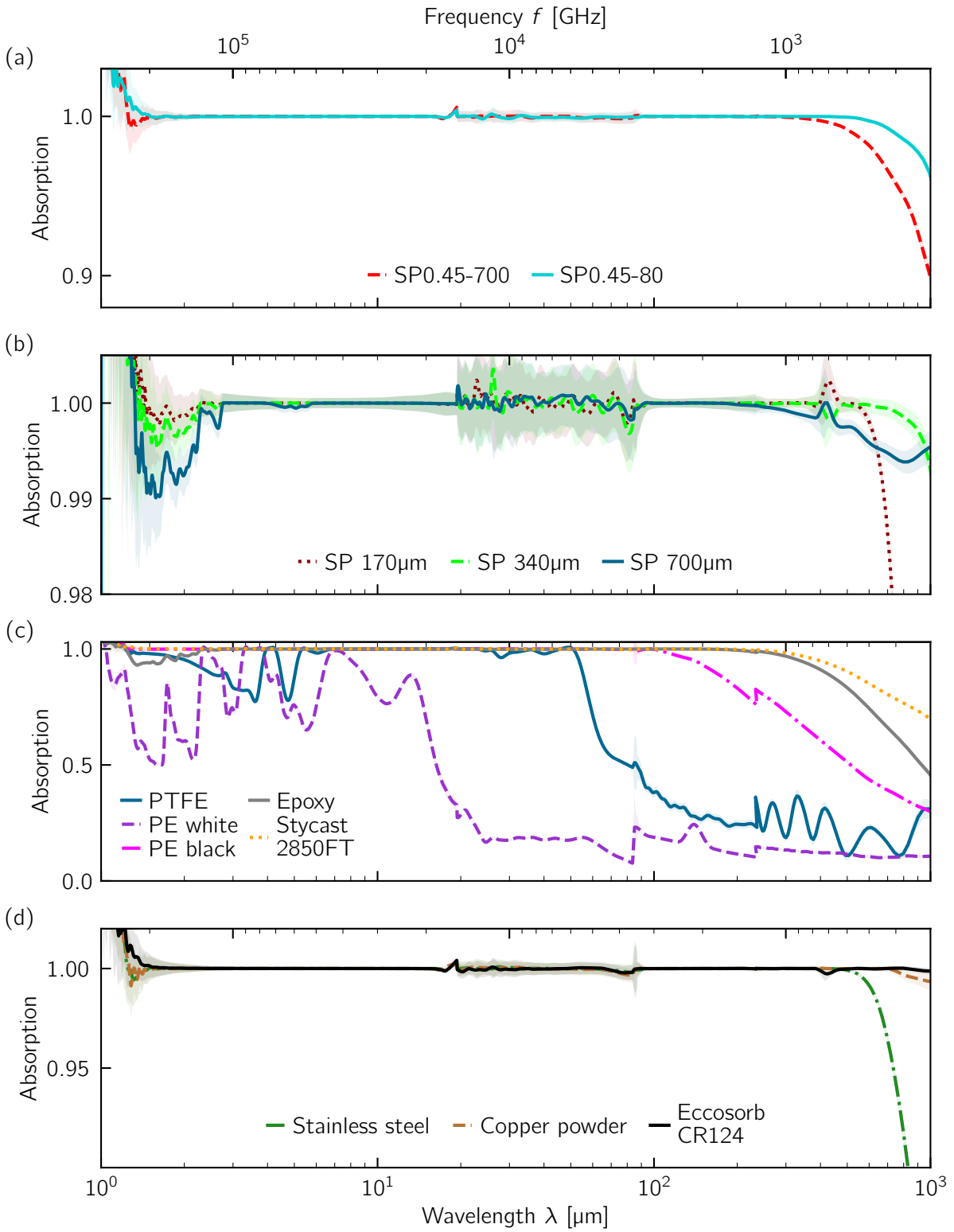

Figure 6.9.: Absorption spectra of various materials at a thickness of 1.5 mm. Different y-axis scales are used. (a) Sapphire powder mixtures SP0.45-80 and SP0.45-700. (b) Single-diameter sapphire powder samples. (c) PTFE, HDPE (transparent and black), epoxy UHU+ Endfest 300, and Stycast 2850FT. (d) Eccosorb CR124 and epoxy resin mixed with metal powders (copper and stainless steel).

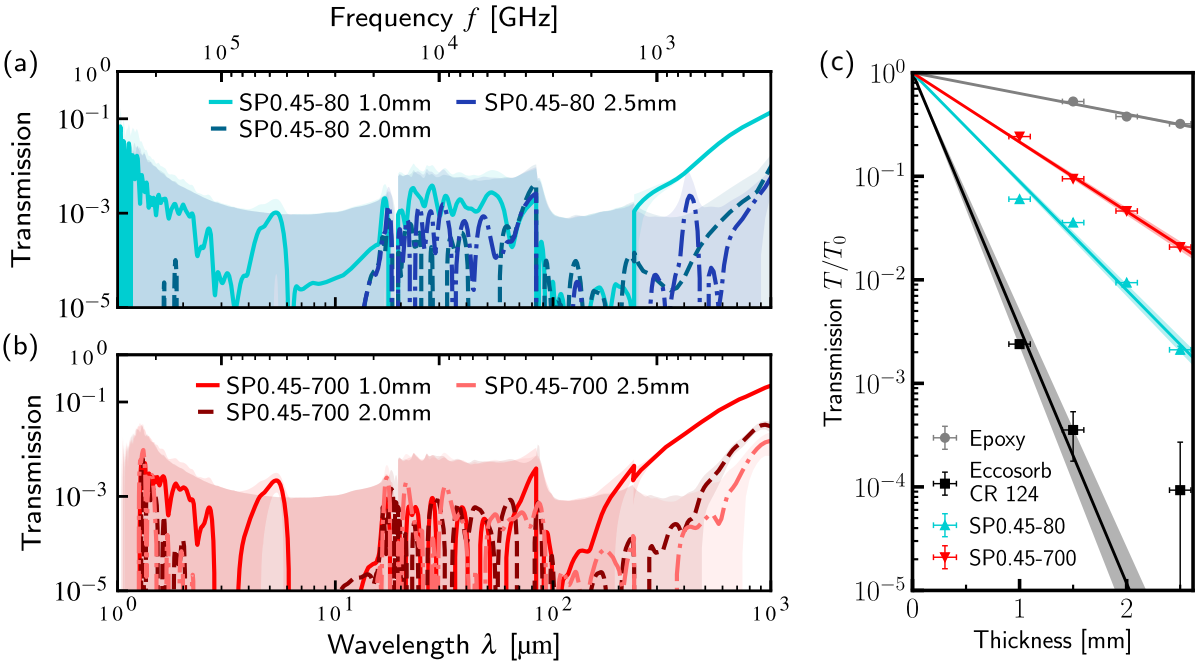

Figure 6.10.: Comparison of different thicknesses: 1.0 mm (solid line), 2.0 mm (dashed line), and 2.5 mm (dot-dashed line). Shaded bands indicate errors. (a) SP0.45-80. (b) SP0.45-700. (c) Transmission as a function of thickness at 864 µm for the sapphire powder mixtures, epoxy resin, and Eccosorb CR124. Solid lines show fits based on the Beer–Lambert law.

6.6.4. Thickness-dependent measurements

Fig. 6.10 shows the transmission through different thicknesses (1 mm, 2 mm, 2.5 mm) of samples from the two sapphire powder mixtures. As expected, the overall transmission decreases with increasing thickness. In most of the MIR regime, the transmission remains at the detector sensitivity limit, apart from features similar to those observed in the 1.5 mm samples discussed above. Additional thickness-dependent transmission data for other materials are presented in Sec. A.8 (Fig. A.13 and Fig. A.14). The same trend of decreasing transmission with increasing thickness is observed.

Fig. 6.10(c) shows the transmission as a function of thickness at 864 µm for the sapphire powder mixtures, epoxy resin, and Eccosorb CR124. The Beer–Lambert law (Eq. 6.1) is fitted to these data to obtain the wavelength-dependent extinction coefficient μ_{ext} for each material. This procedure is applied to all wavelengths above 500 µm, where the transmission is sufficiently high. The resulting extinction coefficients are discussed in Sec. 6.8.

6.7. Microwave characterization of prototype filters

To test the microwave properties of the SP0.45-80 mixture (Sec. 6.7.1) and the metal powder samples (Sec. 6.7.2), prototype coaxial filters are prepared, as illustrated in Fig. 6.11. The mixture is embedded in a copper block with a drilled hole, serving as outer conductor. The diameter of the hole, and therefore of the dielectric, is 2.2 mm, and its length is 8 mm. The inner conductor is a 0.4 mm silver-plated copper wire. Both ends are terminated with non-magnetic SMA connectors. The dimensions are chosen to match the 50 Ω impedance of the microwave

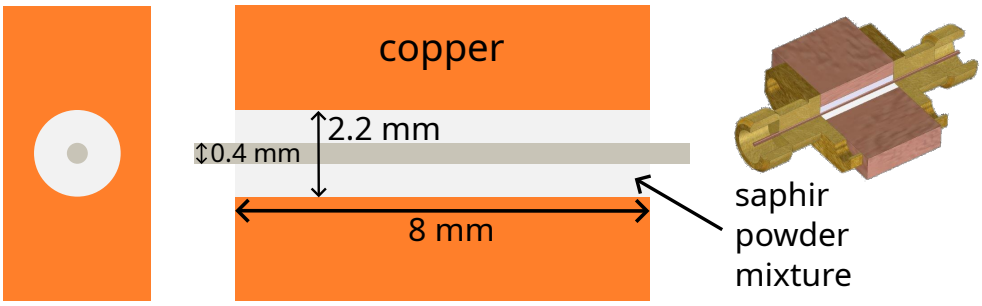

Figure 6.11.: Left: Cross-sectional views (both axes) of a typical coaxial filter sample for microwave measurements. The dimensions and materials are indicated. Right: A 3D cross-section view with SMA connections.

network as closely as possible at millikelvin temperatures. The epoxy in the mixture provides thermal contact between the outer conductor, the inner conductor, and the grains.

6.7.1. Microwave properties of sapphire powder mixtures

The microwave transmission (S21) and reflection (S11) of this prototype filter are measured at room temperature and at millikelvin temperatures. For room-temperature measurements, the cabling setup is calibrated first and then the filter is inserted, which removes the effect of other components in the measurement chain. Cryogenic measurements are performed in a *Bluefors LD250* dilution refrigerator at 15 mK, with the samples mounted on the mixing chamber plate. Calibrations at cryogenic temperatures are more challenging. Microwave lines with low attenuation are calibrated across several cooldowns, after which the filter is connected to one calibrated pair of lines. Additional lines without samples serve as references. Data are recorded using a vector network analyzer (*Keysight E5080B*) over the frequency range 0.1 GHz to 14 GHz. High photon numbers are used to maintain a sufficient signal-to-noise ratio.

Transmission

The microwave transmission through the prototype is shown in Fig. 6.12(a). The red curve corresponds to room-temperature measurements; the transmission decreases from 0 dB at 0 GHz to −0.22 dB at 6 GHz. The blue curve shows data at 15 mK; the absorption is reduced, with a transmission of −0.1 dB at 6 GHz and a more gradual roll-off with frequency. Above 10 GHz, the transmission at millikelvin temperatures drops below the room-temperature value. This is not problematic, because the millikelvin measurement setup and filter design target the range 4 GHz to 10 GHz. Shaded bands show the measurement error, dominated by noise (suppressed in the measurement trace using a running average) and uncertainties propagated from the calibration measurements. The error is larger in the millikelvin data, mainly due to imperfect calibration. Overall, the results show that sapphire-based filters can be engineered to yield very low attenuation in the passband at cryogenic temperatures.

Reflection

Figure 6.12(b) shows the corresponding reflection measurements. At room temperature (red), the reflection reaches −27 dB at 6 GHz. At millikelvin temperatures (blue), the reflection is

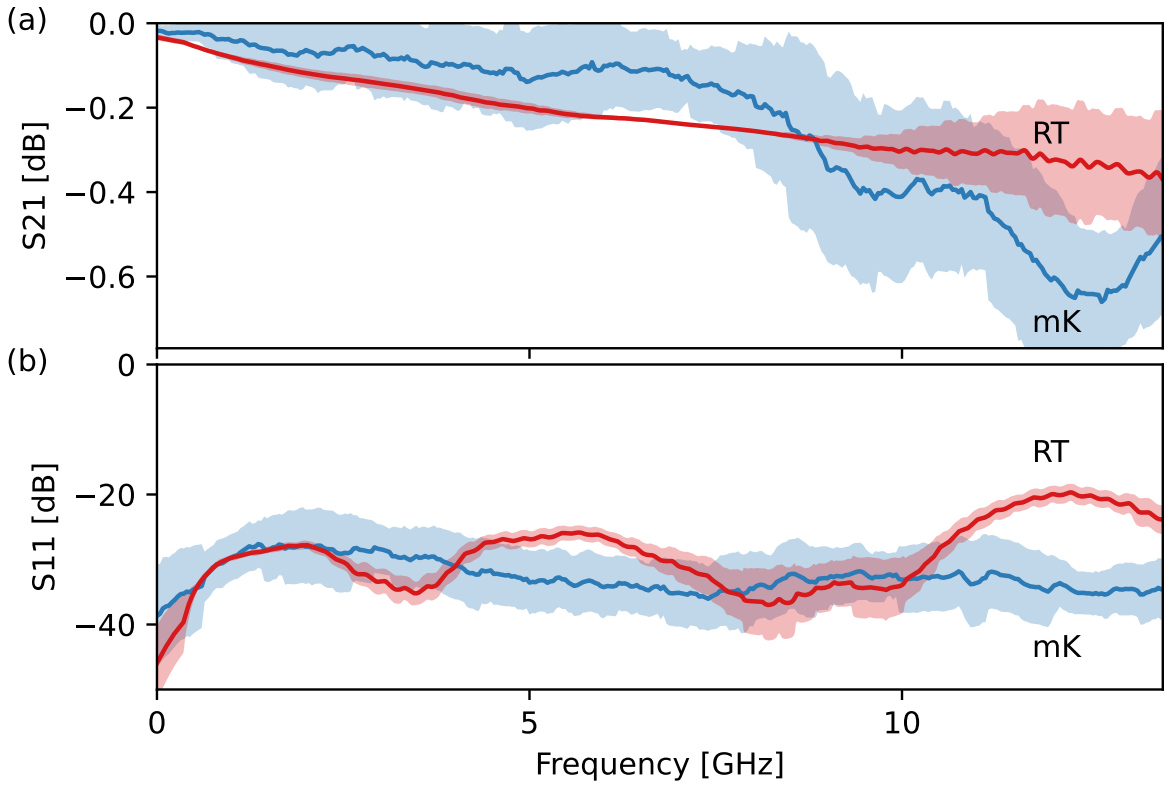

Figure 6.12.: VNA measurements of SP0.45-80 filters with an outer diameter of 2.2 mm. Red (blue) lines represent room-temperature (millikelvin) measurements. (a) Transmission (S21). (b) Reflection (S11).

reduced to −37 dB at the same frequency. From these reflection results, the impedance at 6 GHz can be determined as described in Sec. 4.1.2. This yields effective impedances of $(54.4 \pm 0.6)\,\Omega$ at room temperature and $(51.4 \pm 0.8)\,\Omega$ at millikelvin temperatures. These values deviate slightly from the targeted 50 Ω system impedance at millikelvin but still demonstrate that practical filter dimensions can be adjusted to achieve good impedance matching. The thickness of the filter is the primary parameter; changing it alters the capacitive and inductive characteristics, and thus the effective impedance. Good impedance matching is crucial for maximizing power transfer between the filter and the measurement apparatus. It reduces signal reflections and improves measurement accuracy. The impedance of the coaxial filter also allows extraction of the effective dielectric constant via

$$\epsilon_r = \left(\frac{60}{Z_0 \ln(D/d)} \right)^2 , \tag{6.15}$$

where D is the inner diameter of the copper holder and d is the diameter of the inner conductor. For the prototype filters, $D = 2.2$ mm and $d = 0.4$ mm. Using these values, the extracted dielectric constants at 6 GHz are $\epsilon_r = 3.535(22)$ (room temperature) and $\epsilon_r = 3.966(16)$ (millikelvin).

6.7.2. Microwave properties of other powder mixtures

Coaxial filters based on stainless steel and copper powder in epoxy are fabricated in the same way as the sapphire powder prototype filters. These are measured with the same setup at room temperature. Fig. 6.13 shows the results. The solid lines represent the different samples: stainless

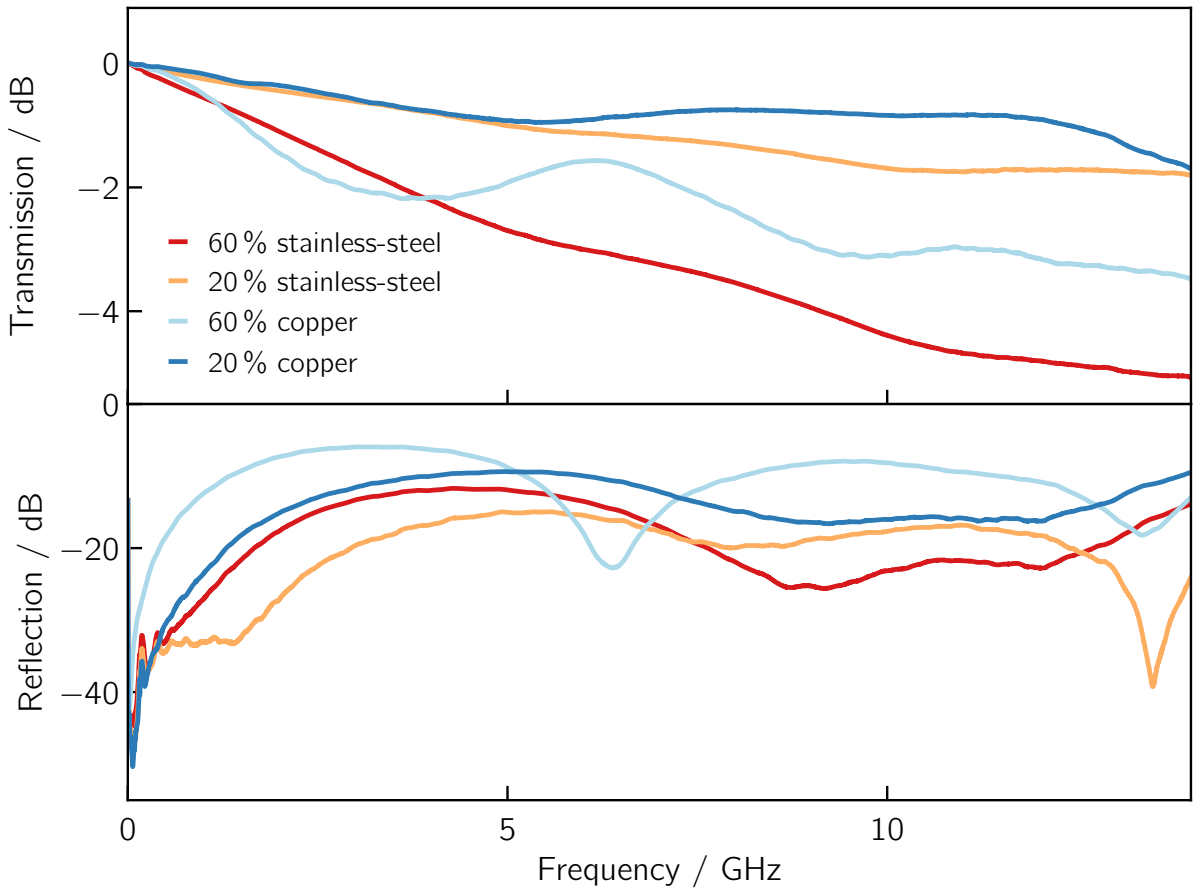

Figure 6.13.: VNA measurements of powder-based coaxial attenuators with an outer diameter of 2.2 mm. Solid (dashed) lines represent room-temperature (70 K) measurements. Top: Transmission (S21). Bottom: Reflection (S11).

steel powder mixed with epoxy at 60 % and 20 % by weight, and copper powder mixed with epoxy at 60 % and 20 % by weight. The top panel shows the transmission. All metal-based samples exhibit lower transmission than the sapphire powder filters. This makes them less suitable as low-loss infrared filters on return lines, but they can function as broadband attenuators on drive or readout lines toward the sample. Such attenuators have a potential advantage over lumped-element attenuators: the electron system can thermalize more effectively with the lattice, which may help address a common problem in qubit devices, namely limiting effective qubit temperatures below 50 mK [217]. The bottom panel in Fig. 6.13 shows the reflection. The reflection is quite high, which is expected since the diameters ($D = 2.2\,\mathrm{mm}$ and $d = 0.4\,\mathrm{mm}$) are not optimized for these materials.

6.8. Broadband performance of candidate filter materials

An ideal infrared filter combines strong attenuation in the infrared regime with very low attenuation in the microwave regime. The extinction coefficient provides a convenient measure of this behavior and is shown in Fig. 6.14 over the full investigated wavelength range. The critical FIR region (below $\lambda = 1.0\,\mathrm{mm}$, corresponding to the long-wavelength limit of the infrared setup) is compared directly with the microwave data. In the FIR regime, the extinction

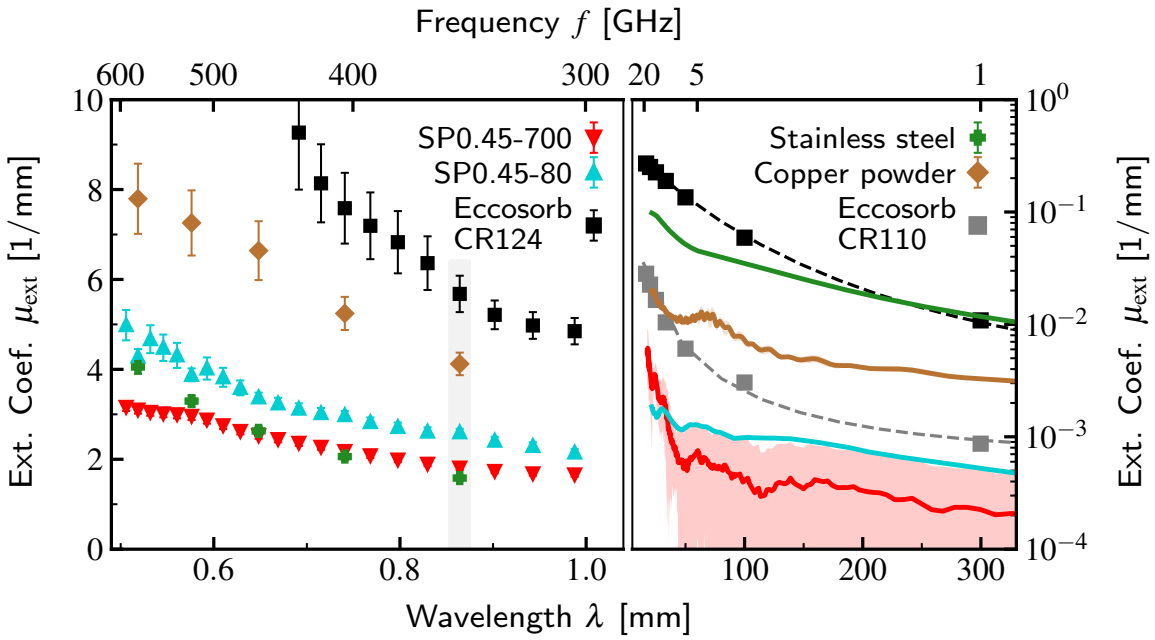

Figure 6.14.: Extinction coefficients of SP mixtures, epoxy resin, and Eccosorb CR124 as a function of wavelength. Left: Infrared range (gray region highlights the fit at 864 µm shown in Fig. 6.10(c)). Right: Microwave range for the SP-based filter in Fig. 6.12 and for copper and stainless steel. Eccosorb CR124 data are taken from Ref. [62]. Note the different y-axis scales for the two panels.

coefficient is extracted from the thickness-dependent measurements described in Sec. 6.6.4. For the microwave regime, the 8 mm prototype filter is used as a single thickness point. The two sapphire powder mixtures are compared to the metal powder samples. Additionally, microwave extinction coefficients for Eccosorb CR124 (used in the infrared measurements) and Eccosorb CR110, another common choice for cryogenic infrared filters, are taken from the datasheet [62][5].

Materials such as copper powder, stainless steel powder, and Eccosorb CR124 exhibit the expected high absorption, approximately twice that of the sapphire powder mixtures in the infrared regime. Based on the measurement data, a lower bound for the absorption of the sapphire powder mixtures of 1.2×10^{-6} (corresponding to 118 dB attenuation) is estimated for a prototype filter length of $l = 8\,\mathrm{mm}$ at $\lambda = 1.0\,\mathrm{mm}$. The measured extinction for SP0.45-700 is lower than for SP0.45-80, which is attributed to a finite-size effect in the infrared measurements. The large spheres (170 µm, 340 µm, and 700 µm) occupy a substantial fraction of the sample volume in the 1 mm to 2.5 mm-thick disks and thus yield a smaller total number of scattering events. In a real filter with $l \gg 2.5\,\mathrm{mm}$, the number of Mie scattering events would be substantially higher, making SP0.45-700 more efficient than suggested by the thin-disk measurements.

In the passband below 10 GHz ($\lambda > 30\,\mathrm{mm}$), Fig. 6.14(right) shows that the SP0.45-700 mixture has an extinction coefficient of approximately $\mu_{ext} \approx 4 \times 10^{-4}\,\mathrm{mm}^{-1}$ at 10 GHz. For comparison, Eccosorb CR124 has $\mu_{ext} \approx 2 \times 10^{-1}\,\mathrm{mm}^{-1}$ at the same frequency. The sapphire powder is therefore about a factor of 200 more transparent in this low-frequency range. The other filter

[5] The values are taken from the datasheet of the Eccosorb sheet materials MF, because corresponding information on the castable CR materials is not available. The absorption probability is expected to be comparable.

materials exhibit extinction coefficients between those of these two extremes. Eccosorb CR110, for example, shows $\mu_{\mathrm{ext}} \approx 1 \times 10^{-2}\,\mathrm{mm}^{-1}$ at this frequency.

Overall, the proposed filter material is a non-magnetic composite of epoxy resin and sapphire spheres of tailored sizes. It combines high infrared attenuation (stopband) with very low microwave attenuation (passband). Unlike magnetically loaded materials such as Eccosorb, aluminum oxide is magnetically neutral and does not introduce stray fields that could disturb sensitive quantum states. Mie scattering theory provides a useful tool for estimating the extinction length in the regime of strong photon–sphere interaction. The composition is simulated using this theory, and the predictions are tested using infrared absorption measurements and compared to several conventional materials used in low-temperature quantum experiments. Based on these calculations, the filter cutoff frequency can be tuned by changing the maximum particle size and its fraction in the mixture, which allows straightforward adaptation to specific experimental requirements. The experimental results confirm the desired low-pass behavior. It shows stopband attenuation similar to that of Eccosorb CR124 but has a passband transmission about 40 times higher at frequencies below 10 GHz.

No significant change at cryogenic temperatures is expected for the SP material in the infrared range. The strong interaction in Mie scattering depends only weakly on temperature and is governed mainly by changes in refractive index, thermal expansion, and polarizability of the material (on the order of 10 %), visible predominantly around the resonant wavelength near 25 µm [214, 218]. In the microwave regime, however, the response is more temperature-dependent. Thermal contraction and changes in the dielectric constant modify the effective impedance, as seen in the measurements above. Further investigations of the temperature dependence will be carried out using low-temperature infrared transmission measurements in Sec. 6.9. Simulations show a decrease in extinction for SP0.45-700 just below the cutoff, suggesting that increasing the fraction of large spheres in a revised mixture would be beneficial. In the thin samples used for infrared spectroscopy, this effect is not visible because it is masked by the reduced total number of scatterers. In conclusion, sapphire powder filters can be optimized to provide extremely low loss at cryogenic temperatures while offering strong infrared attenuation. This makes them attractive for low-temperature measurements of weak signals in quantum experiments where precision and low noise are essential.

6.9. Infrared properties at millikelvin temperatures

The infrared absorption of the sapphire powder mixture at millikelvin temperatures is studied using the setup introduced in Sec. 5.1. This setup allows comparison of multiple materials in situ in a single cooldown and provides both dark and bright reference measurements. Blackbody radiators serve as broadband infrared sources and cover a frequency range from the sub-terahertz regime up to the mid-infrared. This range is particularly relevant for qubit applications. An indirect detection scheme is used: the qubit energy relaxation rate is measured as a function of incident radiation power, and the resulting change in decay rate is used as a proxy for the flux of pair-breaking photons above the superconducting gap. Measurements of this type are analyzed in detail in Ch. 5.

The materials under test are mounted directly at the dispenser to ensure good thermalization at the cryostat base temperature (15 mK). The transmission of the sapphire powder mixture (SP0.45-80) and of Eccosorb CR124 is investigated. Each is prepared in a cylinder of 2 mm diameter and 8 mm length inside a copper tube. Fig. 6.15 shows the results. The main panel

displays the decay rate Γ_1 as a function of the blackbody radiator power on a logarithmic scale on the x-axis; the inset uses a linear power axis. The top axis gives the corresponding blackbody temperature, which is swept between 0.5 K and 18 K. The different curves correspond to different radiation paths: the open path (orange), the path through an 8 mm stretch of sapphire powder mixture (green), the path through an 8 mm stretch of Eccosorb CR124 (blue), and a fully blocked reference path (gray). The lines provide guides to the eye rather than strict linear fits in power. The right axis shows the QP density extracted from Γ_1 using the method described in the previous chapter.

Both the sapphire powder and Eccosorb CR124 suppress the incoming photon flux by several orders of magnitude. The energy relaxation rate changes only slightly with increasing radiation power. At a blackbody radiator power of 1 nW, corresponding to a blackbody temperature of approximately 8 K, no increase in excess QP is observed for either material. For powers above 10 nW, an increase in QP density becomes visible for the sapphire powder sample. However, the measurement uncertainty in this regime is large, because the background also increases. Comparing the measured decay rates to those for the open radiation path (orange curve) yields an attenuation of the incoming photon flux better than 30 dB for both materials. A more precise estimate is not possible with this setup, since at higher blackbody powers (above roughly 50 nW), stray heating and crosstalk between paths become significant. In addition, the coaxial readout line of the qubit is protected only by an 8 mm infrared filter made of the same sapphire powder mixture, which limits the achievable contrast.

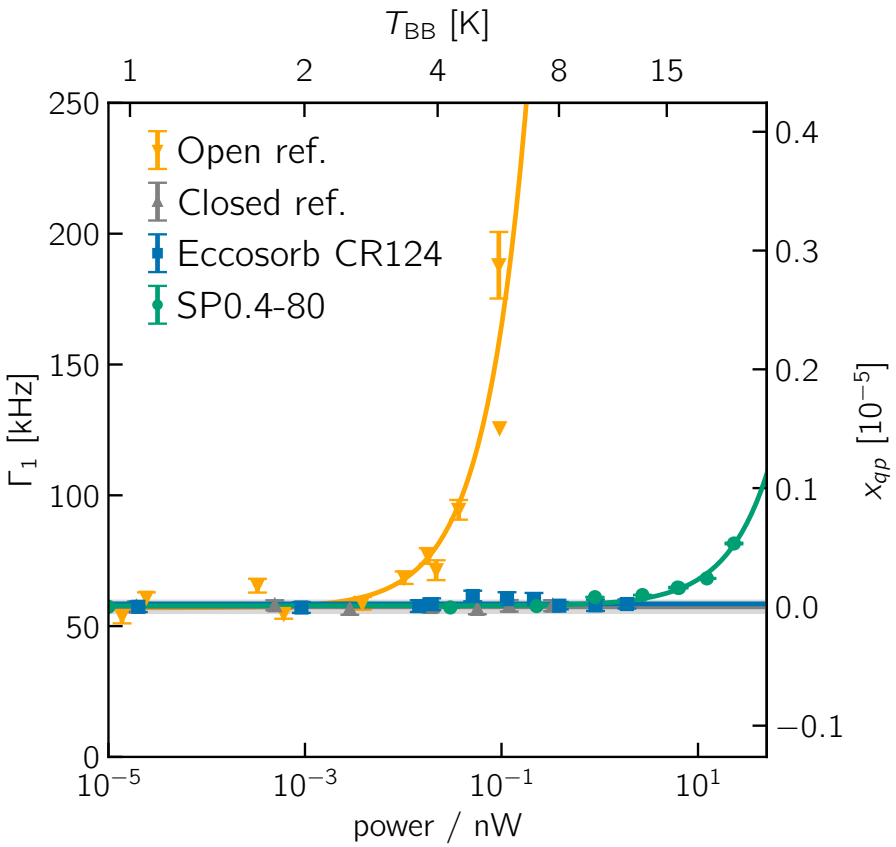

Figure 6.15.: Decay rate Γ_1 of Q60 as a function of incident power along different radiation paths: open path (orange), SP0.45-80 mixture (green), Eccosorb CR124 (blue), and completely blocked reference path (gray).

These measurements demonstrate that the strong infrared attenuation observed at room temperature for these materials (Sec. 6.6) persists at millikelvin temperatures. They also show that such filters provide effective protection of qubits from pair-breaking radiation originating at elevated temperatures and thereby mitigate QP in the qubit. In addition, these measurements probe a part of the stopband that lies outside the range of the spectroscopy measurements. The blackbody experiment probes the region between the cutoff of the waveguide at a wavelength of 2.5 mm and approximately 300 µm for blackbody temperatures of ~ 10 K. This captures the part of the stopband between 1 mm and 2.5 mm that was not resolvable in the spectrometer measurements. The developed sapphire-based filters offer a practical route to lowering QP densities in superconducting qubits by blocking broadband infrared radiation without compromising microwave performance.

7. Conclusion and outlook

The goal of this thesis is to gain insight into quasiparticles (QPs) in superconducting qubits produced by infrared (IR) photons, and to develop and characterize novel infrared filters for mitigating these QPs. To test the influence of infrared photons on qubits, a cryogenic measurement setup is developed that allows probing the qubits with infrared photons in a broad frequency range, starting just above twice the superconducting gap of aluminum at $\sim 87\,\mathrm{GHz} \cdot h$ and extending into the terahertz region.

This setup uses a blackbody radiation source installed in the cryostat, and the blackbody temperature can be controlled between 150 mK and 20 K. From the temperature, the radiated number of photons per second can be estimated, resulting in Planck radiation with a photon number flux reaching up to $1 \times 10^{14}\,\mathrm{s}^{-1}$. This radiation is guided through a circular waveguide into the qubit sample box without significantly heating the cryogenic cold stage or the sample on it. The infrared radiation produces QPs in the superconducting leads of the Josephson junction in the qubit. These QPs can then tunnel through the junction and therefore introduce decoherence or induce shifts in the qubit transition frequency. From measurements of the qubit state population under radiation it is observed that the infrared-induced QPs do not carry enough energy to excite the qubit, meaning they reside very close to the superconducting gap Δ with the QP energy $\varepsilon < \Delta + hf_{01}$. A qubit in the deep transmon regime ($E_J/E_C \approx 200$) is investigated under infrared radiation, and the qubit transition frequency is measured. These measurements are well described by the combination of two theoretical models. First, the transition frequency exhibits a linear, negative shift with the QP density, in agreement with an analytical approximation for the transmon regime mainly brought forward by Catelani et al. [46]. Second, the energy of the infrared photons in this frequency range is low enough that only "cold" QPs are produced that do not have enough energy to cascade through further pair-breaking, resulting in a linear conversion from the incident photon flux to the QP density. This is consistent with the findings on the energy of infrared-induced QPs. Together, these two models result in a linear dependence of the measured frequency shift on the incident photon number flux from the radiator. With the same models, a linear increase in decay rate with the photon number flux is also predicted, which agrees with the measurement of the decay rate while increasing the photon flux.

The model predicts the increase in the pure dephasing rate to be exponentially suppressed compared to the increase in the decay rate [45], which is not found in the measurements. The measured increase in dephasing rate is significant and comparable in magnitude to the increase in the decay rate. This indicates that additional dephasing channels or a more detailed nonequilibrium QP distribution may be relevant beyond the simple quasi-equilibrium assumption used in the theory.

The same measurement is performed for three different qubit samples with different geometry, design, fabrication, and offset-charge sensitivity. Using the theoretical models, the conversion from infrared photon number flux to QP density is found to vary over four orders of magnitude, depending on the qubit architecture, while agreeing well between the two measurement techniques.

The QP conversion time is larger in more offset-charge-sensitive samples, hinting that more charge-sensitive designs effectively provide a smaller absorption of pair-breaking photons. However, the present comparison is not sufficient to distinguish this from other device-specific effects. The infrared photon number flux to QP conversion time, however, is found to overlap well with previous studies using a fixed-frequency laser in the THz regime [51].

In the context of the presented results, it is interesting to investigate other qubit architectures, designs, and fabrication methods under infrared radiation, in order to determine whether one of these factors minimizes the absorption of infrared radiation and therefore the QP density. For example, an investigation of the effect of gap engineering [184] would be possible. This would also test other studies that suggest resonant absorption of radiation due to antenna modes [65, 82, 184, 196]. In the present measurements, no signs of resonant absorption, and thus no clear frequency-dependent absorption signature, are observed in the accessible range between approximately 100 GHz and 1 THz.

To mitigate infrared-induced QPs, this thesis proposes a non-magnetic material compound consisting of epoxy resin and sapphire spheres of tailored sizes to achieve high infrared attenuation (stop band) and minimal attenuation in the microwave range (pass band). The currently predominant filter materials are variants of Eccosorb™, which are very good infrared absorbers but have the disadvantage of a comparatively strong attenuation in the pass band. The sapphire spheres used in the mixture have diameters between 0.45 µm and 700 µm. The fractions of the spheres are chosen to best compensate the scaling of the extinction with effective area. The composition is modeled using Mie scattering theory. This theory is useful for estimating the extinction in the case of strong photon–sphere interaction. This allows prediction of the cutoff frequency between pass band and stop band, and thus the tailoring of the material to specific experimental requirements. The simulation predictions are tested using infrared spectroscopy measurements on the compound and are compared to several conventional materials used in low-temperature quantum applications. The compound shows an extinction exceeding $\mu_{ext} \gtrsim 2\,\mathrm{mm}^{-1}$ up to far-infrared wavelengths. A filter prototype made from the compound is tested at millikelvin temperatures for its microwave absorption, which is found to be $\mu_{ext} \lesssim 4 \times 10^{-4}\,\mathrm{mm}^{-1}$ in the GHz regime. The experimental results confirm the desired low-pass behavior. The prototype exhibits stop band attenuation similar to the Eccosorb CR124 material, but has a pass band transmission that is about 40 times higher at frequencies below 10 GHz. To test the filter performance in the stop band at millikelvin temperatures, the blackbody radiation setup is used. The parallel radiation paths together with the splitter at millikelvin temperature allow the installation of materials in the path to probe their infrared transmission. In contrast to the room-temperature spectroscopy measurement, in this setup the frequency range between 100 GHz and 300 GHz can also be probed. It is found that the sapphire powder mixture also attenuates infrared radiation at millikelvin temperatures over the full stop band. To improve this filter material further, the composition could be adjusted. The simulations suggest that it would be beneficial to increase the fraction of the larger spheres or add even larger spheres.

In summary, this thesis provides new insight into infrared-produced QPs in qubits. In contrast to QPs created by high-energy radiation (for example from cosmic rays [103, 219]), the QPs generated here are close to the gap and can not break further Cooper pairs. The experiments therefore isolate a regime in which infrared photons act primarily as a controllable source of near-gap QPs. Furthermore, the development of tailored infrared filters promises an effective mitigation strategy. Together, these findings contribute to the ongoing effort to diagnose and mitigate QP-induced decoherence in superconducting quantum devices.

Bibliography

[1] P. Krantz, M. Kjaergaard, F. Yan, T. P. Orlando, S. Gustavsson, and W. D. Oliver, »A quantum engineer's guide to superconducting qubits«, Applied Physics Reviews **6**, 021318 (2019) (cit. on pp. 1, 19, 20, 28).

[2] M. Kjaergaard, M. E. Schwartz, J. Braumüller, P. Krantz, J. I.-J. Wang, S. Gustavsson, and W. D. Oliver, »Superconducting Qubits: Current State of Play«, Annual Review of Condensed Matter Physics **11**, 369–395 (2020) (cit. on p. 1).

[3] F. Arute et al., »Quantum supremacy using a programmable superconducting processor«, Nature **574**, 505–510 (2019) (cit. on p. 1).

[4] Y. Wu et al., »Strong Quantum Computational Advantage Using a Superconducting Quantum Processor«, Phys. Rev. Lett. **127**, 180501 (2021) (cit. on p. 1).

[5] Y. Nakamura, Y. A. Pashkin, and J. S. Tsai, »Coherent control of macroscopic quantum states in a single-Cooper-pair box«, Nature **398**, 786–788 (1999) (cit. on pp. 1, 21, 27).

[6] J. E. Mooij, T. P. Orlando, L. Levitov, L. Tian, C. H. van der Wal, and S. Lloyd, »Josephson Persistent-Current Qubit«, Science **285**, 1036–1039 (1999) (cit. on pp. 1, 22).

[7] J. Koch, T. M. Yu, J. Gambetta, A. A. Houck, D. I. Schuster, J. Majer, A. Blais, M. H. Devoret, S. M. Girvin, and R. J. Schoelkopf, »Charge-insensitive qubit design derived from the Cooper pair box«, Phys. Rev. A **76**, 042319 (2007) (cit. on pp. 1, 19, 22–25, 27, 28, 121).

[8] M. Tuokkola, Y. Sunada, H. Kivijärvi, J. Albanese, L. Grönberg, J.-P. Kaikkonen, V. Vesterinen, J. Govenius, and M. Möttönen, »Methods to achieve near-millisecond energy relaxation and dephasing times for a superconducting transmon qubit«, Nat Commun **16**, 5421 (2025) (cit. on pp. 1, 27).

[9] M. P. Bland et al., »Millisecond lifetimes and coherence times in 2D transmon qubits«, Nature **647**, 343–348 (2025) (cit. on pp. 1, 27).

[10] Y. Kim, A. Eddins, S. Anand, K. X. Wei, E. van den Berg, S. Rosenblatt, H. Nayfeh, Y. Wu, M. Zaletel, K. Temme, and A. Kandala, »Evidence for the utility of quantum computing before fault tolerance«, Nature **618**, 500–505 (2023) (cit. on pp. 1, 27).

[11] Google Quantum AI, »Quantum error correction below the surface code threshold«, Nature **638**, `10.1038/s41586-024-08449-y` (2025) (cit. on pp. 1, 2, 27, 124).

[12] M. Xia, C. Zhou, C. Liu, P. Patel, X. Cao, P. Lu, B. Mesits, M. Mucci, D. Gorski, D. Pekker, and M. Hatridge, »Fast superconducting qubit control with subharmonic drives«, Nat Commun, `10.1038/s41467-025-67766-6` (2025) (cit. on p. 1).

[13] Google Quantum AI and Collaborators, »Suppressing quantum errors by scaling a surface code logical qubit«, Nature **614**, 676–681 (2023) (cit. on p. 1).

[14] D. Castelvecchi, »IBM releases first-ever 1,000-qubit quantum chip«, Nature **624**, 238–238 (2023) (cit. on p. 1).

[15] *Fujitsu and RIKEN develop world-leading 256-qubit superconducting quantum computer*, Fujitsu Global, https://www.fujitsu.com/global/about/resources/news/press-releases/2025/0422-01.html (visited on 02/23/2026) (cit. on p. 1).

[16] D. Gao et al., »Establishing a New Benchmark in Quantum Computational Advantage with 105-qubit Zuchongzhi 3.0 Processor«, Phys. Rev. Lett. **134**, 090601 (2025) (cit. on p. 1).

[17] J. M. Gambetta, J. M. Chow, and M. Steffen, »Building logical qubits in a superconducting quantum computing system«, npj Quantum Inf **3**, 2 (2017) (cit. on p. 1).

[18] P. W. Shor, »Scheme for reducing decoherence in quantum computer memory«, Phys. Rev. A **52**, R2493–R2496 (1995) (cit. on p. 1).

[19] A. Yu. Kitaev, »Fault-tolerant quantum computation by anyons«, Annals of Physics **303**, 2–30 (2003) (cit. on p. 1).

[20] B. M. Terhal, »Quantum error correction for quantum memories«, Rev. Mod. Phys. **87**, 307–346 (2015) (cit. on p. 1).

[21] S. Krinner, S. Storz, P. Kurpiers, P. Magnard, J. Heinsoo, R. Keller, J. Lütolf, C. Eichler, and A. Wallraff, »Engineering cryogenic setups for 100-qubit scale superconducting circuit systems«, 29 p. (2019) (cit. on p. 1).

[22] Y. Ye et al., »Logical Magic State Preparation with Fidelity beyond the Distillation Threshold on a Superconducting Quantum Processor«, Phys. Rev. Lett. **131**, 210603 (2023) (cit. on p. 1).

[23] N. Sundaresan, T. J. Yoder, Y. Kim, M. Li, E. H. Chen, G. Harper, T. Thorbeck, A. W. Cross, A. D. Córcoles, and M. Takita, »Demonstrating multi-round subsystem quantum error correction using matching and maximum likelihood decoders«, Nat Commun **14**, 2852 (2023) (cit. on p. 1).

[24] A. G. Fowler, M. Mariantoni, J. M. Martinis, and A. N. Cleland, »Surface codes: Towards practical large-scale quantum computation«, Phys. Rev. A **86**, 032324 (2012) (cit. on p. 1).

[25] N. Lacroix et al., »Scaling and logic in the colour code on a superconducting quantum processor«, Nature **645**, 614–619 (2025) (cit. on p. 1).

[26] J. M. Martinis, K. B. Cooper, R. McDermott, M. Steffen, M. Ansmann, K. D. Osborn, K. Cicak, S. Oh, D. P. Pappas, R. W. Simmonds, and C. C. Yu, »Decoherence in Josephson Qubits from Dielectric Loss«, Phys. Rev. Lett. **95**, 210503 (2005) (cit. on pp. 1, 27).

[27] T. Capelle, E. Flurin, E. Ivanov, J. Palomo, M. Rosticher, S. Chua, T. Briant, P.-F. Cohadon, A. Heidmann, T. Jacqmin, and S. Deléglise, »Probing a Two-Level System Bath via the Frequency Shift of an Off-Resonantly Driven Cavity«, Phys. Rev. Appl. **13**, 034022 (2020) (cit. on p. 1).

[28] J. Lisenfeld, C. Müller, J. H. Cole, P. Bushev, A. Lukashenko, A. Shnirman, and A. V. Ustinov, »Measuring the Temperature Dependence of Individual Two-Level Systems by Direct Coherent Control«, Phys. Rev. Lett. **105**, 230504 (2010) (cit. on p. 1).

[29] J. Lisenfeld, A. Bilmes, A. Megrant, R. Barends, J. Kelly, P. Klimov, G. Weiss, J. M. Martinis, and A. V. Ustinov, »Electric field spectroscopy of material defects in transmon qubits«, npj Quantum Inf **5**, 105 (2019) (cit. on pp. 1, 126).

[30] J. Lisenfeld, A. K. Händel, E. Daum, B. Berlitz, A. Bilmes, and A. V. Ustinov, *Mapping the positions of Two-Level-Systems on the surface of a superconducting transmon qubit*, version 1, (Nov. 7, 2025) http://arxiv.org/abs/2511.05365 (visited on 01/26/2026), pre-published (cit. on pp. 1, 27, 28).

[31] J. Lisenfeld, G. J. Grabovskij, C. Müller, J. H. Cole, G. Weiss, and A. V. Ustinov, »Observation of directly interacting coherent two-level systems in an amorphous material«, Nat Commun **6**, 6182 (2015) (cit. on p. 1).

[32] R. Barends et al., »Coherent Josephson Qubit Suitable for Scalable Quantum Integrated Circuits«, Phys. Rev. Lett. **111**, 080502 (2013) (cit. on p. 1).

[33] J. Burnett, L. Faoro, I. Wisby, V. L. Gurtovoi, A. V. Chernykh, G. M. Mikhailov, V. A. Tulin, R. Shaikhaidarov, V. Antonov, P. J. Meeson, A. Y. Tzalenchuk, and T. Lindström, »Evidence for interacting two-level systems from the 1/f noise of a superconducting resonator«, Nat Commun **5**, 4119 (2014) (cit. on p. 1).

[34] L. Faoro and L. B. Ioffe, »Interacting tunneling model for two-level systems in amorphous materials and its predictions for their dephasing and noise in superconducting microresonators«, Phys. Rev. B **91**, 014201 (2015) (cit. on p. 1).

[35] J. J. Burnett, A. Bengtsson, M. Scigliuzzo, D. Niepce, M. Kudra, P. Delsing, and J. Bylander, »Decoherence benchmarking of superconducting qubits«, npj Quantum Inf **5**, 54 (2019) (cit. on p. 1).

[36] S. Schlör, J. Lisenfeld, C. Müller, A. Bilmes, A. Schneider, D. P. Pappas, A. V. Ustinov, and M. Weides, »Correlating Decoherence in Transmon Qubits: Low Frequency Noise by Single Fluctuators«, Phys. Rev. Lett. **123**, 190502 (2019) (cit. on pp. 1, 50, 51).

[37] M. McEwen et al., »Resolving catastrophic error bursts from cosmic rays in large arrays of superconducting qubits«, Nat. Phys. **18**, 107–111 (2022) (cit. on p. 1).

[38] K. Serniak, M. Hays, G. de Lange, S. Diamond, S. Shankar, L. D. Burkhart, L. Frunzio, M. Houzet, and M. H. Devoret, »Hot Nonequilibrium Quasiparticles in Transmon Qubits«, Phys. Rev. Lett. **121**, 157701 (2018) (cit. on pp. 1, 2, 12, 18, 28).

[39] A. Bespalov, M. Houzet, J. S. Meyer, and Y. V. Nazarov, »Theoretical Model to Explain Excess of Quasiparticles in Superconductors«, Phys. Rev. Lett. **117**, 117002 (2016) (cit. on p. 1).

[40] P. J. de Visser, J. J. A. Baselmans, J. Bueno, N. Llombart, and T. M. Klapwijk, »Fluctuations in the electron system of a superconductor exposed to a photon flux«, Nat Commun **5**, 3130 (2014) (cit. on p. 1).

[41] C. M. Wilson and D. E. Prober, »Quasiparticle number fluctuations in superconductors«, Phys. Rev. B **69**, 094524 (2004) (cit. on p. 1).

[42] J. M. Martinis, M. Ansmann, and J. Aumentado, »Energy Decay in Superconducting Josephson-Junction Qubits from Nonequilibrium Quasiparticle Excitations«, Phys. Rev. Lett. **103**, 097002 (2009) (cit. on p. 1).

[43] J. Gao, J. Zmuidzinas, A. Vayonakis, P. Day, B. Mazin, and H. Leduc, »Equivalence of the Effects on the Complex Conductivity of Superconductor due to Temperature Change and External Pair Breaking«, J Low Temp Phys **151**, 557–563 (2008) (cit. on p. 1).

[44] A. Blais, A. L. Grimsmo, S. M. Girvin, and A. Wallraff, »Circuit quantum electrodynamics«, Rev. Mod. Phys. **93**, 025005 (2021) (cit. on p. 1).

[45] G. Catelani, S. E. Nigg, S. M. Girvin, R. J. Schoelkopf, and L. I. Glazman, »Decoherence of superconducting qubits caused by quasiparticle tunneling«, Phys. Rev. B **86**, 184514 (2012) (cit. on pp. 1, 2, 19, 30, 99, 123).

[46] G. Catelani, R. J. Schoelkopf, M. H. Devoret, and L. I. Glazman, »Relaxation and frequency shifts induced by quasiparticles in superconducting qubits«, Phys. Rev. B **84**, 064517 (2011) (cit. on pp. 1, 2, 11, 17–19, 30–32, 72, 99).

[47] G. Catelani, J. Koch, L. Frunzio, R. J. Schoelkopf, M. H. Devoret, and L. I. Glazman, »Quasiparticle Relaxation of Superconducting Qubits in the Presence of Flux«, Phys. Rev. Lett. **106**, 077002 (2011) (cit. on pp. 1, 16).

[48] L. Glazman and G. Catelani, »Bogoliubov quasiparticles in superconducting qubits«, SciPost Physics Lecture Notes, 031 (2021) (cit. on p. 1).

[49] L. Sun, L. DiCarlo, M. D. Reed, G. Catelani, L. S. Bishop, D. I. Schuster, B. R. Johnson, G. A. Yang, L. Frunzio, L. Glazman, M. H. Devoret, and R. J. Schoelkopf, »Measurements of Quasiparticle Tunneling Dynamics in a Band-Gap-Engineered Transmon Qubit«, Phys. Rev. Lett. **108**, 230509 (2012) (cit. on pp. 1, 2, 124).

[50] C. Wang, Y. Y. Gao, I. M. Pop, U. Vool, C. Axline, T. Brecht, R. W. Heeres, L. Frunzio, M. H. Devoret, G. Catelani, L. I. Glazman, and R. J. Schoelkopf, »Measurement and control of quasiparticle dynamics in a superconducting qubit«, Nat Commun **5**, 5836 (2014) (cit. on pp. 1, 2, 11, 12).

[51] R. Benevides, M. Drimmer, G. Bisson, F. Adinolfi, U. v. Lüpke, H. M. Doeleman, G. Catelani, and Y. Chu, »Quasiparticle Dynamics in a Superconducting Qubit Irradiated by a Localized Infrared Source«, Phys. Rev. Lett. **133**, 060602 (2024) (cit. on pp. 1, 2, 72, 74, 100, 136).

[52] P. Kamenov, T. DiNapoli, M. Gershenson, and S. Chakram, *Suppression of quasiparticle poisoning in transmon qubits by gap engineering*, version 3, (May 13, 2024) `http://arxiv.org/abs/2309.02655` (visited on 02/24/2026), pre-published (cit. on p. 1).

[53] M. McEwen et al., »Resisting High-Energy Impact Events through Gap Engineering in Superconducting Qubit Arrays«, Phys. Rev. Lett. **133**, 240601 (2024) (cit. on pp. 1, 2, 73, 124).

[54] H. Nho, T. Connolly, P. D. Kurilovich, S. Diamond, C. G. L. Bøttcher, L. I. Glazman, and M. H. Devoret, *Recovery dynamics of a gap-engineered transmon after a quasiparticle burst*, (June 11, 2025) `http://arxiv.org/abs/2505.08104` (visited on 08/28/2025), pre-published (cit. on pp. 1, 2, 124).

[55] V. D. Kurilovich et al., *Correlated Error Bursts in a Gap-Engineered Superconducting Qubit Array*, (June 23, 2025) `http://arxiv.org/abs/2506.18228` (visited on 09/08/2025), pre-published (cit. on pp. 1, 2, 124).

[56] R. Barends et al., »Minimizing quasiparticle generation from stray infrared light in superconducting quantum circuits«, Appl. Phys. Lett. **99**, 113507 (2011) (cit. on pp. 1, 2, 12, 77, 78, 124).

[57] E. I. Malevannaya, V. I. Polozov, A. I. Ivanov, A. R. Matanin, N. S. Smirnov, V. V. Echeistov, D. O. Moskalev, D. A. Mikhalin, D. E. Shirokov, Y. V. Panfilov, I. A. Ryzhikov, A. V. Andriyash, and I. A. Rodionov, »An engineering guide to superconducting quantum circuit shielding«, Appl. Phys. Rev. **12**, 031334 (2025) (cit. on pp. 1, 55, 79, 124).

[58] Mini-Circuits, *Eccosorb Filters in Quantum Computing Applications - Mini-Circuits Blog*, (Oct. 8, 2024) https://blog.minicircuits.com/eccosorb-filters-in-quantum-computing-applications/ (visited on 04/02/2025) (cit. on pp. 2, 79).

[59] S. Danilin, J. Barbosa, M. Farage, Z. Zhao, X. Shang, J. Burnett, N. Ridler, C. Li, and M. Weides, »Engineering the microwave to infrared noise photon flux for superconducting quantum systems«, EPJ Quantum Technol **9**, 1 (2022) (cit. on pp. 2, 78, 79).

[60] D. F. Santavicca and D. E. Prober, »Impedance-matched low-pass stripline filters«, Meas. Sci. Technol. **19**, 087001 (2008) (cit. on p. 2).

[61] Laird, *Eccosorb®CRS Datasheet*, (2015) https://www.laird.com/sites/default/files/2021-01/RFP-DS-CRS%2006242020.pdf (visited on 11/09/2024) (cit. on pp. 2, 79, 85).

[62] Laird, *Eccosorb®MF Datasheet, Eccosorb sheet material. MF-XXX is identical to castable Eccosorb CR-XXX. This MF datasheets provides more information on the microwave properites of the material.* (2015) https://www.laird.com/sites/default/files/2021-07/RFP-DS-MF%20061721.pdf (visited on 11/14/2025) (cit. on pp. 2, 95).

[63] A. Anferov, S. P. Harvey, F. Wan, J. Simon, and D. I. Schuster, *Superconducting Qubits Above 20 GHz Operating over 200 mK*, version 2, (Aug. 16, 2024) http://arxiv.org/abs/2402.03031 (visited on 03/13/2025), pre-published (cit. on p. 2).

[64] A. Anferov, F. Wan, S. P. Harvey, J. Simon, and D. I. Schuster, »Millimeter-Wave Superconducting Qubit«, PRX Quantum **6**, 020336 (2025) (cit. on p. 2).

[65] C. H. Liu, D. C. Harrison, S. Patel, C. D. Wilen, O. Rafferty, A. Shearrow, A. Ballard, V. Iaia, J. Ku, B. L. T. Plourde, and R. McDermott, »Quasiparticle Poisoning of Superconducting Qubits from Resonant Absorption of Pair-Breaking Photons«, Phys. Rev. Lett. **132**, 017001 (2024) (cit. on pp. 2, 74, 75, 100).

[66] J. Aumentado, M. W. Keller, J. M. Martinis, and M. H. Devoret, »Nonequilibrium Quasiparticles and 2e Periodicity in Single-Cooper-Pair Transistors«, Phys. Rev. Lett. **92**, 066802 (2004) (cit. on pp. 2, 12).

[67] I. M. Pop, K. Geerlings, G. Catelani, R. J. Schoelkopf, L. I. Glazman, and M. H. Devoret, »Coherent suppression of electromagnetic dissipation due to superconducting quasiparticles«, Nature **508**, 369–372 (2014) (cit. on pp. 2, 12, 22).

[68] U. Vool, I. M. Pop, K. Sliwa, B. Abdo, C. Wang, T. Brecht, Y. Y. Gao, S. Shankar, M. Hatridge, G. Catelani, M. Mirrahimi, L. Frunzio, R. J. Schoelkopf, L. I. Glazman, and M. H. Devoret, »Non-Poissonian Quantum Jumps of a Fluxonium Qubit due to Quasiparticle Excitations«, Phys. Rev. Lett. **113**, 247001 (2014) (cit. on pp. 2, 12).

[69] S. Gustavsson et al., »Suppressing relaxation in superconducting qubits by quasiparticle pumping«, Science **354**, 1573–1577 (2016) (cit. on pp. 2, 12).

[70] L. Grünhaupt, N. Maleeva, S. T. Skacel, M. Calvo, F. Levy-Bertrand, A. V. Ustinov, H. Rotzinger, A. Monfardini, G. Catelani, and I. M. Pop, »Loss Mechanisms and Quasiparticle Dynamics in Superconducting Microwave Resonators Made of Thin-Film Granular Aluminum«, Phys. Rev. Lett. **121**, 117001 (2018) (cit. on pp. 2, 12).

[71] K. Serniak, S. Diamond, M. Hays, V. Fatemi, S. Shankar, L. Frunzio, R. Schoelkopf, and M. Devoret, »Direct Dispersive Monitoring of Charge Parity in Offset-Charge-Sensitive Transmons«, Phys. Rev. Appl. **12**, 014052 (2019) (cit. on pp. 2, 12).

[72] L. Cardani et al., »Reducing the impact of radioactivity on quantum circuits in a deep-underground facility«, Nat Commun **12**, 2733 (2021) (cit. on pp. 2, 16, 78, 124).

[73] D. Ristè, C. C. Bultink, M. J. Tiggelman, R. N. Schouten, K. W. Lehnert, and L. DiCarlo, »Millisecond charge-parity fluctuations and induced decoherence in a superconducting transmon qubit«, Nat Commun **4**, 1913 (2013) (cit. on pp. 2, 28).

[74] S. E. de Graaf, L. Faoro, L. B. Ioffe, S. Mahashabde, J. J. Burnett, T. Lindström, S. E. Kubatkin, A. V. Danilov, and A. Ya. Tzalenchuk, »Two-level systems in superconducting quantum devices due to trapped quasiparticles«, Science Advances **6**, eabc5055 (2020) (cit. on p. 2).

[75] F. Henriques et al., »Phonon traps reduce the quasiparticle density in superconducting circuits«, Appl. Phys. Lett. **115**, 212601 (2019) (cit. on pp. 2, 124).

[76] R.-P. Riwar and G. Catelani, »Efficient quasiparticle traps with low dissipation through gap engineering«, Phys. Rev. B **100**, 144514 (2019) (cit. on pp. 2, 124).

[77] A. Bargerbos, L. J. Splitthoff, M. Pita-Vidal, J. J. Wesdorp, Y. Liu, P. Krogstrup, L. P. Kouwenhoven, C. K. Andersen, and L. Grünhaupt, »Mitigation of Quasiparticle Loss in Superconducting Qubits by Phonon Scattering«, Phys. Rev. Appl. **19**, 024014 (2023) (cit. on pp. 2, 124).

[78] V. Iaia, J. Ku, A. Ballard, C. P. Larson, E. Yelton, C. H. Liu, S. Patel, R. McDermott, and B. L. T. Plourde, »Phonon downconversion to suppress correlated errors in superconducting qubits«, Nat Commun **13**, 6425 (2022) (cit. on pp. 2, 124).

[79] G. Catelani and D. M. Basko, »Non-equilibrium quasiparticles in superconducting circuits: photons vs. phonons«, SciPost Physics **6**, 013 (2019) (cit. on pp. 2, 14, 19).

[80] G. Catelani, »Parity switching and decoherence by quasiparticles in single-junction transmons«, Phys. Rev. B **89**, 094522 (2014) (cit. on pp. 2, 31).

[81] M. Houzet, K. Serniak, G. Catelani, M. H. Devoret, and L. I. Glazman, »Photon-Assisted Charge-Parity Jumps in a Superconducting Qubit«, Phys. Rev. Lett. **123**, 107704 (2019) (cit. on pp. 2, 18, 34, 35, 72).

[82] S. Diamond, V. Fatemi, M. Hays, H. Nho, P. D. Kurilovich, T. Connolly, V. R. Joshi, K. Serniak, L. Frunzio, L. I. Glazman, and M. H. Devoret, »Distinguishing Parity-Switching Mechanisms in a Superconducting Qubit«, PRX Quantum **3**, 040304 (2022) (cit. on pp. 2, 28, 72, 74, 75, 77, 100, 136).

[83] M. Tinkham, *Introduction to superconductivity*, 2nd ed, International Series in Pure and Applied Physics (McGraw Hill, New York, 1996), 454 pp. (cit. on pp. 5, 7, 11, 16, 30).

[84] K. Serniak, »Nonequilibrium Quasiparticles in Superconducting Qubits« (2019) (cit. on pp. 5, 14, 17–19, 24, 29, 34).

[85] H. Kamerlingh Onnes, Commun. Leiden **120b, 122b,124c** (1911) (cit. on p. 5).

[86] W. Meissner and R. Ochsenfeld, »Ein neuer Effekt bei Eintritt der Supraleitfähigkeit«, Naturwissenschaften **21**, 787–788 (1933) (cit. on p. 5).

[87] J. Bardeen, L. N. Cooper, and J. R. Schrieffer, »Microscopic Theory of Superconductivity«, Phys. Rev. **106**, 162–164 (1957) (cit. on p. 5).

[88] V. L. Ginzburg and L. D. Landau, »On the Theory of Superconductivity«, in *On Superconductivity and Superfluidity: A Scientific Autobiography*, edited by V. L. Ginzburg (Springer, Berlin, Heidelberg, 2009), pp. 113–137 (cit. on p. 5).

[89] L. P. Gor'kov, »Microscopic derivation of the Ginzburg–Landau equations in the theory of superconductivity«, Sov. Phys. - JETP (Engl. Transl.); (United States) **9:6** (1958) (cit. on p. 5).

[90] B. D. Josephson, »Possible new effects in superconductive tunnelling«, Physics Letters **1**, 251–253 (1962) (cit. on p. 6).

[91] V. Ambegaokar and A. Baratoff, »Tunneling Between Superconductors«, Phys. Rev. Lett. **10**, 486–489 (1963) (cit. on p. 6).

[92] N. N. Bogoljubov, V. V. Tolmachov, and D. V. Širkov, »A New Method in the Theory of Superconductivity«, Fortschr. Phys. **6**, 605–682 (1958) (cit. on p. 8).

[93] J. G. Valatin, »Comments on the theory of superconductivity«, Nuovo Cim **7**, 843–857 (1958) (cit. on p. 8).

[94] *Aluminum - Atomic Number - Atomic Mass - Density of Aluminum | nuclear-power.com*, Nuclear Power, (Nov. 26, 2021) https://www.nuclear-power.com/aluminum-atomic-number-mass-density/ (visited on 01/20/2026) (cit. on p. 10).

[95] J. N. Ullom, P. A. Fisher, and M. Nahum, »Magnetic field dependence of quasiparticle losses in a superconductor«, Appl. Phys. Lett. **73**, 2494–2496 (1998) (cit. on p. 11).

[96] J. Wenner et al., »Excitation of Superconducting Qubits from Hot Nonequilibrium Quasiparticles«, Phys. Rev. Lett. **110**, 150502 (2013) (cit. on p. 12).

[97] P. B. Fischer and G. Catelani, »Nonequilibrium quasiparticle distribution in superconducting resonators: Effect of pair-breaking photons«, SciPost Phys. **17**, 070 (2024) (cit. on pp. 12, 16).

[98] F. C. Wellstood, C. Urbina, and J. Clarke, »Hot-electron effects in metals«, Phys. Rev. B **49**, 5942–5955 (1994) (cit. on p. 12).

[99] D. V. Nguyen, »Dissipation in a superconducting artificial atom due to a single nonequilibrium quasiparticle«, Phys. Rev. B **96**, 10.1103/PhysRevB.96.214508 (2017) (cit. on p. 14).

[100] S. B. Kaplan, C. C. Chi, D. N. Langenberg, J. J. Chang, S. Jafarey, and D. J. Scalapino, »Quasiparticle and phonon lifetimes in superconductors«, Phys. Rev. B **14**, 4854–4873 (1976) (cit. on p. 14).

[101] A. P. Vepsäläinen, A. H. Karamlou, J. L. Orrell, A. S. Dogra, B. Loer, F. Vasconcelos, D. K. Kim, A. J. Melville, B. M. Niedzielski, J. L. Yoder, S. Gustavsson, J. A. Formaggio, B. A. VanDevender, and W. D. Oliver, »Impact of ionizing radiation on superconducting qubit coherence«, Nature **584**, 551–556 (2020) (cit. on p. 16).

[102] F. D. Dominicis et al., *Evaluating radiation impact on transmon qubits in above and underground facilities*, version 3, (July 3, 2025) http://arxiv.org/abs/2405.18355 (visited on 01/28/2026), pre-published (cit. on pp. 16, 124).

[103] X. Li et al., »Cosmic-ray-induced correlated errors in superconducting qubit array«, Nat Commun **16**, 4677 (2025) (cit. on pp. 16, 100).

[104] R. Anthony-Petersen et al., »A stress-induced source of phonon bursts and quasiparticle poisoning«, Nat Commun **15**, 6444 (2024) (cit. on p. 16).

[105] M. A. Nielsen and I. L. Chuang, *Quantum computation and quantum information*, 10th anniversary edition (Cambridge university press, Cambridge, 2010) (cit. on p. 19).

[106] G. Benenti, G. Casati, and G. Strini, *Principles of quantum computation and information* (World Scientific, Hackensack, N.J, 2004), 2 pp. (cit. on p. 19).

[107] J. M. Martinis and K. Osborne, *Superconducting Qubits and the Physics of Josephson Junctions*, (Feb. 16, 2004) http://arxiv.org/abs/cond-mat/0402415 (visited on 11/29/2025), pre-published (cit. on pp. 19, 126).

[108] R. P. Feynman, »Simulating physics with computers«, Int J Theor Phys **21**, 467–488 (1982) (cit. on p. 19).

[109] BSI, *Entwicklungsstand Quantencomputer*, BSI Project 477 (Bundesamt für Sicherheit in der Informationstechnik, Bonn, 2023), p. 217 (cit. on p. 21).

[110] M. H. Devoret, J. M. Martinis, D. Esteve, and J. Clarke, »Resonant Activation from the Zero-Voltage State of a Current-Biased Josephson Junction«, Phys. Rev. Lett. **53**, 1260–1263 (1984) (cit. on p. 21).

[111] M. H. Devoret, »Quantum Fluctuations in electrical Circuits«, in *Les Houches Session LXIII* (Elsevier Science BV, 1995), pp. 351–386 (cit. on p. 21).

[112] M. H. Devoret, J. M. Martinis, and J. Clarke, »Measurements of Macroscopic Quantum Tunneling out of the Zero-Voltage State of a Current-Biased Josephson Junction«, Phys. Rev. Lett. **55**, 1908–1911 (1985) (cit. on p. 21).

[113] J. Clarke, A. N. Cleland, M. H. Devoret, D. Esteve, and J. M. Martinis, »Quantum Mechanics of a Macroscopic Variable: The Phase Difference of a Josephson Junction«, Science **239**, 992–997 (1988) (cit. on p. 21).

[114] *Nobel Prize in Physics 2025*, NobelPrize.org, `https://www.nobelprize.org/prizes/physics/2025/advanced-information/` (visited on 01/25/2026) (cit. on p. 21).

[115] J. Clarke and A. I. Braginski, eds., *The SQUID handbook* (Wiley-VCH, Weinheim, 2004), 2 pp. (cit. on p. 21).

[116] J. M. Martinis, M. H. Devoret, and J. Clarke, »Energy-Level Quantization in the Zero-Voltage State of a Current-Biased Josephson Junction«, Phys. Rev. Lett. **55**, 1543–1546 (1985) (cit. on p. 21).

[117] J. M. Martinis, »Superconducting phase qubits«, Quantum Inf Process **8**, 81–103 (2009) (cit. on p. 22).

[118] V. E. Manucharyan, J. Koch, L. I. Glazman, and M. H. Devoret, »Fluxonium: Single Cooper-Pair Circuit Free of Charge Offsets«, Science **326**, 113–116 (2009) (cit. on p. 22).

[119] F. Yan, S. Gustavsson, A. Kamal, J. Birenbaum, A. P. Sears, D. Hover, T. J. Gudmundsen, D. Rosenberg, G. Samach, S. Weber, J. L. Yoder, T. P. Orlando, J. Clarke, A. J. Kerman, and W. D. Oliver, »The flux qubit revisited to enhance coherence and reproducibility«, Nat Commun **7**, 12964 (2016) (cit. on pp. 22, 28).

[120] A. F. Kockum and F. Nori, »Quantum Bits with Josephson Junctions«, in *Fundamentals and Frontiers of the Josephson Effect*, edited by F. Tafuri (Springer International Publishing, Cham, 2019), pp. 703–741 (cit. on p. 22).

[121] M. H. Devoret, A. Wallraff, and J. M. Martinis, *Superconducting Qubits: A Short Review*, (Nov. 6, 2004) `http://arxiv.org/abs/cond-mat/0411174` (visited on 08/30/2024), prepublished (cit. on p. 22).

[122] S. M. Girvin, »Circuit QED: superconducting qubits coupled to microwave photons«, in *Quantum Machines: Measurement and Control of Engineered Quantum Systems*, edited by M. Devoret, B. Huard, R. Schoelkopf, and L. F. Cugliandolo, 1st ed. (Oxford University PressOxford, June 12, 2014), pp. 113–256 (cit. on pp. 22, 34).

[123] J. Gambetta, A. Blais, D. I. Schuster, A. Wallraff, L. Frunzio, J. Majer, M. H. Devoret, S. M. Girvin, and R. J. Schoelkopf, »Qubit-photon interactions in a cavity: Measurement-induced dephasing and number splitting«, Phys. Rev. A **74**, 042318 (2006) (cit. on pp. 23, 28).

[124] A. P. Sears, A. Petrenko, G. Catelani, L. Sun, H. Paik, G. Kirchmair, L. Frunzio, L. I. Glazman, S. M. Girvin, and R. J. Schoelkopf, »Photon shot noise dephasing in the strong-dispersive limit of circuit QED«, Phys. Rev. B **86**, 180504 (2012) (cit. on pp. 23, 28).

[125] Z. Wang, S. Shankar, Z. Minev, P. Campagne-Ibarcq, A. Narla, and M. Devoret, »Cavity Attenuators for Superconducting Qubits«, Phys. Rev. Appl. **11**, 014031 (2019) (cit. on pp. 23, 28).

[126] J. M. Chow, L. DiCarlo, J. M. Gambetta, F. Motzoi, L. Frunzio, S. M. Girvin, and R. J. Schoelkopf, »Optimized driving of superconducting artificial atoms for improved single-qubit gates«, Phys. Rev. A **82**, 040305 (2010) (cit. on p. 24).

[127] M. Werninghaus, D. J. Egger, F. Roy, S. Machnes, F. K. Wilhelm, and S. Filipp, »Leakage reduction in fast superconducting qubit gates via optimal control«, npj Quantum Inf **7**, 14 (2021) (cit. on p. 24).

[128] E. Hyyppä, A. Vepsäläinen, M. Papič, C. F. Chan, S. Inel, A. Landra, W. Liu, J. Luus, F. Marxer, C. Ockeloen-Korppi, S. Orbell, B. Tarasinski, and J. Heinsoo, »Reducing Leakage of Single-Qubit Gates for Superconducting Quantum Processors Using Analytical Control Pulse Envelopes«, PRX Quantum **5**, 030353 (2024) (cit. on p. 24).

[129] B. Chiaro and Y. Zhang, »Active Leakage Cancellation in Single Qubit Gates«, Phys. Rev. Lett. **135**, 130601 (2025) (cit. on p. 24).

[130] K. N. Nesterov and I. V. Pechenezhskiy, »Measurement-induced state transitions in dispersive qubit-readout schemes«, Phys. Rev. Appl. **22**, 064038 (2024) (cit. on p. 25).

[131] E. Jaynes and F. Cummings, »Comparison of quantum and semiclassical radiation theories with application to the beam maser«, Proceedings of the IEEE **51**, 89–109 (1963) (cit. on p. 25).

[132] J. Zotova, S. Sanduleanu, G. Fedorov, R. Wang, J. S. Tsai, and O. Astafiev, »Control and readout of a transmon using a compact superconducting resonator«, Appl. Phys. Lett. **124**, 102601 (2024) (cit. on pp. 25, 26, 121).

[133] A. Wallraff, D. I. Schuster, A. Blais, L. Frunzio, R.-S. Huang, J. Majer, S. Kumar, S. M. Girvin, and R. J. Schoelkopf, »Strong coupling of a single photon to a superconducting qubit using circuit quantum electrodynamics«, Nature **431**, 162–167 (2004) (cit. on p. 27).

[134] J. Braumüller, »Quantum simulation experiments with superconducting circuits«, `10.5445/IR/1000080698` (2018) (cit. on p. 27).

[135] A. A. Houck, J. A. Schreier, B. R. Johnson, J. M. Chow, J. Koch, J. M. Gambetta, D. I. Schuster, L. Frunzio, M. H. Devoret, S. M. Girvin, and R. J. Schoelkopf, »Controlling the Spontaneous Emission of a Superconducting Transmon Qubit«, Phys. Rev. Lett. **101**, 080502 (2008) (cit. on pp. 27, 56).

[136] E. Jeffrey et al., »Fast Accurate State Measurement with Superconducting Qubits«, Phys. Rev. Lett. **112**, 190504 (2014) (cit. on p. 27).

[137] E. A. Sete, J. M. Martinis, and A. N. Korotkov, »Quantum theory of a bandpass Purcell filter for qubit readout«, Phys. Rev. A **92**, 012325 (2015) (cit. on p. 27).

[138] P. A. Spring, L. Milanovic, Y. Sunada, S. Wang, A. F. van Loo, S. Tamate, and Y. Nakamura, »Fast Multiplexed Superconducting-Qubit Readout with Intrinsic Purcell Filtering Using a Multiconductor Transmission Line«, PRX Quantum **6**, 020345 (2025) (cit. on p. 27).

[139] P. W. Anderson, B. I. Halperin, and C. M. Varma, »Anomalous low-temperature thermal properties of glasses and spin glasses«, Philosophical Magazine **25**, 1–9 (1972) (cit. on p. 27).

[140] W. A. Phillips, »Tunneling states in amorphous solids«, J Low Temp Phys **7**, 351–360 (1972) (cit. on p. 27).

[141] J. Lisenfeld, C. Müller, J. H. Cole, P. Bushev, A. Lukashenko, A. Shnirman, and A. V. Ustinov, »Rabi spectroscopy of a qubit-fluctuator system«, Phys. Rev. B **81**, 100511 (2010) (cit. on p. 27).

[142] C. Müller, J. H. Cole, and J. Lisenfeld, »Towards understanding two-level-systems in amorphous solids: insights from quantum circuits«, Rep. Prog. Phys. **82**, 124501 (2019) (cit. on p. 27).

[143] K. D. Crowley et al., »Disentangling Losses in Tantalum Superconducting Circuits«, Phys. Rev. X **13**, 041005 (2023) (cit. on p. 27).

[144] D. Wang, Y. Wu, N. Pieczulewski, P. Garg, M. C. C. Pace, C. G. L. Bøttcher, B. Mazumder, D. A. Muller, and H. X. Tang, »All-nitride superconducting qubits based on atomic layer deposition«, Nat. Mater., 1–6 (2026) (cit. on p. 27).

[145] M. Sandberg, M. R. Vissers, J. S. Kline, M. Weides, J. Gao, D. S. Wisbey, and D. P. Pappas, »Etch induced microwave losses in titanium nitride superconducting resonators«, Appl. Phys. Lett. **100**, 262605 (2012) (cit. on pp. 27, 47).

[146] A. Bilmes, A. Megrant, P. Klimov, G. Weiss, J. M. Martinis, A. V. Ustinov, and J. Lisenfeld, »Resolving the positions of defects in superconducting quantum bits«, Sci Rep **10**, 3090 (2020) (cit. on pp. 27, 28).

[147] H. Paik, D. I. Schuster, L. S. Bishop, G. Kirchmair, G. Catelani, A. P. Sears, B. R. Johnson, M. J. Reagor, L. Frunzio, L. I. Glazman, S. M. Girvin, M. H. Devoret, and R. J. Schoelkopf, »Observation of High Coherence in Josephson Junction Qubits Measured in a Three-Dimensional Circuit QED Architecture«, Phys. Rev. Lett. **107**, 240501 (2011) (cit. on p. 27).

[148] M. Bal et al., »Systematic improvements in transmon qubit coherence enabled by niobium surface encapsulation«, npj Quantum Inf **10**, 43 (2024) (cit. on pp. 27, 48, 126).

[149] E. Daum, B. Berlitz, S. Deck, A. V. Ustinov, and J. Lisenfeld, *Investigation of Parasitic Two-Level Systems in Merged-Element Transmon Qubits*, (Sept. 26, 2025) `http://arxiv.org/abs/2509.22593` (visited on 01/26/2026), pre-published (cit. on p. 27).

[150] G. Zhang, Y. Liu, J. J. Raftery, and A. A. Houck, »Suppression of photon shot noise dephasing in a tunable coupling superconducting qubit«, npj Quantum Inf **3**, 1–4 (2017) (cit. on p. 28).

[151] J. Lisenfeld, A. Bilmes, S. Matityahu, S. Zanker, M. Marthaler, M. Schechter, G. Schön, A. Shnirman, G. Weiss, and A. V. Ustinov, »Decoherence spectroscopy with individual two-level tunneling defects«, Sci Rep **6**, 23786 (2016) (cit. on pp. 28, 74, 75).

[152] B. G. Christensen, C. D. Wilen, A. Opremcak, J. Nelson, F. Schlenker, C. H. Zimonick, L. Faoro, L. B. Ioffe, Y. J. Rosen, J. L. DuBois, B. L. T. Plourde, and R. McDermott, »Anomalous charge noise in superconducting qubits«, Phys. Rev. B **100**, 140503 (2019) (cit. on p. 28).

[153] D. M. Tennant, L. A. Martinez, K. M. Beck, S. R. O'Kelley, C. D. Wilen, R. McDermott, J. L. DuBois, and Y. J. Rosen, »Low-Frequency Correlated Charge-Noise Measurements Across Multiple Energy Transitions in a Tantalum Transmon«, PRX Quantum **3**, 030307 (2022) (cit. on p. 29).

[154] C. D. Wilen, S. Abdullah, N. A. Kurinsky, C. Stanford, L. Cardani, G. D'Imperio, C. Tomei, L. Faoro, L. B. Ioffe, C. H. Liu, A. Opremcak, B. G. Christensen, J. L. DuBois, and R. McDermott, »Correlated charge noise and relaxation errors in superconducting qubits«, Nature **594**, 369–373 (2021) (cit. on p. 29).

[155] Y. Asano, *Andreev Reflection in Superconducting Junctions*, SpringerBriefs in Physics (Springer, Singapore, 2021), 132 pp. (cit. on p. 30).

[156] G. Ithier, E. Collin, P. Joyez, P. J. Meeson, D. Vion, D. Esteve, F. Chiarello, A. Shnirman, Y. Makhlin, J. Schriefl, and G. Schön, »Decoherence in a superconducting quantum bit circuit«, Phys. Rev. B **72**, 134519 (2005) (cit. on p. 30).

[157] D. M. Pozar, *Microwave engineering*, 4th ed (Wiley, Hoboken, NJ, 2012), 732 pp. (cit. on pp. 37, 38, 41, 59).

[158] S. Probst, F. B. Song, P. A. Bushev, A. V. Ustinov, and M. Weides, »Efficient and robust analysis of complex scattering data under noise in microwave resonators«, Rev. Sci. Instrum. **86**, 024706 (2015) (cit. on p. 39).

[159] W. Thomson and J. P. Joule, »I. On the thermal effects of fluids in motion«, Proc. R. Soc. Lond. **8**, 41–42 (1857) (cit. on p. 39).

[160] P. W. Atkins, J. De Paula, and J. Keeler, *Atkins' physical chemistry*, Twelfth edition (Oxford University Press, New York, NY, 2023), 927 pp. (cit. on p. 39).

[161] C. Enss and S. Hunklinger, *Low-temperature physics*, Nachdr. (Springer, Berlin, 2009), 573 pp. (cit. on p. 39).

[162] M. M. Wildermuth, »Quantum Tunneling of Josephson Vortices in High-Impedance Long Junctions«, `10.5445/KSP/1000158887` (2023) (cit. on p. 40).

[163] C. Macklin, K. O'Brien, D. Hover, M. E. Schwartz, V. Bolkhovsky, X. Zhang, W. D. Oliver, and I. Siddiqi, »A near–quantum-limited Josephson traveling-wave parametric amplifier«, Science **350**, 307–310 (2015) (cit. on p. 42).

[164] A. Lukashenko and A. V. Ustinov, »Improved powder filters for qubit measurements«, Review of Scientific Instruments **79**, 014701 (2008) (cit. on pp. 42, 79).

[165] R. Gebauer, »A Flexible FPGA-based Control Platform for Superconducting Multi-Qubit Experiments«, PhD thesis (2022) (cit. on p. 46).

[166] R. Gartmann, »Digitally controllable integrated RF electronics for manipulation and readout of qubits«, MA thesis (Karlsruhe Institute of Technology, Karlsruhe, 2019) (cit. on p. 46).

[167] R. Gebauer, N. Karcher, D. Gusenkova, M. Spiecker, L. Grünhaupt, I. Takmakov, P. Winkel, L. Planat, N. Roch, W. Wernsdorfer, A. V. Ustinov, M. Weber, M. Weides, I. M. Pop, and O. Sander, »State preparation of a fluxonium qubit with feedback from a custom FPGA-based platform«, AIP Conf. Proc. **2241**, 020015 (2020) (cit. on p. 46).

[168] R. Gartmann, O. Krömer, R. Weller, N. Karcher, L. E. Ardila-Perez, and O. Sander, »Super Heterodyne Mixer Front-End Module for Qubit Readout and Manipulation«, in 2024 IEEE International Conference on Quantum Computing and Engineering (QCE), Vol. 02 (Sept. 2024), pp. 567–568 (cit. on p. 46).

[169] R. Gartmann, V. Stumpert, L. Scheller, R. Weller, L. E. Ardila-Perez, and O. Sander, »Mixerless RFSoC Microwave Signal Generation for Superconducting Circuit Applications«, in 2024 IEEE International Conference on Quantum Computing and Engineering (QCE), Vol. 02 (Sept. 2024), pp. 565–566 (cit. on p. 46).

[170] qkitgroup, *Qkit*, version 0.5, Karlsruhe, 2025 (cit. on p. 46).

[171] T. H. Group and Q. Koziol, *HDF5-Version 1.12.0*, Lawrence Berkeley National Laboratory (LBNL), Berkeley, CA (United States), 2020 (cit. on p. 46).

[172] A. Schneider, »Quantum Sensing Experiments with Superconducting Qubits«, PhD thesis (Karlsruhe Institute of Technology, Karlsruhe, Jan. 31, 2020) (cit. on p. 47).

[173] M. R. Vissers, J. Gao, J. S. Kline, M. Sandberg, M. P. Weides, D. S. Wisbey, and D. P. Pappas, »Characterization and in-situ monitoring of sub-stoichiometric adjustable superconducting critical temperature titanium nitride growth«, Thin Solid Films **548**, 485–488 (2013) (cit. on p. 47).

[174] J. B. Chang, M. R. Vissers, A. D. Córcoles, M. Sandberg, J. Gao, D. W. Abraham, J. M. Chow, J. M. Gambetta, M. Beth Rothwell, G. A. Keefe, M. Steffen, and D. P. Pappas, »Improved superconducting qubit coherence using titanium nitride«, Appl. Phys. Lett. **103**, 012602 (2013) (cit. on p. 47).

[175] H. Deng et al., »Titanium Nitride Film on Sapphire Substrate with Low Dielectric Loss for Superconducting Qubits«, Phys. Rev. Appl. **19**, 024013 (2023) (cit. on p. 47).

[176] A. Melville, G. Calusine, W. Woods, K. Serniak, E. Golden, B. M. Niedzielski, D. K. Kim, A. Sevi, J. L. Yoder, E. A. Dauler, and W. D. Oliver, »Comparison of dielectric loss in titanium nitride and aluminum superconducting resonators«, Appl. Phys. Lett. **117**, 124004 (2020) (cit. on p. 47).

[177] A. Schneider, J. Braumüller, L. Guo, P. Stehle, H. Rotzinger, M. Marthaler, A. V. Ustinov, and M. Weides, »Local sensing with the multilevel ac Stark effect«, Phys. Rev. A **97**, 062334 (2018) (cit. on p. 47).

[178] A. S. Aasen, A. Di Giovanni, H. Rotzinger, A. V. Ustinov, and M. Gärttner, »Readout error mitigated quantum state tomography tested on superconducting qubits«, Commun Phys **7**, 301 (2024) (cit. on p. 47).

[179] Sonnet Software, Inc, *Sonnet Suites*, Sonnet Software, Inc, 2024 (cit. on p. 49).

[180] C. Müller, J. Lisenfeld, A. Shnirman, and S. Poletto, »Interacting two-level defects as sources of fluctuating high-frequency noise in superconducting circuits«, Phys. Rev. B **92**, 035442 (2015) (cit. on pp. 50, 51).

[181] D. A. Rower, L. Ding, H. Zhang, M. Hays, J. An, P. M. Harrington, I. T. Rosen, J. M. Gertler, T. M. Hazard, B. M. Niedzielski, M. E. Schwartz, S. Gustavsson, K. Serniak, J. A. Grover, and W. D. Oliver, »Suppressing Counter-Rotating Errors for Fast Single-Qubit Gates with Fluxonium«, PRX Quantum **5**, 040342 (2024) (cit. on p. 53).

[182] C. Wang, F.-M. Liu, H. Chen, Y.-F. Du, C. Ying, J.-W. Wang, Y.-H. Huo, C.-Z. Peng, X. Zhu, M.-C. Chen, C.-Y. Lu, and J.-W. Pan, »Longitudinal and Nonlinear Coupling for High-Fidelity Readout of a Superconducting Qubit«, Phys. Rev. Lett. **135**, 060803 (2025) (cit. on p. 53).

[183] F. Marxer et al., *Above 99.9% Fidelity Single-Qubit Gates, Two-Qubit Gates, and Readout in a Single Superconducting Quantum Device*, (Aug. 22, 2025) `http://arxiv.org/abs/2508.16437` (visited on 02/04/2026), pre-published (cit. on p. 53).

[184] X. Pan, Y. Zhou, H. Yuan, L. Nie, W. Wei, L. Zhang, J. Li, S. Liu, Z. H. Jiang, G. Catelani, L. Hu, F. Yan, and D. Yu, »Engineering superconducting qubits to reduce quasiparticles and charge noise«, Nat Commun **13**, 7196 (2022) (cit. on pp. 55, 74, 75, 100).

[185] G. Ponchak, J. Papapolymerou, and M. Tentzeris, »Excitation of coupled slotline mode in finite-ground CPW with unequal ground-plane widths«, IEEE Transactions on Microwave Theory and Techniques **53**, 713–717 (2005) (cit. on p. 56).

[186] qkitgroup, *TIP*, version 2.0.1, Karlsruhe: Karlsruhe Institute of Technology, 2025 (cit. on p. 58).

[187] ennoLogic, *Ultimate-Emissivity-Table*, Emissivity Table for infarared Thermometer Readings, (2018) `https://ennologic.com/wp-content/uploads/2018/07/Ultimate-Emissivity-Table.pdf` (visited on 02/20/2026) (cit. on p. 59).

[188] K. I. GmbH, *Emissivity Table*, Emissivity Table, (2019) `https://www.kleiberinfrared.com/index.php/en/applications/emissivity.html` (visited on 02/20/2026) (cit. on p. 59).

[189] J. Park, D. Kim, H. Kim, J. Lee, and W. Chung, »Thermal Radiative Copper Oxide Layer for Enhancing Heat Dissipation of Metal Surface«, Nanomaterials **11**, 2819 (2021) (cit. on p. 59).

[190] M. M. Hasan, G. Sheets II, M. E. Kordesch, and F. Rahman, »Cupric oxide photonic microcavities and their omnidirectional high-efficiency light-trapping characteristics«, Optical Materials **148**, 114945 (2024) (cit. on p. 59).

[191] C. Enss, ed., *Cryogenic particle detection*, Topics in Applied Physics v. 99 (Springer, Berlin ; New York, 2005), 507 pp. (cit. on pp. 60, 61).

[192] F. P. Incropera and F. P. Incropera, eds., *Fundamentals of heat and mass transfer*, 6th ed (John Wiley, Hoboken, NJ, 2007), 997 pp. (cit. on p. 60).

[193] D. W. Bloom, D. H. Lowndes Jr., and L. Finegold, »Low Temperature Specific Heat of Copper: Comparison of Two Samples of High Purity«, Rev. Sci. Instrum. **41**, 690–695 (1970) (cit. on p. 61).

[194] K. Steinberg, M. Scheffler, and M. Dressel, »Quasiparticle response of superconducting aluminum to electromagnetic radiation«, Phys. Rev. B **77**, 214517 (2008) (cit. on p. 73).

[195] T. Thorbeck, A. Eddins, I. Lauer, D. T. McClure, and M. Carroll, »Two-Level-System Dynamics in a Superconducting Qubit Due to Background Ionizing Radiation«, PRX Quantum **4**, 020356 (2023) (cit. on p. 74).

[196] O. Rafferty, S. Patel, C. H. Liu, S. Abdullah, C. D. Wilen, D. C. Harrison, and R. McDermott, *Spurious Antenna Modes of the Transmon Qubit*, (Apr. 6, 2021) `http://arxiv.org/abs/2103.06803` (visited on 02/14/2026), pre-published (cit. on pp. 74, 75, 100).

[197] M. Griedel, M. Kristen, B. Gasharova, Y.-L. Mathis, A. V. Ustinov, and H. Rotzinger, *Low-loss Material for Infrared Protection of Cryogenic Quantum Applications*, (Jan. 8, 2026) `http://arxiv.org/abs/2601.05147` (visited on 02/17/2026), pre-published (cit. on p. 77).

[198] A. D. Córcoles, J. M. Chow, J. M. Gambetta, C. Rigetti, J. R. Rozen, G. A. Keefe, M. Beth Rothwell, M. B. Ketchen, and M. Steffen, »Protecting superconducting qubits from radiation«, Appl. Phys. Lett. **99**, 181906 (2011) (cit. on p. 78).

[199] R. Rehammar and S. Gasparinetti, »Low-Pass Filter With Ultrawide Stopband for Quantum Computing Applications«, IEEE Transactions on Microwave Theory and Techniques **71**, 3075–3080 (2023) (cit. on p. 78).

[200] L. Andersson, B. Olsson, S. Gasparinetti, and R. Rehammar, *Co-designed reflective and leaky-waveguide low-pass filter for superconducting circuits*, version 1, (Aug. 4, 2025) http://arxiv.org/abs/2508.02475 (visited on 08/28/2025), pre-published (cit. on p. 78).

[201] C. P. Scheller, S. Heizmann, K. Bedner, D. Giss, M. Meschke, D. M. Zumbühl, J. D. Zimmerman, and A. C. Gossard, »Silver-epoxy microwave filters and thermalizers for millikelvin experiments«, Appl. Phys. Lett. **104**, 211106 (2014) (cit. on p. 79).

[202] A. Fukushima, A. Sato, A. Iwasa, Y. Nakamura, T. Komatsuzaki, and Y. Sakamoto, »Attenuation of microwave filters for single-electron tunneling experiments«, IEEE Transactions on Instrumentation and Measurement **46**, 289–293 (1997) (cit. on p. 79).

[203] G. Spahn, N. Kurinsky, S. Lewis, D. Bowring, and M. Hollister, »Epoxy IR Filters for Superconducting Resonators«, J Low Temp Phys **209**, 1032–1037 (2022) (cit. on p. 79).

[204] J. M. Kreikebaum, A. Dove, W. Livingston, E. Kim, and I. Siddiqi, »Optimization of infrared and magnetic shielding of superconducting TiN and Al coplanar microwave resonators«, Supercond. Sci. Technol. **29**, 104002 (2016) (cit. on p. 79).

[205] A. Paquette, J. Griesmar, G. Lavoie, R. Albert, F. Blanchet, A. Grimm, U. Martel, and M. Hofheinz, »Absorptive filters for quantum circuits: Efficient fabrication and cryogenic power handling«, Applied Physics Letters **121**, 124001 (2022) (cit. on p. 79).

[206] G. Mie, »Beiträge zur Optik trüber Medien, speziell kolloidaler Metallösungen«, Annalen der Physik **330**, 377–445 (1908) (cit. on pp. 79, 80).

[207] J. Krupka, K. Derzakowski, A. Abramowicz, M. Tobar, and R. Geyer, »Use of whispering-gallery modes for complex permittivity determinations of ultra-low-loss dielectric materials«, IEEE Transactions on Microwave Theory and Techniques **47**, 752–759 (1999) (cit. on p. 79).

[208] M. Kudra, J. Biznárová, A. Fadavi Roudsari, J. J. Burnett, D. Niepce, S. Gasparinetti, B. Wickman, and P. Delsing, »High quality three-dimensional aluminum microwave cavities«, Appl. Phys. Lett. **117**, 070601 (2020) (cit. on p. 79).

[209] A. Beer, »Bestimmung der Absorption des rothen Lichts in farbigen Flüssigkeiten«, Annalen der Physik und Chemie **86**, 78–88 (1852) (cit. on p. 80).

[210] M. Kerker, »CHAPTER 3 - scattering by a sphere«, in *The scattering of light and other electromagnetic radiation*, Vol. 16, edited by M. I. L. T. O. N. KERKER, Physical Chemistry: A Series of Monographs (Academic Press, 1969), pp. 27–96 (cit. on pp. 80, 140).

[211] UHU, *Plus Endfest 300 Datenblatt*, (2025) https://dosieren.de/media/2d/fc/1b/1631520815/uhu_end_50n_tds_de.pdf (visited on 04/01/2025) (cit. on pp. 80, 85).

[212] C. F. Bohren and D. R. Huffman, »Absorption and Scattering by a Sphere«, in *Absorption and Scattering of Light by Small Particles* (John Wiley & Sons, Ltd, 1998), pp. 82–129 (cit. on pp. 81, 82).

[213] S. Prahl, *Miepython: Pure python calculation of Mie scattering*, version 2.5.5, Zenodo, Dec. 2, 2024 (cit. on p. 83).

[214] M. R. Querry, *Optical Constants*, Technical Report CRDC-CR-85034 (University of Missouri; U.S. Army Chemical Research and Development Center (CRDC), Kansas City, Missouri, June 1985) (cit. on pp. 83, 84, 96, 137).

[215] F. A. Materials, *2MS.001 FINAL Advanced Materials - Alumina Powder*, (July 11, 2024) https://www.final-materials.com/gb/index.php?controller=attachment&id_attachment=115 (cit. on p. 84).

[216] A. Savitzky and M. J. E. Golay, »Smoothing and Differentiation of Data by Simplified Least Squares Procedures.«, Anal. Chem. **36**, 1627–1639 (1964) (cit. on p. 88).

[217] J.-H. Yeh, J. LeFebvre, S. Premaratne, F. C. Wellstood, and B. S. Palmer, »Microwave attenuators for use with quantum devices below 100 mK«, J. Appl. Phys. **121**, 224501 (2017) (cit. on p. 94).

[218] M. Halpern, H. P. Gush, E. Wishnow, and V. D. Cosmo, »Far infrared transmission of dielectrics at cryogenic and room temperatures: glass, Fluorogold, Eccosorb, Stycast, and various plastics«, Appl. Opt., AO **25**, 565–570 (1986) (cit. on pp. 96, 140, 141).

[219] P. M. Harrington et al., »Synchronous detection of cosmic rays and correlated errors in superconducting qubit arrays«, Nat Commun **16**, 6428 (2025) (cit. on p. 100).

[220] M. D. Reed, L. DiCarlo, B. R. Johnson, L. Sun, D. I. Schuster, L. Frunzio, and R. J. Schoelkopf, »High-Fidelity Readout in Circuit Quantum Electrodynamics Using the Jaynes-Cummings Nonlinearity«, Phys. Rev. Lett. **105**, 173601 (2010) (cit. on p. 121).

[221] V. E. Manucharyan, »Superinductance«, PhD thesis (Yale University, Yale, 2012) (cit. on pp. 121, 122).

[222] K. Fujii, *Introduction to the Rotating Wave Approximation (RWA) : Two Coherent Oscillations*, (May 23, 2014) `http://arxiv.org/abs/1301.3585` (visited on 11/30/2025), pre-published (cit. on p. 121).

[223] G. Marchegiani, L. Amico, and G. Catelani, »Quasiparticles in Superconducting Qubits with Asymmetric Junctions«, PRX Quantum **3**, 040338 (2022) (cit. on p. 124).

[224] G. Bratrud et al., »Measurement of correlated charge noise in superconducting qubits at an underground facility«, Nat Commun **16**, 9906 (2025) (cit. on p. 124).

[225] J. Huschle, »Charge Sensitive Superconducting Transmon Qubits for Infrared Radiation Detection«, MA thesis (Karlsruhe Institute of Technology, Karlsruhe, 2025) (cit. on p. 125).

[226] A. Potts, P. R. Routley, G. J. Parker, J. J. Baumberg, and P. A. J. de Groot, »Novel fabrication methods for submicrometer Josephson junction qubits«, Journal of Materials Science: Materials in Electronics **12**, 289–293 (2001) (cit. on p. 125).

[227] F. Lecocq, I. M. Pop, Z. Peng, I. Matei, T. Crozes, T. Fournier, C. Naud, W. Guichard, and O. Buisson, »Junction fabrication by shadow evaporation without a suspended bridge«, Nanotechnology **22**, 315302 (2011) (cit. on p. 125).

[228] F. Habashi, »Niobium, Physical and Chemical Properties«, in *Encyclopedia of Metalloproteins* (Springer, New York, NY, 2013), pp. 1552–1554 (cit. on p. 125).

[229] G. J. Dolan, »Offset masks for lift-off photoprocessing«, Appl. Phys. Lett. **31**, 337–339 (1977) (cit. on p. 126).

[230] G. Jülg, »Development and Characterization of Superconducting Transmon Qubits«, MA thesis (Karlsruhe Institute of Technology, Karlsruhe, 2024) (cit. on p. 126).

[231] A. Bilmes, A. K. Händel, S. Volosheniuk, A. V. Ustinov, and J. Lisenfeld, »In-situ bandaged Josephson junctions for superconducting quantum processors«, Supercond. Sci. Technol. **34**, 125011 (2021) (cit. on p. 126).

[232] A. Perot and C. Fabry, »On the Application of Interference Phenomena to the Solution of Various Problems of Spectroscopy and Metrology«, The Astrophysical Journal **9**, 87 (1899) (cit. on p. 140).

[233] J. E. Chamberlain and H. A. Gebbie, »Dispersion Measurements on Polytetrafluorethylene in the Far Infrared«, Appl. Opt., AO **5**, 393–396 (1966) (cit. on p. 141).

[234] H. R. Carlon, »Refractive Indices of Infrared-Transmitting Substrate Materials Calculated Using Standard Spectrophotometer Transmittance Curves«, Appl. Opt., AO **8**, 1179–1182 (1969) (cit. on p. 141).

[235] N. I. Afanas'eva, E. G. Brame, B. V. Lockshin, and V. A. Yakovlev, »Infra-red spectra and optical constants of polytetrafluoroethylene films«, Polymer **27**, 503–509 (1986) (cit. on p. 141).

List of publications

[1] M. Griedel, M. Kristen, B. Gasharova, Y.-L. Mathis, A. V. Ustinov, and H. Rotzinger, *Low-loss Material for Infrared Protection of Cryogenic Quantum Applications*, (Jan. 8, 2026) http://arxiv.org/abs/2601.05147 (visited on 02/17/2026), pre-published.

[2] M. Griedel, J. Huschle, H. Rotzinger, and A. V. Ustinov, *Infrared Induced Quasiparticles in Superconducting Qubits*, (2026) in preparation.

A. Appendix

A.1. Derivation steps for QP tunneling hamiltonian

Starting at Eq. 2.39 and plugging in the definitions of the Bogoliubon QP creation and anhilation operators one gets:

$$\begin{aligned}\hat{H}_{\mathrm{QP},\hat{\varphi}} = t\sum_{l,r}\Bigg[& e^{i\hat{\varphi}/2}\left(u_r\hat{\gamma}_{r\uparrow}^{\dagger}+v_r\hat{\gamma}_{r\downarrow}\right)\left(u_l\hat{\gamma}_{l\uparrow}+v_l\hat{\gamma}_{l\downarrow}^{\dagger}\right)\\ & - e^{-i\hat{\varphi}/2}\left(u_r\hat{\gamma}_{r\uparrow}^{\dagger}+v_r\hat{\gamma}_{r\downarrow}\right)\left(u_l\hat{\gamma}_{l\uparrow}+v_l\hat{\gamma}_{l\downarrow}^{\dagger}\right)\\ & + e^{i\hat{\varphi}/2}\left(-v_r\hat{\gamma}_{r\uparrow}^{\dagger}+u_r\hat{\gamma}_{r\downarrow}\right)\left(-v_l\hat{\gamma}_{l\uparrow}+u_l\hat{\gamma}_{l\downarrow}^{\dagger}\right)\\ & - e^{-i\hat{\varphi}/2}\left(-v_r\hat{\gamma}_{r\uparrow}^{\dagger}+u_r\hat{\gamma}_{r\downarrow}\right)\left(-v_l\hat{\gamma}_{l\uparrow}+u_l\hat{\gamma}_{l\downarrow}^{\dagger}\right)\Bigg]\end{aligned} \tag{A.1}$$

Where the sum over the spin is written explicitly. It can be assumed again, that the u's and v's are real, since the full phase information is fixed by the qubit phase φ. From their one can multiply out:

$$\begin{aligned}\hat{H}_{QP,\varphi} = \; t\sum_{l,r}\Bigg[& e^{i\hat{\varphi}/2}\Big(u_r u_l\hat{\gamma}_{r\uparrow}^{\dagger}\hat{\gamma}_{l\uparrow}+u_r v_l\hat{\gamma}_{r\uparrow}^{\dagger}\hat{\gamma}_{l\downarrow}^{\dagger}\\ & \qquad + v_r u_l\hat{\gamma}_{r\downarrow}\hat{\gamma}_{l\uparrow}+v_r v_l\hat{\gamma}_{r\downarrow}\hat{\gamma}_{l\downarrow}^{\dagger}\Big)\\ & + e^{-i\hat{\varphi}/2}\Big(-u_r u_l\hat{\gamma}_{r\uparrow}^{\dagger}\hat{\gamma}_{l\uparrow}^{\dagger}-u_r v_l\hat{\gamma}_{r\uparrow}^{\dagger}\hat{\gamma}_{l\downarrow}\\ & \qquad - v_r u_l\hat{\gamma}_{r\downarrow}\hat{\gamma}_{l\uparrow}^{\dagger}-v_r v_l\hat{\gamma}_{r\downarrow}\hat{\gamma}_{l\downarrow}\Big)\\ & + e^{i\hat{\varphi}/2}\Big(-v_r u_l\hat{\gamma}_{r\downarrow}^{\dagger}\hat{\gamma}_{l\uparrow}+v_r v_l\hat{\gamma}_{r\downarrow}^{\dagger}\hat{\gamma}_{l\uparrow}^{\dagger}\\ & \qquad - u_r v_l\hat{\gamma}_{r\uparrow}\hat{\gamma}_{l\downarrow}^{\dagger}+u_r u_l\hat{\gamma}_{r\uparrow}\hat{\gamma}_{l\downarrow}\Big)\\ & + e^{-i\hat{\varphi}/2}\Big(-v_r v_l\hat{\gamma}_{r\downarrow}^{\dagger}\hat{\gamma}_{l\uparrow}+v_r u_l\hat{\gamma}_{r\downarrow}^{\dagger}\hat{\gamma}_{l\uparrow}^{\dagger}\\ & \qquad + u_r v_l\hat{\gamma}_{r\uparrow}\hat{\gamma}_{l\downarrow}-u_r u_l\hat{\gamma}_{r\uparrow}\hat{\gamma}_{l\downarrow}^{\dagger}\Big)\Bigg],\end{aligned} \tag{A.2}$$

And then group together in terms of operator products,

$$\begin{aligned}\hat{H}_{\mathrm{QP},\hat{\varphi}} = t\sum_{l,r}\Bigg[&\left(u_r u_l e^{i\hat{\varphi}/2} - v_r v_l e^{-i\hat{\varphi}/2}\right)\hat{\gamma}^\dagger_{r\uparrow}\hat{\gamma}_{l\uparrow} \\ &+ \left(v_r u_l e^{i\hat{\varphi}/2} - u_r v_l e^{-i\hat{\varphi}/2}\right)\hat{\gamma}^\dagger_{r\downarrow}\hat{\gamma}_{l\uparrow} \\ &+ \left(v_r u_l e^{i\hat{\varphi}/2} - u_r v_l e^{-i\hat{\varphi}/2}\right)\hat{\gamma}^\dagger_{r\uparrow}\hat{\gamma}_{l\downarrow} \\ &+ \left(v_r v_l e^{i\hat{\varphi}/2} - u_r u_l e^{-i\hat{\varphi}/2}\right)\hat{\gamma}^\dagger_{r\downarrow}\hat{\gamma}_{l\downarrow} \\ &- \left(u_r u_l e^{-i\hat{\varphi}/2} - v_r v_l e^{i\hat{\varphi}/2}\right)\hat{\gamma}^\dagger_{r\uparrow}\hat{\gamma}^\dagger_{l\downarrow} \\ &- \left(v_r u_l e^{-i\hat{\varphi}/2} - u_r v_l e^{i\hat{\varphi}/2}\right)\hat{\gamma}^\dagger_{r\downarrow}\hat{\gamma}^\dagger_{l\downarrow} \\ &- \left(v_r u_l e^{-i\hat{\varphi}/2} - u_r v_l e^{i\hat{\varphi}/2}\right)\hat{\gamma}^\dagger_{r\uparrow}\hat{\gamma}^\dagger_{l\uparrow} \\ &- \left(v_r v_l e^{-i\hat{\varphi}/2} - u_r u_l e^{i\hat{\varphi}/2}\right)\hat{\gamma}^\dagger_{r\downarrow}\hat{\gamma}^\dagger_{l\uparrow}\Bigg].\end{aligned} \tag{A.3}$$

Now, it can be summed over the spins again, arriving at

$$\begin{aligned}\hat{H}_{\mathrm{QP},\hat{\varphi}} = t\sum_{l,r,s}\Big[&\left(u_r u_l e^{i\hat{\varphi}/2} - v_r v_l e^{-i\hat{\varphi}/2}\right)\hat{\gamma}^\dagger_{rs}\hat{\gamma}_{ls} \\ &+ \left(u_r v_l e^{i\hat{\varphi}/2} + v_r u_l e^{-i\hat{\varphi}/2}\right)\hat{\gamma}^\dagger_{rs}\hat{\gamma}^\dagger_{l\bar{s}}\Big] + \mathrm{H.c.}\end{aligned} \tag{A.4}$$

where $\bar{s}$ denotes the oposite spin of s. By converting the complex exonents into sin and cos, one arrives at Eq. 2.40.

A.2. Dispersive readout

In the standard Jaynes–Cummings approach, the qubit is treated as an effective two-level system (spin). Following the derivations of Koch *et al.* (2007) [7], Reed *et al.* (2010) [220], and Zotova *et al.* (2024) [132], the dispersive shifts can be calculated by treating the coupling term perturbatively. Consider combined qubit–resonator states $|\alpha, i\rangle$, where α labels qubit eigenstates, in this section denoted as *g,e,f,...*, and i denotes the photon number in the resonator $(0, 1, 2, \dots)$. States with a fixed photon number in the resonator have energies $E_{\alpha,i} = E_\alpha + ih\omega_r$. Interaction-induced shifts of the energy level $E_{\alpha,i}$ by $\delta E_{\alpha,i}$ are given by second-order perturbation theory [221]:

$$\delta E_{\alpha,i} = g^2 \sum_{\beta\neq\alpha} \frac{i\,|n_{\alpha\beta}|^2}{E_\alpha - E_\beta + h\omega_r} + g^2 \sum_{\beta\neq\alpha} \frac{(i+1)\,|n_{\alpha\beta}|^2}{E_\alpha - E_\beta - h\omega_r}. \tag{A.5}$$

Each term represents an energy shift due to level repulsion from a state $|\beta, j\rangle$. Only nearest-neighbor photon transitions contribute, due to $\hat{a}|i\rangle = \sqrt{i}\,|i-1\rangle$. Fig. A.1 illustrates this for the example states $|g, i\rangle$ and $|f, i\rangle$; the thin lines show the interactions (terms in the sum in Eq. A.5), connecting levels that contribute to the shift of the level. The strength of the interaction depends on the distance of the two levels, through the energy scale in the denominator in Eq. A.5.

The dispersive shift of the resonator for a qubit state α is defined as $\chi_\alpha = (E_{\alpha,i+1} - E_{\alpha,i})/h$. Applying a rotating-wave approximation [222], which neglects rapidly oscillating terms in the interaction Hamiltonian and is valid near resonance and for weak coupling, yields a dispersive shift that is independent of the cavity photon number i to second order in the coupling strength g:

$$\chi_\alpha = g^2 \sum_{\beta\neq\alpha} |n_{\alpha\beta}|^2 \frac{2\omega_{\alpha\beta}}{\omega_{\alpha\beta}^2 - \omega_r^2}, \tag{A.6}$$

where $\omega_{\alpha\beta} = (E_\alpha - E_\beta)/h$. Each term in the sum corresponds to a virtual transition in the atomic spectrum (Fig. A.1). This expression is valid as long as $\chi_\alpha/g \ll 1$ and away from the pole at $|\omega_{\alpha\beta}| = \omega_r$. This breakdown at the pole corresponds to a vacuum Rabi resonance between the qubit transition $\alpha \leftrightarrow \beta$ and the readout mode at ω_r, with Rabi frequency $\Omega_{\alpha\beta} = 2g|n_{\alpha\beta}|$.

So far, the expression is general for any artificial atom coupled to a resonator. For the special case of a transmon, treated as a weakly anharmonic oscillator with $n_{12} = \sqrt{2}\,n_{01}$ and other matrix elements set to zero, and with anharmonicity $\alpha = \omega_{21} - \omega_{01} \ll \omega_{01}$, the two dispersive shifts become

$$\chi_g = g^2|n_{01}|^2 \frac{2\omega_{01}}{\omega_{01}^2 - \omega_r^2}, \tag{A.7}$$

$$\chi_e = g^2|n_{01}|^2 \left(\frac{-2\omega_{01}}{\omega_{01}^2 - \omega_r^2} + \frac{4\omega_{21}}{\omega_{21}^2 - \omega_r^2} \right). \tag{A.8}$$

A detailed derivation can be found in Ref. [132].

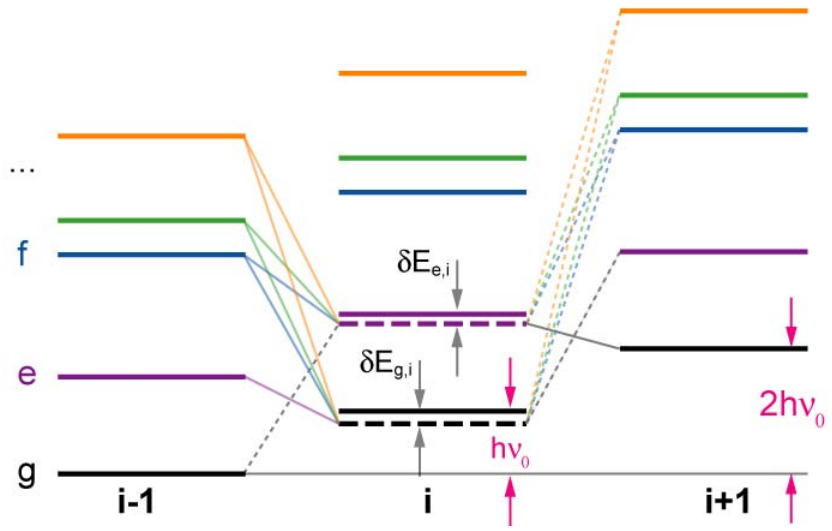

Figure A.1.: Level repulsion due to a dispersive shift of an arbitrary spectrum by the resonator. The full diagram shows a cutout of possible states of the hybridized resonator–qubit system, which is vertically stretched to group the levels by their quanta in the resonator. The levels of the spectrum are labeled $g,e,f,\ldots$; the levels of the resonator are labeled $i-1,i,i+1$. This illustrates Eq. A.5, where the levels are grouped by their number of quanta in the resonator. The thin lines indicate *repulsion forces*; due to selection rules, only levels from neighboring spectra (the groups of quanta in the resonator) can repel each other. Each line corresponds to a term in the sum in Eq. A.5, and the dashed lines represent the weaker interaction due to the energy scaling in the denominator of Eq. A.5. Adapted from Ref. [221].

A.3. Derivation of QP effects on T_ϕ

Sec. 3.1 introduced the density matrix (Eq. 3.6), where the off-diagonal elements ρ^+ encode the dephasing time. The master equation for the off-diagonal part of the density matrix is

$$\frac{d\rho^+}{dt} = i(\omega_{01} + \delta\omega)\rho^+ - \frac{1}{2T_1}\rho^+ - \Gamma_\phi\rho^+, \tag{A.9}$$

with the solution (cf. Sec. 3.1)

$$\rho_+(t) = \rho_+(0)\, e^{i(\omega_{01}+\delta\omega)t} e^{-t(\Gamma_\phi + 1/2T_1)}. \tag{A.10}$$

The total dephasing rate thus has three contributions: the energy relaxation via $1/(2T_1)$, the pure dephasing rate Γ_ϕ, and a possible contribution through fluctuations of the transition frequency $\delta\omega$. QPs contribute to all three parts. The contributions to the energy relaxation and the transition frequency were discussed above; the following derives how QPs contribute to the pure dephasing rate.

Starting from the master equation for the density matrix, one can derive an expression for the dephasing rate. Follwoing Catelani et al. [45], the resulting pure dephasing rate is given by the sum of two contributions:

$$\Gamma_\phi = \Gamma_\phi^c + \Gamma_\phi^s, \tag{A.11}$$

$$\Gamma_\phi^c = \frac{32E_J}{\pi}\left|A_c\right|^2 \int_0^{+\infty} \mathrm{d}x\; f\left[(1+x)\Delta\right]\left\{1 - f\left[(1+x)\Delta\right]\right\}, \tag{A.12}$$

$$\Gamma_\phi^s = \frac{32E_J}{\pi}\left|A_s\right|^2 f_0(1-f_0)\ln\frac{4\delta E}{\Gamma_\phi}, \tag{A.13}$$

where $|A_k|^2$ are matrix elements and $f(\varepsilon)$ is the QP distribution function with f_0 the typical occupation probability at energy δE. The larger of the two contributions (Eq. A.12 and Eq. A.13) sets the relevant dephasing rate. The dominance of one term over the other primarily depends on the matrix elements $|A_s|^2$ and $|A_c|^2$, which are given by

$$A_s = \frac{1}{2}\left(\langle 1|\sin\frac{\hat\varphi}{2}|1\rangle - \langle 0|\sin\frac{\hat\varphi}{2}|0\rangle\right), \tag{A.14}$$

$$A_c = \frac{1}{2}\left(\langle 1|\cos\frac{\hat\varphi}{2}|1\rangle - \langle 0|\cos\frac{\hat\varphi}{2}|0\rangle\right). \tag{A.15}$$

In the second term Γ_ϕ^s (Eq. A.13), the divergence of the spectral density at zero frequency is removed by introducing a broadening set by the decay rate. It is assumed that the dephasing rate is small compared to the characteristic energy scale δE of the QPs, $h\Gamma_\phi \ll \delta E$, such that terms of order $\Gamma_\phi/\delta E$ can be neglected. Note also that Eq. A.13 is a self-consistent equation, which can be solved iteratively to

$$\Gamma_\phi^s \approx \frac{32E_J}{\pi}\left|A_s\right|^2 f_0(1-f_0)\ln\frac{\pi\delta E}{8E_J\left|A_s\right|^2 f_0(1-f_0)}. \tag{A.16}$$

From here it is continued in the main text in Sec. 3.3.

A.4. Mitigating quasiparticle effects

Over the past years, considerable effort has been devoted to mitigating QP-induced decoherence in superconducting qubits. Different strategies have been pursued, either to suppress the formation of QPs in the first place or to reduce the rate of QP tunneling through the junction.

Quasiparticle traps

In this approach, QPs are kept away from the junction by trapping them in regions of lower gap, at vortex cores, or in normal-metal islands. This strategy has been investigated experimentally and theoretically, with mixed results [49, 75–78].

Gap engineering

Significant progress toward mitigating tunneling events has been made in recent years by *gap engineering* [11, 53–55]. Here, the superconducting energy gaps of the junction leads are modified to create a gap difference $\delta\Delta = \Delta_l - \Delta_r$. Most QPs have energies close to the gap; therefore, they cannot overcome a sufficiently large gap difference, which suppresses tunneling and thus the dominant mechanism limiting qubit coherence.

This gap engineering can be implemented by using different superconductors or different film thicknesses, since the energy gap of thin films depends on the thickness [223]. Importantly, the energy gap of at least one junction lead must be the largest gap in the entire qubit. If, for example, a capacitor pad is made from a higher-gap material than the junction leads, QPs originating in the high-gap material will still be able to tunnel through the junction.

Limiting the production of QPs

Another approach is to limit QP production itself. This is achieved by cooling the qubit chips to temperatures far below the critical temperature of the superconductors used, taking advantage of the exponential suppression of thermal QPs, and by operating in deep underground laboratories to mitigate high-energy impacts [72, 102, 224].

However, lower-energy photons, such as blackbody radiation from higher temperature stages in the cryostat or from room temperature, can also generate QPs. Therefore, effective shielding of the qubit is necessary [56, 57]. A particular challenge is the readout line, which will be investigated in detail in Ch. 6.

In practice, state-of-the-art devices typically combine several of these strategies to suppress QP-induced decoherence effectively.

A.5. Fabrication

A.5.1. OCS transmon Q27

The sample is fabricated in the cleanroom facility as one of 52 chips on a two-inch wafer. Jonathan Huschle performed major tasks of the fabrication during his master thesis [225], in close collaboration with the author. The individual fabrication steps are depicted in Fig. A.2(a) and outlined in the following.

For this sample the Manhattan[1] junction-fabrication technique [226] is used, first employed in superconducting qubits by Martinis' group at UCSB [227], creates a Josephson junction at the overlap of two perpendicular aluminum fingers evaporated at an angle into perpendicular resist trenches. The shadow geometry created by the resist prevents aluminum from being evaporated onto the perpendicular finger. Overhanging resist structures prevent aluminum deposition on the sidewall of the resist. Between the two evaporations, a barrier is formed by oxidation of the first finger. The entire process occurs *in situ* without breaking vacuum, yielding clean oxide barriers.

As a first step, the native oxide of the silicon wafer is removed in a hydrofluoric acid (HF) dip. The OCS transmon sample in the gigahertz regime requires sub-µm Josephson junctions. Therefore, electron-beam (e-beam) lithography is used to define and pattern a suitable resist mask. In order to ensure proper lift-off after deposition, the resist mask consists of an MMA/PMMA[2] stack. The higher sensitivity to e-beam exposure of the MMA leads to an undercut in the resist stack, which avoids sidewall material deposition. The resist is developed in a 1:3 mixture of water and isopropanol at a temperature of 6 °C for two minutes. The two different resist layers are used due to their different sensitivity to the electron beam; the bottom layer has a higher sensitivity to the electron beam, such that a moderate dose structures only the bottom resist, allowing an undercut to form. This undercut later prevents material from being evaporated onto the sidewalls during evaporation.

The deposition of the aluminum fingers is carried out in a Plassys™ MEB 550 S evaporation chamber. The fingers have thicknesses of 40 nm and 60 nm, respectively. The oxidation is performed at 5.5 mbar for 15 min. The junction is oxidized again after deposition in the process chamber to allow controlled oxide growth on the thin film surfaces. The resist is lifted off in DMSO[3] at 90 °C for multiple hours, followed by an ultrasonic bath.

Optical lithography is used for the larger structures such as the capacitor pads, transmission line, and resonators. For this, an approximately 1800 nm thick S1818 resist is applied on the wafer and is exposed with a 660 W UV lamp for 50 s. The resist is developed in a 3:2 mixture of AZ developer and water for 65 s. For evaporation, the wafer is again placed into the Plassys™ shadow evaporator.

First, an argon milling cleaning step is employed to remove the oxide at the contact between the junction leads and the capacitor pads. The process temperature of electron-beam-evaporated niobium is large compared to the widely used aluminum because of its melting point of 2500 °C [228]. In order to improve the thermalization of the resist, a 15 nm thick aluminum film is deposited prior to the niobium deposition (100 nm). A 8 nm thick aluminum film is used as capping layer

[1] The resist forms an orthogonal structure akin to Manhattan's high-rise buildings and intersecting streets.
[2] 600 nm MMA EL13 and 400 nm PMMA A4 950K.
[3] Dimethyl sulfoxide.

for the niobium because of the lower loss tangent of aluminum oxide compared to niobium oxides [148]. The resist is lifted off in DMSO, following the same procedure as for the e-beam resist. A protective S1818 resist layer is spun on the sample before the wafer is metallized on the backside with a 100 nm niobium layer, passivated with a thin silver capping layer. The wafer is divided into 52 chips of 5 mm × 5 mm, the protective resist is stripped in a DMSO bath, and the chips are cleaned using TechniClean™, acetone, and isopropanol. As a last step, the individual chips are cleaned in an O_2 plasma cleaner.

A.5.2. Intermediate transmon sample Q60

For the sample in the intermediate transmon regime, with $E_J/E_C \approx 70$, the *Dolan bridge* technique is used, developed by G. J. Dolan in 1977 [229]. The Dolan bridge technique relies on a double-layer resist stack to create a suspended sub-µm-scale bridge that functions as a shadow mask. This geometry is used with different angles during the e-beam evaporation to form the Josephson junction under the bridge. For this sample again a *Josephson-junction-first* process is chosen. However, the larger optically defined niobium structures such as pads and resonators are patterned with a dry etching process. The fabrication was performed in collaboration with Gabriel Jülg during his master thesis [230]. The double resist stack for the shadow mask consists of MMA/PMMA. The larger sensitivity to e-beam exposure of the MMA resist is used to form a PMMA resist bridge with the desired junction dimensions.

The two aluminum fingers with a thickness of 50 nm each are evaporated in the Plassys™ shadow evaporator. The junction leads end in large structures that later form a stray junction to the capacitor pad. This junction is very large and can therefore be ignored in the qubit system [107].[4] The resist is lifted off in DMSO and the sample is cleaned in an ultrasonic bath.

The chip is mounted in the Plassys™ e-beam evaporator, and an argon milling step at 400 V for 4 min is performed, to remove some of the aluminum oxide on the fingers but not damage the junction. A 100 nm layer of niobium is evaporated onto the chip, with capping of 8 nm aluminum to prevent niobium oxidation. The aluminum is oxidized in the evaporation tool. The optical lithography with S1805 resist is followed by an inductively coupled plasma (ICP) process where mainly the aluminum is etched by a dry Ar/Cl_2 plasma. The wafer is subsequently cleaned from the resist and the aluminum layer is used as a hard mask for the second dry etching step in a reactive ion etch (RIE) tool. The used Ar/SF_6 mixture etches niobium effectively, while aluminum shows very low etch activity, allowing for this selective process. However, the silicon substrate underneath is etched, reducing the dielectric material surrounding the junction.

All fabrication parameters can be found, together with similar samples and processes, in the thesis of G. Jülg [230].

[4] It has been found that these stray junctions host a large number of TLS [29]. Therefore, they are typically avoided by a bandaging step (a milling step followed by an evaporation at a different angle), where the junction is protected by the bridge [231]. This was not easily possible here due to the JJF approach. An argon milling step is performed before contacting the leads; if this is strong enough, the whole oxide should be removed, but strong milling damages the junction, which is not protected in this approach. Therefore, a large stray junction is chosen to avoid the necessity of very strong milling.

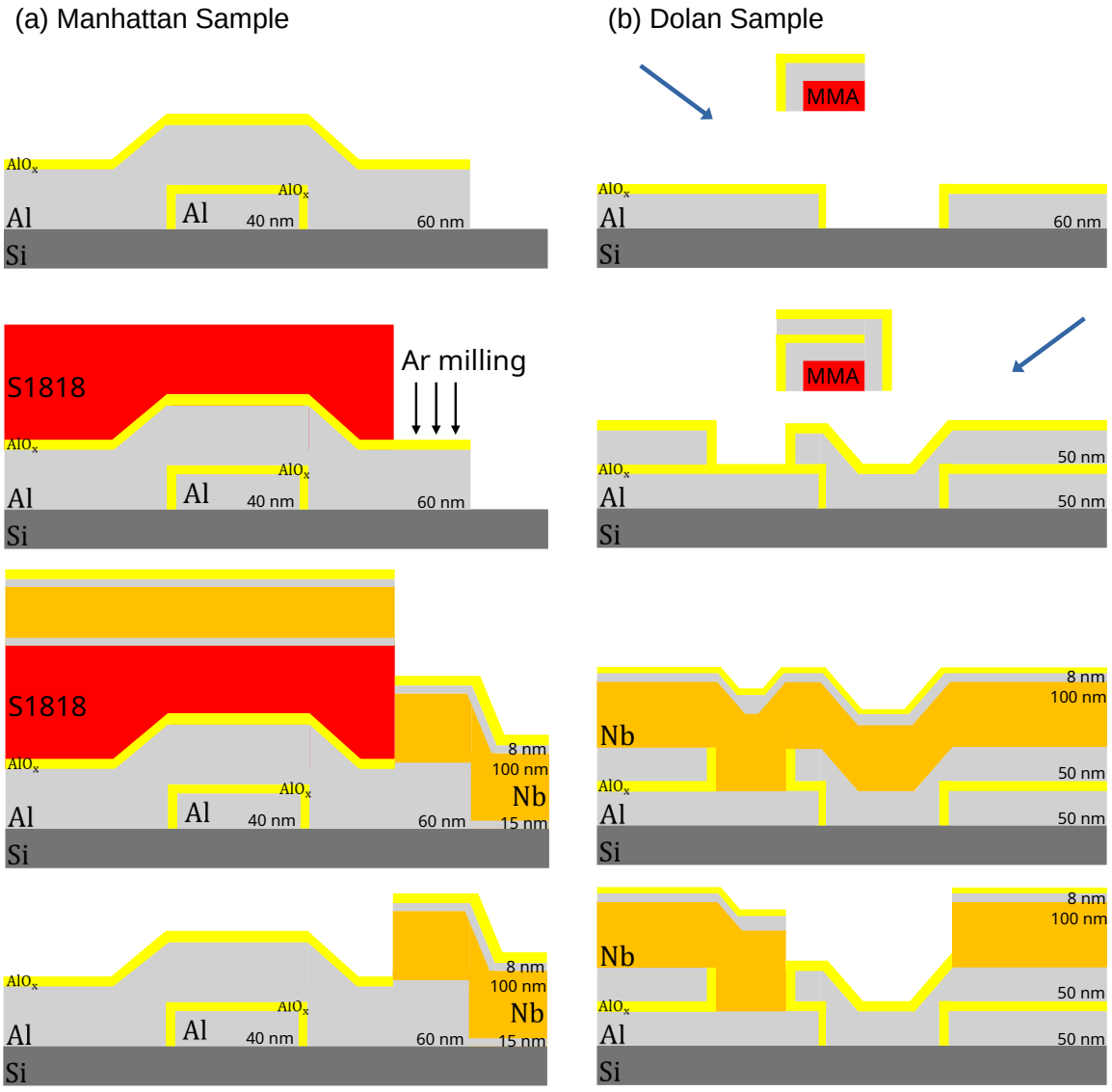

Figure A.2.: Illustration of the core fabrication steps. (a) For the Manhattan sample: the two junction leads are evaporated from two angles into resist trenches with an oxidation step in between, resulting in frame 1. A resist is applied and the oxide is removed by argon milling (frame 2). A trilayer of aluminum, niobium, and aluminum is then evaporated (frame 3). In the last step, the resist is lifted off (frame 4). (b) For the Dolan sample: in the first two frames, the evaporation of the junction leads from the two angles is shown (frames 1–2). The resist is lifted off and the oxide is removed with an argon milling step (not shown). Then niobium with a thin aluminum capping layer is evaporated (frame 3). The structures for capacitances and resonators are then etched (frame 4).

A.6. Linear correlation fits of the heaters

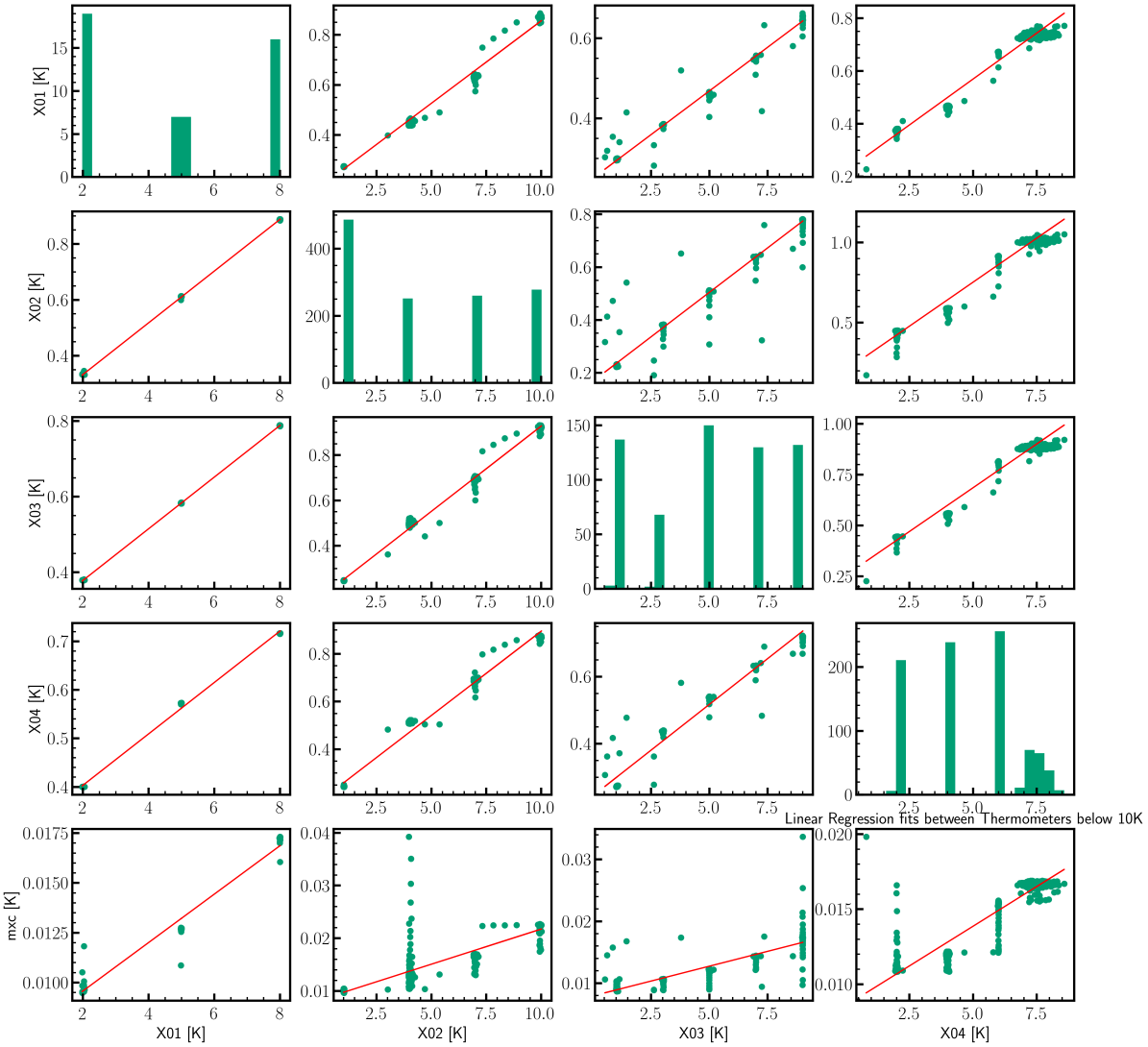

Figure A.3.: Without propper shielding: Linear fits to optain correlation between the different heaters. Used to optain Fig. 5.5.

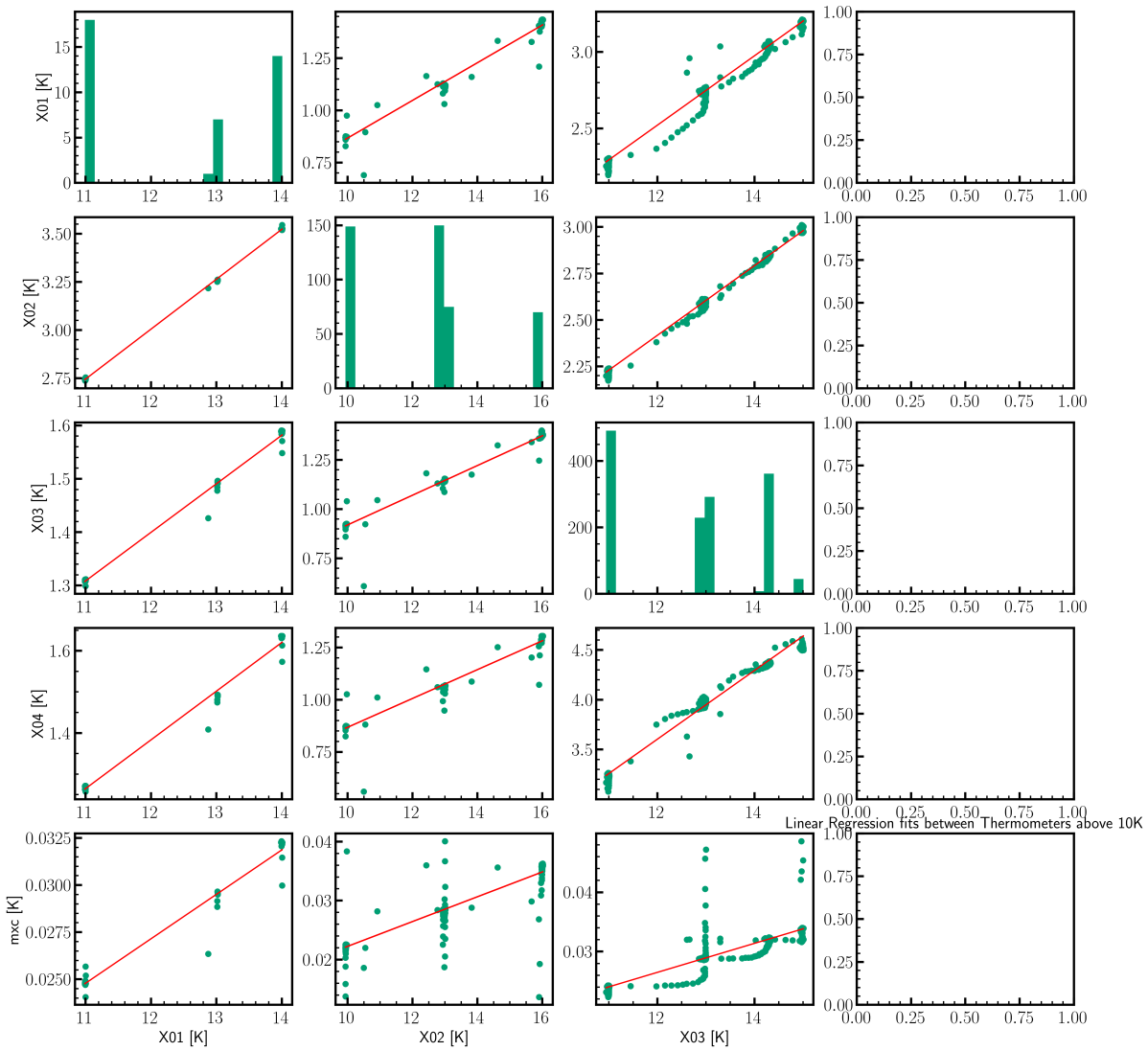

Figure A.4.: With propper shielding: Linear fits to optain correlation between the different heaters. Used to optain Fig. 5.5.

A.7. Further measurements and aquired data in the infrared setup

A.7.1. Γ_1 background measurements

Fig. A.5 illustrates the importance of proper shielding of the radiators. It shows the increase in qubit energy-relaxation rate Γ_1 with increasing blackbody temperature for an early iteration of the setup which was used for the measurements of the Q200 sample. Even with the direct radiation path blocked, a significant increase in Γ_1 is observed. This effect is attributed to crosstalk between radiators due to stray radiation and heating. In comparison for the improved shielding no increase is observed. This improved shielding is used for measurements on sample Q60 and Q27.

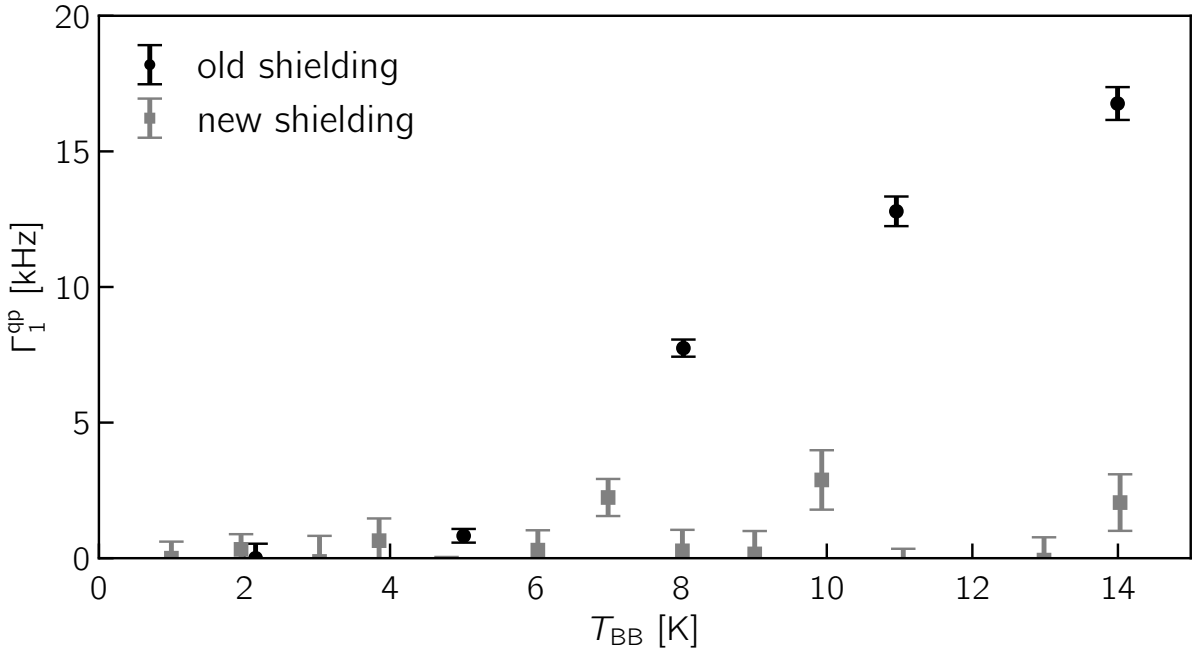

Figure A.5.: Induced qubit energy-relaxation rate $\Gamma_1^{qp} = \Gamma_1(T) - \Gamma_1(T_0)$ measured in an early setup iteration without proper shielding (black) and with the shielding (gray), as a function of increasing radiation temperature.

A.7.2. Histograms data for Q27 at different blackbody temperatures

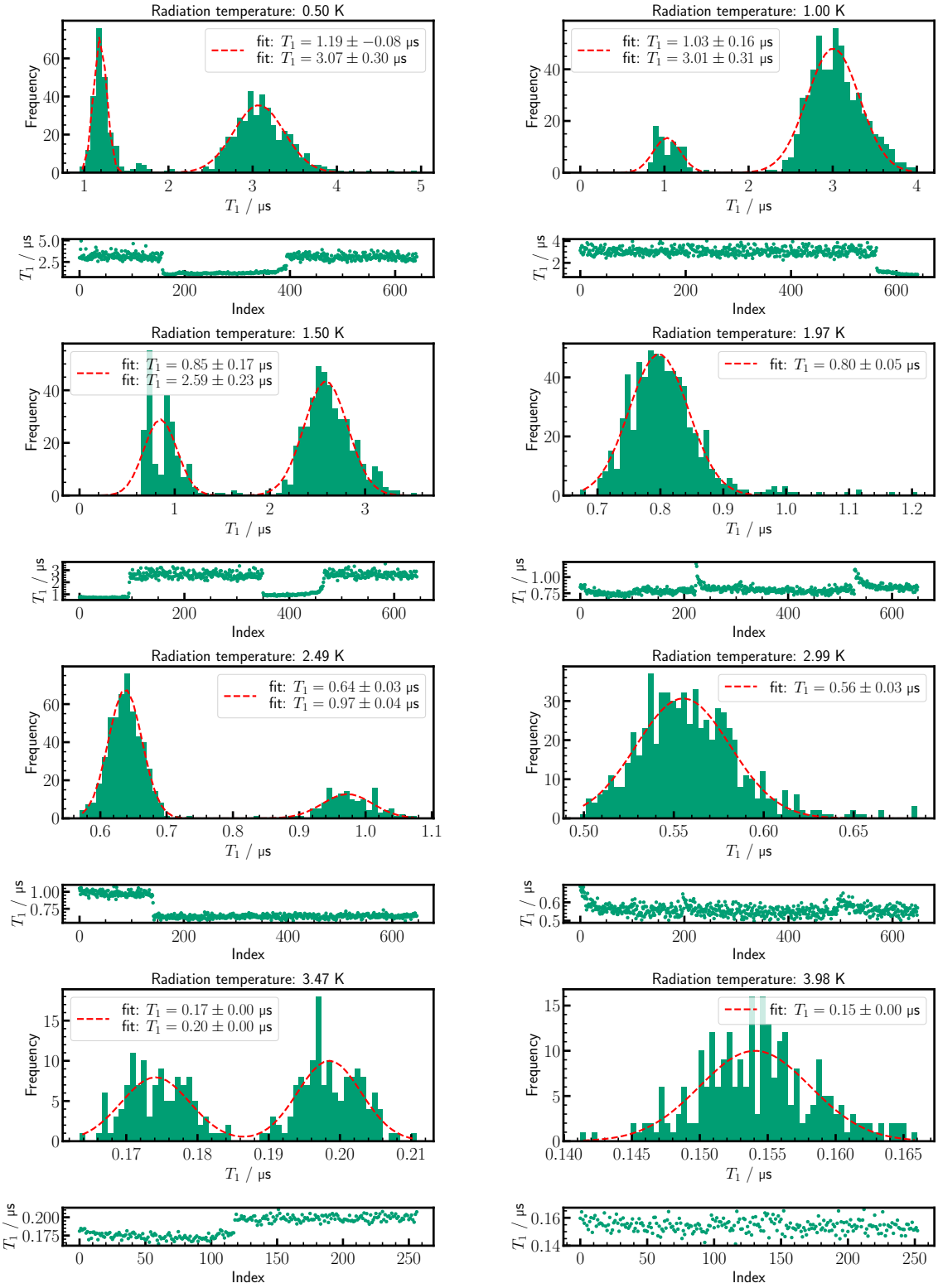

Figure A.6.: Histogram of the energy relaxation results and time traces, similar to the measurements Sec. 4.4.4. The two individual regimes are visible. The individual panels correspond to the different blackbody temperatures. From this data the values plotted in Fig. 5.10(c) are extracted.

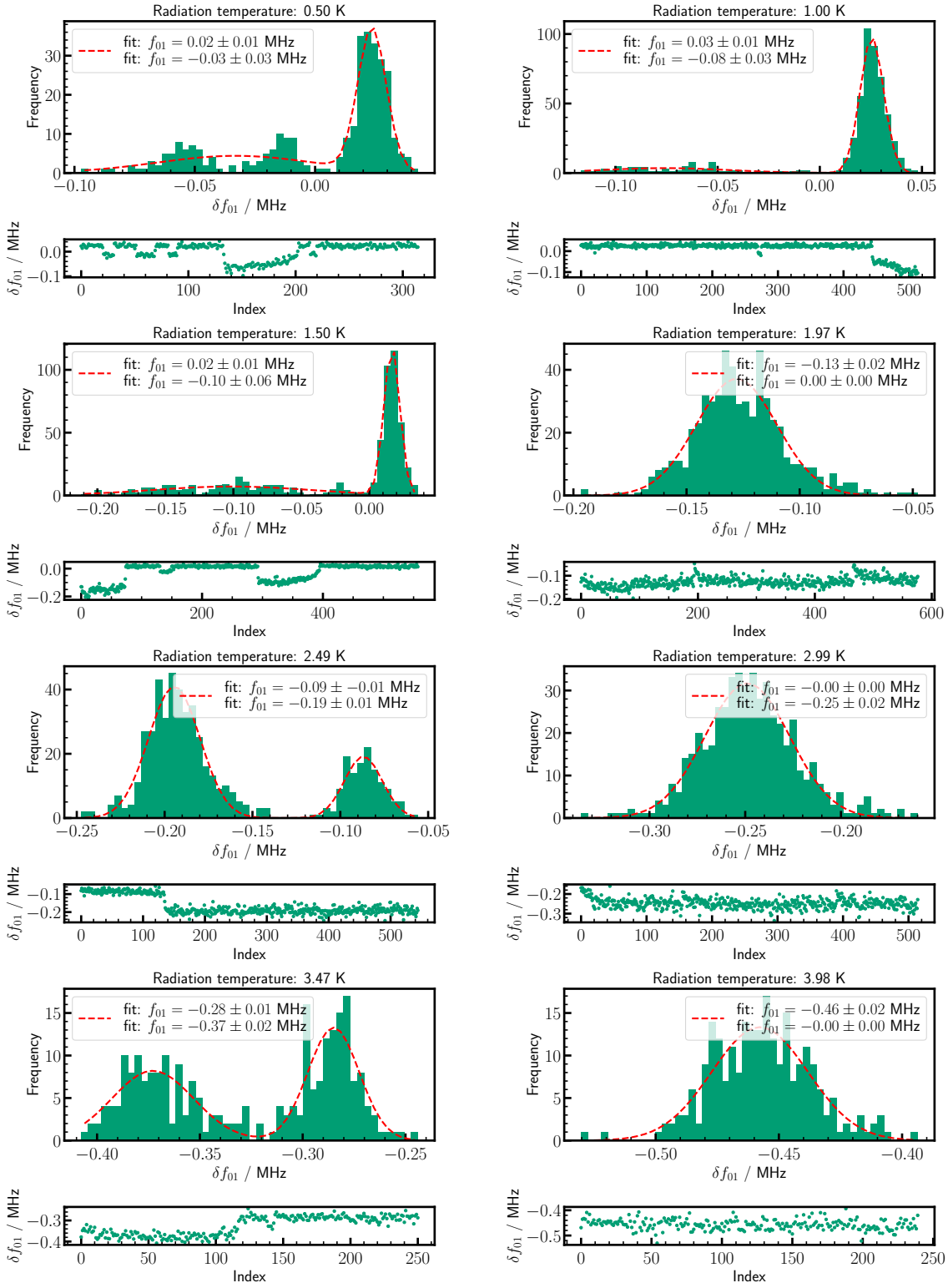

Figure A.7.: Histogram of the qubit frequency shift in the Ramsey experiments and corresponding time traces, similar to the measurements Sec. 4.4.4. The individual panels correspond to the different blackbody temperatures. From this data the values plotted in Fig. 5.12(c) are extracted.

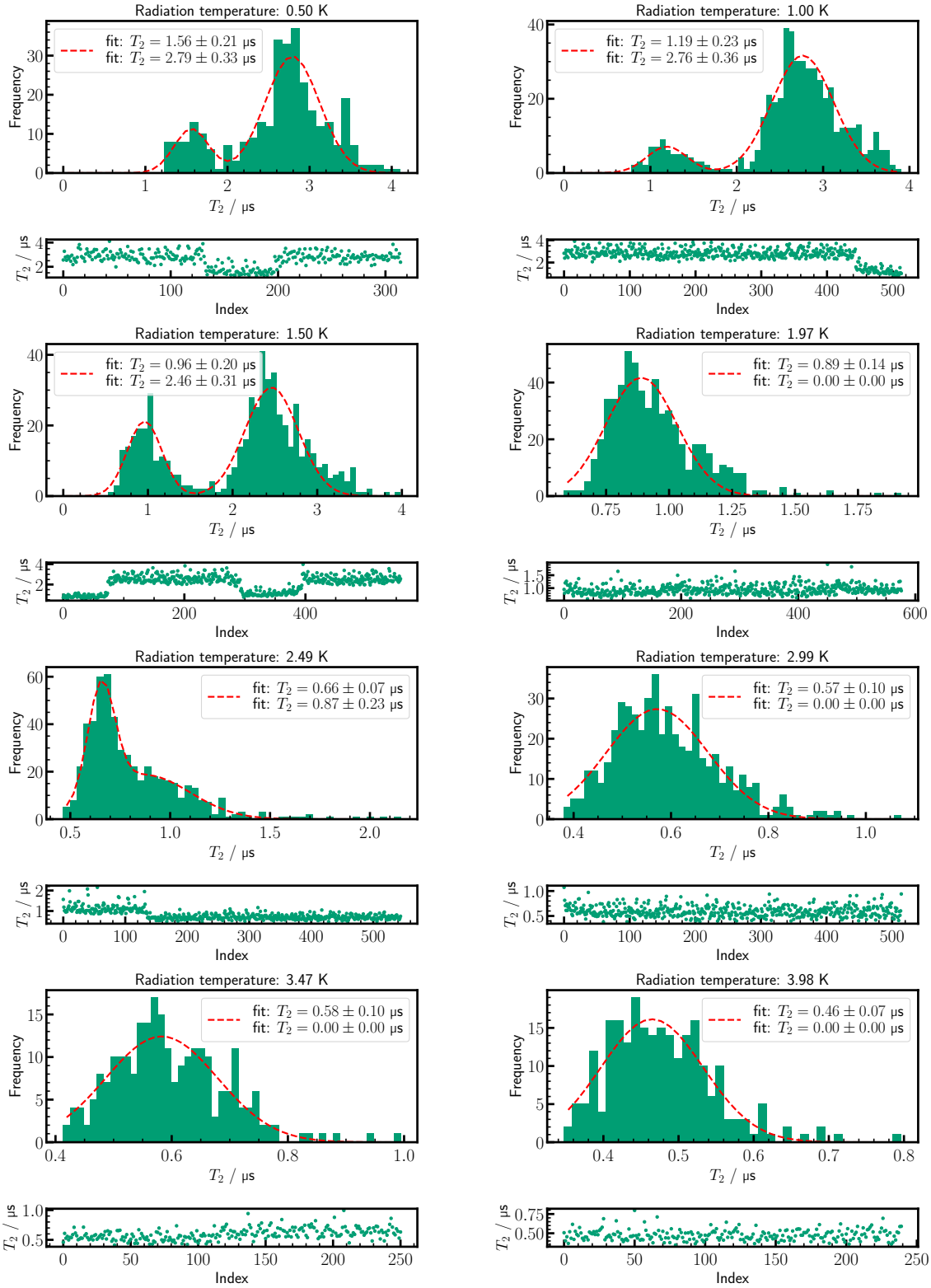

Figure A.8.: Histogram of the Ramsey decoherence time results and time traces, similar to the measurements Sec. 4.4.4. The individual panels correspond to the different blackbody temperatures. From this data the values plotted in Fig. 5.14 are extracted.

A.7.3. Additional measurement on intermediate transmon Q60q2

Characterization of Q60q2, the sample second from the right on the same chip.

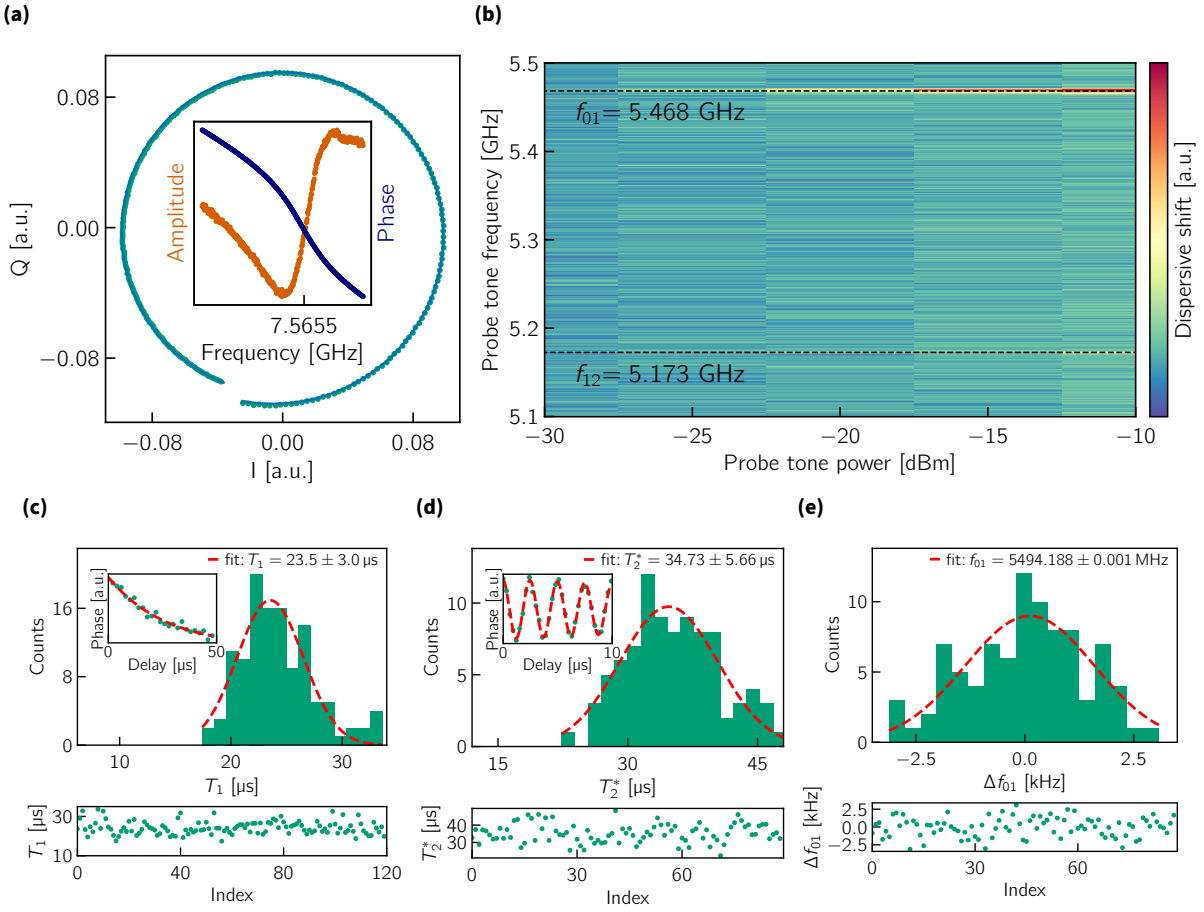

Figure A.9.: Characterization of Q60q2, the sample second from the right on the same chip. (a) Resonator circle fit; inset shows fitted amplitude and phase response. (b) Two-tone spectroscopy as a function of drive frequency and power, showing the first two qubit transitions. (c) Qubit relaxation time T_1: histogram of individual fit results (top), time trace over measurement index (bottom), and a representative decay fit (inset). (d) Ramsey dephasing time T_2: histogram and time trace of fitted values, with a representative Ramsey decay fit (inset). (e) Histogram and time evolution of the extracted qubit frequency from the Ramsey fits.

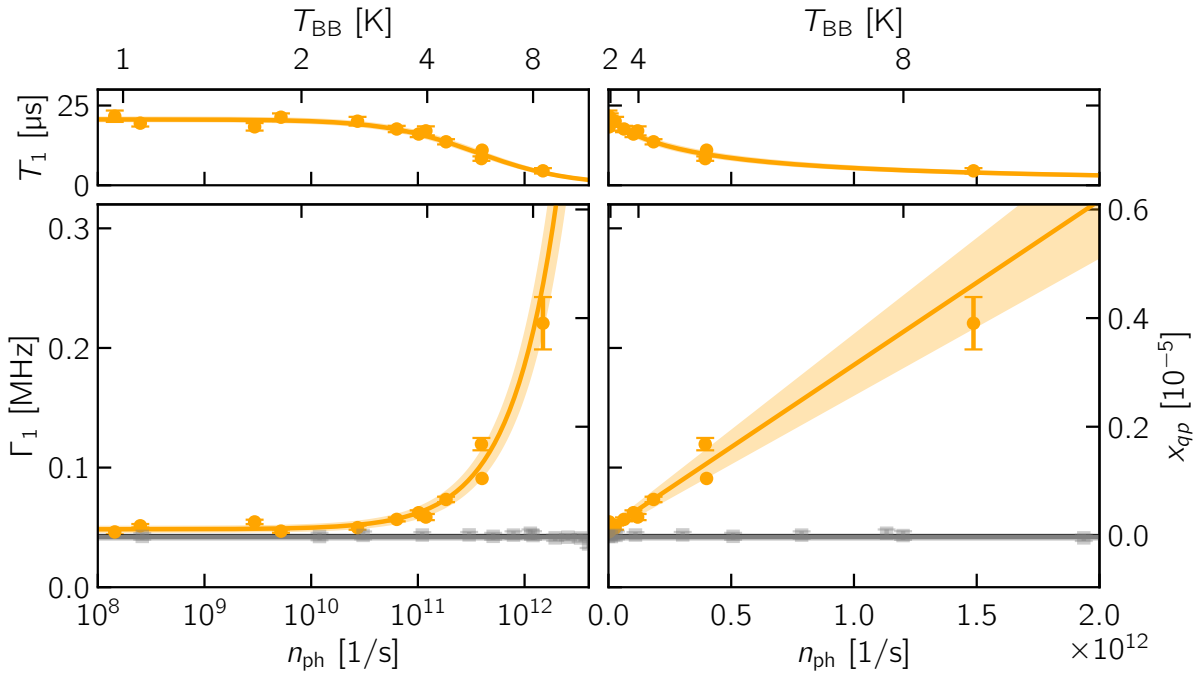

Figure A.10.: Measurements of the decay rate of Q60q2 under radiation with open path (orange) and blocked radiation path for background measurement (gray). Similar to Fig. 5.9.

Table A.1.: Characterisation data for qubit 2 of the intermediate–transmon chip (labelled here as Q60q2).

Parameter	Q60q2
Resonator frequency f_r (GHz)	7.560
Internal quality factor Q_i ($\times 10^3$)	53.5
Coupling quality factor Q_c ($\times 10^3$)	2.3
Qubit transition f_{01} (GHz)	5.484 186(1)
E_C/h (MHz)	261
E_J/h (GHz)	15.8
E_J/E_C	60.6
Coupling strength $g/2\pi$ (MHz)	50
Mean relaxation time $\langle T_1 \rangle$ (µs)	23.6(3)
Mean dephasing time $\langle T_2^* \rangle$ (µs)	34.9(6)
Charge dispersion δf_{01} (kHz)	<1

A.7.4. Choosing power as reference axis

In Sec. 2.5.2 it was motivated that their is a linear relation between photon number flux and QP denstiy. In other publication [51, 82] a linear relation between power and QP density is assumed, however their only single frequency modes are taken into account. For a single frequency the power and photon flux are proportional. The measurement below (Fig. A.11) motivates from a experimental point, that the data is better described by the photon number model used in the main text (compare Fig. 5.9).

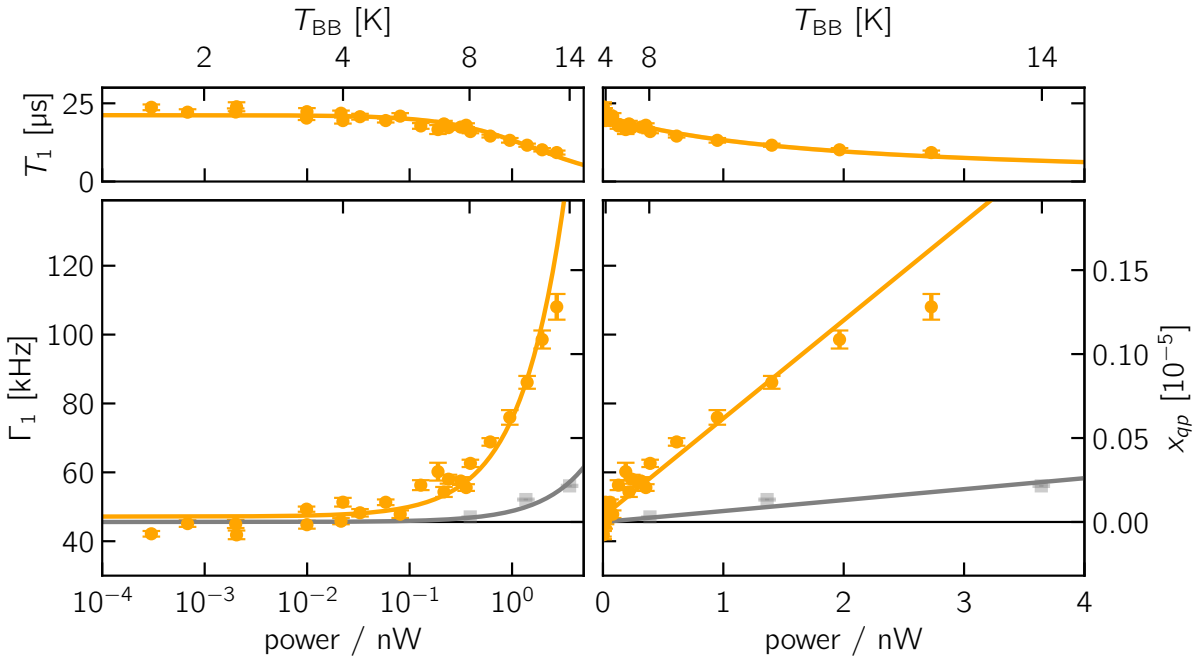

Figure A.11.: Plot similar to Fig. 5.9(a) but with power instead of photon number on the x-axis. The linear fit does not describe the data as good as for the photon number case.

A.8. Further infrared spectroscopy data

A.8.1. Refractive index of sapphire

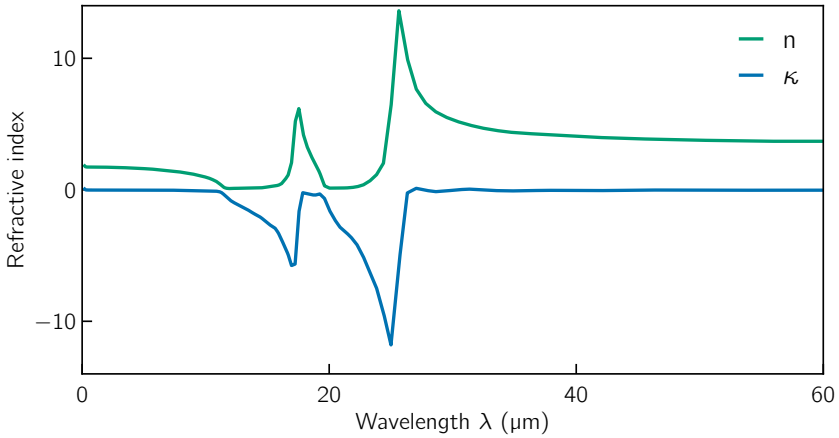

Figure A.12.: Real part (n) and imaginary part (κ) of the refractive index of bulk sapphire as a function of wavelength. Data taken from Ref. [214].

A.8.2. Raw transmission data

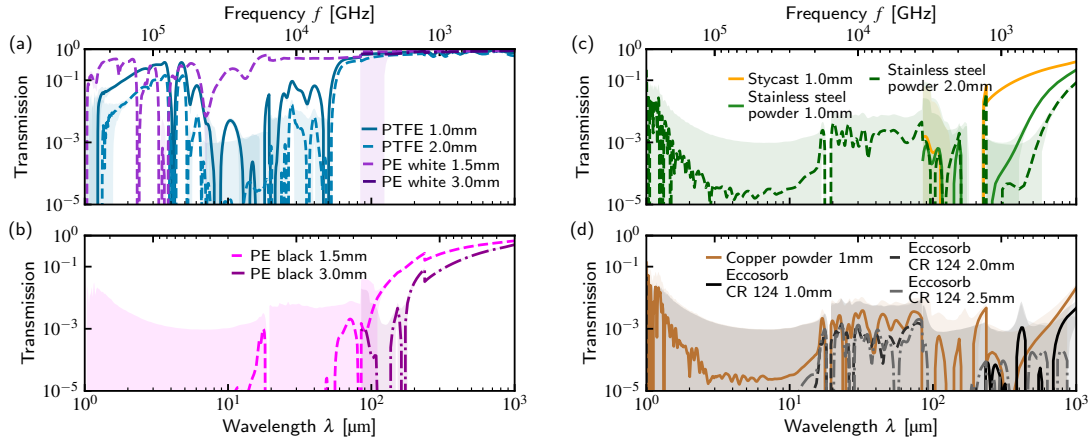

Figure A.13.: Transmission of the investigated materials as function of wavelength. Shaded area represents the error. a: Commercial materials: PTFE and HDPE (transparent). b: HDPE (black). c: Stycast 2850FT and stainless steel powder sample. d: copper powder sample and Eccosorb CR124.

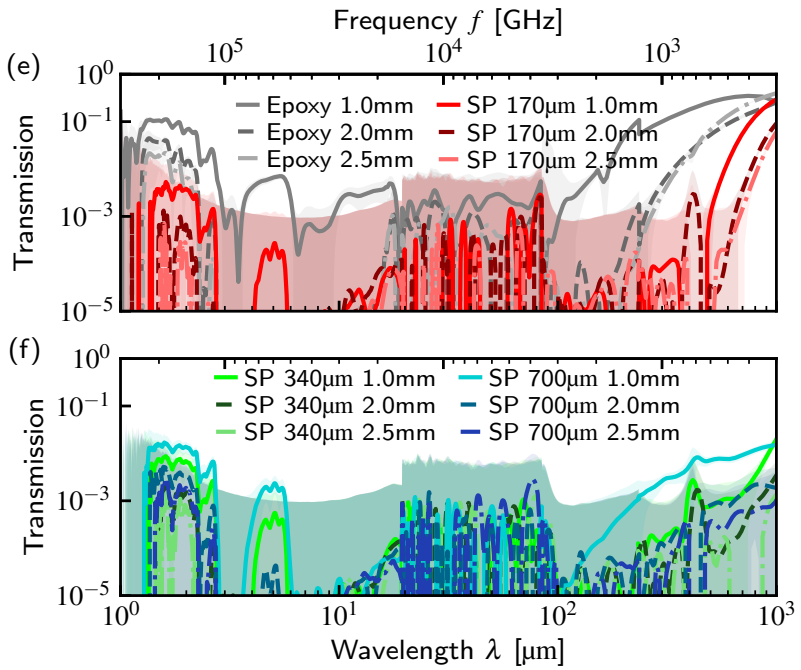

Figure A.14.: Transmission of the investigated materials (continued). e: UHU plus Endfest 300 and SP 170µm. f: SP 340µm and SP 700µm.

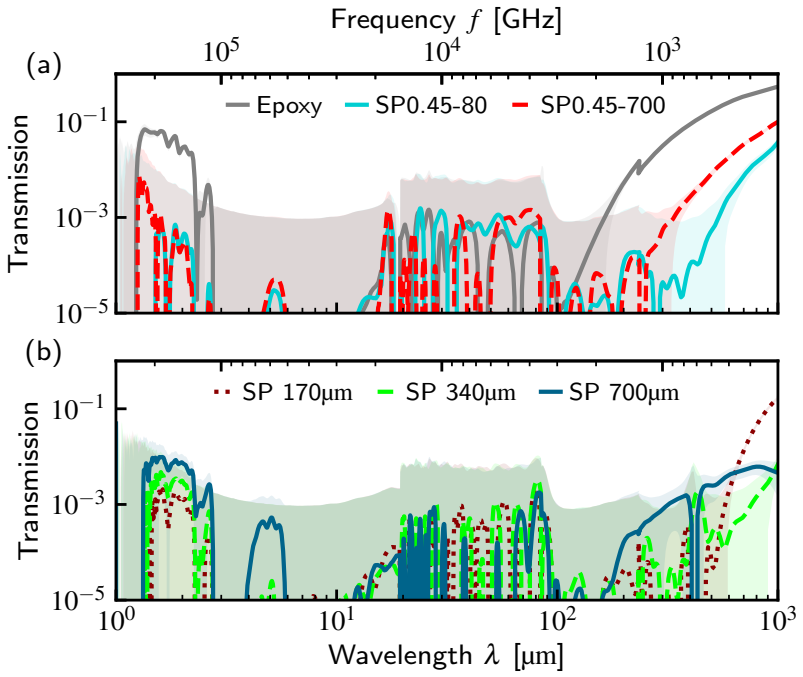

Figure A.15.: Transmission of SP mixed with epoxy resin with a thickness of 1.5 mm. Shaded area represents the error. a: Transmission of the two SP mixtures (SP0.45-80: light blue, SP0.45-700: red) as well as of epoxy resin (gray) b: Transmission through single sized spheres (170 µm: blue, 340 µm: green, 700 µm: dark red).

Table A.2.: Additional data for the sample with thickness $d = 1\,\text{mm}$, $d = 1.5\,\text{mm}$, $d = 2\,\text{mm}$ and $d = 2.5\,\text{mm}$.

Material	d [mm]	$\lambda = 2\,\mu\text{m}$	$\lambda = 40\,\mu\text{m}$	$\lambda = 200\,\mu\text{m}$	$\lambda = 500\,\mu\text{m}$	$\lambda = 700\,\mu\text{m}$
UHU+ 300	1.0	$6.69(16) \times 10^{-2}$	$2.6(11) \times 10^{-3}$	$4.47(44) \times 10^{-2}$	$2.71(21) \times 10^{-1}$	$3.50(26) \times 10^{-1}$
UHU+ 300	1.5	$2.89(11) \times 10^{-2}$	$8.2(76) \times 10^{-4}$	$5.15(14) \times 10^{-3}$	$1.722(68) \times 10^{-1}$	$3.32(13) \times 10^{-1}$
UHU+ 300	2.0	$1.440(77) \times 10^{-2}$	$1.14(63) \times 10^{-3}$	$2.07(69) \times 10^{-4}$	$5.98(63) \times 10^{-2}$	$1.45(17) \times 10^{-1}$
UHU+ 300	2.5	$6.24(54) \times 10^{-3}$	$3.7(64) \times 10^{-4}$	$4.3(52) \times 10^{-5}$	$7.12(39) \times 10^{-2}$	$2.01(10) \times 10^{-1}$
PTFE	1.0	$1.214(12) \times 10^{-1}$	$6.63(72) \times 10^{-2}$	$7.95(68) \times 10^{-1}$	$9.06(24) \times 10^{-1}$	$9.05(34) \times 10^{-1}$
PTFE	1.5	$4.632(51) \times 10^{-2}$	$2.09(29) \times 10^{-2}$	$7.55(76) \times 10^{-1}$	$8.90(24) \times 10^{-1}$	$8.29(22) \times 10^{-1}$
PTFE	2.0	$2.190(39) \times 10^{-2}$	$6.52(71) \times 10^{-3}$	$6.84(69) \times 10^{-1}$	$8.62(24) \times 10^{-1}$	$7.79(14) \times 10^{-1}$
HDPE (trans.)	1.5	$3.966(45) \times 10^{-1}$	$8.234(84) \times 10^{-1}$	$8.84(18) \times 10^{-1}$	$8.87(21) \times 10^{-1}$	$8.98(25) \times 10^{-1}$
HDPE (trans.)	3.0	$3.985(46) \times 10^{-1}$	$5.109(55) \times 10^{-1}$	$8.55(27) \times 10^{-1}$	$8.707(87) \times 10^{-1}$	$8.769(88) \times 10^{-1}$
HDPE (black)	1.5	$<1 \times 10^{-5}$	$<1 \times 10^{-5}$	$1.677(22) \times 10^{-1}$	$4.92(11) \times 10^{-1}$	$6.06(17) \times 10^{-1}$
HDPE (black)	3.0	$<1 \times 10^{-5}$	$<1 \times 10^{-5}$	$1.58(10) \times 10^{-1}$	$4.64(21) \times 10^{-1}$	$5.79(26) \times 10^{-1}$
Stycast 2850 FT	1.0	$<1 \times 10^{-5}$	$<1 \times 10^{-5}$	$<1 \times 10^{-5}$	$1.76(14) \times 10^{-1}$	$2.83(22) \times 10^{-1}$
Stycast 2850 FT	1.5	$<1 \times 10^{-5}$	$<1 \times 10^{-5}$	$1.509(95) \times 10^{-3}$	$9.98(38) \times 10^{-2}$	$1.930(75) \times 10^{-1}$
Eccosorb CR124	1.0	$<1 \times 10^{-5}$	$<1 \times 10^{-5}$	$<1 \times 10^{-5}$	$<1 \times 10^{-5}$	$9.3(67) \times 10^{-5}$
Eccosorb CR124	1.5	$<1 \times 10^{-5}$	$<1 \times 10^{-5}$	$<1 \times 10^{-5}$	$<1 \times 10^{-5}$	$8.4(16) \times 10^{-4}$
Eccosorb CR124	2.0	$<1 \times 10^{-5}$	$6.5(60) \times 10^{-4}$	$1.3(14) \times 10^{-3}$	$1.3(14) \times 10^{-3}$	$1.3(14) \times 10^{-3}$
Eccosorb CR124	2.5	$<1 \times 10^{-5}$	$7.4(94) \times 10^{-4}$	$<1 \times 10^{-5}$	$1.59(94) \times 10^{-4}$	$<1 \times 10^{-5}$
Copper	1.0	$<1 \times 10^{-5}$	$<1 \times 10^{-5}$	$1.03(76) \times 10^{-3}$	$<1 \times 10^{-5}$	$2.86(22) \times 10^{-3}$
Copper	1.5	$<1 \times 10^{-5}$	$<1 \times 10^{-5}$	$5.0(11) \times 10^{-5}$	$<1 \times 10^{-5}$	$<1 \times 10^{-5}$
Stainless steel	1.0	$<1 \times 10^{-5}$	$<1 \times 10^{-5}$	$<1 \times 10^{-5}$	$1.227(45) \times 10^{-2}$	$8.5(11) \times 10^{-2}$
Stainless steel	1.5	$<1 \times 10^{-5}$	$<1 \times 10^{-5}$	$<1 \times 10^{-5}$	$9.9(16) \times 10^{-4}$	$3.23(38) \times 10^{-2}$
Stainless steel	2.0	$1.6(43) \times 10^{-4}$	$1.6(19) \times 10^{-3}$	$<1 \times 10^{-5}$	$5.9(16) \times 10^{-4}$	$1.868(54) \times 10^{-2}$
SP0.45-80	1.0	$1.52(56) \times 10^{-3}$	$1.3(16) \times 10^{-3}$	$2.9(60) \times 10^{-5}$	$1.99(18) \times 10^{-2}$	$6.58(76) \times 10^{-2}$
SP0.45-80	1.5	$3.8(33) \times 10^{-4}$	$<1 \times 10^{-5}$	$1.06(66) \times 10^{-4}$	$5.73(67) \times 10^{-4}$	$6.87(72) \times 10^{-3}$
SP0.45-80	2.0	$<1 \times 10^{-5}$	$2.0(68) \times 10^{-4}$	$<1 \times 10^{-5}$	$3.5(11) \times 10^{-4}$	$1.74(20) \times 10^{-3}$
SP0.45-80	2.5	$<1 \times 10^{-5}$	$<1 \times 10^{-5}$	$<1 \times 10^{-5}$	$<1 \times 10^{-5}$	$5.1(11) \times 10^{-4}$
SP0.45-700	1.0	$1.54(36) \times 10^{-3}$	$2.9(71) \times 10^{-4}$	$1.62(12) \times 10^{-3}$	$4.38(17) \times 10^{-2}$	$1.043(52) \times 10^{-1}$
SP0.45-700	1.5	$2.6(34) \times 10^{-4}$	$<1 \times 10^{-5}$	$<1 \times 10^{-5}$	$8.76(61) \times 10^{-3}$	$3.24(23) \times 10^{-2}$
SP0.45-700	2.0	$1.2(33) \times 10^{-4}$	$1.2(49) \times 10^{-4}$	$<1 \times 10^{-5}$	$1.80(25) \times 10^{-3}$	$1.13(14) \times 10^{-2}$
SP0.45-700	2.5	$<1 \times 10^{-5}$	$1.1(70) \times 10^{-4}$	$3.0(85) \times 10^{-5}$	$3.53(62) \times 10^{-4}$	$1.88(90) \times 10^{-3}$
SP180 μm	1.0	$3.82(34) \times 10^{-3}$	$<1 \times 10^{-5}$	$<1 \times 10^{-5}$	$1.48(37) \times 10^{-3}$	$5.14(56) \times 10^{-2}$
SP180 μm	1.5	$1.45(46) \times 10^{-3}$	$<1 \times 10^{-5}$	$<1 \times 10^{-5}$	$<1 \times 10^{-5}$	$1.18(13) \times 10^{-2}$
SP180 μm	2.0	$6.5(41) \times 10^{-4}$	$<1 \times 10^{-5}$	$<1 \times 10^{-5}$	$<1 \times 10^{-5}$	$3.07(40) \times 10^{-3}$
SP180 μm	2.5	$<1 \times 10^{-5}$	$<1 \times 10^{-5}$	$<1 \times 10^{-5}$	$<1 \times 10^{-5}$	$1.29(15) \times 10^{-3}$
SP340 μm	1.0	$6.86(40) \times 10^{-3}$	$<1 \times 10^{-5}$	$<1 \times 10^{-5}$	$7.70(27) \times 10^{-4}$	$1.34(18) \times 10^{-3}$
SP340 μm	1.5	$3.13(38) \times 10^{-3}$	$<1 \times 10^{-5}$	$<1 \times 10^{-5}$	$2.7(18) \times 10^{-4}$	$5.27(84) \times 10^{-4}$
SP340 μm	2.0	$1.52(40) \times 10^{-3}$	$<1 \times 10^{-5}$	$<1 \times 10^{-5}$	$<1 \times 10^{-5}$	$2.27(27) \times 10^{-4}$
SP340 μm	2.5	$6.7(38) \times 10^{-4}$	$<1 \times 10^{-5}$	$<1 \times 10^{-5}$	$9.6(60) \times 10^{-5}$	$<1 \times 10^{-5}$
SP700 μm	1.0	$1.376(43) \times 10^{-2}$	$<1 \times 10^{-5}$	$5.32(64) \times 10^{-4}$	$7.29(21) \times 10^{-3}$	$8.92(29) \times 10^{-3}$
SP700 μm	1.5	$7.51(47) \times 10^{-3}$	$<1 \times 10^{-5}$	$1.58(52) \times 10^{-4}$	$2.47(18) \times 10^{-3}$	$5.13(11) \times 10^{-3}$
SP700 μm	2.0	$3.67(36) \times 10^{-3}$	$<1 \times 10^{-5}$	$1.5(79) \times 10^{-5}$	$8.19(40) \times 10^{-4}$	$1.36(19) \times 10^{-3}$
SP700 μm	2.5	$1.86(40) \times 10^{-3}$	$<1 \times 10^{-5}$	$4.6(40) \times 10^{-5}$	$3.8(14) \times 10^{-4}$	$6.04(85) \times 10^{-4}$

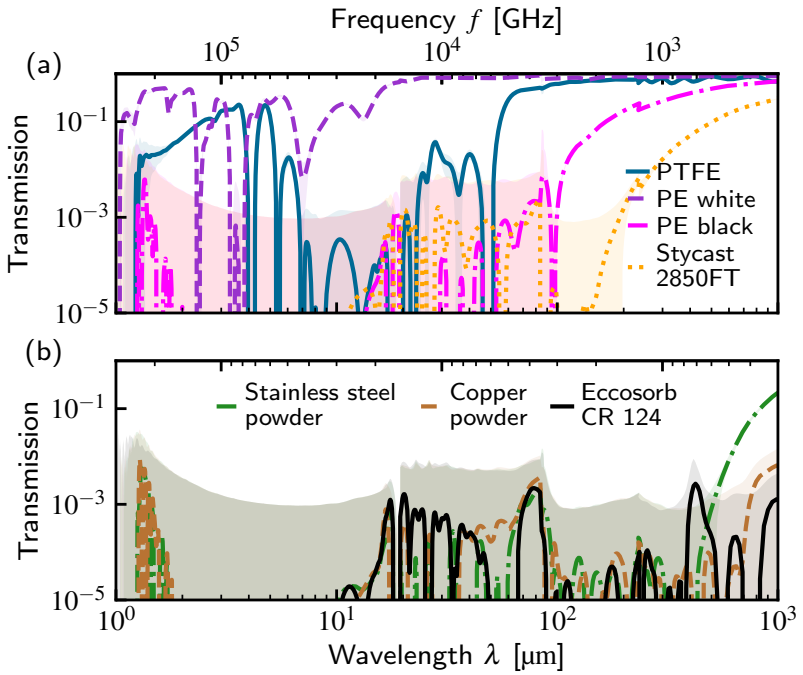

Figure A.16.: Transmission of additionally investigated materials as function of wavelength. Shaded area represents the error. a: Commercial materials: PTFE, HDPE (transparent), HDPE (black). b: Eccosorb CR124, Stycast 2850FT and metal powder samples (copper and stainless steel).

A.8.3. Fitting sub-terahertz absorption and Fabry-Perot fringes

Thin slabs show Fabry-Perot fringes in their infrared transmission, arising from internal reflection in the medium [210, 232]. Following Halpern et al. [218], the transmission of a thin slab of nonlossy dielectric can be fitted in the sub-terahertz regime.

The following expressions describe reflection and transmission at the interface of a lossless dielectric slab of thickness l and real refractive index n for a given frequency f.

The admittance at the front surface is given by

$$Y(f) = n\left(\frac{\cos(2\pi nfl) + in\sin(2\pi nfl)}{n\cos(2\pi nfl) + i\sin(2\pi nfl)}\right). \tag{A.17}$$

The electric field reflection coefficient is

$$\rho = \frac{1 - Y(f)}{1 + Y(f)}. \tag{A.18}$$

The power reflection and transmission coefficients are

$$R = \rho\rho^*, \qquad T = 1 - R. \tag{A.19}$$

Next, the above expressions are extended to a lossy dielectric by considering a poor conductor, $\sigma \ll 2\pi f\epsilon$, where σ is the conductivity and ϵ the permittivity. The complex permittivity is then

$$\epsilon_c = \epsilon\left(1 + \frac{\sigma}{i\omega\epsilon}\right), \tag{A.20}$$

A complex admittance can be derived in the same way that Eq. (A.17) is obtained. The result is

$$Y(f) = \frac{1}{\eta'}\left(\frac{\eta' \cosh(\gamma l) + \sinh(\gamma l)}{\cosh(\gamma l) + \eta' \sinh(\gamma l)}\right), \tag{A.21}$$

where the complex wave vector is

$$\gamma = i\omega\sqrt{\mu\epsilon_c} = \alpha/2 + 2\pi i n f, \tag{A.22}$$

where α is the frequency-dependent absorption coefficient. It is assumed that the absorption coefficient follows a power law

$$\alpha = a f^b, \tag{A.23}$$

with a and b being free parameters.

The bulk impedance is

$$\eta' = \sqrt{\mu/\epsilon_c} = \frac{1}{n\sqrt{1 + \alpha/2\pi i n f}}. \tag{A.24}$$

The electric field reflection coefficient is again given by Eq. (A.18). The coefficients for reflected and transmitted power are

$$R = \rho\rho^*, \qquad T = \exp(-\alpha l)(1 - R). \tag{A.25}$$

This transmission function is then fitted to transmission data taken with the spectrometer for Teflon. The free fit parameters are the two parameters describing the absorption coefficient, a and b, the thickness l, and the real refractive index n, which is assumed to be constant in this frequency range. The frequency is given here in units of wavenumber as cm^{-1}. In Fig. A.17 the data and fit are shown for a 0.5 mm thick sample (a) and a 1 mm thick sample (b). From the theory, one expects that the fit parameters match for both thicknesses. For the refractive index, this condition is nearly fulfilled, with the fit value of the 0.5 mm sample being $n = 1.4$ and for the 1 mm sample $n = 1.7$. This value agrees with literature values for Teflon (PTFE) of $n = 1.3$ to $n = 1.6$ [218, 233–235]. However, this agreement does not hold for the other parameters, which are given in the plot. Most remarkably, the fitted thickness of the 0.5 mm sample matches quite well, with a value of $l = 0.52$ mm, while for the 1 mm sample the fitted thickness is $l = 0.42$ mm. The 1 mm sample is formed by stacking two 0.5 mm slabs on top of each other; therefore Fabry-Perot fringes matching thicknesses of 0.5 mm and 1 mm are expected. This results in the smaller fitted thickness, which better matches 0.5 mm. This also explains the mismatch of the fit parameters for the absorption coefficient, a and b.

For the other samples this analysis was not possible, since only data down to a frequency of $5\,\mathrm{cm}^{-1}$ were measured, the low-frequency limit is not observable, and the absorption was too high to resolve the Fabry-Perot fringes. Also, the fit has many free parameters; therefore, precise knowledge of the thickness would be beneficial.

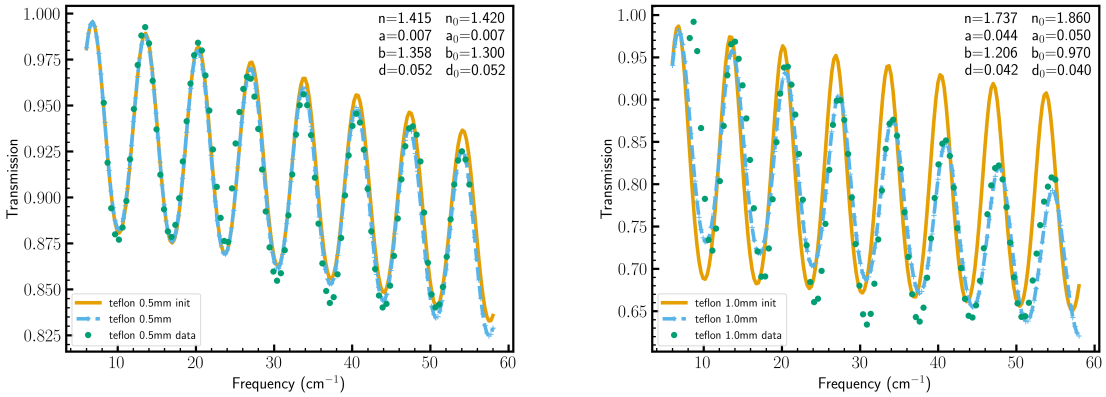

Figure A.17.: Transmission of Teflon (green points) and the fit to the measurement data (blue dashed line). The orange line shows the initial guess. (left): For a sample thickness of 0.5 mm. (right): For a sample thickness of 1 mm. The corresponding fit values are given in the respective plot.

A.8.4. Individual measurement settings

Table A.3.: Details of the IR spectrometer measurement setting for each individual measurement.

Material	Thickness [mm]	Detector	Beamsplitter	Resolution [cm^{-1}]	Aperature [mm]
SP180 μm	1.0	1.6K bolometer, 100 cm^{-1}	multilayerMylar	1	4
SP180 μm	1.0	1.6K bolometer, 35 cm^{-1}	125Mylar	1	8
SP180 μm	1.0	RT-DLaTGS	KBr	2	8
SP180 μm	1.0	RT-DTGS-FIR	KBr	2	8
SP180 μm	1.5	1.6K bolometer, 100 cm^{-1}	multilayerMylar	1	4
SP180 μm	1.5	1.6K bolometer, 35 cm^{-1}	125Mylar	1	8
SP180 μm	1.5	RT-DLaTGS	KBr	2	8
SP180 μm	1.5	RT-DTGS-FIR	KBr	2	8
SP180 μm	2.0	1.6K bolometer, 100 cm^{-1}	multilayerMylar	1	4
SP180 μm	2.0	1.6K bolometer, 35 cm^{-1}	125Mylar	1	8
SP180 μm	2.0	RT-DLaTGS	KBr	2	8
SP180 μm	2.0	RT-DTGS-FIR	KBr	2	8
SP180 μm	2.5	1.6K bolometer, 100 cm^{-1}	multilayerMylar	1	4
SP180 μm	2.5	1.6K bolometer, 35 cm^{-1}	125Mylar	1	8
SP180 μm	2.5	RT-DLaTGS	KBr	2	8
SP180 μm	2.5	RT-DTGS-FIR	KBr	2	8
SP180 μm	3.0	1.6K bolometer, 100 cm^{-1}	multilayerMylar	1	4
SP180 μm	3.0	1.6K bolometer, 35 cm^{-1}	125Mylar	1	8
SP340 μm	1.0	1.6K bolometer, 100 cm^{-1}	multilayerMylar	1	4
SP340 μm	1.0	1.6K bolometer, 35 cm^{-1}	125Mylar	1	8
SP340 μm	1.0	RT-DLaTGS	KBr	2	8
SP340 μm	1.0	RT-DTGS-FIR	KBr	2	8
SP340 μm	1.5	1.6K bolometer, 100 cm^{-1}	multilayerMylar	1	4
SP340 μm	1.5	1.6K bolometer, 35 cm^{-1}	125Mylar	1	8
SP340 μm	1.5	RT-DLaTGS	KBr	2	8
SP340 μm	1.5	RT-DTGS-FIR	KBr	2	8
SP340 μm	2.0	1.6K bolometer, 100 cm^{-1}	multilayerMylar	1	4

Continued on next page

Material	Thickness [mm]	Detector	Beamsplitter	Resolution [cm^{-1}]	Aperature [mm]
SP340 μm	2.0	1.6K bolometer, 35 cm^{-1}	125Mylar	1	8
SP340 μm	2.0	RT-DLaTGS	KBr	2	8
SP340 μm	2.0	RT-DTGS-FIR	KBr	2	8
SP340 μm	2.5	1.6K bolometer, 100 cm^{-1}	multilayerMylar	1	4
SP340 μm	2.5	1.6K bolometer, 35 cm^{-1}	125Mylar	1	8
SP340 μm	2.5	RT-DLaTGS	KBr	2	8
SP340 μm	2.5	RT-DTGS-FIR	KBr	2	8
SP340 μm	3.0	1.6K bolometer, 100 cm^{-1}	multilayerMylar	1	4
SP340 μm	3.0	1.6K bolometer, 35 cm^{-1}	125Mylar	1	8
SP700 μm	1.0	1.6K bolometer, 100 cm^{-1}	multilayerMylar	1	4
SP700 μm	1.0	1.6K bolometer, 35 cm^{-1}	125Mylar	1	8
SP700 μm	1.0	RT-DLaTGS	KBr	2	8
SP700 μm	1.0	RT-DTGS-FIR	KBr	2	8
SP700 μm	1.5	1.6K bolometer, 100 cm^{-1}	multilayerMylar	1	4
SP700 μm	1.5	1.6K bolometer, 35 cm^{-1}	125Mylar	1	8
SP700 μm	1.5	RT-DLaTGS	KBr	2	8
SP700 μm	1.5	RT-DTGS-FIR	KBr	2	8
SP700 μm	2.0	1.6K bolometer, 100 cm^{-1}	multilayerMylar	1	4
SP700 μm	2.0	1.6K bolometer, 35 cm^{-1}	125Mylar	1	8
SP700 μm	2.0	RT-DLaTGS	KBr	2	8
SP700 μm	2.0	RT-DTGS-FIR	KBr	2	8
SP700 μm	2.5	1.6K bolometer, 100 cm^{-1}	multilayerMylar	1	4
SP700 μm	2.5	1.6K bolometer, 35 cm^{-1}	125Mylar	1	8
SP700 μm	2.5	RT-DLaTGS	KBr	2	8
SP700 μm	2.5	RT-DTGS-FIR	KBr	2	8
SP700 μm	3.0	1.6K bolometer, 100 cm^{-1}	multilayerMylar	1	4
SP700 μm	3.0	1.6K bolometer, 35 cm^{-1}	125Mylar	1	8
Epoxy + copper	1.0	1.6K bolometer, 100 cm^{-1}	150Mylar	4	3
Epoxy + copper	1.0	1.6K bolometer, 35 cm^{-1}	150Mylar	4	3
Epoxy + copper	1.0	RT-DLaTGS	KBr	4	3
Epoxy + copper	1.0	RT-DTGS-FIR	KBr	4	3
Epoxy + copper	1.5	1.6K bolometer, 100 cm^{-1}	150Mylar	4	3
Epoxy + copper	1.5	1.6K bolometer, 100 cm^{-1}	multilayerMylar	1	4
Epoxy + copper	1.5	1.6K bolometer, 35 cm^{-1}	125Mylar	1	8
Epoxy + copper	1.5	1.6K bolometer, 35 cm^{-1}	150Mylar	4	3
Epoxy + copper	1.5	1.6K bolometer, 35 cm^{-1}	50Mylar	1	3
Epoxy + copper	1.5	RT-DLaTGS	KBr	4	8
Epoxy + copper	1.5	RT-DTGS-FIR	KBr	4	8
Eccosorb CR124	1.0	1.6K bolometer, 100 cm^{-1}	multilayerMylar	1	4
Eccosorb CR124	1.0	1.6K bolometer, 35 cm^{-1}	125Mylar	1	8
Eccosorb CR124	1.5	1.6K bolometer, 100 cm^{-1}	multilayerMylar	1	4
Eccosorb CR124	1.5	1.6K bolometer, 35 cm^{-1}	125Mylar	1	8
Eccosorb CR124	1.5	1.6K bolometer, 35 cm^{-1}	150Mylar	4	3
Eccosorb CR124	1.5	1.6K bolometer, 35 cm^{-1}	50Mylar	1	3
Eccosorb CR124	1.5	RT-DLaTGS	KBr	4	8
Eccosorb CR124	1.5	RT-DLaTGS	KBr	4	8
Eccosorb CR124	1.5	RT-DTGS-FIR	KBr	4	8
Eccosorb CR124	1.5	RT-DTGS-FIR	KBr	4	8
Eccosorb CR124	2.0	RT-DLaTGS	KBr	4	8

Continued on next page

Material	Thickness [mm]	Detector	Beamsplitter	Resolution [cm^{-1}]	Aperature [mm]
Eccosorb CR124	2.0	RT-DTGS-FIR	KBr	4	8
Eccosorb CR124	2.5	1.6K bolometer, 100 cm^{-1}	multilayerMylar	1	4
Eccosorb CR124	2.5	1.6K bolometer, 35 cm^{-1}	125Mylar	1	8
Eccosorb CR124	2.5	RT-DLaTGS	KBr	4	8
Eccosorb CR124	2.5	RT-DTGS-FIR	KBr	4	8
SP0.45-80	1.0	1.6K bolometer, 100 cm^{-1}	150Mylar	4	3
SP0.45-80	1.0	1.6K bolometer, 100 cm^{-1}	150Mylar	4	3
SP0.45-80	1.0	1.6K bolometer, 100 cm^{-1}	150Mylar	4	3
SP0.45-80	1.0	1.6K bolometer, 100 cm^{-1}	multilayerMylar	1	4
SP0.45-80	1.0	1.6K bolometer, 35 cm^{-1}	125Mylar	1	8
SP0.45-80	1.0	1.6K bolometer, 35 cm^{-1}	150Mylar	4	3
SP0.45-80	1.0	1.6K bolometer, 35 cm^{-1}	150Mylar	4	3
SP0.45-80	1.0	RT-DLaTGS	KBr	4	3
SP0.45-80	1.0	RT-DTGS-FIR	KBr	4	3
SP0.45-80	1.5	1.6K bolometer, 100 cm^{-1}	multilayerMylar	1	4
SP0.45-80	1.5	1.6K bolometer, 35 cm^{-1}	125Mylar	1	8
SP0.45-80	1.5	1.6K bolometer, 35 cm^{-1}	150Mylar	4	3
SP0.45-80	1.5	1.6K bolometer, 35 cm^{-1}	50Mylar	1	3
SP0.45-80	1.5	RT-DLaTGS	KBr	4	8
SP0.45-80	1.5	RT-DLaTGS	KBr	4	8
SP0.45-80	1.5	RT-DTGS-FIR	KBr	4	8
SP0.45-80	1.5	RT-DTGS-FIR	KBr	4	8
SP0.45-80	2.0	1.6K bolometer, 100 cm^{-1}	150Mylar	4	3
SP0.45-80	2.0	1.6K bolometer, 100 cm^{-1}	multilayerMylar	1	4
SP0.45-80	2.0	1.6K bolometer, 35 cm^{-1}	125Mylar	1	8
SP0.45-80	2.0	1.6K bolometer, 35 cm^{-1}	150Mylar	4	3
SP0.45-80	2.0	RT-DLaTGS	KBr	4	8
SP0.45-80	2.0	RT-DLaTGS	KBr	2	8
SP0.45-80	2.0	RT-DTGS-FIR	KBr	4	8
SP0.45-80	2.0	RT-DTGS-FIR	KBr	2	8
SP0.45-80	2.5	1.6K bolometer, 100 cm^{-1}	multilayerMylar	1	4
SP0.45-80	2.5	1.6K bolometer, 35 cm^{-1}	125Mylar	1	8
SP0.45-80	2.5	RT-DLaTGS	KBr	4	8
SP0.45-80	2.5	RT-DTGS-FIR	KBr	4	8
SP0.45-700	1.0	1.6K bolometer, 100 cm^{-1}	multilayerMylar	1	4
SP0.45-700	1.0	1.6K bolometer, 35 cm^{-1}	125Mylar	1	8
SP0.45-700	1.0	1.6K bolometer, 35 cm^{-1}	50Mylar	1	3
SP0.45-700	1.0	RT-DLaTGS	KBr	4	8
SP0.45-700	1.0	RT-DTGS-FIR	KBr	4	8
SP0.45-700	1.5	1.6K bolometer, 100 cm^{-1}	multilayerMylar	1	4
SP0.45-700	1.5	1.6K bolometer, 35 cm^{-1}	125Mylar	1	8
SP0.45-700	1.5	1.6K bolometer, 35 cm^{-1}	50Mylar	1	3
SP0.45-700	1.5	RT-DLaTGS	KBr	4	8
SP0.45-700	1.5	RT-DTGS-FIR	KBr	4	8
SP0.45-700	2.0	1.6K bolometer, 100 cm^{-1}	multilayerMylar	1	4
SP0.45-700	2.0	1.6K bolometer, 35 cm^{-1}	125Mylar	1	8
SP0.45-700	2.0	1.6K bolometer, 35 cm^{-1}	50Mylar	1	3
SP0.45-700	2.0	RT-DLaTGS	KBr	4	8
SP0.45-700	2.0	RT-DTGS-FIR	KBr	4	8

Continued on next page

Material	Thickness [mm]	Detector	Beamsplitter	Resolution [cm^{-1}]	Aperature [mm]
SP0.45-700	2.5	1.6K bolometer, 100 cm^{-1}	multilayerMylar	1	4
SP0.45-700	2.5	1.6K bolometer, 35 cm^{-1}	125Mylar	1	8
SP0.45-700	2.5	1.6K bolometer, 35 cm^{-1}	50Mylar	1	3
SP0.45-700	2.5	RT-DLaTGS	KBr	4	8
SP0.45-700	2.5	RT-DTGS-FIR	KBr	4	8
SP0.45-700	3.0	1.6K bolometer, 100 cm^{-1}	multilayerMylar	1	4
SP0.45-700	3.0	1.6K bolometer, 35 cm^{-1}	125Mylar	1	8
HDPE (black)	1.5	1.6K bolometer, 100 cm^{-1}	multilayerMylar	1	4
HDPE (black)	1.5	1.6K bolometer, 35 cm^{-1}	125Mylar	1	8
HDPE (black)	1.5	1.6K bolometer, 35 cm^{-1}	50Mylar	1	3
HDPE (black)	1.5	RT-DLaTGS	KBr	4	8
HDPE (black)	1.5	RT-DTGS-FIR	KBr	4	8
HDPE (black)	1.5	1.6K bolometer, 100 cm^{-1}	150Mylar	4	3
HDPE (black)	1.5	1.6K bolometer, 35 cm^{-1}	150Mylar	4	3
HDPE (black)	1.5	RT-DLaTGS	KBr	4	8
HDPE (black)	1.5	RT-DTGS-FIR	KBr	4	8
HDPE (black)	3.0	1.6K bolometer, 100 cm^{-1}	150Mylar	4	3
HDPE (black)	3.0	1.6K bolometer, 35 cm^{-1}	150Mylar	4	3
HDPE (transparent)	1.5	1.6K bolometer, 100 cm^{-1}	multilayerMylar	1	4
HDPE (transparent)	1.5	1.6K bolometer, 35 cm^{-1}	50Mylar	1	3
HDPE (transparent)	1.5	RT-DLaTGS	KBr	4	8
HDPE (transparent)	1.5	RT-DTGS-FIR	KBr	4	8
HDPE (transparent)	1.5	1.6K bolometer, 100 cm^{-1}	150Mylar	4	3
HDPE (transparent)	1.5	1.6K bolometer, 35 cm^{-1}	150Mylar	4	3
HDPE (transparent)	1.5	RT-DLaTGS	KBr	4	8
HDPE (transparent)	1.5	RT-DTGS-FIR	KBr	4	8
HDPE (transparent)	3.0	1.6K bolometer, 100 cm^{-1}	150Mylar	4	3
HDPE (transparent)	3.0	1.6K bolometer, 35 cm^{-1}	150Mylar	4	3
Epoxy + stainless steel	1.0	1.6K bolometer, 100 cm^{-1}	150Mylar	4	3
Epoxy + stainless steel	1.0	1.6K bolometer, 35 cm^{-1}	150Mylar	4	3
Epoxy + stainless steel	1.5	1.6K bolometer, 100 cm^{-1}	multilayerMylar	1	4
Epoxy + stainless steel	1.5	1.6K bolometer, 35 cm^{-1}	125Mylar	1	8
Epoxy + stainless steel	1.5	1.6K bolometer, 35 cm^{-1}	50Mylar	1	3
Epoxy + stainless steel	1.5	RT-DLaTGS	KBr	4	8
Epoxy + stainless steel	1.5	RT-DTGS-FIR	KBr	4	8

Continued on next page

Material	Thickness [mm]	Detector	Beamsplitter	Resolution [cm^{-1}]	Aperature [mm]
Epoxy + stainless steel	2.0	1.6K bolometer, 100 cm^{-1}	150Mylar	4	3
Epoxy + stainless steel	2.0	1.6K bolometer, 35 cm^{-1}	150Mylar	4	3
Epoxy + stainless steel	2.0	RT-DLaTGS	KBr	4	3
Epoxy + stainless steel	2.0	RT-DLaTGS	KBr	4	8
Epoxy + stainless steel	2.0	RT-DTGS-FIR	KBr	4	3
Epoxy + stainless steel	2.0	RT-DTGS-FIR	KBr	4	8
Stycast 2850FT	1.0	1.6K bolometer, 100 cm^{-1}	150Mylar	4	3
Stycast 2850FT	1.0	1.6K bolometer, 35 cm^{-1}	150Mylar	4	3
Stycast 2850FT	1.5	1.6K bolometer, 100 cm^{-1}	150Mylar	4	3
Stycast 2850FT	1.5	1.6K bolometer, 100 cm^{-1}	multilayerMylar	1	4
Stycast 2850FT	1.5	1.6K bolometer, 35 cm^{-1}	125Mylar	1	8
Stycast 2850FT	1.5	1.6K bolometer, 35 cm^{-1}	150Mylar	4	3
Stycast 2850FT	1.5	1.6K bolometer, 35 cm^{-1}	50Mylar	1	3
Stycast 2850FT	1.5	RT-DLaTGS	KBr	4	8
Stycast 2850FT	1.5	RT-DLaTGS	KBr	4	8
Stycast 2850FT	1.5	RT-DTGS-FIR	KBr	4	8
Stycast 2850FT	1.5	RT-DTGS-FIR	KBr	4	8
PTFE	1.0	1.6K bolometer, 100 cm^{-1}	multilayerMylar	1	4
PTFE	1.0	1.6K bolometer, 35 cm^{-1}	125Mylar	1	8
PTFE	1.0	1.6K bolometer, 35 cm^{-1}	50Mylar	1	3
PTFE	1.0	RT-DLaTGS	KBr	4	8
PTFE	1.0	RT-DTGS-FIR	KBr	4	8
PTFE	1.5	1.6K bolometer, 100 cm^{-1}	multilayerMylar	1	4
PTFE	1.5	1.6K bolometer, 35 cm^{-1}	125Mylar	1	8
PTFE	1.5	1.6K bolometer, 35 cm^{-1}	50Mylar	1	3
PTFE	1.5	RT-DLaTGS	KBr	4	8
PTFE	1.5	RT-DTGS-FIR	KBr	4	8
PTFE	2.0	1.6K bolometer, 100 cm^{-1}	multilayerMylar	1	4
PTFE	2.0	1.6K bolometer, 35 cm^{-1}	125Mylar	1	8
PTFE	2.0	RT-DLaTGS	KBr	2	8
PTFE	2.0	RT-DTGS-FIR	KBr	2	8
UHU plus Endfest 300	1.0	1.6K bolometer, 100 cm^{-1}	150Mylar	4	3
UHU plus Endfest 300	1.0	1.6K bolometer, 35 cm^{-1}	150Mylar	4	3
UHU plus Endfest 300	1.0	RT-DLaTGS	KBr	4	3
UHU plus Endfest 300	1.0	RT-DTGS-FIR	KBr	4	3
UHU plus Endfest 300	1.5	1.6K bolometer, 100 cm^{-1}	150Mylar	4	3
UHU plus Endfest 300	1.5	1.6K bolometer, 100 cm^{-1}	multilayerMylar	1	4
UHU plus Endfest 300	1.5	1.6K bolometer, 35 cm^{-1}	125Mylar	1	8

Continued on next page

Material	Thickness [mm]	Detector	Beamsplitter	Resolution [cm^{-1}]	Aperature [mm]
UHU plus Endfest 300	1.5	1.6K bolometer, 35 cm^{-1}	150Mylar	4	3
UHU plus Endfest 300	1.5	1.6K bolometer, 35 cm^{-1}	150Mylar	4	3
UHU plus Endfest 300	1.5	1.6K bolometer, 35 cm^{-1}	50Mylar	1	3
UHU plus Endfest 300	1.5	RT-DLaTGS	KBr	4	8
UHU plus Endfest 300	1.5	RT-DLaTGS	KBr	4	8
UHU plus Endfest 300	1.5	RT-DTGS-FIR	KBr	4	8
UHU plus Endfest 300	1.5	RT-DTGS-FIR	KBr	4	8
UHU plus Endfest 300	2.0	1.6K bolometer, 100 cm^{-1}	150Mylar	4	3
UHU plus Endfest 300	2.0	1.6K bolometer, 100 cm^{-1}	multilayerMylar	1	4
UHU plus Endfest 300	2.0	1.6K bolometer, 35 cm^{-1}	125Mylar	1	8
UHU plus Endfest 300	2.0	1.6K bolometer, 35 cm^{-1}	150Mylar	4	3
UHU plus Endfest 300	2.0	RT-DLaTGS	KBr	4	8
UHU plus Endfest 300	2.0	RT-DLaTGS	KBr	2	8
UHU plus Endfest 300	2.0	RT-DTGS-FIR	KBr	4	8
UHU plus Endfest 300	2.0	RT-DTGS-FIR	KBr	2	8
UHU plus Endfest 300	2.5	1.6K bolometer, 100 cm^{-1}	multilayerMylar	1	4
UHU plus Endfest 300	2.5	1.6K bolometer, 35 cm^{-1}	125Mylar	1	8
UHU plus Endfest 300	2.5	RT-DLaTGS	KBr	4	8
UHU plus Endfest 300	2.5	RT-DTGS-FIR	KBr	4	8
UHU plus Endfest 300	3.0	1.6K bolometer, 100 cm^{-1}	multilayerMylar	1	4
UHU plus Endfest 300	3.0	1.6K bolometer, 35 cm^{-1}	125Mylar	1	8

Acknowledgements

When the final high-school physics lecture was delivered, a restless whisper said, “This cannot be the end; the universe still holds countless mysteries.” Fueled by that conviction, I set out on a grand expedition toward a deeper understanding of nature’s foundations. The voyage has already passed spectacular landmarks — a bachelor-level expedition at the LHCb experiment (CERN) and a master-level adventure with the ECHo project — and now crowns its highest summit (so far) in this thesis. This towering ascent would never have been possible without a legion of extraordinary companions, to whom I owe profound gratitude.

First and foremost, I thank Dr. Hannes Rotzinger, who caught me in Heidelberg at the precise moment a new adventure was sought, and escorted me on the journey to Karlsruhe. The early PhD drives between the two cities, filled with spirited physics debates, supplied essential knowledge of the field and of KIT, necessary for the start in a new city and research field. Throughout the research Hannes has been the daily touchstone and guidance for every question — from laboratory experiments and clean-room fabrication to theoretical modelling.

I am deeply grateful to Prof. Alexey V. Ustinov for accepting me as a PhD student, for placing unwavering trust in my work, and for providing the freedom, generous infrastructure, and funding that created a fertile ground for the research to flourish. I also thank Prof. Mathieu Le Tacon for his time and interest as my second advisor.

My thanks extend to all current and former members of the research group. Their relentless tinkering in the lab, proofreading of my work, animated physics discussions, and the convivial moments shared at conferences have been indispensable. Special appreciation goes to Jonathan and Gabriel, whose meticulous clean-room efforts helped to produce the functional qubit samples that form the core of the thesis results. The delicate device fabrication would not have been possible without the extraordinary dedication of Lukas Radke, Dr. Silvia Divas, and Aina Quintilla.

The development of the experimental setup inside the cryostat required many small but essential tweaks. For this, the mechanical workshop under the leadership of Michael Meyer was of inestimable value, crafting custom parts over numerous iterations. I am also grateful to Dr. Yves Laurent Mathis and Dr. Biliana Gasharova for enabling the infrared–filter spectroscopy measurements, and to Robert and Lukas from the IPE for their prompt, insightful help with the time–domain measurement electronics.

Finally, endless encouragement from my family — foremost my parents and my brother — and friends — especially Ronja, Julia, Larissa and my volleyball team — sustained me through long evenings, weekends, sport and vacations, providing the rejuvenating breaks required for each new stride. A very special tribute goes to Marcel, whose relentless push, unwavering support, and caring presence prevented many moments of surrender and kept the expedition on course. Their belief in me was the wind in my sails during the inevitable doldrums of a PhD.

Karlsruhe, March 2026 Markus Griedel